Alternate Slicing and Deposition Strategies for Fused Deposition Modelling

Bin Huang

A thesis submitted to
Auckland University of Technology in fulfilment of the requirement for the degree of Doctor of Philosophy

January 2014

School of Engineering

Table of Contents

List of Figures v

List of Tables xiv

List of Publications xv

List of terms and Abbreviations xvii

FDM Terminology xix

Mathematical symbols used in the thesis xxi

Attestation of Authorship xxii

Abstract xxiv

Chapter 1 Introduction 1

1.1 From rapid prototyping to additive manufacturing 1

1.2 Additive manufacturing; processes and limitations 6

Stereolithography Apparatus (SLA) 6

Fused Deposition Modelling (FDM) 7

Selective Laser Sintering (SLS) 8

Selective Laser Melting (SLM) 9

Electron Beam Melting (EBM) 10

Laser Engineered Net Shaping (LENS) 11

Ink-Jet Printing (IJP) 12

1.3 Fused Deposition Modelling (FDM) 14

1.4 Mechanism of material consolidation in FDM and possible means of process enhancements 19

1.5 Research proposal 23

Chapter 2 Literature review, research gaps, questions and objectives 27

2.1 Background 27

2.2 Literature review....28
2.2.1 Fused Deposition Modelling; limitations and process evaluation 28
2.2.2 Mechanisms and mechanics of materials consolidation 42
2.2.3 Materials for FDM 45
2.2.4 Effects of raster orientation.... 51
2.2.5 Slicing strategies 54
2.3 Research gaps, hypotheses and questions 63
2.4 Methodologies and objectives 69
Chapter 3 Adaptive Slicing for Fused Deposition Modelling....72
3.1 Adaptive slicing; early attempts and general impressions....72
3.1.1 Basic adaptive slicing 73
3.1.2 Advanced adaptive slicing based on .stl files 80
3.1.3 Advanced adaptive slicing based on other format files 82
3.2 Mechanism of material consolidation and critical factors in FDM 85
3.3 Analytical modelling of the role of adaptive slicing 91
3.4 Time-dependent analytical modelling of the role of adaptive slicing 100
3.5 Experimental evaluation of adaptive slicing 107
Chapter 4 Raster orientation effects in FDM 119
4.1 The role of the raster angle in FDM 119
4.2 A preliminary experimental assessment of the role of raster angle....125
4.3 Tensile modulus vs. raster angle; an analytical model 130
4.4 Results and discussion based on the analytical models predicting the raster angle mechanics 142
4.5 Correlation between analytical and experimental results 152
Chapter 5 Curved Layer Slicing for FDM 159
5.1 Flat layer slicing; some shortcomings 159
5.2 Curved layer slicing....162
5.3 Current mathematical algorithms for curved layer slicing 165
5.4 Enhanced curved layer slicing models 171
Surface data collection from .stl format file 172

Surface data offsetting 175
Curved layer offsetting; some difficulties 181
Deposition path generation 184
5.5 Implementation and experimental evaluation of CLFDM 186
5.6 Role of Curved Layer Slicing and significant observations 193
Chapter 6 Integrated alternative slicing and deposition strategies for FDM 196
6.1 Alternative slicing and deposition strategies; a retrospective 196
6.2 Adaptive flat layer FDM; a practical implementation 198
6.3 Adaptive flat and uniform curved layer slicing; a comparison 206
6.4 Curved layer adaptive slicing 209
6.5 Mixed-mode slicing; combined flat and curved layer slicing 222
6.5.1 Dividing the total volume into different sub-regions 223
6.5.2 Reconstruction of flat layer regions 227
6.5.3 Combined flat and curved layer slicing 231
6.6 Integrated alternative slicing and deposition; some case studies 235
Case 1 238
Case 2 240
Case 3 242
6.7 Discussion on integrated alternative slicing and deposition strategies and conclusions 251
Chapter 7 Conclusions 259
7.1 Fused deposition modelling; some general observations 259
7.2 Analytical and experimental investigations and generic conclusions 261
7.3 Significant conclusions drawn based on the results of the current research 268
Adaptive flat layer slicing 268
Raster angle mechanics 269
Uniform curved layer slicing 270
Integrated alternative slicing 271
7.4 Future work 273
References 275

Appendices 288

Appendix 1 Evaluation of meso structures with varying print speed and raster angle orientations 288

Appendix 2 Evaluation of test result with varying print speed and build style.....297

Appendix 3 Load deflection of bending tests with varying printing speed.....301

List of Figures

Fig. 1.1 Swainson's photochemical process for 3D construction 3

Fig. 1.2 Schematic of the SLA Process 7

Fig. 1.3 Schematic of the FDM Process 8

Fig. 1.4 Schematic of the SLS Process 9

Fig. 1.5 Schematic of the EBM Process 11

Fig. 1.6 Schematic of the LENS or 3D Laser Cladding Process 12

Fig. 1.7 Schematic of the Ink-Jet Printing Process 13

Fig. 1.8 FDM process in detail 15

Fig. 1.9 Schematic of the Extrusion Head 16

Fig. 1.10 Warping due to thermal variations 19

Fig 1.11 Failure modes of the specimens: (a) FDM-axial (b) FDM-transverse (c) 3D printer-axial (d) Nano composite deposition system (NCDS)-axial 21

Fig. 2.1 Surface Errors 29

Fig. 2.2 Thin build layers better represent complex surfaces 30

Fig. 2.3 Internal Defects 32

Fig. 2.4 Improvement for sub-perimeter voids (a) Negative Offset, (b) Alternative Corner Turning and (c) Equidistant Path 33

Fig. 2.5 Non-sequential raster segments 35

Fig. 2.6 Geometrical features resulting in repeatability issues 38

Fig. 2.7 Bond formation process between two filaments: (1) surface contacting (2) neck growth (3) molecular diffusion at interface and randomization 43

Fig. 2.8 Uni-directional and laminate deposition styles (a) Unidirectional deposition with standard meso-structure, (b) Unidirectional deposition with skewed meso-structure and (c) Laminate configuration.....52

Fig. 2.9 Accurate exterior and fast interior procedure 56

Fig. 3.1 Uniform layer slicing..... 74

Fig. 3.2 Layers of varying thickness resulting from the basic adaptive slicing method 75

Fig. 3.3 A specific shortcoming of the basic adaptive slicing method 75

Fig. 3.4 Sliced results using the stepwise uniform refinement method 77

Fig. 3.5 Problem existing by using basic stepwise uniform refinement method 77

Fig. 3.6 A common problem with the basic adaptive slicing 79

Fig. 3.7 Adaptive slicing using the accurate exterior, fast interior method..... 81

Fig. 3.8 Slicing results based on local adaptive slicing 81

Fig. 3.9 Results of region-based adaptive slicing 82

Fig. 3.10 General meso-structure of an FDM part 85

Fig. 3.11 Bond formation process between two filaments: (1) surface contacting (2) neck growth (3) molecular diffusion at interface and randomization 86

Fig. 3.12 Neck growth evolution for ABS P400 at constant temperature (200˚C) 88

Fig. 3.13 Schematic of deposition and cooling of a filament in FDM process 89

Fig. 3.14 Model predictions for the dimensionless neck growth profile for ABS P400 90

Fig. 3.15 Cross-sectional area of a square shape with precise filling: (a) Single layer, (b) Two layers, (c) Three layers, and (d) Multi layers 93

Fig. 3.16 Coalescence, second moment of area, and bending load vs. number of layers based on the model for print speed effects (Speed of printing = 60mm/s) 98

Fig. 3.17 Coalescence, second moment of area, and bending load vs. print speed based on the model for print speed effects (No. of layers = 10) 98

Fig. 3.18 Two nozzles with different diameters 102

Fig. 3.19 Road shape of each cross-sectional area in two different nozzle settings 104

Fig. 3.20 Coalescence, second moment of area, and bending load vs. number of layers based on the model for print time effects (Total print time = 75s) 106

Fig. 3.21 Coalescence, second moment of area, and bending load vs. total time based on the model for print time effects (Number of layers =10) 106

Fig. 3.22 The experimental setup 108

Fig. 3.23 Load deflection diagrams from three point bending tests of thinner layer parts with print speed at 35 mm/s 112

Fig. 3.24 Load deflection diagrams from three point bending tests of thinner layer parts with print speed at 40 mm/s 112

Fig. 3.25 Load deflection diagrams from three point bending tests of thinner layer parts with print speed at 45 mm/s 112

Fig. 3.26 Load deflection diagrams from three point bending tests of thinner layer parts with print speed at 50 mm/s 113

Fig. 3.27 Load deflection diagrams from three point bending tests of thinner layer parts with print speed at 55 mm/s 113

Fig. 3.28 Load deflection diagrams from three point bending tests of thinner layer parts with print speed at 60 mm/s 113

Fig. 3.29 Comparison between analytical predictions and the experimental results using thinner layer printing (layer thickness of 0.5 mm) 114

Fig. 3.30 Comparison between analytical predictions and the experimental results using thicker layer printing (layer thickness of 1.0 mm) 115

Fig. 3.31 Stress vs. print speed and print time on prediction produced with layers of thickness 0.5 mm and 1.0 mm (part size 50mm X 20mm X 4mm) 117

Fig. 4.1 Process-dependent material structures (a) injection moulding part and (b) FDM part 120

Fig. 4.2 Definition of coordinates in a plate 121

Fig. 4.3 Tensile modulus vs. Raster angle orientation 124

Fig. 4.4 Test specimens with unidirectional orientation 126

Fig. 4.5 meso-structure of the FDM test specimen 127

Fig. 4.6 Experimental setup during a tensile test 128

Fig. 4.7 Load-elongation curve from the tensile test 129

Fig. 4.8 Raster angle results (a) Load versus raster angle and (b) Stress versus raster angle 130

Fig. 4.9 Force system in multi-strand component of a specific raster angle 132

Fig. 4.10 Internal resultant forces exerted on a FDM road section 133

Fig. 4.11 Cross-sectional area of a square shape with precise filling; (a) Single layer, (b) Two layers, (c) Three layers, and (d) Multi layers 133

Fig. 4.12 General dimensions and areas of FDM section; (a) Isotropic view area A_α , (b) front view area A_y, (c) side view area A_x , and (d) top view A_α 134

Fig. 4.13 General deformation of the FDM section; (a) normal stress on the random section, (b) strain in the x-direction, (c) strain in the y-direction, and (d) shear strain 134

Fig. 4.14 Strain in transverse and axial direction; (a) transverse and (b) axial 136

Fig. 4.15 Resultant forces on a single strand of the FDM part 141

Fig. 4.16 Theoretical normal stress versus raster angle 144

Fig. 4.17 Theoretical normal strain versus raster angle 145

Fig. 4.18 Theoretical tensile modulus versus raster angle 146

Fig. 4.19 Theoretical shear stress versus raster angle 149

Fig. 4.20 Theoretical shear strain versus raster angle 150

Fig. 4.21 Theoretical shear modulus versus raster angle 151

Fig. 4.22 Correlation between experimental analytical values of normal stress 152

Fig. 4.23 Strength of unidirectional ABS material with aligned configuration against raster angle reported by Rodriguez et al. 153

Fig. 4.24 Correlation between experimental and analytical values of normal stress 154

Fig. 4.25 Theoretical prediction of the variation of Poisson's ratio with varying raster angle and coalescence 156

Fig. 4.26 Plastic spin versus raster angle with varying coalescence 157

Fig.5.1 Fabricating a thin shell type part in FDM 160

Fig. 5.2 Fabricating a slight curved part in FDM 160

Fig. 5.3 Geometrical forms that cannot be handled even with the best-build orientation method: (a) thin shell hemispherical shape and (b) bi-directional curved part 161

Fig. 5.4 The concept of Curved Layer deposition: (a) A curved model, (b) flat layers, (c) Curved layer and (d) An application 163

Fig.5.5 Solid model of the test part and cutter path data: (a) Solid model and (b) Top surface cutter path data 167

Fig. 5.6 Deposition path data based on a free form surface 167

Fig. 5.7 Modified cross product method considering nodes on a vertical plane 169

Fig. 5.8 Selection of surface facets for the support structure 170

Fig. 5.9 Support structure deposition path generation 170

Fig. 5.10 Continuity of the top surface 173

Fig. 5.11 Facet grouping procedure 174

Fig. 5.12 Top facet grouping 175

Fig. 5.13 Reference surface on the CAD file and facet offsetting for curved layer slicing 176

Fig. 5.14 Typical situations in the offsetting procedure; (a) Two imaginary vertical auxiliary planes, (b) One adjacent linked facet and an imaginary auxiliary vertical plane, and (c) Two adjacent linked facets 177

Fig. 5.15 Curved layer slicing based on facet-offsetting 181

Fig. 5.16 Curved slicing of the model with slanted side surfaces 182

Fig. 5.17 Curved layer offsetting based on the top reference surface 182

Fig. 5.18 Unconnected points after offsetting 182

Fig. 5.19 Deposition path generation; (a) a standard .stl file and (b) slicing a triangulated object 184

Fig. 5.20 An example of how the .stl file is sliced and tool path generated for CLFDM; (a) .stl Model, (b) Curved layer slicing, and (c) deposition path generation 186

Fig. 5.21 Parts printed using Fabepoxy: (a) Flat layers and (b) Curved layers 187

Fig. 5.22 Test part loaded for 3-point bending test 188

Fig. 5.23 Combined tool path of FDM part, support structure and raft 190

Fig. 5.24 The test piece printed by curved layer FDM on the Makerbot system 190

Fig. 5.25 Flat and curved parts printed using ABS polymer; (a) Flat layer part, (b) Curved layer part, and (c) continuous filaments in CLFDM 191

Fig. 5.26 Load deflection diagrams from tensile tests: (a) Flat layer parts and (b) Curved layer parts 192

Fig. 5.27 Close-up views of deformation patterns: (a) Flat layer FDM and (b) Curved layer FDM 194

Fig. 5.28 SEM photos of factures: (a) Flat layer FDM and (b) Curved layer FDM 194

Fig. 6.1 Issues arising out of uniform flat layers; (a) cusp height, (b) missing features, (c) negative error (Left) and positive error (Right), and (d) missing surface profile 199

Fig.6.2 Layer thickness and cusp height geometry 200

Fig. 6.3 Adaptive slicing based on the cusp height criterion 201

Fig. 6.4 Evaluation of the residual height; (a) tessellated .stl file, (b) sliced facets grouped together, and (c) the residual height consideration 202

Fig. 6.5 Adaptive slicing using (a) cusp height criterion alone and (b) both cusp and residual height criteria 204

Fig. 6.6 Adaptive flat layer slicing applied to the light-curved part; (a) adaptive slices and (b) raster paths 204

Fig. 6.7 Uniform flat layer slicing and raster path generation for the light-curved part 207

Fig.6.8 Uniform and adaptive flat layer and uniform curved layer parts printed with ABS polymer 208

Fig. 6.9 Area definitions for a .stl format file 211

Fig. 6.10 Offsetting adaptive curved layers; (a) .stl file, (b) upper and lower limits of the top surface, (c) offset zone, and (d) offset curved layer 212

Fig. 6.11 Curved layer adaptive slicing issues; (a) upside-down offsetting, (b) unconnected points, (c) multi nodes, and (d) facet reconstruction 213

Fig. 6.12 Voids or interference caused by deleted facets 214

Fig. 6.13 overall scheme of the curved layer adaptive slicing algorithm 215

Fig.6.14 A light-curved part with bevelled end faces 216

Fig. 6.15 A light-curved part with a fine projecting feature 216

Fig.6.16 Adaptive curved layer slicing of a .stl format file and raster path generation 217

Fig.6.17 Adaptive curved layer slicing and deposition path generation; (a) three-central-layers, (b) two-central-layers, and (c) one-central-layer 220

Fig. 6.18 Adaptive curved layer specimens printed; (a) three-central-layers, (b) two-central-layers, and (c) one-central-layer 220

Fig. 6.19 Issues with flat layer deposition and solutions; (a) bending phenomenon during deposition, (b) Multi-layer solution, and (c) reduced gaps 224

Fig. 6.20 Boundary connection between flat and curved layers; (a) ideal connection, (b) tool path connection, and (c) actual connection 225

Fig. 6.21 Bending deposited strands; (a) uniform load forming a gap of deflection and (b) geometrical relationship of the chordal deflection between two consecutive layers 226

Fig. 6.22 Facets on the side face crossing the boundary between flat and curved regions 228

Fig. 6.23 Reconstruction of the flat layer region by offsetting points 229

Fig. 6.24 reconstruction of flat layer region using the existing facets 230

Fig. 6.25 Point-selection criteria for facet reconstruction 231

Fig. 6.26 Sample part with a curved surface; (a) .stl file, (b) subdivision into zones and slicing, (c) tool path generation, (d) actual printed part with support structure, and (e) final part 233

Fig. 6.27 Sample part with a curved surface and a cut out feature; (a) .stl file, (b) zone subdivision and slicing, (c) tool paths generation, (d) actual printed part with support structure, and (e) final part 235

Fig. 6.28 overall scheme of the integrated alternative slicing scheme 237

Fig. 6.29 Integrated slicing in Case 1; (a) identification of the top surface, (b) segregation of curved and flat layer zones, (c) adaptive curved layer slicing, (d) restructuring the flat layer zone in .stl form, and (e) adaptive flat layer slicing in the flat layer zone 239

Fig. 6.30 Case 1; deposition paths generated; (a) 30° raster orientations and (b) 90° raster orientations 240

Fig. 6.31 Case 1; practical implementation (a) 30° raster orientation and (b) 90° raster orientation 240

Fig. 6.32 Case 2; a more general solid model 242

Fig. 6.33 A more complex solid model (bearing housing); (a) .stl format file and (b) top and bottom surfaces 243

Fig. 6.34 Generation of sub-zones; (a) Zone A, (b) Zone B, (c) Zone C, (d) Zone D, and (e) Zone E 243

Fig. 6.35 Curved layer slicing and rasterisation in the upper part of zone A 244

Fig. 6.36 Adaptive curved layer slicing and rasterisation in the bottom portion of Zone A 245

Fig. 6.37 Adaptive flat layer slicingin Zone B 246

Fig. 6.38 Uniform curved layer slicing in Zone C 247

Fig. 6.39 Uniform curved layer slicing in Zone D 248

Fig. 6.40 Adaptive flat layer slicing in Zone E 250

Fig. 6.41 Building the bearing housing from the bottom upwards 250

Fig. 6.42 Integrated alternative slicing scheme applied to the bearing housing 251

Fig. 6.43 A Comparative evaluation of printed samples in Case 1 252

Fig. 6.44 A comparative assessment in case 2; (a) CAD drawing, (b) processed using integrated slicing, and (c) processed using uniform flat layer slicing 254

Fig. 6.45 Case 3: Uniform flat layer slicing with thinner layers (a) overall view, (b) top circular profile, (c) central hole, and (d) the curved side fillet 256

Fig.6.46 Case 3: Uniform flat layer slicing with thicker layers (a) overall view, (b) top circular profile, (c) central hole, and (d) the curved side fillet 256

Fig. 6.47 Case 3: Integrated alternative slicing (a) overall view, (b) top circular profile, (c) central hole, and (d) the curved side fillet 257

List of Tables

Table 3.1 Mechanical properties of the test material (ABS) 109

Table 3.2 Results from three point bending tests on specimens produced with thin layers of 0.5 mm thickness 114

Table 3.3 Results from three point bending tests on parts produced with thick layers of 1.0 mm thickness 115

Table 3.4 Comparative performance of thin and thick layer samples with different build time settings 116

Table 4.1 Tensile test result for different raster orientation 129

Table 5.1 Results of three-point bending tests for different deposition strategies 192

Table 6.1 layer thicknesses and ranges of angles 201

Table 6.2 Included angle and layer thickness combinations together with residual heights 203

Table 6.3. Three point bending results comparing uniform and adaptive flat layer and uniform curved layer slicing 209

Table 6.4 Results of three point bending tests on specimens produced with adaptive curved layer printing 221

Table 6.5 Comparative build times for different deposition strategies 233

List of Publications

Journal Articles

1. Singamneni, S., Roychoudhury, A., Diegel, O., and **Huang, B.,** (2012). "Modelling and evaluation of curved layer fused deposition," Journal of Materials Processing Technology 212(1): 27-35.

2. **Huang, B.,** and Singamneni, S., (2012). "Slicing and Speed and Time Dependent Consolidation Mechanisms in Fused Deposition Modelling," Accepted for publication, and currently in print, Proceedings of the Institution of engineers UK, Part B, Journal of Engineering Manufacture.

3. **Huang, B.** and Singamneni, S., (2013). "Raster angle mechanics in Fused Deposition Modeling," Accepted for publication, and is currently in press, Journal of Composite Materials.

4. **Huang, B.** and Singamneni, S., (2013). "Curved Layer Adaptive Slicing (CLAS) for Fused Deposition Modelling," Accepted for publication, and currently in print, Rapid Prototyping Journal.

5. **Huang, B.** and Singamneni, S., "A mixed layer approach combining both flat and curved layer slicing for fused deposition modelling," Accepted for publication, and currently in print, Proceedings of the Institution of engineers UK, Part B, Journal of Engineering Manufacture.

Conference papers turned into journal articles

1. Singamneni, S., Joe, R., A., and **Huang, B.,** (2012). "Adaptive Slicing for Fused Deposition Modeling and Practical Implementation Schemes." Advanced Materials Research 428: 137-140.

2. **Huang, B.** and Singamneni, S., (2012). "Alternate slicing and deposition strategies for fused deposition modelling of light curved parts." Journal of Achievements in Materials and Manufacturing Engineering 55(2): 511-517.

3. **Huang, B.** and Singamneni, S., (2013) "Curved Layer Fused Deposition Modeling with Varying Raster Orientations." Applied Mechanics and Materials 446 (2014): 263-269.

Conference Publications

1. Singamneni, S., Joe, R., A., **Huang, B.,** (2011). Adaptive slicing for Fused Deposition Modelling and practical implementation schemes. International Symposium on Material Science and Engineering Technology, ISMSET 2011, Dubai, UAE.

2. **Huang, B.** and Singamneni, S., (2012). Evaluation of Deposition Strategies for a Curved Fused Deposition Modeling Part. GCMM2012. Auckland, New Zealand.

3. Singamneni, S., **Huang, B.,** and Davidson, K., (2012). Polystyrene in granular form for Fused Deposition Modeling. In Proceedings of the ASME/ISCIE International Symposium on Flexible Automation, ISFA 2012 (pp. 469-473).

4. **Huang, B.,** and Singamneni, S., (2013). "Curved Layer Fused Deposition Modeling with Varying Raster Orientation", Asia Conference on Mechanical and Material Engineering (ACMME 2013), Oct.8-9, 2013, Wuhan, China.

List of terms and Abbreviations

.amf or AMF: Additive Manufacturing Format

.dxf or DXF: Drawing Exchange Format

.stl or STL: Stereolithography format

3DP: Three Dimensional Printing

ABS: Acrylonitrile-Butadiene-Styrene

AM: Additive Manufacturing

ASTM: American Society for Testing and Materials

BPM: Ballistic Particle Manufacturing

CAD: Computer Aided Design

CAM: Computer Aided Manufacturing

CLFDM: Curved Layer Fused Deposition Modeling

CLLOM: Curved Layer Laminated Object Manufacturing

CLI: Common Layer Interface

CNC: Computer Numerical Control

EBM: Electron Beam Melting

FDC: Fused deposition of Ceramics

FDM: Fused Deposition Modeling

FDMC: Fused Deposition of Multiple Ceramics

FDMM: Fused Deposition Modelling of Metals

FLC: filament location curve

IGES: Initial Graphics Exchange Specification

IJP: Ink-Jet Printing

MED: mini extruder deposition

MLS: moving-least square

LDNI: Layer Depth Normal Image

LENS: Laser Engineered Net-Shaping

LOM: Laminated Object Manufacturing

NCDS: Nano composite deposition system

NURBS: Non-Uniform Rational B-Spline

PCL: poly caprolactone

PMMA: poly methylmethacrylate

PVA: Polyvinyl alcohol

RM: Rapid Manufacturing

RP: Rapid Prototyping

RT: Rapid Tooling

SLA: Stereolithography apparatus

SLM: Selective Laser Melting

SLS: Selective Laser Sintering

STEP: Standard for the Exchange of Product

UV: ultraviolet

FDM Terminology

Chordal approximation: Also called chord approximation means use of a series of straight line segments to represent a curve. The maximum distance between the straight segment and the curve is close and within acceptable tolerance limits.

Cusp Height: the maximum perpendicular distance between the line joining two points and a third point below the line.

Meso-structure: The structure between micro structure and macro structure. This structure is visible compared to microstructure but not determining the final property by the individual structure compared to macro structure.

Roads: The printed strands in fused deposition modelling are referred to as roads

Inter-road bonding: The bonding between strands in the meso-structure.

Staircase effects: Due to layer-by-layer fabrication, external surfaces of parts made by FDM often suffer from a loss of quality. Uniform flat layers used to build inclined or curved surfaces clearly show these errors as stair-case effects

Sub-perimeter voids: One of the defects that can occur in filament based manufacturing resulting from changes in the direction of the printed strands.

Raster angle: The angle at which individual strands are printed with reference to the longitudinal axis of the printed part.

Mathematical symbols used in the thesis

Γ: Surface tension

μ: Material viscosity

T: processing temperature

R: Universal gas constant

ρ: void density

E: Tensile module

G: Shear module

v: Poisson's ratio

t: Time

σ: Stress

M: Bending moment

d: Distance from the neutral axis

I: Second moment of area

C: Coalescence

v: Velocity

τ: Shear stress

ϵ: Strain

γ: Shear strain

ω: Plastic spin

Note: Please note that the equations included from other references use different symbols, as explained along with each equation individually

Attestation of Authorship

I hereby declare that this submission is my own work and that, to the best of my knowledge and belief, it contains no material previously published or written by another person (except where explicitly defined in the acknowledgement), nor material which to a substantial extent has been submitted for the award of any other degree or diploma of a university or other institution of higher learning.

Acknowledgements

There are a number of people without whom this thesis might not have been written, and to whom I am greatly indebted. I would like to express my profound gratitude to the primary supervisor, Assoc. Professor Sarat Singamneni, for his valuable support, encouragement, supervision and useful suggestions throughout this research work. His moral support and continuous guidance enabled me to complete my work successfully. I am also thankful to Prof Olaf Diegel and Prof Thomas Neitzert for being the second supervisors at different times during the course of this research.

I am also grateful to AUT Additive Manufacturing Research Centre and the School of Engineering for providing me with all the experimental and computational facilities. In particular special thanks are due to the University for funding this research through a Faculty Contestable Grant which provided partial support for me and also allowed the necessary equipment to be procured.

I am as ever, especially indebted to my wife, Yizhen Yuan, and my parents, Mr. Zexi Huang and Mrs. Jiqing Xu, for their love and support throughout my life. I am also thankful to Mr. Kevin Huang, Mr. Vincent Zhang, and Mr. Adrian Law, who guided me giving proper direction to my studies and life in New Zealand from the beginning. Moreover, my sincere thanks go to my friends, who shared their experiences with me.

Bin Huang

Abstract

Fused deposition modelling is one of the most widely used rapid prototyping processes, considering the relative simplicity, availability, and ease of use. The proliferation of numerous systems at all possible price ranges led to a more widespread usage recently. A semisolid polymer such as acrylonitrile butadiene styrene (ABS) is deposited line-by-line, to build three dimensional objects in layers. Being capable of desk-top manufacturing, the process finds wide application in a variety of situations, be it making a mould for the rapid production of an industrial tool or the production of models for preoperative planning of complex cranial reconstructive surgery.

While these are predominantly prototyping applications, fused deposition modelling is capable of direct production of end-use parts and believed to be a possible replacement for injection moulding in specific applications. However, there are shortcomings such as inferior material attributes, flat layer deposition resulting in poor surface and part qualities, and undesirably higher number of layers in specific cases leading to high production times, which need to be resolved before realising the full potential of the process.

Attempts are made in the past by means of varying raster orientations, adaptive flat layer and even curved layer slicing and deposition schemes to overcome some of the shortcomings with fused deposition modelling. While stair case effects can be minimised to varying degrees by adaptive flat layers, mechanical properties are plausibly enhanced by curved layers, due to continuity in fibres and the possible elimination of inter-layer weaknesses. Further, the mechanism of material deposition and the mechanics of subsequent consolidation involve time

and temperature dependent inter-strand and inter-layer sintering. Overall, the internal meso-structure is characterised by the partly fused polymer strands and the intertwining air gaps.

Research efforts in different directions, attempting improvements in materials as well as deposition techniques as evident in the literature, allowed some progress towards betterment. Although these improvements, especially in slicing algorithms led to significant progress in FDM processing, the part surface quality and geometric accuracy are still a major concern. Reducing build time and increasing part surface quality are two factors that contradict each other. Though proclaimed to be a solution to both, practical implementation of adaptive slicing has been limited and there is very little understanding of the typical influences of speed and time of printing on the mechanics of material consolidation and the ensuing meso-structures. Curved layer slicing on the other hand evolved as a means of improving surface quality and fibre continuity, but can only be effective in certain regions, close to curved outer surfaces of specific solid models.

Considering all these aspects, process enhancements are envisioned in fused deposition modelling, through identification of proper combinations of different slicing and deposition schemes together with appropriate raster orientations. This forms the basis for the current research, envisioning better solutions, combining different slicing and deposition strategies, targeting the most favourable meso-structures in order to achieve the best mechanical and surface qualities for a given part.

Theoretical and experimental evaluation of the mechanics of adaptive slicing and raster orientation effects need to be undertaken first, in order to understand the underlying principles

governing the typical aspects of fused deposition modelling. Development of mathematical algorithms and practical implementation schemes will follow next, considering different slicing and deposition strategies, evaluating their abilities both individually and in combinations. Based on the results, different approaches will be integrated into an overall selection algorithm to develop the best combination of slicing and raster orientation schemes for processing different zones of specific components with given print orientations.

The analytical and experimental evaluations on adaptive slicing and the ensued results established that the inter-road and inter-layer coalescence depends on the filament size as well as the sintering time allowed for a unit length of deposition. Evidently, a proper adjustment of filament size, print speed and total time of printing will be essential to realise the true benefits of adaptive slicing. Raster angle orientation is found to significantly influence the overall characteristics of materials built layer-by-layer. Practical implementation and experimental results showed curved layer printing to be effective in improving the surface quality as well as the part strength as a result of the fibre continuity. Slanting side surfaces and projecting finer details in specific solid models are sufficiently resolved using adaptive flat and curved layer slicing. The integrated alternative slicing approaches performed well developing appropriate slicing schemes in different regions of specific solid models. Overall, different approaches help overcome different shortcomings of fused deposition modelling, but a combination of several possible alternatives is usually the best solution for a given part. Due consideration must be given to the internal mechanics and the resulting meso-structures in order to establish the best combination of the alternative slicing and deposition schemes available for fused deposition modelling.

Chapter 1 Introduction

1.1 From rapid prototyping to additive manufacturing

Traditional manufacturing by means of material removal, also known as subtractive manufacturing dominated the manufacturing industry for years, in particular with components of complex shapes. In the past half century, manufacturing techniques of this kind were greatly improved with the help from Computer Aided Design (CAD) and Computer Aided Manufacturing (CAM). Computer Numerical Controlled (CNC) machining together with CAD and CAM approaches formed the basis for the production in most situations requiring for complex three dimensional shapes. However, subtractive processes are time consuming due to the repetitive nature of the process, require complex tooling and prove to be expensive, as material is removed. Also, it becomes increasingly difficult while handling parts with complex features like undercuts and re-entrant sections. Other manufacturing techniques help to varying degrees, but for most part are better adopted economically for large runs when mass production is needed, considering complex tooling requirements, which in turn depend on subtractive manufacturing.

The global economy and competition drove manufacturers towards rapid product development and the ever increasing demand to market goods as fast as possible. Two significantly challenging tasks arose as a result; (1) substantial reduction in product development times and (2) improvement in flexibility for manufacturing small batch size products and a variety of types of products [1]. The main bottleneck is often the early design stage, in terms of making

prototypes and testing. Computer-Aided Design and Manufacturing (CAD and CAM), together with Computer Numerically Controlled (CNC) programming and proper process planning strive to narrow the gap between conceptual design and mass manufacturing stages with any new product. However, there were problems still, in terms of achieving rapid creation of 3D prototypes and functional parts and cost-effective production of patterns and moulds with complex surfaces [2].

Realising the need for the automatic generation of complex 3D objects in physical reality, Wyn Kelly Swainson envisioned a photochemical process and an embodiment device design, with patent numbers 4041476 [3], and 4288861 [4] respectively. In Swainson's design, as shown in Fig. 1.1, the medium of the object has two active components, such as thermo-chromic or photochromic elements. These elements are selectively sensitive to dissimilar parameters of electromagnetic radiation. Two radiation beams focused on the medium make activation occurring inside the medium to form a real image element. Then the radiation beams trace the coordinates on the figure and continue to activate the medium until the object is fully constructed.

The first commercial implementation of Rapid Prototyping (RP) began through the mid-eighties with Charles W. Hull bringing forth the Stereolithography apparatus (SLA) technique in 1986, through the U.S Patent No.4575330 [5] which marks the beginning of the RP era. The following decade saw RP gaining further momentum through new technologies emerging such as Fused Deposition Modelling (FDM), Laminated Object Manufacturing (LOM), Ballistic Particle Manufacturing (BPM), Three Dimensional Printing (3DP), Selective Laser Sintering (SLS), etc. Product features, quality, cost, and time to market are important factors for manufacturers to be

competitive. RP systems provided opportunities for reduction in cost and risk, early visualization of product design, and time conservation.

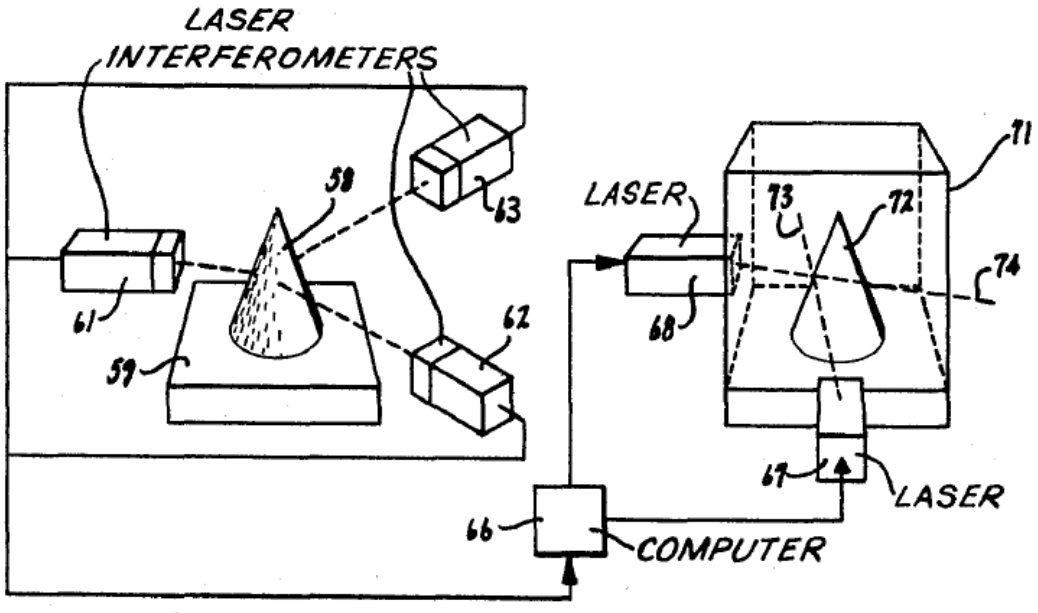

Fig. 1.1 Swainson's photochemical process for 3D construction (Image source: Swainson [3]**)**

The product development time usually depends on how early the designers can visualize the prototype product during the design process and Rapid Prototyping processes filled this gap through the layer-by-layer fabrication of three-dimensional physical models directly from computer-aided design (CAD) models [6]. Virtual designs from CAD or some other animation Modelling software are transformed into thin, horizontal layers and then stacked together in physical space, one over the other until the physical model is completed.

During the initial stages, RP technologies were mainly used to produce models and prototype parts for visualization and at times physical testing of certain products like airfoils in the wind tunnel. Subsequently, RP systems also played a significant role in the rapid production of industrial tooling, often referred to as Rapid Tooling (RT); polymer prototypes used as sacrificial

patterns to produce moulds for investment casting, rapid casting of non-ferrous products using 3D printed moulds are a couple of examples. The purpose of RT is not directly manufacturing the final functional product, but rapidly developing tools for mass production [7]. However, with both process and material enhancements, certain RP techniques overcame the initial stages of infancy and emerged as promising methods for producing functional end-use parts directly from CAD files. With Fused Deposition Modelling, Selective Laser Sintering and Selective Laser Melting at the forefront, the scenario gradually changed from Rapid Prototyping and tooling to Rapid Manufacturing (RM).

Defined as "the manufacture of end-use products using additive manufacturing techniques (solid imaging)" [8], Rapid Manufacturing allows for the generation of final functional components and parts direct from geometry files. These final components need to be used for the entire product life cycle or for defined minimal periods with wearing parts [9]. RM may involve production of custom or replacement parts in short run or series production scenarios; the common benefit in all these cases is being able to produce parts direct from digital data. Further, RM eliminates the need for complex tooling, thus enhancing the flexibility and freedom of manufacturing, apart from further advantages in speed and cost, compared to traditional approaches like injection molding or die casting.

While the evolution of rapid prototyping into rapid tooling and then into rapid manufacturing continued, there has been an increased commercial use of the technologies and in 2009, the ASTM F-42 committee announced Additive Manufacturing (AM) as a common term to describe all these processes [10]. According to their first standard, additive manufacturing is defined as:

"*The process of joining materials to make objects from 3D model data, usually layer upon layer, as opposed to subtractive manufacturing technologies*."

Additive manufacturing encompasses all technologies that allow Rapid Prototyping (RP), Rapid Tooling (RT), Rapid Manufacturing (RM), and production customizations. The past three decades saw the development of additive manufacturing from simple 3D printers used for rapid prototyping in non-functional resin to sophisticated rapid manufacturing of end-use products without any complex tooling and other intermediate processes. Apart from all the benefits associated with RP, RT, and RM, additive manufacturing also has lesser environmental impact and other potential benefits as follows over conventional manufacturing [11]:

- Efficient use of raw materials/feedstock. When machining a part in conventional cutting material, up to 80-90 percent of the material becomes scrap. By using additive manufacturing process, the scrap rate can be reduced to 10 percent or less.
- Reduction in the use of energy-inefficient processes.
- Reduced need for fixed asset tooling. Additive manufacturing processes are more adaptive and require fewer pieces of specialty capital equipment.
- Lighter parts. Bulky and complex structures can be reduced. Concomitant transportation and fuel efficiencies can be improved.
- More efficient heating or cooling channels, fluid paths, and other internal features that are not producible using conventional techniques.
- Potential for more localized production. Products can be downloaded and manufacturing locally, supplanting long distance transport and associated fuel.

- Inventory and warehousing can be reduced. Additive manufacturing process makes on-demand manufacturing possible.
- Consolidation of many parts into one. Additive manufacturing processes reduce tooling and manufacturing, part numbers, assembly, certification paper work, and maintenance.

Eventually, Additive Manufacturing has emerged from its early days as a prototyping process into a set of advanced processes that are becoming increasingly accessible to businesses, government organisations, and individual consumers. Although the industry has grown significantly in recent years, opportunities remain for advancing the state of additive manufacturing and furthering its economic, educational, and environmental benefits.

1.2 Additive manufacturing; processes and limitations

There are about half a dozen technologies that saw commercial viability and qualify with varying degrees for additive manufacturing. The most important ones are reviewed here, before converging on the process to be investigated further as part of this work.

Stereolithography Apparatus (SLA)

Introduced by Charles W. Hull and then commercialized by 3D System, Inc., Stereo-lithography uses a programmed beam of ultraviolet (UV) light directly focused on a photo-curable liquid to solidify a thin layer of solid out of the liquid. The spot on the surface moves along with the movable UV light source to form a solid cross-section of the object. Then, the object moves down from the liquid surface by the thickness of one layer, and the next section is formed adhered to the previous layer. This process is continued until the entire object is formed. A

newer version of the SLA process called micro stereo-lithography is developed with a higher resolution allowing for layers of thickness less than 10 μm to be achieved [12]. Fig. 1.2 shows the basic schematic of the SLA process.

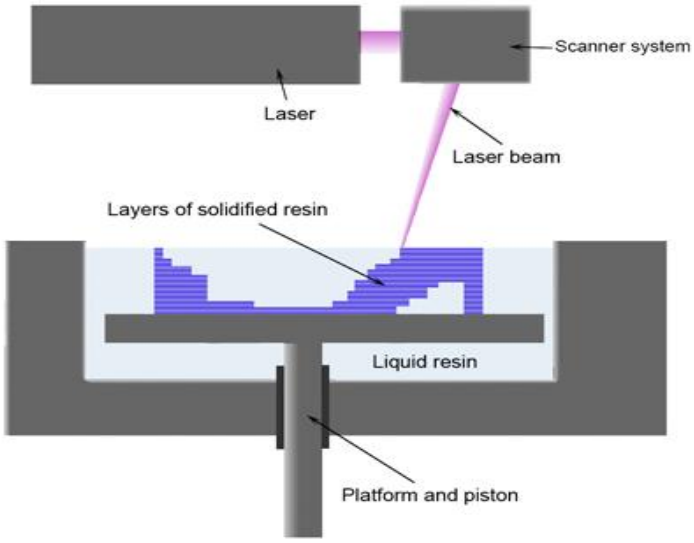

Fig. 1.2 Schematic of the SLA Process (Image source: Wikipedia [13])

Fused Deposition Modelling (FDM)

S. Scott Crump invented an apparatus using a movable dispensing head with a supply of material which solidifies at a predetermined temperature to form a three-dimensional object [14] (United States Patent Number 5121329), which became known as Fused Deposition Modelling (FDM). In this apparatus, the material is heated to be in a fluid or half molten state in the dispensing head. Heating temperature is set to be 1˚C higher than the solidification temperature. The material in the fluid state is flown out at a rate controlled by a computer. Then the material adheres onto a substrate or base in the form of a thin layer. The base rests on a movable

horizontal work platform. The work platform is controlled by a computer to form the cross-section of the shape. Once the cross-section is done, the Z axis lifts the dispensing head up to the next level and continues the deposition. The entire process continues until the 3D object is formed. Compared to SLA, this method allows for various materials, including waxes, thermoplastic resins, and metals in specific forms to be used to print three-dimensional shapes. Fig. 1.3 shows the basic schematic of the FDM process and a more detailed discussion of this will be presented later.

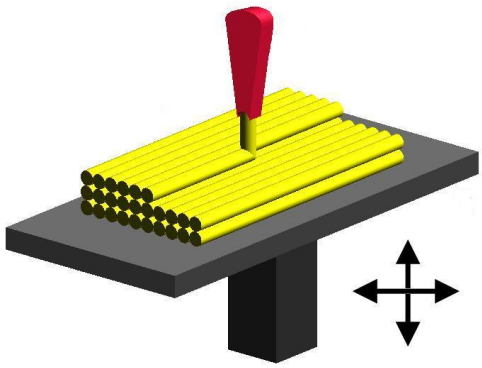

Fig. 1.3 Schematic of the FDM Process (Image source: Wikipedia [15])

Selective Laser Sintering (SLS)

Carl R. Deckard developed and patented the Selective Laser Sintering (SLS) process in 1989 [16]. In this process, a laser control system directs the laser beam and modulates the laser to selectively sinter a layer of the powder dispensed into the target area. The control system operates to selectively sinter only the powder disposed within defined boundaries to produce the desired layer of the part. Once a layer is done, the work platform lowers by one layer thickness.

A new layer of powder is spread on top of the previous layer and the sintering process coalescence powder particles within a layer and between successive layers. The process is repeated until the required part is built and Fig. 1.4 shows the basic schematic of the SLS process.

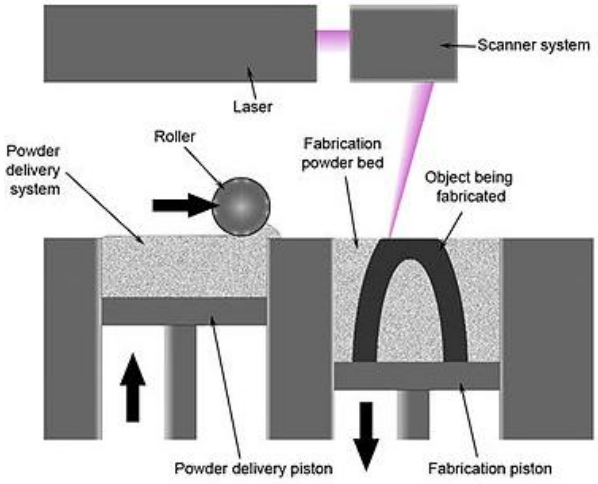

Fig. 1.4 Schematic of the SLS Process (Image source: Wikipedia [17])

Selective Laser Melting (SLM)

Markus Lindemann and Daniel Graf of Germany envisioned the Selective Laser Melting (SLM) process and patented it in Germany, and later developed a SLM system in 2002 based on the US Patent Number 7047098 [18]. In this process, a layer of powder is applied to a leveling device from a reservoir. A focused laser beam is used to melt the powder which further solidifies on the substrate or the previous layer to form the shape of the current layer. The energy of the laser beam is used to completely melt the powder over the entire layer thickness at the point of the incidence. The laser beam is guided over the predetermined area of the powder layer in a

plurality of tracks and successive laser tracks overlap the preceding tracks. At the same time, a shielding gas atmosphere is maintained above the zone of interaction between the laser and the metallic powder in order to avoid defects caused by oxidation. Further, like in other processes, the powder bed is lowered by a layer thickness, a new layer of powder is dispersed on the bed and the process is repeated until the 3D part is completely sintered. The schematic of SLM is similar to that of SLS, but, SLS usually melts powder particles only partially, while SLM is based on full melting, with the resulting internal structures more even and the inter-particle bonds stronger.

Electron Beam Melting (EBM)

Ralf Larson introduced the Electron Beam Melting (EBM) system, for cost-effective and quick manufacturing of models, prototypes or finished products, and patented it in 1998 [19] which was eventually commercialized by Arcam AB Limited in Sweden. This system includes an energy producing device, which comprises of at least one electrode, forming one of the poles in a circuit. The other pole is constituted of the said medium, which is electrically conducting or semi conducting when connected to the voltage source. Energy waves are formed between the electrode and the medium in the form of electric arc or heat, the physical characteristics of particles in the selected area are changed and the powder particles are connected together as a result of the energy waves. The EBM process operates at elevated temperatures, typically between 700 and 1000 ℃, producing parts that are virtually free from residual stresses, and eliminating the need for heat treatment after the build. Compared to SLM, EBM generally has a superior build rate because of its higher energy density and scanning method. Fig. 1.5 presets the basic schematic of the EBM process.

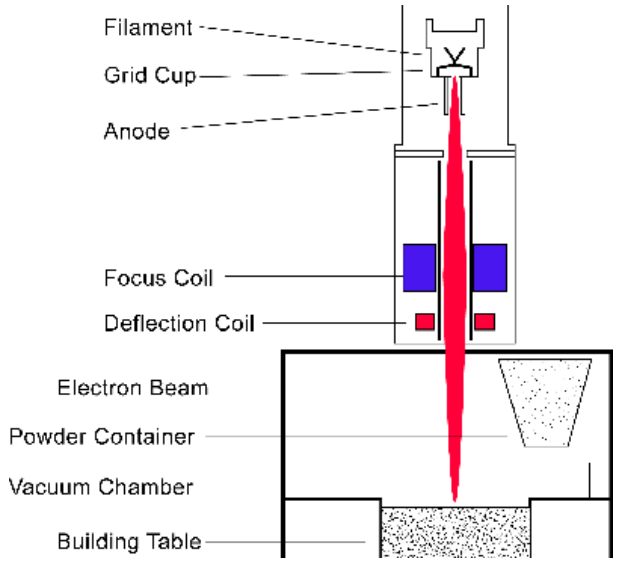

Fig. 1.5 Schematic of the EBM Process (Image source: EE Times [20])

Laser Engineered Net Shaping (LENS)

Jeantette et al. [21] from Sandia National Laboratories developed the method and a system for producing objects of complex shapes by means of Laser Engineered Net-Shaping (LENS). Later, a more realistic system [22] was developed from the same laboratory to fabricate complex three-dimensional shapes, which are ready or nearly ready for use. The LENS system, also known as 3D laser cladding system, includes unique components to ensure uniform and continuous flow of powdered materials. A laser beam strikes a growth surface to form a molten puddle or pool. Feed powder is injected into the molten puddle from a converging flow and a portion of the feed powder becomes incorporated into the molten puddle and forces some of the puddle contents to freeze on the growth surface in order to add the layer of material. The control unit ensures that the molten powdered materials can form complex, three-dimensional, near net-shaped objects.

Compared to other additive manufacturing processes, LENS can produce components with material densities varying from 90% of theoretical to fully dense, as well as a variety of controlled physical properties. Furthermore, two or more different materials can be composited and the components can be transitioned from one material to another. Fig. 1.6 shows the basic schematic of LENS.

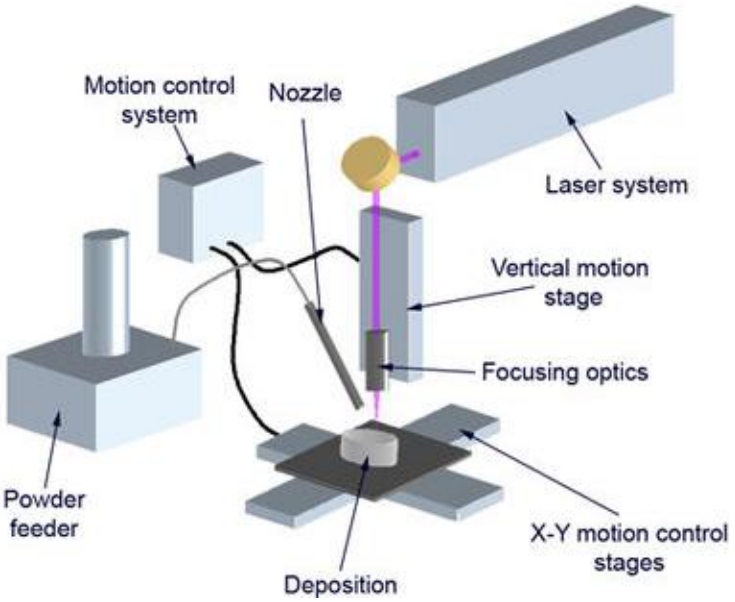

Fig. 1.6 Schematic of the LENS or 3D Laser Cladding Process (Image source: Wikipedia [23])

Ink-Jet Printing (IJP)

Hanan Gothait developed a 3-D printing system by using at least one row of ink-jet nozzles for ejecting interface materials [24] which was later commercialized by Objet Geometries Ltd. As depicted in Fig. 1.7, the system includes a print head having a plurality of nozzles, a dispenser connected to the print head for selectively dispensing interface materials in layers and a curing means for optionally curing each of the layers deposited. The depth of each deposited layer is

controlled by selectively adjusting the output from each of the nozzles. US patents numbered 7231275 [25] and 7467837 [26] were issued to the Australian inventor Kia Silverbrook for a three-dimensional object printing system. Inspired by the existing inkjet printer, which is able to print images in the form of pixels, the concept of printing a three-dimensional object by printing in voxels was conceived in this design. A group of print heads were put together to become a group-head; each print head prints an individual substrate; or in other words, multiple substrates could be printed at the same time. The print material is similar to the one on the ordinary inkjet printer and ejects in the form of droplets. According to the information mentioned in the patents, multi materials could be used and multi layer thicknesses could be coped within the scope of this design.

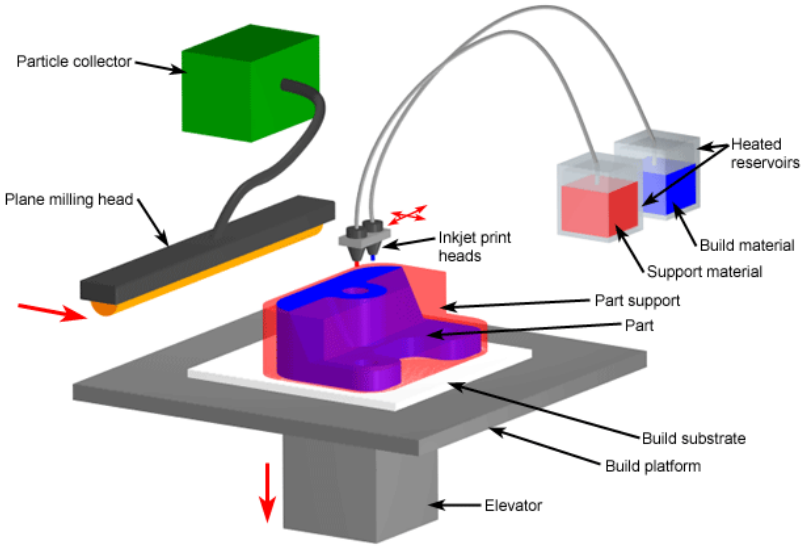

Fig. 1.7 Schematic of the Ink-Jet Printing Process (Image source: CustomPartNet [27])

1.3 Fused Deposition Modelling (FDM)

The most significant of the additive manufacturing technologies are briefly reviewed above, and since fused deposition modelling is the focus of the current research, further attention is paid to this technology in this section. Fused Deposition Modelling (FDM) is based on the extrusion of a softened material and subsequent printing on a substrate within a three axes CNC system. Like any other additive manufacturing process, FDM also mostly utilizes the triangulated CAD (.stl) data as its input and works on a layer-by-layer principle. Inside a temperature-controlled chamber, a polymer or other suitable material in the form of a filament is unwound from a coil and fed to an extrusion nozzle which is capable of X- and Y- motions. A heating element provides the energy for softening the feed filament and the semi-solid material is pushed through a fine nozzle to be printed on a platform. The work table is usually provided with the Z-motion to control the layer thickness and a programmatically controlled deposition path pattern finally allows complex 3D shapes to be printed. The setup of an FDM system and associated essential components are depicted in Fig. 1.8.

The extrusion head with the narrow orifice is at the heart of the FDM system. The nozzle head is a movable unit in both horizontal (X and Y) axis directions, by means of a numerical control system embedded in the FDM machine, whereas the worktable usually provides motion in the vertical direction (Z direction).The schematic [28] of components in the extrusion head is shown in Fig. 1.9. It consists of drive blocks, a heating chamber and a nozzle tip. The drive blocks feed the raw material, and consist of two wheels mounted at the back of the head. They are controlled by a computer and are capable of loading and unloading the filament precisely. The heating chamber is a tube wrapped with a heating element and bent at 90˚. It is used to change the

filament flow from the horizontal to the vertically downward direction and also serves as the melting chamber for the material, which is the main function. The tip is externally threaded and screwed into the heating chamber outlet and reduces the diameter of the extruded filament diameter which will eventually control both surface and part qualities.

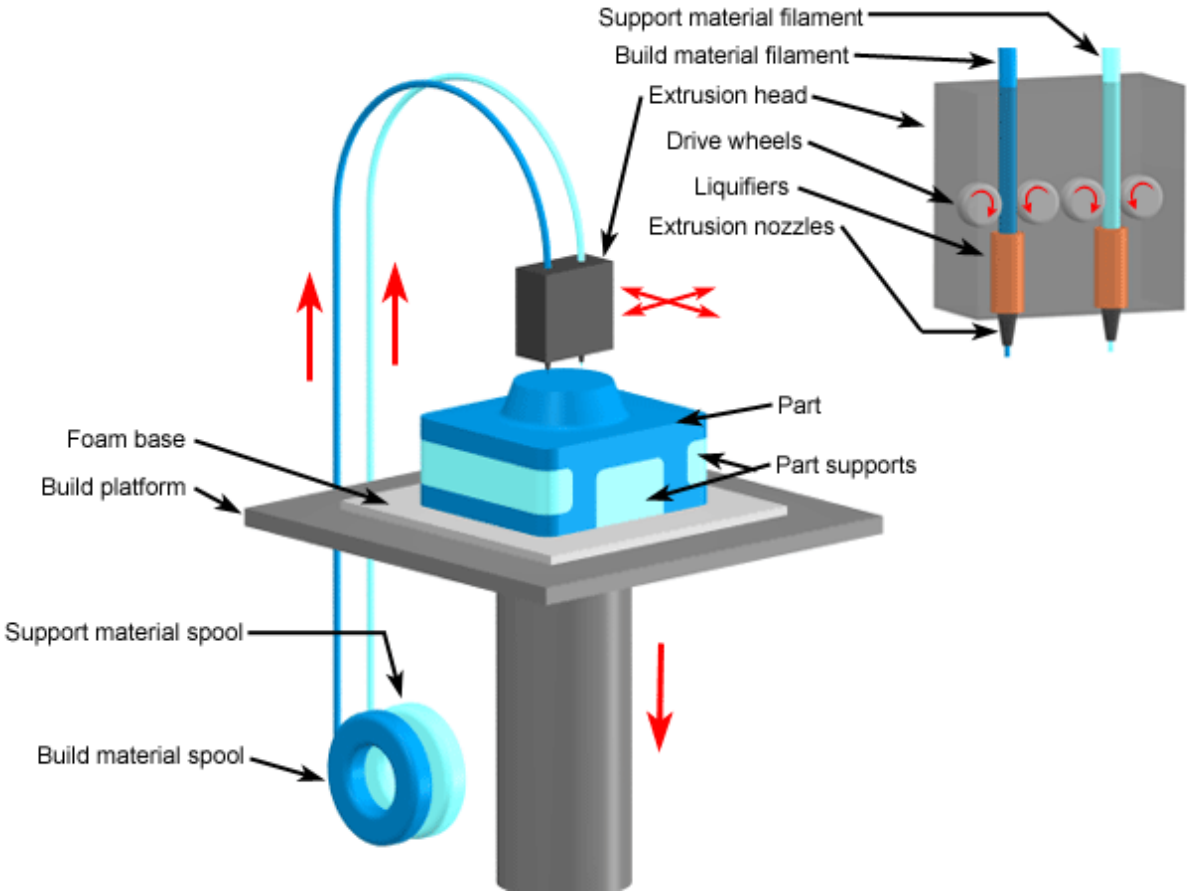

Fig. 1.8 FDM process in detail (Image source: CustomPartNet [29])

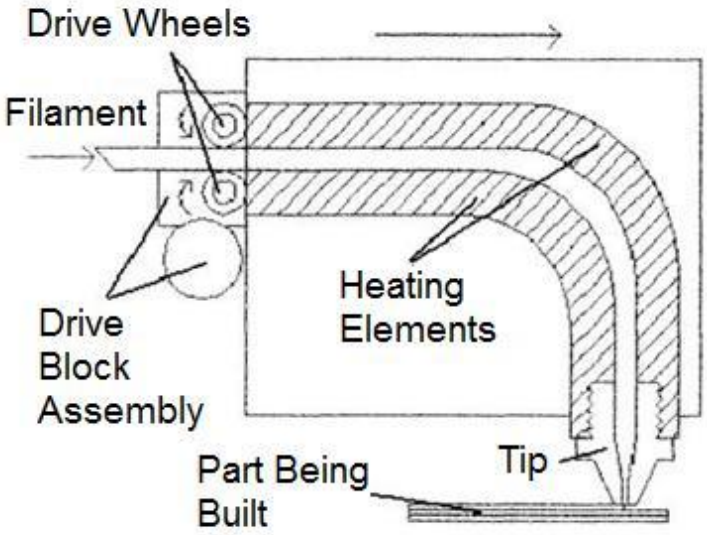

Fig. 1.9 Schematic of the Extrusion Head (Image source: Cooper [28])

FDM is commonly used for Modelling, prototyping, and production applications and according to Stratasys, the commercial provider of the technology, typical applications fall into four categories [30]

- Concept Models

  FDM can effectively evaluate, optimize and communicate the prototype design, mostly used in early stages of product development. FDM models reduce costs and shorten the development timelines.

- Functional Prototypes

  FDM plays an important role in testing as the product's design evolves from concept to functional prototype. FDM functional prototypes allow to be tested in real-world environment and help decision making.

- End-use Parts

  FDM can produce end-use parts tough enough for integration into the final product without the expense and lead time of traditional tooling or machining.

- Manufacturing Tools

  FDM can produce manufacturing tools such as jigs and fixtures, tooling master and production tooling in hours.

In real world commercial applications, technicians from Bell Helicopter used the Fortus FDM system to build tough polycarbonate wiring conduits for the experimental tail-wiring upgrade of the heavy-lift "tilt-rotor" Osprey hybrid aircraft. FDM Parts, such as flame-retardant vents and housing, camera mounts, large pod doors, and many custom fixtures, are used on National Aeronautics and Space Administration (NASA) next generation rover for space exploration. To improve productivity, worker comfort, ease-of-use, and process repeatability, BMW uses FDM to enhance the ergonomics of its hand-held assembly devices. The freedom of design allows engineers to create configurations that improve handling, reduce weight, and improve balance. Automobili Lamborghini S.p.A. made extensive use of FDM to make functional prototypes for the newly designed seven-speed transmission for the Aventador that offers 50 milli-second shift times, the fastest on any production vehicle. There are further examples of FDM applications, and in particular, it has a significant role to play in bio-medical applications, considering the developments in bio-materials and bio-polymer composites.

While offering these benefits together with a wide range of applications mentioned, there are also specific shortcomings associated with processing by FDM. An early evaluation by Weeren

et al. [31] allowed identification of hardware, software and build strategy limitations as typical sources of defects in FDM parts. Part defects can be classified into two categories; surface and internal defects. Most of the surface defects are primarily due to the inherent nature of layer-by-layer manufacturing. However, the internal defects are mostly due to the limitations of FDM systems and processing strategies and mainly occur in systematic and repeatable manners in the parts. Agarwala et al. [32] identified several internal defects specific to FDM, and a detailed discussion of the nature, causes, and possible solutions will be presented as part of the literature review in Chapter 2.

Further, FDM also suffers from limited materials options, although most thermoplastic polymers, certain polymer composites and biopolymers are candidate materials. Ceramic and metal mixtures in feed filament forms are also researched for FDM, but not to be commonly available for commercial use. In FDM processing, the temperature of the heating chamber normally reaches up to 400˚C to 500˚C depending on the materials used, while the envelope temperature in the print chamber is kept at around 100˚C. Polymeric materials might shrink after exiting the extrusion nozzle due to the relatively larger temperature gradients, especially with materials having higher shrinkage rates, such as polyethylene. In injection molding, the moulds are locked after injection and the entire part cools down at the same time. Compared to that, the FDM part cools down layer by layer during the deposition, and in spite of the envelope temperature, there is thermal variation and differential cooling rates from one layer to the other. This might result in unpredictable internal stresses between layers. These conditions result in restrictions on size; and uneven shrinkage, warping and associated problems are likely to arise as shown in the example in Fig. 1.10, with relatively larger parts. Also, some materials with higher thermal conductivities

such as polypropylene might solidify straight after extruding from the nozzle, without allowing for any inter-road or inter-layer coalescence. While these shortcomings exist, there is research being conducted into the mechanics of material consolidation as well as alternative means of overcoming some of these problems.

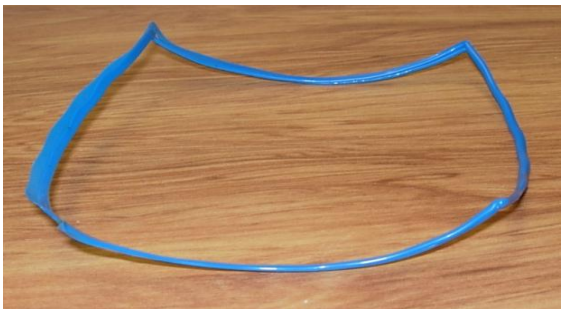

Fig. 1.10 Warping due to thermal variations

1.4 Mechanism of material consolidation in FDM and possible means of process enhancements

In Fused Deposition Modelling (FDM), the heated plastic filament is extruded through a nozzle and deposited on a base as closely spaced strands or roads within each layer, while successive layers are stacked one over the other to build the 3D form. The thermal energy associated with the semi-molten material drives the inter-road bonding and as the material is deposited, it bonds with the surrounding material, cools and solidifies [33]. The resulting parts are orthotropic composites of partially bonded polymer filaments and voids. Two successive roads are bound by a sintering process, the first step of which is the establishment of interfacial molecular contact by wetting, followed by molecular motions toward preferred configurations to achieve the

absorptive equilibrium. Molecules either diffuse or form chemical bonds across the interface and randomisation can only be achieved through extensive inter-diffusion of chain segments under critical conditions. While the size of the neck formed due to the inter-strand sintering indicates the quality of the bonding, it was shown that the neck growth is negligible below 200˚C, and temperatures above 240˚C result in degradation when working with ABS filaments.

Based on the Newtonian polymer sintering model, together with a heat transfer analysis, it was shown that most sintering occurs within seconds following the extrusion of the polymer onto the substrate, the rate and level of wetting being highly dependent on extrusion and envelop temperatures, and convection conditions. As the filaments are not maintained at above glass transition temperature for long, the bond strengths are insufficient and the part characteristics are inferior. While the major controlling factor for the mechanical properties is the meso-structure, which can be controlled by the adjustable fabrication parameters, the molecular orientation is also significant and can be affected by the extrusion process [34-36]. Elastic moduli values 11 to 37 per cent lower and strength values 22 to 57 percent lower than the ABS monofilament were noted. While similar observations were also made in comparison with injection moulded counterparts, the build style and road structure were noted to have significant influences on the final part characteristics [35, 36].

Evidently, the mechanical properties of FDM prototypes are governed by the mesostructures, which in turn get affected by manufacturing parameters including width of the filaments, layer thickness, deposition orientation, speed and time of deposition and air gaps. Apart from the porous internal materials structure, the external surfaces are affected by stair-step effects

resulting from the stacking of flat layers and the part orientation. The faceted stereolithography format (.stl) model is sliced with horizontal planes, and the contour of each layer is generated. The FDM deposition head traces the slicing pattern and builds the physical part in thin layers, which exhibit the "stair-step" effect. This becomes more obvious on curved surfaces and particularly when using thicker layers. In some specific cases, for example, thin shell components, discontinuous filaments deteriorate the anisotropy phenomenon, which causes part failure as shown in Fig. 1.11 [37].

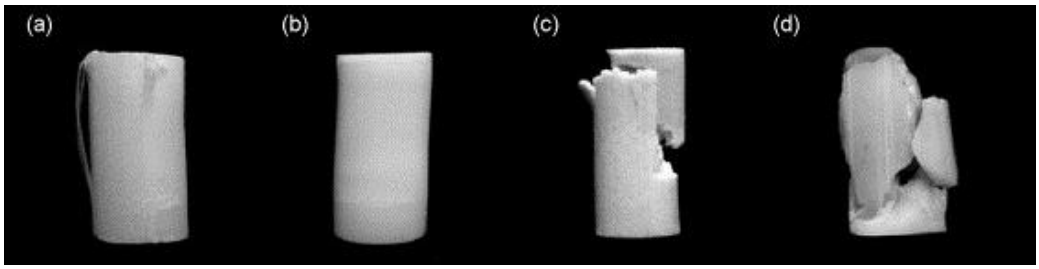

Fig 1.11 Failure modes of the specimens: (a) FDM-axial (b) FDM-transverse (c) 3D printer-axial (d) Nano composite deposition system (NCDS)-axial (Image source: Lee et al.[37])

Internal defects such as sub-perimeter voids have been successfully eliminated by multiple techniques and one of these solutions is now being commercially used in FDM systems. Inter-road defects can be either minimized or completely eliminated in some instances through process control resulting in optimization of feed filament quality, build environment temperature, etc. Complete elimination of inter-road defects due to extremely long vector lengths requires more robust solutions. One of these solutions by means of providing a negative gap between adjacent roads as a function of vector length has been successfully used in the fabrication of simple

ceramic shapes. Most of the other internal defects such as core voids can be simply avoided by selection of appropriate build strategies and conditions based on the FDM systems.

Further to slicing a CAD model, deposition path data is generated for the print head to follow while printing each successive layer. Referred to as the raster paths, these are usually parallel lines, aligned in each plane at a particular angle, the raster orientation. It was established clearly that raster orientation would have significant influences on the final mechanical characteristics of FDM parts. Theoretical investigations based on lamination theories also indicate the same, as the strand structure and the consequent meso-structure are dependent on the raster orientation.

Surface defects arise mainly due to the current limitations in the state of Solid Freeform Fabrication SFF technologies (stair-step formation and chordal approximation) or poor optimization of the build parameters in the FDM control software for a given material (start/stop errors). Post-processing methods come to some sort of assistance, but are undesirable, considering additional costs and time. Further, the process variations also result in variations in meso-structures, which will eventually influence the final part characteristics. Apart from these, the external shape of the part will require special considerations, particularly when finer details or curved outer profiles are involved. Very fine layers can overcome some of these problems to some extent but at the cost of increased production times. Adaptive slicing, characterized by layers of varying thicknesses evolved as a possible means of overcoming some of these external problems.

A fairly recent development is modelling material deposition using curved layers, in particular with parts having light-curved surfaces. While the stair case effect can be significantly minimized, mechanical properties will also be enhanced due to fibre continuity and the

elimination of the inherent inter-lamellar weaknesses. However, this needs a completely different approach to the handling of the CAD model, and the slicing and deposition processes. A couple of curved layer solutions already exist and analytical observations are indicative of promising results especially in terms of better surface quality as well as internal fibre structures in specific cases.

1.5 Research proposal

Considering the numerous advantages of Additive Manufacturing in general, and the specific attributes of FDM in particular in terms of being suitable for a variety of materials, it becomes an important process and perhaps an economical alternative to injection moulding in certain cases when small to medium scale production is essential. Also, considering the abilities to process biopolymers and biopolymer composites, and with gradual improvements in materials characteristics, FDM is also likely to play a key role in future applications of additive manufacturing in biomedical fields, for tissue engineering and fabrication of patient-specific implants. However, there are certain shortcomings associated with the process, which require significant research attention, and development and implementation of novel processing strategies before completely realising the full potential of FDM.

Raster angle orientation is a predominant factor controlling the FDM part characteristics. Theoretical evaluation of raster orientation effects was already attempted, but a more consolidated understanding is necessary in order to be able to clearly establish the true role of raster orientations in FDM. Similarly, adaptive slicing was introduced earlier as a means of

overcoming the stair-case effects and missing finer part details. However, considering the practical limitations of driving a semi-solid material from a nozzle to be printed into 3D forms, it is very difficult to sharply vary filament sizes to accommodate adaptive slicing. Consequently, filament size variations are associated with variations in print speeds as well as the total time of printing for a given part. None of the existing models actually considers all these aspects together and it is essential that the true influences of adaptive slicing together with the time and speed of printing to be theoretically modelled and experimentally validated.

Curved layer slicing was envisioned mainly as to overcome the stair-step effects and also to improve the part strength through better fibre continuity. However, existing solutions are quite cumbersome and not very practical. Better curved layer slicing algorithms together with improved practical implementation schemes need to be developed in order to further ascertain the true benefits. In addition, uniform flat layer, adaptive flat layer and curved layer slicing are all attempted so far only individually, and in fact, for a given part, it may be readily visualised that the best printing scheme would require a smart combination of all these methods. It will also be essential to consider further enhancements such as adaptive curved layer slicing together with varying raster orientation aspects. Once the individual aspects are thoroughly understood, an overall slicing algorithm needs to be developed that chooses the best combinations of slicing strategies for different regions, together with the optimum raster plans for individual or groups of layers for a given part with a selected print orientation.

The current research is focussed in this direction, targeting mathematical and practical solutions for different deposition schemes and then testing the effectiveness of them both individually and

in combinations and finally integrating successful schemes into an overall selection algorithm that produces the best combination of the deposition schemes for processing different zones of a given component for a given orientation. The overarching hypothesis is that each part requires a suitable combination of different slicing and deposition schemes with appropriate raster orientations to be able to achieve the best internal material structure and consequent mechanical characteristics for a given print orientation.

A proof of this premise involves answering several questions surrounding the mechanics of raster orientations, adaptive and curved layer slicing and responses to specific combinations of different strategies. The material used for printing will have significant effects on all these aspects and could become an important experimental factor, but considering the overall volume of the work, the current research is confined to the normal ABS polymer in filament form as used commonly for FDM. Chapter 2 presents a detailed literature review on all significant aspects leading to a clear identification of the research gaps and questions, while the following are the main objectives of the current research:

- Evaluation of the raster mechanics in fused deposition modelling
- Evaluation of the mechanics of adaptive slicing with print speed and time interactions duly considered
- Evaluation and further improvement of the curved layer slicing algorithms, practical implementation and assessment of the true significance
- Evaluation of existing adaptive slicing schemes and implementation of one of them with possible enhancements and correlation of the true effects with experimental results.

- Consolidating influences of raster orientation, flat, curved and adaptive slicing schemes and development of an algorithm to selectively implement the most suitable combinations for specific solid models with given print orientations.

Experimental evaluation of the role of raster orientation and theoretical models developed to evaluate the mechanics of raster orientations are presented in Chapter 3. Analytical models capturing the effects of adaptive slicing on mechanical properties together with print speed and time variations are developed and presented in Chapter 4, with experimental verification and validation within certain ranges of process parameters, as possible with the test facilities developed. Chapter 5 presents a review of the existing curved layer slicing models and improved algorithms developed as part of the current research. Practical implementation of the curved layer scheme using a selected test piece of light-curved shape and evaluation of the true significance of curved layer printing are also included. Chapter 6 includes mathematical algorithms and implementations in CAD models of combinations of approaches such as adaptive curved layer slicing, curved layer slicing with varying raster orientations, and mixed mode slicing combining uniform and adaptive flat and curved layer slicing together. A couple of typical case studies are considered eventually to evaluate the effectiveness of the mixed-mode slicing algorithms developed.

Chapter 2 Literature review, research gaps, questions and objectives

2.1 Background

Fused Deposition Modelling is an Additive Manufacturing process potentially capable of substituting for the costly and time consuming injection moulding methods, in certain applications, requiring one-off or small to medium scale production. Evidently, the process also has a significant role to play in biomedical applications. In spite of all this, and additional benefits arising out of the very nature of material consolidation in additive manufacturing, through line-by-line addition of the constituent material, the application of FDM is still limited considering limited materials options and typical shortcomings associated with the process.

Inferior surface qualities resulting from stair-step effects, insufficient mechanical properties due to internal meso-structures resulting from the stacking up of solidified strands with incomplete inter-road and inter-layer coalescence are by far the most intriguing aspects. This research proposes to evaluate methods attempted earlier, investigate plausible means of improvements, and integrate potential solutions in combinations in order to be able to improve overall part quality through better meso-structures. Existing literature and other sources of relevant background information are reviewed in this chapter to identify the research gaps and formulate the hypothesis and research questions.

2.2 Literature review

2.2.1 Fused Deposition Modelling; limitations and process evaluation

In fused deposition process, the feed material undergoes phase transitions twice [38]. This subjects the material to very complex thermal and flow boundary conditions that continually affect and change its thermo-fluidic states dynamically. The first step is the conversion of the material into the form of a filament and stocking it wound on a spool. Then the filament is mechanically pushed into the liquefier where it melts with the heat generated by the heating element. The molten material, subjected to the pressure applied by the incoming filament, is consequently extruded through the nozzle. Because of the adhesion of the material to the walls, the velocity field of the molten plastic has a parabolic profile. When the molten plastic reaches the nozzle, the velocity distribution has a large gradient in the radial direction due to the small area of the orifice. At the exit of the nozzle, the molten flow quickly assumes the conditions typical of a plug flow, causing a radial expansion of the melt due to the sudden absence of the lateral forces, often referred to as the swelling phenomenon. The second phase transition takes place when the extruded molten plastic touches the platform or the previous layer and quickly solidifies according to the temperature and the thermal properties of the substrate. Due to different thermal boundary conditions, the evolution of roads in the first layer is different from that of the successive layers. In summary, Bellini [38] consolidated this process into five specific stages; (1) Melt flow in the liquefier, (2) Extrusion through the nozzle, (3) Free extrusion and swelling of the melt at the exit of the nozzle, (4) Evolution of the road in the first deposited layer, and (5) Evolution of the road in the successively deposited layers.

One of the early research concerns with FDM was the inherent nature of material consolidation giving rise to plausible defects in parts fabricated. Weeren et al. [31] noticed that defects occur in the FDM parts mainly due to hardware, software and build strategy limitations and classified them into two categories; surface and internal defects.

Surface Defects

Surface defects include staircase and chordal errors as shown in Fig 2.1. Staircase errors are caused by the slicing method, while chordal errors originate from the .stl format file.

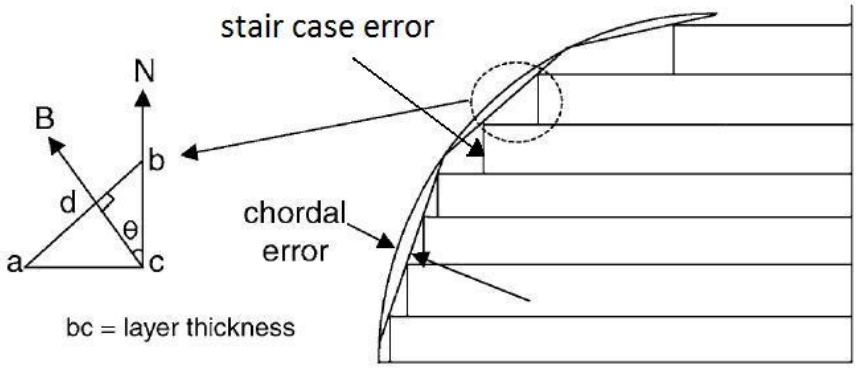

Fig. 2.1 Surface Errors (Image source: Choi et al. [39])

Staircase or registering effect

Stair-case or Stair-step effect [40], is a significant limitation of all RP processes, and is more prevalent in particular with FDM. It is caused as a result of the basic approach in layer-by-layer processing using horizontal flat layers and the part orientation during the deposition. The faceted

.stl model is sliced with certain horizontal planes, and the contour of each layer is generated. The RP system, no matter whether using a laser or a deposition head, traces the slicing pattern and builds the physical part in thin layers, which exhibit the "stair-step" effect, as shown in Fig. 2.1. It may also be noticed that stair-step effects become more obvious on curved surfaces and particularly when using thicker layers. While dimensional accuracy and surface quality are paramount to any engineered product, achieving the same in FDM requires use of finer layers, leading to abnormally high part build times [41]. However, finer layers allow better part resolution, with reduced stair-step effects, as shown in Fig. 2.2.

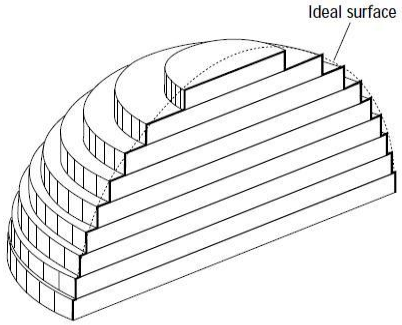

Fig. 2.2 Thin build layers better represent complex surfaces (Image source: Sabourin et al. [41])

Chordal or curve-approximation errors

The de facto standard for linking a CAD model design with any additive manufacturing system is the .stl (Stereolithography) file [42]. In a .stl format file, part surfaces are tessellated or triangulated and eventually, each surface is represented by a set of triangles. Curves are necessarily linearized due to current requirements by the hardware control. In FDM systems, the linearization of curved surfaces while generating .stl files can be reduced to shorter vector

lengths to improve the representation of such surfaces. However, this solution leads to build files of very large sizes and also increases the build time of the part.

Top/bottom surfaces

The first layer of deposition in FDM is in contact with the print platform with its own degree of surface roughness and texture. As a result, the bottom surface picks up the surface texture from the build platform. This can be eliminated by building the actual part on a raised platform that can be removed later. The top layer deposited has a ridged surface resulting from the structure of the substrate strands. Again, finer roads reduce these effects, but at the cost of increased build times and there is always a limitation on how fine the extruded filament could be, in view of other practical limitations.

Start/stop errors

In most FDM systems, the build process is usually planned with a closed loop outer profile of each layer to be printed first. Each closed loop includes a start and a stop point. When the nozzle moves to either the start or the end points, the extruded material needs to be controlled to prevent any overflow or underflow. This is to be done by controlling the feed rollers and the motion of the filament into the liquefier. However, the backpressure in the liquefier continues to extrude the polymer material even after the filament is instantaneously stopped from feeding. Further, a void segment or an excess material filling might take place if the rollers are stopped either too early or too late respectively at the stop-point. Thus a controlled co-ordination of the movement

of the liquefier head and the rotation of the extruder is critical at the start and the end of each perimeter, and often results in start/stop errors.

Support structure burrs

Support structures are required when the part has overhanging or complex internal features. The removal of the support structures leaves burrs or fine scale holes on the surfaces in contact with them. Usually, post-process finishing techniques aid in reducing such defects.

Internal Defects

Internal defects arising out of a combination of hardware and software limitations and materials characteristics as shown in Fig 2.3 (a), (b), and (c) respectively include sub-perimeter voids, inter-road voids and defects due to variations in the road thickness. Sub-perimeter voids are caused by the incomplete filling of the area inside the perimeter of the FDM part. Inter-road voids and variations in road thickness are caused by inconsistent material flow due to both slipping in the filament feed mechanism and variations in the filament diameter. Most of the internal defects occur in a systematic and repeatable manner.

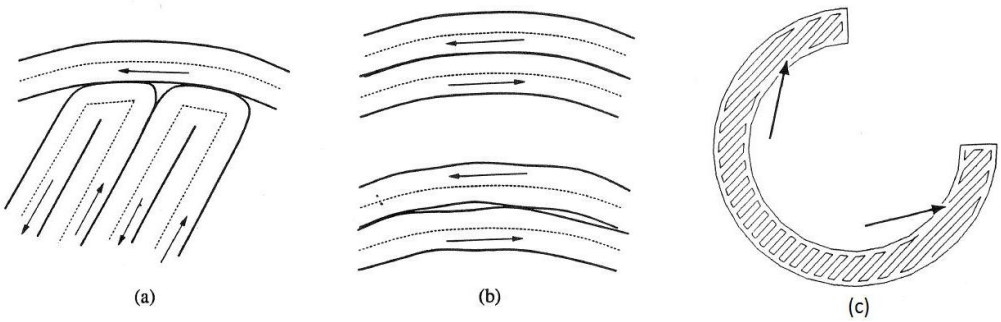

Fig. 2.3 Internal Defects (Image source: Weeren et al. [31])

Sub-perimeter voids

During the deposition, the extruded material is filled inside the outer contour of a sliced layer with a given raster pattern and orientation. When the extruder nozzle reaches the end of a particular road, it needs to turn around and continue printing the next road. The algorithm used to generate the deposition path strives to make the turning tool path close to be tangential to the boundary of the geometry as shown in Fig. 2.3 (a).These sharp turnings in the deposition paths often lead to incomplete filling and result in voids, although the path generation program attempts to achieve complete filling at these locations. Further, the constant velocity of the extruder nozzle would cause high centripetal accelerations at the corners, resulting in an inappropriate material flow at these intersections. The size and occurrence of the sub-perimeter void depend on the build conditions (road width, thickness, etc) and the angle between the raster line and the perimeter curve. Since sub-perimeter voids are predictable and the cause of their formation is known exactly, several solutions are possible for eliminating these defects, such as negative offset, alternative corner turning and equidistant tool path generation [43] as shown in Fig. 2.4 (a) to (c).

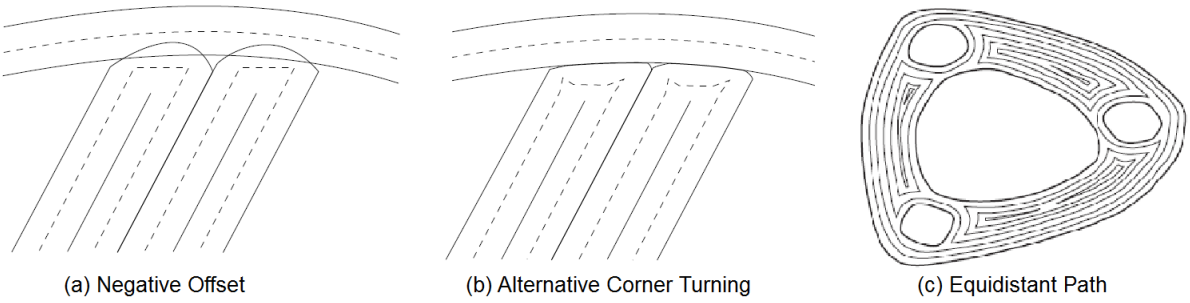

Fig. 2.4 Improvement for sub-perimeter voids: (a) Negative Offset, (b) Alternative Corner Turning ((Image source: Agarwala et al. [32]) and (c) Equidistant Path (Image source: Yang et al. [43])

Inter-road defects

Defects between adjacent roads (inter-road defects), as shown in Fig. 2.3 (b), can occur in one of the following two forms [32]:

(1) Voids, which might occur due to no physical contact between adjacent roads.

(2) Weak Links occurring due to weak bonding across the physical contact between adjacent roads.

These defects depend on the degree of bonding between adjacent roads, which in turn depends on the temperature of the roads, the lateral flow of the material and the time allowed for consolidation.

Vector-length effects

As the extrusion nozzle follows the raster path, its movement becomes a vector and the distance it moves is called the vector length. When depositing the extruded material along long vector lengths, if the time delay is high, the temperature decay in the previously laid road is large. Therefore, due to significant temperature differences, the bonding between two adjacent roads might be weaker. The unwanted cooling may occur not only between the roads in a given layer, but also between successive layers. These weak interfaces are seriously deleterious to the structural integrity of the part. If the substrate cooling is extremely high or if there is a high shrinkage of roads while cooling, then there is also a possibility for complete de-bonding between such roads, causing inter-road voids.

Non-sequential raster segments

Weak interfaces might also occur due to the deposition strategy in some locations with specific geometries, such as the non-convex areas. In these areas, a single continuous raster pattern is not possible to fill the entire area. Therefore, under such circumstances, the area is filled by more than one continuous raster pattern, with a start and end point for each filling, as shown in Fig. 2.5. Also, depositions of these non-continuous raster patterns are not always sequential and adjacent during the deposition. These discontinuous fill patterns occur because the algorithm cannot process the raster paths when the outside contour is a tangent at the point of intersection. Due to non-sequential deposition, there is a possibility of excessive substrate cooling between two adjacent roads of different raster patches. This may result in insufficient bonding between the adjacent roads, thus causing weak interfaces or even voids between such roads.

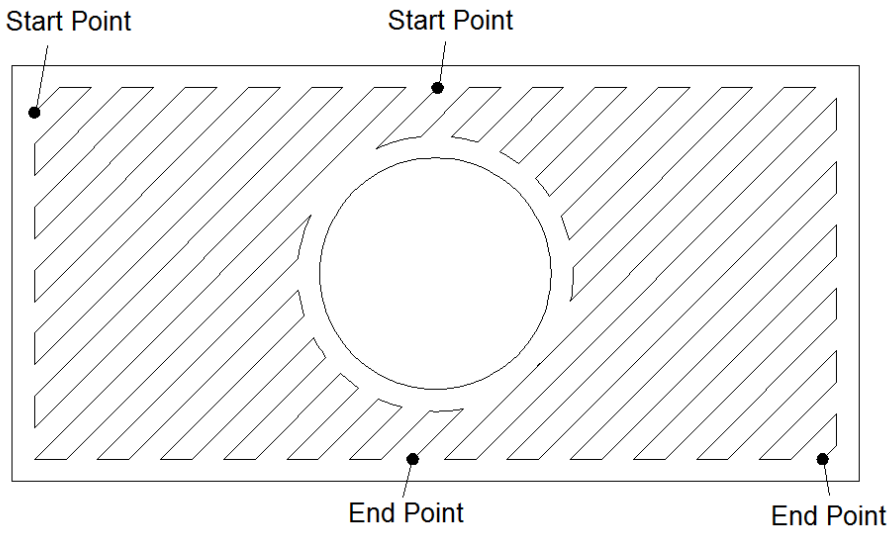

Fig. 2.5 Non-sequential raster segments

Non-uniform filament diameter

A FDM system deposits the material extruded through the nozzle based on a constant diameter feed filament with a specific feed velocity. The rate of filament feeding and the roller speeds are pre-determined based on specified deposition conditions and assuming that the filament diameter is uniform throughout its length. However, filament diameters could be varying due to manufacturing defects. The variations in the filament diameter affect the flow rates of the material being extruded out of the extrusion nozzle and might not match with the required rates. Such variations in the filament diameter may lead to underflow or overflow which can result in poor bonding between adjacent roads or non-uniform road width or layer thickness respectively.

Filament slippage between rollers

Filament slippage between rollers might occur due to mismatching roller and filament surface patterns or use of improper groove depths. Insufficient thermal energy in the heating chamber and consequent adverse temperature conditions inside the extrusion chamber might lead to the filament slipping between the rollers or buckling after passing through the rollers. Eventually, the slippage affects the flow rate of the deposition material and hence the bonding between adjacent roads and the nature of the inter-road bonding.

Core voids

This generally occurs when contour filling or equidistant filling patterns are used. When filling thin wall sections, if only a couple of roads could be accommodated, a possible void arises where the third line of deposition could not be squeezed in. One possible solution is to calculate the

exact road width to be able to fill the whole area with a certain number of equidistant raster deposition paths. However, the filament diameter is a restricted parameter in FDM and cannot be assumed to be continuously varying. Also, in more complicated geometries, this solution may not be practical due to the complexities to be resolved and perhaps the resulting high computational times.

Other Defects

While investigating the optimum print orientations, Masood et al. [44] noted the stair case errors as the major and unavoidable defect in FDM process. They developed a methodology by computing the volumetric error to select optimal orientations for the objects and parts built by FDM systems. Volumes of original objects or parts were calculated by dividing the complex shapes into a number of basic primitive volumes. The total volumetric error combines errors in primitive volumes and is used to determine the optimal orientations at different angles by comparing with the theoretical and experimental results. The results indicate that parallel or perpendicular directions with the axes of motion were the best orientations for most of the parts except the pyramid-like parts.

Repeatability is yet another problem in FDM and generally occurs with symmetrical features repeated in different directions. Fig. 2.6 shows a typical component with symmetric features repeated on two mutually perpendicular axes. The same boss feature is repeated on all four faces of the component. During the deposition, the raster orientations are different in different sets of the projecting bosses and will eventually result in widely varying properties.

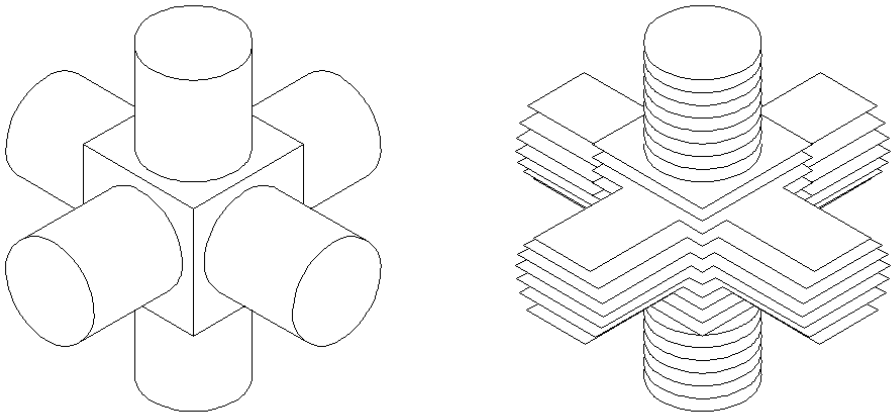

Fig. 2.6 Geometrical features resulting in repeatability issues

Process Attributes and Evaluation

Other aspects that attracted sufficient research attention in FDM were process attributes and evaluation. Anitha et al. [45] used the Taguchi technique, considering critical parameters such as thickness, road width and print speed and based on experimental evaluation of 18 components found that the layer thickness was effective to 49.37% at 95% of significance without pooling, while it accounted for 57.57% at 99% level of significance with pooling. Based on similar analyses using design of experiments, Montero et al. [46, 47] concluded that the air gap and the raster orientation affect the tensile strength of the FDM parts while road width, temperature and colour have little effects. A multi-objective decision support system was also developed to aid proper setting of FDM process variables in order to achieve specific build goals and desired part characteristics [48].

Non-random porous structures were found to influence the mechanical properties of FDM parts by Too et al. [49]. They used the Stratasys FDM 1650 system to build the scaffold structures by adjusting the raster gap to form varying pore sizes. Further investigations were carried out

examining the microstructure, porosity, pore diameter, and mechanical strength, leading to an empirical relationship for the porosity. It was found that the raster gap size has a significant effect on porosity, pore diameter, and finally the compressive strength of the FDM part. Sood et al. [50], instead of the conventional Taguchi method, used grey Taguchi Method to generate a single response from different performance characteristics, which considered the percentage change in length, width and thickness of build parts. Five control factors were chosen in their experimental settings; orientation, layer thickness, raster angle, raster width, and air gap. It was observed that shrinkage was predominant in length and width directions, but the dimension increased from its desired value in the direction of thickness. After further analysis, it was concluded that higher layer thickness (0.254mm), 0˚ orientation, maximum raster angle (60˚), medium raster width (0.4564 mm) and maximum air gap (0.008mm) were desirable along the length while medium raster angle (30˚) and air gap (0.004mm) were desirable along the width. It was obvious that large numbers of conflicting factors independently may influence the dimensional accuracy and so, the fabrication process must be based on optimum settings obtained through a structured methodology.

Ahn et al. [51] investigated the actual surface roughness characteristics of FDM and established a theoretical model to express the deviation in the roughness values with respect to the surface angle considering critical factors. Sood et al. [52] attempted to understand the relationship between mechanical properties and process parameters. Simple FDM parts were produced by a Stratasys FDM machine with ABS P400 and tested by different test systems based on a central composite design. Five main process parameters were considered, such as layer thickness, orientation, raster angle, raster width and air gap, that influenced tensile, flexural and impact

strengths. The models were validated by ANOVA and the major reason for weakness was attributed to distortion within or in between layers.

Yardimci et al. [53] developed heat transfer models to describe the temperature profile of the deposited roads in FDM. The first model was a simple computational model, which can predict effective thermal conductivity of a particle-loaded heterogeneous system. Observations from this model showed that the effective material thermal conductivity is the sensitive binder thermal conductivity. Further, in a two dimensional model, they considered the adiabatic effects of the work table, the thermal history of the deposition head, and layers built one over the other, and the results showed that the temperature distributions had significant effects on the previous three roads in the same substrate. Hence the bonding enhancement per pass was greater for less populated road areas. Consideration of the raster or build style showed that different areas in the layer experience different thermal histories during the FDM process and together with geometrical factors, lead to the existence of bonding metric gradients across the part. The top layers experience lower values of bonding metric, due to the absence of all-round heating as in the case of lower level layers.

Sun et al. [54] investigated different process planning techniques for FDM, considering key process parameters targeting optimum processing times, mechanical properties and surface qualities. One of the most interesting findings is that the temperature history of interfaces plays an important role in controlling the bond quality. Experimental results showed both the envelope temperature and variation in the convective conditions within the build chamber to have significant effects on the mesostructure and the overall quality of the bond strength between

filaments. They also suggested that a critical control of cooling conditions would help better the mechanical properties and accuracy of the final part in FDM.

Galantucci et al. [55] studied the surface roughness of FDM prototypes and found the slice height and the raster width to be more significant, as against the direction of the movement of the extrusion nozzle. They also introduced a chemical treatment process as a means of post-processing improvements. Boschetto et al. [56] built a theoretical model for the average roughness as a function of the process parameters and the part shape. The model was claimed to be effective in predicting the effects of all critical parameters and surface roughness parameter could be used to determine the best part orientation.

Jin et al. [57] emphasised the process planning as a critical task in additive manufacturing and developed an adaptive process planning approach based on a mixed tool-path generation scheme. The algorithm uses Non-Uniform Rational B-Spline (NURBS) based curves to represent the boundary contours of the sliced layers and zigzag tool paths for the internal area. The overall effectiveness of the FDM process and geometrical accuracies were reported to be improved. Croccolo et al. [58] investigated the influences of process parameters on mechanical properties by using ABS M40 and developed an analytical model to predict the strength and the stiffness characteristics based on the number of contours deposited around the component edge and the setting of the other deposition parameters. Based on the experimental results and the analytical model, both strength and elastic modulus values were found to increase from 23.9 MPa to 29.7 Mpa and 1812 MPa to 2117 MPa respectively with increasing number of contours.

The foregoing review ascertains the presence of certain defects in FDM parts, arising mainly from the deposition styles and specific geometrical constraints. It is also clear that the process parameters significantly influence the part characteristics, together with the part print orientation. Evidently, these are variations at a relatively macro level. The thermal history of the process has a major role to play in all this, and eventually, based on the combined effects of all these aspects, the inter-road and inter-layer coalescence will vary. The final result is a typical meso-structure that will control the mechanical behaviour of the FDM parts. Aspects of the material consolidation mechanisms and mechanics are reviewed next.

2.2.2 Mechanisms and mechanics of materials consolidation

FDM prototypes are composites of partially bonded filaments and voids. The formation of bonds in the FDM process is driven by the thermal energy of the semi-molten material and can be described as shown in Fig 2.7. Ideally, the cross section of a filament can be considered as a circle of size equal to the nozzle diameter. When the extruded filament is laid on to the previous road or layer, the semi melt filament with high thermal energy re-melts the boundary of the exiting road or layer and establishes a contact at the interface resulting in the wetting phenomenon. Then, the molecular chains in both new and previous roads are randomised through the contact area [59]. Using the residual thermal energy from both roads and the energy from the envelope, the molecules diffuse by chemical bonds and entangle together by randomization until the wetting area disappears. Two different models are often used to describe the behavior of the molecules in the two stages; (1) sintering and (2) diffusion models.

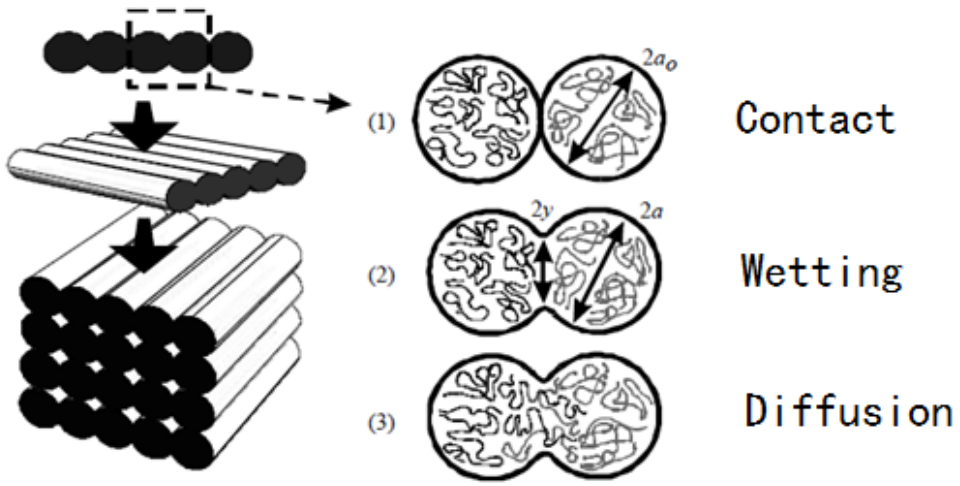

Fig. 2.7 Bond formation process between two filaments: (1) surface contacting, (2) neck growth, and (3) molecular diffusion at interface and randomization (Image source: Bellehumeur et al. [54])

Sintering Models

The sintering model is used to describe the establishment of the contact area. The formation and the growth of the neck require an environment with sufficient temperature. Li et al. [60] pointed out that the neck growth becomes insignificant below 200˚C and defined it as the threshold temperature for ABS P400. Though there are several models, the model proposed by Pokluda et al. [61] is the most commonly referred in FDM literature, and was originally developed for predicting the sintering between two polymer particles. Eq 2.1 is reproduced from the paper by Pokulda et al. [61] based on Newtonian flow (the viscous stress of the fluid arising from its flow and has a constant viscosity tensor) and viscoelastic flows (the fluid has the property exhibiting both viscous and elastic characteristics):

$$\frac{d\theta}{dt} = \frac{\Gamma}{a_0 \mu} \frac{2^{-\frac{5}{3}} \cos\theta \sin\theta \, (2 - \cos\theta)^{\frac{1}{3}}}{(1 - \cos\theta)(1 + \cos\theta)^{\frac{1}{3}}} \qquad (Eq. 2.1)$$

with $\theta = sin^{-1} \, y/a$ in which y and a, the neck parameters are as shown in Fig. 2.7. The model is valid for the coalescence between two particles and predicts the neck growth between the particles as a non-linear function of time *t*, material viscosity μ, initial particle radius a_o, and surface tension Γ.

Diffusion Models

The diffusion model is used to describe the degree of randomization of the polymer molecules through inter-strand contact; a process also called polymer healing. This is an important step and determines the strength of the inter-road or inter-layer bonding. Most of the general healing models developed consider isothermal conditions and might not be suitable for FDM considering thermal variations. Yang et al. [62] presented a diffusion model to describe the direct contact healing under non-isothermal conditions which is included here as Eq. 2.2:

$$D_h(t) = \frac{\sigma}{\sigma_\infty} = \left[\int_0^t \frac{1}{t_w(T)} dt \right]^{\frac{1}{4}} \qquad (Eq. 2.2)$$

Where t_w (T) is the temperature dependent welding time, σ_∞ is the strength of the fully healed interface, and σ is the stress in the FDM part.

For a given temperature history, and a given temperature dependence of the welding time, the degree of healing can be evaluated using Eq. 2.2. Sun et al. [63] adapted this model as the diffusion model in the FDM consolidation theory by replacing the temperature dependent welding time function with temperature profiles in conjunction with the extruded ABS P400 welding time developed by Rodr ǵuez [64], which is:.

$$t_w = Ce^{\frac{Q_d}{RT}} \qquad (Eq.2.3)$$

where T is the processing temperature, C is the pre-exponential factor, Q_d is the activation energy and R is the universal gas constant. Here, Q_d = 388.7 kJ/mol and C = 1.080×10^{-47} s.

Considering that the polymer chains are randomly bonded at the interface, the time is the only key parameter to influence the randomization. Kim et al. [65] reported the tensile strength to be increasing with increasing annealing time. While the theoretical models presented here are based on the general mechanics of material consolidation in FDM, the actual material system being processed is also of importance. The next section presents a review of materials currently investigated for processing by FDM.

2.2.3 Materials for FDM

Considering the line-by-line and layer-by-layer fabrication of parts, FDM often needs two different material systems; one for the actual part and the other for the support structures in case of overhanging features. The material used for the support structures should essentially allow for

easy removal both mechanically or otherwise, so that complex re-entrant sections could also be thoroughly cleaned. A water-soluble material, such as Polyvinyl alcohol (PVA), can be used for making temporary supports while printing is in progress and this soluble support material is quickly dissolved using a precisely heated sodium hydroxide solution with specialized equipment for mechanical agitation.

As for the actual deposition material, all commercial FDM systems invariably use Acrylonitrile-Butadiene-Styrene (ABS) considering the immediate suitability for the process mechanics. Alternative material systems attempted include both thermoplastics other than ABS and non-plastic materials and even polymer and biopolymer composites of late. Considering non-thermoplastics, Danforth et al. [66] introduced fused deposition modelling of ceramics and Jafari et al. [67] further extended it to Fused Deposition of Multiple Ceramics (FDMC) by using multi-material ceramics. Polymer composites, including metal/polymer mixtures [68], also attempted mixing iron particles in a nylon type matrix, or a piezo-composite [69]. With thermoplastics, medical-grade polymethylmethacrylate (PMMA) [70], polypropylene [71], and polycaprolactone (PCL) [72] are a few examples of the research on alternative material systems. Though the material system is not the main focus of the current research, a brief introduction to specific materials attempted for FDM is given here.

Acrylonitrile-Butadiene-Styrene (ABS)

ABS plastic is widely used in the industry and it is also one of the most common materials for FDM. The first grade of ABS used in FDM process was ABS P400 developed by Stratasys and is relatively weak in mechanical properties compared to the general ABS. Rodriguez et al. [35]

studied the relationship between the manufacturing process, meso-structure, and mechanical behaviour of ABS. They used different settings of the FDM 1600 system, such as extrusion temperature, envelope temperature, air gap, etc, in order to optimise the mechanical performance of fused deposition under a given set of service loading conditions. They found that voids are the main characteristics of the meso-structure of the FDM part and defined the void density and bond length density respectively as follows:

$$\rho_i \equiv \frac{Void\ Area}{Cross\ sectional\ Area} \qquad (Eq. 2.4)$$

$$Bond\ length\ density \equiv \frac{\sum Bond\ lengths\ over\ the\ circumference}{Total\ fiber\ circumference\ length} \qquad (Eq. 2.5)$$

They found that extrusion temperature, envelope temperature, air gap, flow rate and interlayer translation configuration are the critical parameters influencing the meso-structure. Based on experimental results it was shown that the void density and the extent of bonding between contiguous fibres depended strongly on the fibre gap and extrusion flow rate. Void and bond length densities in the plane transverse to the fibre extrusion direction varied from 4 to 16 percent and 39 to 73 percent respectively. They also quantified the important meso-structural features as a function of the process variables and developed a basis for evaluation of other candidate materials. Rodr ́guez et al. [36] also conducted an experimental evaluation of the mechanical behaviour of ABS assuming the properties of ABS materials as a function of the adjustable FDM parameters. They noticed four constants could be defined by the in-plane loading experimental result; the longitudinal modulus E_1, the modulus in the transverse direction E_2, Poisson's ratio v_{12} and shear modulus G_{12} defined as follows:

$$E_1 = \frac{1}{\varepsilon_x^L}\frac{P}{A} \qquad (Eq.2.6)$$

$$E_2 = \frac{1}{\varepsilon_x^T}\frac{P}{A} \qquad (Eq.2.7)$$

$$v_{12} = -\frac{\varepsilon_y^L}{\varepsilon_x^L} \qquad (Eq.2.8)$$

$$G_{12} = \frac{1}{2\frac{v_{12}}{E_1} + \frac{1}{\sin^2\theta\cos^2\theta}\left(\frac{1}{E_x} - \frac{\cos^4\theta}{E_1} - \frac{\sin^4\theta}{E_2}\right)} \qquad (Eq.2.9)$$

Where P is the load, A the apparent cross-section area, ε_x^L the strain in the load direction for the longitudinal specimen, ε_x^T the strain in the load direction for the transverse specimen, and ε_y^L the transverse strain for the longitudinal specimen. E_x is the apparent tensile modulus in the loading direction, and θ the angle between the fibre and loading. Their results showed significant meso-structural influences on the stress-strain response. FDM parts could only reach up to 89 percent of the modulus values and 78 percent of strength in the longitudinal direction, and 63 percent modulus and 43 per cent strength in the transverse direction compared to the injection moulded counterparts.

Ceramics

Fused deposition of Ceramics (FDC) was attempted using ceramic-polymer feedstock materials. Extruded material in the feedstock form was used to feed material for fabrication of three-dimensional green ceramic objects using a commercial FDM system and characterized for inter-

road and inter-layer bonding. Green FDC parts can be created similar to the polymer parts and then can be fired to obtain nearly fully dense components with no defects induced during post-FDC processing steps such as binder removal and sintering (brown FDC part). However, Exposure to high temperature thermal cycles results in undesirable mechanical performance characteristics and cracks in the finished part due to the presence of voids and/or poor inter-layer and inter-road bonding characteristics [73]. For the FDC parts, compressive elastic modulus determines the load carrying ability of the filament and the viscosity determines the resistance to extrusion (or extrusion pressure). Venkataraman et al. [74] developed a methodology for characterizing the compressive mechanical properties of FDC filament feedstock. It was found that feedstock materials with a ratio greater than a critical value do not buckle during FDC while those with a ratio below the critical value buckle. It has been established that a balance of the properties such as stiffness and viscosity is necessary for the successful functioning of FDC filament feedstock material. Frequent buckling failures cause interruption of the process during the extrusion phase in road formation, as well as the backpressure encountered during deposition. Anna et al. [75] designed and developed a new set-up, called the mini extruder deposition (MED) consisting of a mini-extruder mounted on a high precision positioning system, to avoid most of the material preparation steps in a filament-based system.

Metal/Polymer Matrix

Masood et al. [68] developed a new metal-based composite material for FDM, aimed at direct rapid tooling of injection moulded dies and inserts. Iron powder is mixed with P301 Nylon binder material to form the composite, which is then used to make the feedstock material. They also developed a proper formulation and mixture of constituent materials for obtaining certain

properties of the composite material that can be produced in filament form for use in the FDM process. The iron/nylon material filament developed 37-54 MPa in tensile modulus and 2.44-3.87 MPa tensile stress at peak loading. Characterisation of this new material displayed desirable mechanical properties, allowing for the fabrication of flexible feedstock filaments for producing functional parts and tooling directly on the FDM system. It was claimed that the material was especially suitable for direct rapid tooling applications as no binder burnout or infiltration was required which saves a great deal of time in rapid tooling development. Test results of injection moulding inserts fabricated on a FDM system using this material proved the inserts to exhibit acceptable mechanical properties.

Bioresorbable polymer poly ε-caprolactone (PCL)

Zein et al. [76] applied FDM to design and fabricate bioresorbale scaffolds with a fully interconnected channel network using a bioresorbable polymer, poly ε-caprolactone (PCL) developed for FDM to produce porous scaffolds. The PCL scaffolds were produced with a range of channel sizes 160–700 mm, filament diameters 260–370 mm and porosity 48–77%, and as regular geometrical honeycomb pores, depending on the process parameters. The scaffolds of different porosity also exhibited a pattern of compressive stress–strain behaviour characteristic of porous solids under such loading. The compressive stiffness ranged from 4 to 77 MPa, yield strength from 0.4 to 3.6MPa and yield strain from 4% to 28%.

Metal material (Bi58Sn42 and Sn60Bi40)

Mireles et al. [77] extended traditional FDM to Fused Deposition Modelling of Metals (FDMM) by using a straight liquefier design and successfully deposited tin-bismuth (Bi58Sn42 and Sn60Bi40) alloys, with low melting temperatures (below 300˚C). Microstructural analysis demonstrated good interlayer bonding with variations in the coarseness of microstructures along the layer interface that affects mechanical and conductive properties. It was envisaged that various applications can benefit from metallic FDM, including building jigs and fixtures, electroforming mandrels, encapsulation moulds, dies, electronic joining applications, as well as printing three-dimensional circuitry. Applications being limited to low-melting and low-strength alloys as well as the possibility for oxidation during the build process due to the lack of a controlled environment were the shortcomings noted.

Thermoplastics are by far the most suitable candidate materials for FDM, though other options like polymer, ceramic and metal composites were attempted with varying degrees of success. Nevertheless, the mechanisms of consolidation are similar and also the possibilities to develop one or the other types of defects are influenced by geometrical and process parameters. One of the significant factors is the raster pattern used while printing as it has a direct bearing on the resulting meso-structures. Attention is now paid towards the existing literature evaluating the raster orientation effects in FDM.

2.2.4 Effects of raster orientation

Meso-structure is a mechanical property of the FDM part and the raster orientation is one of the locally controlled properties affecting the meso-structure. Raster orientation refers to the

structure of roads deposited in each layer of a FDM sample. Raster orientations can be categorized into two different types: (1) Unidirectional deposition with different meso-structure and (2) Laminate configuration orientations as shown in Fig. 2.8. Mechanical properties of FDM parts are locally controlled by both the raster orientation and the density of deposition [78].

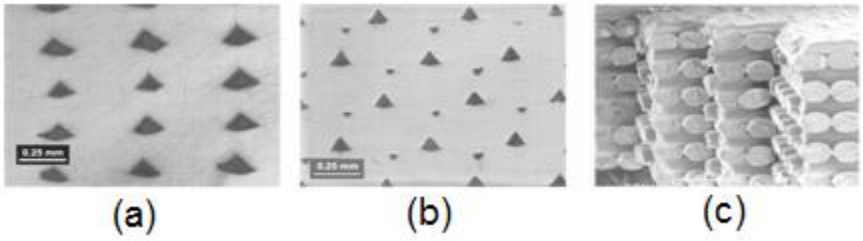

Fig. 2.8 Uni-directional and laminate deposition styles (a) Unidirectional deposition with standard meso-structure, (b) Unidirectional deposition with skewed meso-structure (Image source: Lee et al. [35]) and (c) Laminate configuration (Image source: Ahn et al. [47])

Further, FDM parts are orthotropic composites of ABS filaments, bonding between filaments and voids, and result in anisotropic [47] or pseudo-isotropic properties [73]. Tensile strength, modulus of rupture, and impact resistance are found to vary with different layer orientations. Es-Said et al. [79] found that the ultimate and yield strengths were the highest for the 0˚ orientation, at 20.6 and 16.3 MPa, respectively. The 45˚/0˚ scored second (14.0 and 13.6 Mpa), followed by the standard orientation, 45˚/-45˚, (13.7 and 10.4 Mpa). The weakest orientations were the 90˚ and 45˚ patterns. They also found that fracture paths were controlled by interlayer porosity. Weak interlayer bonding was probably due to the residual stresses caused by volumetric shrinkage of the polymer layers during solidification from the melt. Weak interlayer bonding could also be caused by the low molecular diffusion and low cross-linking between the polymer layers during deposition. In addition, the interlayer porosity reduced the load-bearing area across

the layers and hence provided an easy fracture path. The moduli of rupture are highest for the 0˚ orientation (44.4 Mpa). The 45˚/-45˚, 45˚/0˚ and 45˚ orientations had the next highest strengths, and the 90˚ orientation had the lowest strength (19.6 Mpa). During impact tests, the absorbed energy values are the highest for the 0˚ orientation (4.12J) and the lowest for the 90˚ orientation (0.36J).

Lee et al. [80] used the Taguchi method to find the optimal process parameters for the best elastic performance of ABS prototypes. Based on orthogonal arrays, the main effects, signal to noise ratio and analysis of variance were used to ascertain the role of the raster angle in the elastic deformation of FDM test samples. It was found that both raster angle and layer thickness play equally significant roles at 15˚ deflection of the test samples. Fatimatuzahraa et al. [81] focussed on the mechanical properties and meso-structures of FDM parts produced with two raster orientations; cross (0˚/90˚) and crisscross (45˚/-45˚). Tensile, bending, impact and deflection tests on ABS specimens showed the crisscross sample to perform better. The inter-road contact areas were observed to be higher with the crisscross raster patterns.

Evidently, the raster orientation influences the meso-structure, which in turn will control the final part characteristics in FDM. While the raster orientation is a typical feature of a single layer, variations in successive layers will have further confounding effects on the internal meso-structures. The layer structure depends on the slicing strategies used to process the CAD model for deposition by raster means. Eventually, the layer styles and structures become important in significantly contributing towards the internal meso-structure and would require some attention now.

2.2.5 Slicing strategies

StereoLithography (.stl) files have been used as the de facto standard to link CAD models and prototype fabrication in all FDM systems. .stl file-format specifies both ASCII and binary representation and describe only the surface geometry of a three dimensional model without any representation of color, texture or other common CAD model attributes. A raw unstructured triangulated surface is described by the unit normal and vertices (ordered by the right-hand rule) of the triangles using a three-dimensional Cartesian coordinate system. Theoretically, if the slice thickness is infinitesimally small, the 3D part should be identical with the 3D model. However, the thickness of the layer cannot be below a certain minimum thickness in reality, and there are also other factors that may affect the precision which result in errors [82, 83]. For better surface quality, Adaptive Slicing and Direct Slicing techniques were attempted.

Adaptive Slicing

While part quality is paramount in any manufacturing method, in FDM, better parts were envisioned to be made by reducing the layer thickness, though at the cost of increased build times. Adhesive strength between layers or across filaments is weaker than the strength of a continuous filament and the air gap and raster orientations affect the tensile strength of the FDM parts. Different approaches were attempted in the past to improve surface and overall part qualities. While optimum part orientation and alternative print styles were methods reported for better surface quality, different slicing strategies evolved, targeting better part quality and build times.

Suh et al. were the first to investigate the concept of adaptive slicing for solid freeform fabrication [84], and then quite a few others followed suit. Sabourin et al. [41] presented a new adaptive slicing method in which, the .stl model was first sliced uniformly into slabs of thickness equal to the maximum available fabrication thickness, and then each slab is re-sliced uniformly as dictated by the required surface accuracy. The experimental results indicated a 50-75 percent improvement in slicing speed with spatial partitioning. The partitioning was also essential for parallel computations since it facilitated the distribution for sub-tasks among available processors. Kulkarni and Dutta [85] presented another adaptive slicing method using the cusp height as the slicing reference standard, which is similar to the tolerance in the conventional manufacturing. The cusp height was determined before the slicing, and used to determine the minimum layer thickness, which, together with the uniform layer thickness was used in the processing. The result showed adaptive slicing procedures resulting in less cusp height errors and reduced build layers compared to the uniform slicing procedures.

Sabourin et al. [86] considered three software approaches; the first one using a thicker build layer, the second one with varying build layer thickness according to the local part geometry and the third one with with sparse interior lattice structures. Based on these considerations, they presented a new approach to a rapid layered manufacturing technique based on the concept of building parts with precise exterior and a rapidly built interior region as shown in Fig. 2.9. Contour offsetting and variable layer thickness were used in the accurate exterior, fast interior methods respectively. As a result, the exterior might use the same time as the conventional slicing; however, the interior region was fabricated 5.2 times faster, resulting in an overall 50-80% reduction in build time without affecting the surface quality or part integrity. Additional

savings in fabrication time could be realized by continuing to increase the fill rate in the interior region.

Unlike the previous adaptive slicing methods, Hope et al. [87] used a sloping layer approach, which is based on the surface curvature and the angle of the surface normal. Tyberg et al. [88] noticed that conventional adaptive slicing methods produce unnecessary layers that contribute to increased fabrication times without improving the overall quality of the part surfaces and presented a new approach that first identifies the individual parts and features that comprise each layer in a given build. This technique improved upon existing adaptive slicing algorithms by eliminating most of the slices that do not effectively enhance the overall part surface quality. It was also implemented on an FDM 1600 rapid prototyping system, and had demonstrated a 17-37 percent reduction in fabrication times compared to that of conventional adaptive slicing methods.

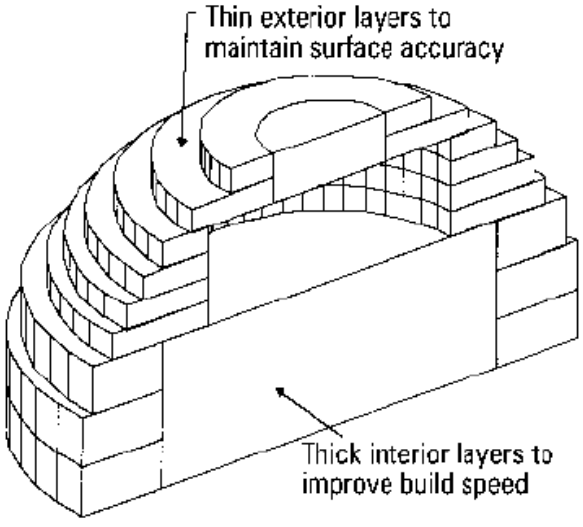

Fig. 2.9 Accurate exterior and fast interior procedure (Image source: Sabourin et al. [86])

Cormier et al. [89] presented an interactive procedure for gathering cusp height requirements for different faces of a part. The procedure starts by applying an edge finding algorithm to the .stl file and grouping facets together according to the face to which each facet belongs. The procedure utilizes functions from the OpenGL graphics library to render the faceted model and to highlight faces one at a time. By allowing non-uniform cusp heights to be specified, the potential to further improve adaptive slicing algorithms was demonstrated as measured by a reduction in build times. Kumar et al. [90] found that the number of layers is drastically reduced by using sloping layer walls in adaptive slicing. They presented a method that approximates the outer wall between two successive contours by a series of taut cubic spline patches. The slicing procedure was specified by choosing from uniform slicing and various adaptive slicing methods. Slicing tests were done on various surfaces with both the existing first order method and the proposed strategy of predicting cusp height. When applied to the same surface, it was found that the first order method resulted in thicker and consequently lesser number of slices for the same allowable cusp height. Lin [91] further extended these concepts and introduced the advanced adaptive slicing algorithm by combining different adaptive slicing approaches [41, 86, 88].

Thrimurthulu et al. [92] presented a single objective optimization scheme by adding average part surface roughness and build time to determine the optimum part deposition orientation using a genetic algorithm. Average part surface roughness was evaluated by slicing the .stl model adaptively. Build time was estimated indirectly by considering the number of adaptive slices and weighing with the ratio of supported area to the total surface area. Based on the case studies considered, it was concluded that the methodology could be used to determine optimum part deposition orientation for any complex part.

Zhou et al. [93] proposed an approach for adaptive direct slicing with non-uniform cusp heights independent of the CAD system using the Standard for the Exchange of Product model data (STEP) format [94]. The cusp height is related to the curvature of the corresponding surface along the build direction and the CAD model is sliced adaptively with different cusp heights. Meanwhile, Ma et al. [95] presented a different adaptive slicing algorithm with a selective hatching strategy. A non-uniform rational B-spline (NURBS) surface model was directly sliced with adaptive thicknesses in order to obtain an accurate and smooth part surface and the test samples were practically printed using a Stratasys FDM 3000 RP system based on the QuickSlice software together with an adaptive slicing module. The build time was reported to have significantly reduced while improving the surface quality. However, the plausible variations in mechanical attributes were not paid any attention and the actual variation in thickness was still quite small. Zeng et al. [96] developed another adaptive slicing algorithm based on a Layer Depth Normal Image (LDNI), approach and reported the method to reduce the size of the storage and increase the efficiency of slicing. Wang et al. [97] used the finite element-based method to subdivide the object into a group of tetrahedral elements and used basic adaptive slicing algorithms for slicing.

Direct Slicing

Stereolithography (.stl) format files offer easy universal transfer of data from CAD to RP and are currently used on all commercial RP systems. However, limitations soon became apparent. Jamieson et al. [98] noticed that tessellation of the .stl file is likely to result in shortcomings such as large data size of the CAD file, limitations due to CAD systems, varying consistency, long

slicing times and lack of scope for modifications. They presented a direct slicing method from the original CAD models. The open format named Common Layer Interface (CLI) was used for the direct slicing method and managed to process with a relatively small sized file compared to the .stl file. It was concluded that the open format file enables a change of format and traditional arguments that sliced data were difficult to manipulate and create supports had been proved to be wrong.

Chen et al. [99] studied and compared several slicing methods such as slicing from .stl files, tolerate-errors slicing, adaptive slicing, direct slicing, and adaptive direct slicing. In order to meet rapid prototyping slicing demands, they proposed a direct slicing approach based on PowerSHAPE models. In their method, lines, arcs and Bezier curves were used to describe the section contours and will probably be a future solution to many existing slicing problems.

Starly et al. [100] observed that the geometric description used to represent solid CAD objects significantly affects the accuracy and quality of the final parts produced especially in the case of freeform shapes, such as the scaffold structures in tissue engineering. The process of tessellation and representation in .stl format is inadequate for designing biomimetic scaffolds with a complex internal architecture. A direct slicing algorithm was presented for layered freeform fabrication based on a neutral, international standard (ISO 10303) STEP-formatted Non-Uniform Rational B-spline (NURBS) geometric representation and was intended to be independent of any commercial CAD software. Optimal build direction was determined based upon STEP-based NURBS models, adaptive subdivision of NURBS data for geometric refinement and ray-casting

slice generation into sets of raster patterns. It was concluded that the direct slicing method overcame a typical deficiency of .stl format files; the loss of information.

Connections between points are absent in the direct slicing process, as the input is in the form of discrete point data. The lack of a global structure might lead to failures while handling complex shapes with multi-contoured slices and even loss of accuracy with some critical features. To overcome these limitations, Qiu et al. [101] presented a method to extract the topological structure from the point cloud data first, and then applying a moving-least square (MLS) surface-based direct slicing process on the structure. With the extracted topological information, the contour numbers and the start points for tracing each contour could be determined, so the slicing process was able to efficiently and correctly handle complex shapes with multi-contoured slices. The topological information also helps preserve important features and reduces the errors caused by changes, if any. The proposed direct slicing method was tested on different sets of point cloud data, and the improvements were validated by experimental results.

The geometric description used to represent solid objects significantly affects the accuracy and quality of the final parts produced with additive manufacturing technology. Direct Slicing is only concerned with the representation of geometry without using a proper thickness for the layers. In order to achieve both, Zhao and Laperriere [102] developed an adaptive direct slicing for RP that potentially enables part fabrication with higher accuracy and production efficiency. The slicing strategy consists of two stages; detecting the features of the model and dividing it into corresponding blocks; and optimizing the layer thickness in each block. The optimal layer thickness and features of the model were obtained by comparing the area deviation and topology

information of the adjacent slices. The algorithm was developed and implemented using Microsoft Visual C++ and AutoCAD Object ARX with the .dxf files and was found to be simple and practical, and equally effective for both polyhedral and faceted models. However, the models were never practically implemented to produce test pieces.

Curved layer slicing

Most of the existing rapid prototyping processes are based on flat layer slicing due to the fact that most of the existing rapid prototyping machines are two-and-a-half axis based systems. In other words, these systems are only sensitive in x and y directions but not along the z axis. In view of these hardware limitations, all current existing software solutions are based on flat layer slicing. Although very effective in turning complex three dimensional shapes into more simple two dimensional shapes, flat layer slicing suffers from vertical discontinuities. Developing a real three dimensional rapid prototyping, or additive manufacturing system, would be a new trend in the near future [103], similar to how the CNC counter parts are evolving into five and more axes systems.

Klosterman et al. [104] developed a curved layer Laminated Object Manufacturing (LOM) process for rapid prototyping. The process was designed for efficient fabrication of curved layer structures made from ceramics and fibre reinforced composites. A new machine was also developed using ceramic tapes and fibre Pre-pregs as feedstock and fabricating curved structures by stacking curved layers, one over the other. Software and hardware were developed in order to achieve the curved layer LOM process. After the implementation, they found the curved layer LOM process was a significant departure from the existing process and a significant

development in both software and hardware were required, as well as the materials and process engineering. But there were definite benefits, and the curved layer process afforded the advantages of eliminated stair step effect, increased build speed, reduced waste and maintenance of continuous fibres in the direction of curvature.

Specifically, while producing shapes like thin, slightly curved shell-type structures (skull bones, turbine blades etc.) conventional flat layer additive manufacturing is poorly suited and may result in a lack of strength, stair-step effects (poor surface finish) or a large number of layers (higher build time). Chakraborty et al. [105] presented an extrusion path generation scheme for FDM, named Curved Layer Fused Deposition Modelling (CLFDM). This technique assumes deposition of material in curved layers in contrast to flat layers used in conventional FDM and was envisioned to overcome stair-step effects without the need for excessive number of layers, while improving the part strength. However, it was mainly a theoretical model based on parametric representation of freeform surfaces and offsetting curved layers using surface-surface intersection and orthogonal offsetting algorithms. Genetic algorithms were used to evaluate optimum shapes of surfaces to offset when multiple peaks exist. Later, as part of a master's research, the author [106] developed curved layer FDM still further through development of mathematical models, software and hardware systems and their integration and final implementation. While these initial studies allowed proof of concept, a number of avenues for improvement were indentified, together with the possibility of integrating the approach with other slicing and deposition methodologies.

While emphasizing the significance and typical drawbacks of current additive manufacturing processes, Chen et al. [107] developed the Computer Numerically Controlled (CNC) Accumulation process. By incorporating multi-axis tool motion, the CNC accumulation process could be beneficial for applications such as plastic part repairing, addition of new design features, and building around inserts. Choi et al. [108] developed a flexible and mobile FDM system by reversing the z stage in a Stratasys FDM 3000 machine. This new configuration was successfully used to build a cylinder on flat and 3D cupped surfaces, including building a horizontally oriented cylinder on a wall by orienting the FDM system in the horizontal position. Additional flexibility was demonstrated by printing directly on a complex curved surface, thus illustrating the possibilities for using additive manufacturing (a traditional 2D layer-stacking processing technique) in conformal printing applications. The curved layer approach will also find significant applications in the future, as new techniques like these are commercialized.

2.3 Research gaps, hypotheses and questions

In summary, FDM is a significant additive manufacturing process and a promising candidate for the direct manufacture of end-use products in the future. Nevertheless, there are specific shortcomings, mainly due to the unfavourable meso-structures resulting from geometrical and process conditions. The transient thermal fields also will have significant influences on the process in general. Novel approaches such as adaptive slicing, curved layer slicing, and optimum build patterns and raster orientations are apparently methods researched and suggested as possible means of overcoming some of these difficulties. However, each of these methods addresses a particular aspect of several issues governing the overall quality of printed parts.

While the true influences of each of these approaches are not clearly understood yet, the research gap also lies in the fact that there have been no attempts made to bring different solutions together in combinations to find optimal printing schemes for given parts, in given orientations.

Unlike the injection moulding process, fused deposition modelling is governed by the inter-filament coalescence and results in anisotropic properties. Based on a modified Frenkel-Eshelby model [109], Bellehumer et al. [33] observed the extruded filaments as not usually at the required temperatures long enough for complete coalescence between adjacent strands to occur. The general FDM structure, also called the meso-structure, is formed by semi-molten filaments partially bonded together due to solid state sintering and solidified eventually. This meso-structure significantly influences the final part characteristics as evident from the experimental stress-strain responses reported [35]. The meso-structure in turn is affected by the choice of process parameters.

The actual mechanism through which the internal meso-structure influences the characteristics of the FDM part is complex and involves the individual and combined effects of different parameters [110]**.** Literature suggests five important parameters predominantly controlling the strength of FDM processed components; layer thickness, part build orientation, raster angle, road width and air gap [52]. According to Es-Said et al. [79], the anisotropy properties are caused by the polymer molecules aligning themselves with the direction of flow, formation of pores in preferred orientations and weak interlayer bonding. It is pertinent to point out at this stage that the raster angle is central to all this and was in fact established by Ahn et al. [47] as the most significant parameter, based on tensile, three-point bending and impact test results. The

classical lamination theory and Tsai-Wu failure criterion [78, 111] were attempted to predict relationships between the raster angle and tensile strengths or to determine the elastic modulus values of the FDM parts.

Evidently, there is a definite relationship between the raster angle and the mechanical properties of FDM parts. Experimental and analytical evaluations were attempted earlier and results from both models were shown to be closely correlating. However, the models developed were mostly based on assumptions that the elastic and shear modulus values are constant and equal to the bulk material properties. Considering the highly anisotropic nature of the composite material constituted of partly coalesced intricate network of polymer strands interspersed with air gaps, this appears to be over simplifying the problem. This necessitates further theoretical and experimental evaluations to be taken up for better understanding of the actual role of the raster angle in FDM.

While optimum part orientation [112] and alternative print styles [113] were methods reported for better surface quality in FDM, different slicing strategies evolved, targeting better overall part quality and build times. Variable thickness slicing for optimum number of slices and cusp-height presented by Kulkarni and Dutta [85], step-wise uniform refinement approach developed by Sabourin et al. [41], adaptive slicing based on surface curvature and angle presented by Hope et al. [87]**,** precise exterior and rapidly built interior approach suggested by Sabourin et al. [86] and the method of identifying individual parts in a given model reported by Tyberg et al. [88] are notable examples. However, most of these slicing techniques were based on mere mathematical

algorithms and practical implementation and testing was limited, while the confounding effects of filament size with the speed of extrusion and printing were completely ignored.

Apparently, FDM literature presents numerous adaptive slicing approaches, but mainly as mathematical models, without any experimental backup and optimum raster orientations that are not directly supported by the theories of material consolidation. It was observed by Bellini [38] that higher mass deposition rates could be achieved during the road formation by reducing the speed of deposition. This brings up yet another factor, the print speed into focus. It is necessary to view adaptive slicing in terms of the consolidation mechanisms, with due consideration to the time-dependency, in order to explain the plausible effects.

Although these improvements, especially in slicing algorithms mentioned above, lead to some progress in FDM processing, the part surface quality and geometric accuracy are still a major concern. Reducing build time and increasing part surface quality are two factors that contradict each other. Several different attempts have been brought forward in the literature, aiming at better solutions for curved surfaces; however, they still have their own limitations, especially for thin curved shell-type parts. The promise of true engineering products being slowly realised through machine and material improvements, both surface quality and strength of parts become critical in particular in the direct manufacture of end-use parts. Inspired by the curved layer LOM process [104], Chakraborthy et al. [105] initiated the curved layer FDM mainly to address the surface quality and fibre continuity problems in thin shell type FDM parts. The author also developed some preliminary analytical models and hardware and software solutions for processing and practical implementation of curved layer slicing earlier [106]. But the methods

require further refinement, while there is also need for a true experimental validation of the approach.

It may also be noted that raster angle studies, adaptive and curved layer approaches have been investigated individually in the past. The raster orientation presumably decides the mechanical behaviour of the resulting material. Adaptive slicing is predominantly used to better represent intricate details and overcome the stair-step effects. Curved layer slicing is a relatively recent addition and is expected to better handle the stair-step effects in specific situations. Ideally, in a given part, it may give better results if both adaptive and curved layer slicing are combined, so that the areas close to the top surface are printed using curved layers, while the interior is filled with adaptive flat layers. Once the merit in this is realised, several possible combinations would arise for investigation; uniform flat layers, adaptive flat layers, uniform and adaptive curved layers and adaptive curved and flat layer slicing, together with varying raster orientations. Considering that the final meso-structure actually dictates the mechanical behaviour of the resulting material and the fact that each of these approaches can vary the internal structure to different degrees, an interesting approach is to combine different methods in combinations in a given component and evaluate the effects. There is no existing literature reporting any previous attempts in this direction, and will be attempted as part of the current research.

Based on the literature review and the foregoing discussion, flat and curved layer slicing, adaptive slicing and optimisation of raster orientations are some schemes developed mostly individually, by different researchers, for improving the quality of parts produced by FDM. The current research is built on the belief that better solutions can be developed by combining one or

more of these deposition strategies, in order to be able to achieve the best mechanical and surface qualities for a given part. The optimum solution essentially targets the most favourable meso-structure. The hypothesis for the current research is:

”An appropriate deposition scheme, consisting of a combination of layers of flat or curved orientations and uniform or varying thickness with appropriate internal road structure would result in the most optimum characteristics of parts produced in FDM”.

The research to be done must first look at the fundamental mechanics of the influences of raster angle orientations on the mechanical properties of the resulting material structures in FDM. Further, theoretical and experimental evaluation of the role of varying filament sizes and consequent layer thicknesses must be considered. Further to developing a fundamental understanding of these aspects, a proof of the proposed hypothesis requires finding answers to several questions that arise around practical problems and the ensuing effects of implementing curved and flat layers and adaptive slicing both individually and in certain combinations. The following are the significant research questions to be addressed:

- How do variations in raster orientations affect the critical mechanical attributes of material structures resulting from fused deposition modelling?
- What is the true role of varying layer thickness in fused deposition modelling and how does this alter with speed and time of printing and their interactions?

- What are the limitations of the current curved layer slicing models and what alternative approaches can be employed for better slicing and practical implementation and what will be the effects on the critical attributes of a typical component?
- How can adaptive slicing be implemented in real and practical situations? What consequent effects this will have on the part mechanical characteristics
- How do combinations of flat, curved, uniform and adaptive slicing schemes, together with different raster orientations in each layer influence the mesostructures and eventually the final part characteristics?
- How can these be integrated in order to implement the best combination of slicing and deposition styles within a given part with a given print orientation?

2.4 Methodologies and objectives

The current research is designed to investigate and find answers to the questions listed above and the methodology involves theoretical and experimental evaluation of the mechanics of raster orientations and adaptive slicing and development of mathematical algorithms for different slicing schemes followed by the practical implementation of the same. Experiments aimed at investigating the part characteristics for different combinations of process parameters and deposition styles will need development of test facilities and appropriate procedures. Test pieces resulting from different print strategies will be evaluated considering mechanical properties as well as internal meso and micro structures. Different deposition schemes will eventually be integrated into a model that processes a given part and divides the domain into a number of

regions for the deposition of the material in different styles for the best overall characteristics of the part. It may be noted that the current research methodologies are only briefly presented here, while detailed descriptions of all methods employed will be presented at appropriate places in the following chapters.

The raster angle effects are to be evaluated considering the force equilibrium of internal strands and further evaluation of the mechanics of the multiple strand structure representative of the internal road structure in FDM. Theoretical models for evaluating the effects of adaptive layers will be built considering the second moment of area of the cross section of the multi-strand specimen with varying degrees of inter-road and inter-layer coalescence. Next, mathematical algorithms will be developed for both curved and adaptive slicing schemes. While curved layer slicing is relatively new, a couple of solutions currently exist, but more practical and efficient algorithms need to be developed. On the other hand, adaptive slicing is extensively researched already, and a comprehensive literature review is necessary, followed by the identification of a suitable method for the practical implementation, with some further improvements. The next stage is to develop test beds that can be used as FDM systems for the practical implementation of the deposition strategies developed, both individually and in different combinations. Further, test piece printing and experimental investigations leading to the establishment of mechanical and micro structural characteristics would have to be carried out to be able to establish the significance of different deposition strategies both individually and combined. The final stage is to combine different deposition strategies into a selection algorithm that can be used on given solid shapes to establish the most favorable deposition schemes in different regions. The

following is a list of the objectives set for the analytical and experimental investigations planned to be carried out to prove the hypothesis stated:

1. Experimental evaluation of the influence of varying raster angles on critical mechanical properties of test pieces, analytical modelling of the same considering the mechanics of material consolidation in a multi-strand material system and correlation of the two results.
2. Analytical modelling of the effects of varying filament and layer sizes considering both speed and time of printing and experimental validation of the models.
3. A comprehensive state-of-the-art literature review on CAD file slicing procedures covering uniform flat layer, adaptive flat layer, and curved layer slicing.
4. Development of appropriate test facilities for the practical implementation of different deposition schemes investigated.
5. Development of improved algorithms for curved layer slicing and experimental evaluation of the true effects of curved layer slicing through practical implementations close to the reality
6. Development of deposition path modelling algorithms for both flat and curved layers.
7. Integration of alternative slicing and raster orientation approaches into an overall selection scheme and developing an integrated algorithm that allows development of the best combination of deposition schemes for a given part, in a given orientation.

Chapter 3 Adaptive Slicing for Fused Deposition Modelling

3.1 Adaptive slicing; early attempts and general impressions

From the early stages of rapid prototyping through to additive manufacturing, the layer-by-layer processing technique always suffered from inferior surface quality emanating from stair-step effects and missing finer details, in specific cases. Use of flat layers of varying thicknesses was envisioned as a possible means of resolving these issues, in particular with fused deposition modelling. The basic approach is to use finer layers at places where surface quality is affected or very fine details need to be reproduced from CAD files and fill the rest of the part domain with thicker layers. Mathematical algorithms were developed to programmatically construct adaptive slices for given components and either the slope of the bounding surface or the resulting cusp or step height are normally used as criteria for choosing layers of varying thicknesses in different zones.

One of the advantages often used to substantiate the adaptive slicing scheme is that the stair-step and other issues could be resolved without sacrificing much on the time of production. Presumably, this means that the speed of printing remains the same and the thicker layers used in non-critical areas would save the time as against the time lost with thinner layers to be employed in critical areas. However, this argument may not stand much ground if the thermal variation of the process is truly considered together with varying layer thicknesses. For example, if the speed of printing is kept constant, the overall time given for the sintering of a unit length of the

filament is lesser in the case of thicker layers and considering the time-dependent nature of coalescence, this should lead to inferior part qualities. The confounding nature of the influences of the critical parameters being obvious, the mechanics of adaptive slicing needs to be properly modelled. This is attempted now reviewing the critical aspects of the existing models first, before presenting the actual analytical models developed. While the discussion here is limited to the mechanics of adaptive slicing by analytical means and a direct experimental validation of the models developed, the implementation of adaptive flat and curved layers in specific cases is differed to Chapter 6.

3.1.1 Basic adaptive slicing

As in any Additive Manufacturing process, the tessellated CAD file needs to be sliced before processing on a FDM system. Solid models are created in a CAD environment and then tessellated into Stereolithgraphy format (.stl) or Additive Manufacturing format (.amf) files. During slicing, the three dimensional solid model is cut into layers with a series of horizontal flat planes, to obtain a two dimensional contour representing each section of the solid. The simplest method is to consider a series of equidistant horizontal cutting planes and obtain slices of uniform thickness as shown in Fig. 3.1. However, the surface defects and the internal defects mentioned in previous chapters are unavoidable and often exemplified further due to uniform slicing. Layers of uniform thickness also bring in the conflict between the overall surface quality and the total time of production [114]. Further, Uniform layers often result in loss of CAD data when finer details exist on a part and use of very fine layers again contradicts with the general requirements to reduce the overall production time.

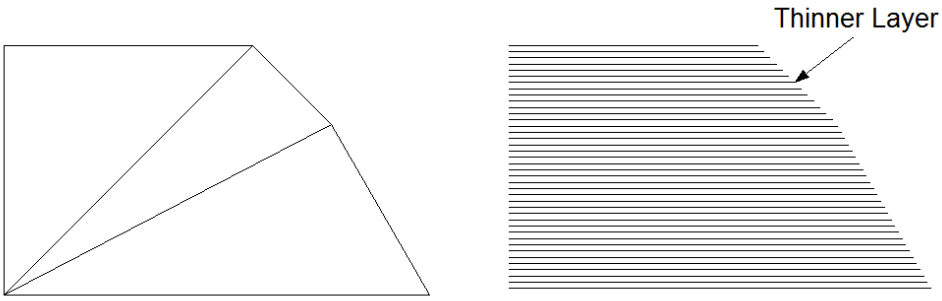

Fig. 3.1 Uniform layer slicing

The basic concept of adaptive slicing was first introduced to balance the process parameters between two contradicting requirements; better part quality and lesser production time. Dolenc and Makela [115] stated the problem of manufacturing a part as accurately as possible with a minimal number of layers and considered use of a range of layer thicknesses, restricting the surface quality within a user-specified tolerance and without the loss of the finer features of the model. The cusp height was defined as the user-specified tolerance C_{max}. The location of the next slice is estimated using the normal evaluated along the last slice. If $\boldsymbol{N} = (N_x \quad N_y \quad N_z)$ is the unit normal at point P, then $\boldsymbol{C} = c\boldsymbol{N}$ must satisfy $\|\boldsymbol{C}\|_2 = c \leq C_{max}$. Since C_{max} is given, the calculations are straightforward with:

$$l = C_{max}/N_z \qquad (Eq.3.1)$$

Where l is the layer thickness. Fig. 3.2 shows how the basic adaptive slicing alters the layer thicknesses based on the varying slopes of the boundary surfaces of the example part shown in Fig. 3.1. However, there are limitations to this adaptive slicing approach. When the slicing plane

and a typical feature such as a corner are too close together, a layer of appropriate thickness may not be accommodated even with the finest thickness, and a missing detail will result as shown in Fig. 3.3.

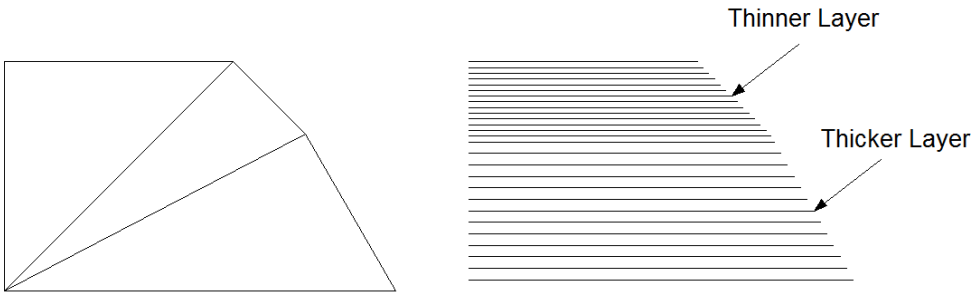

Fig. 3.2 Layers of varying thickness resulting from the basic adaptive slicing method

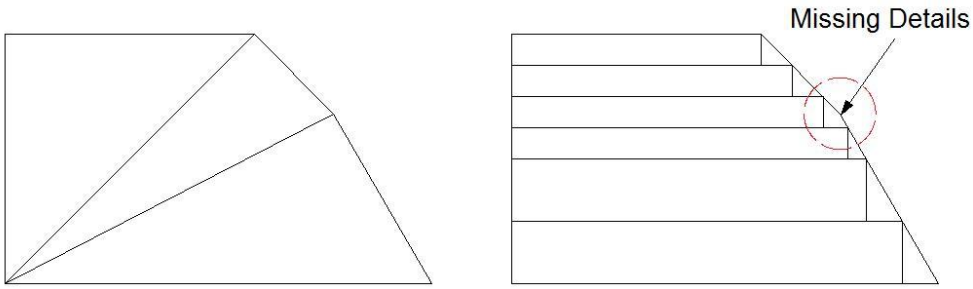

Fig. 3.3 A specific shortcoming of the basic adaptive slicing method

The basic adaptive slicing by Dolenc and Makela only emphasized the importance of recognizing and accommodating extreme or peak features and flat horizontal areas and associated features might still be missed out. Considering this, Sabourin et al. [41] presented

adaptive slicing by stepwise uniform refinement. The solid model is first subdivided into thick, uniform, horizontal slabs of thickness equal to the maximum acceptable layer thickness L_{max}. Then the slabs are sliced with thinner layers to satisfy the maximum cusp height restriction, C_{max}. Finally, the slab is examined both from its bottom slice looking upward and from its top slice looking downward. This dual-direction examination is to avoid missing out any high-curvature regions. They also developed the algorithm to decide the number of sliced layers of uniform thickness a particular slab is to be subdivided into:

$$\alpha_{slab} = \text{int}\left(\frac{L_{max}}{C_{max}} \max\{n_{z_{bottom}} \quad n_{z_{top}}\}\right)$$
$$\alpha_{slab} \in [1, \alpha_{max}], \quad \alpha_{max} = \text{int}\left(\frac{L_{max}}{L_{min}}\right) \qquad (Eq. 3.2)$$

Where $\{n_{z_{bottom}}\}$ and $\{n_{z_{top}}\}$ are the sets of unit normal z components for the points across the bottom and top slice levels of a particular slab, respectively. The resulting uniform layer thickness with a particular slab therefore becomes:

$$l = L_{max}/\alpha_{slab} \qquad (Eq. 3.3)$$

Where l is the layer thickness. Fig. 3.4 shows an example of the application of the stepwise uniform refinement method. Although this method is an improvement over the basic adaptive slicing, it still has certain limitations; for example, it may result in unwanted regions filled with finer slices, in specific examples such as the one shown in Fig. 3.5.

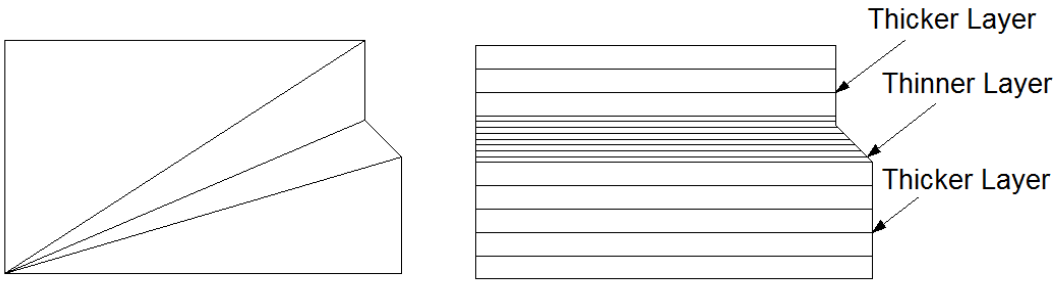

Fig. 3.4 Sliced results using the stepwise uniform refinement method

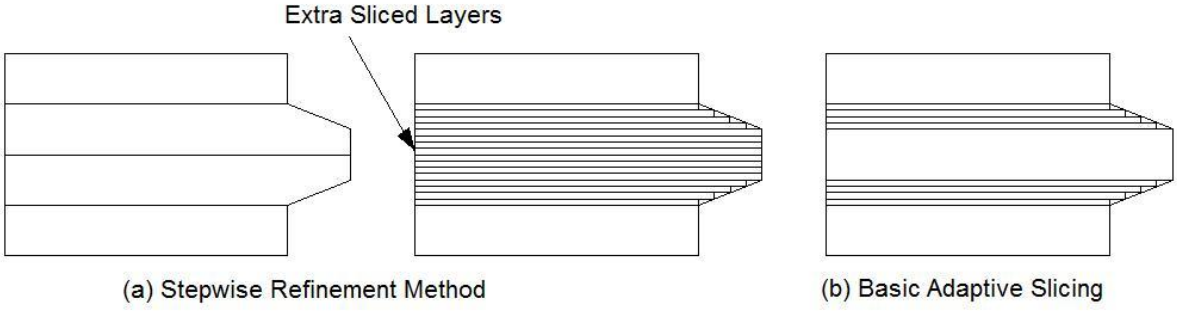

Fig. 3.5 Problem existing by using basic stepwise uniform refinement method

Pandey et al. [116] noticed that the cusp height and limited deviation of cross-sectional area of the part attempt adaptive slicing for optimum production times, but fail to consider the part surface quality. They introduced another method based on limiting the surface roughness (R_a) value, called real time adaptive slicing and presented an equation for R_a to determine the slice thickness at 99% confidence:

$$t = \frac{R_a \cos\theta}{70.82} \qquad (Eq.3.4)$$

Where R_a is the local surface roughness in μm, t is the layer thickness in mm and θ is the build orientation angle between the vertical and the surface tangent. The average part surface quality is given by:

$$R_{a_{av}} = \frac{\sum R_{a_i}}{\sum A_i} \qquad (Eq.3.5)$$

where $R_{a_{av}}$ is average surface roughness of the part, R_{a_i} is the roughness of the ith slice or trapezium and A_i is the area of the surface of the cylinder. The real time adaptive slicing method was reported to reduce the number of slices and the build time. The major advantage is the part quality is expressed in terms of the standard R_a value used in design and manufacturing.

Adaptive slicing improves the surface quality by varying the layer thickness according to the changes in the surface geometry. In order to examine the deposition accuracy, the percentage volumetric error,E_{v}, is defined by Lin [91] as

$$E_{\mathrm{v}} = \left[\left(V_{\mathrm{p}} - V_{\mathrm{m}}\right)/V_{\mathrm{m}}\right] \times 100\% \qquad (Eq.3.6)$$

Where V_{m} is the total volume of the STL model and V_{p} is the volume of the deposited part. The volume V can be calculated using:

$$V = \sum_{i=1}^{N} A_i H_i \qquad (Eq.3.7)$$

Where

$$A_i = \frac{1}{2}\sum_{j=1}^{m+1}\left(x_j y_{j+1} - x_{j+1} y_j\right) \qquad (Eq.3.8)$$

Where H_i is the thickness for the i^{th} layer, A_i is polygon (contour) area for the ith layer, m is the polygon edge number of a contour, and x and y are the coordinates of the polygon vertices.

Comparatively, for the same volumetric error, the basic adaptive slicing achieved less number of layers and smaller cusp height values. Similarly, a comparison between the basic adaptive slicing and the stepwise refinement method showed that the volumetric error of the former method was only half of the latter one under the same surface accuracy conditions.

Although the basic adaptive slicing improves the surface quality and the efficiency, the effectiveness actually depends on the surface geometry of the model. The flatter the surface normal, the thicker the layer will be. The selection of the layer thickness usually depends on the minimum surface slope and once chosen, the same value will be used for the entire layer in order to be able to satisfy the slicing accuracy requirement easily. However, this might make the fabrication process inefficient in specific cases, as depicted in Fig. 3.6. In Fig. 3.6(a), Part A on the left needs to be sliced with thinner layers while Part B on the right only needs to be sliced with thicker layers. In Fig. 3.6(b), the left side of the solid model requires finer slicing while the right surface requires thinner layers, resulting in a conflict and at the end a compromising solution using thinner layers throughout.

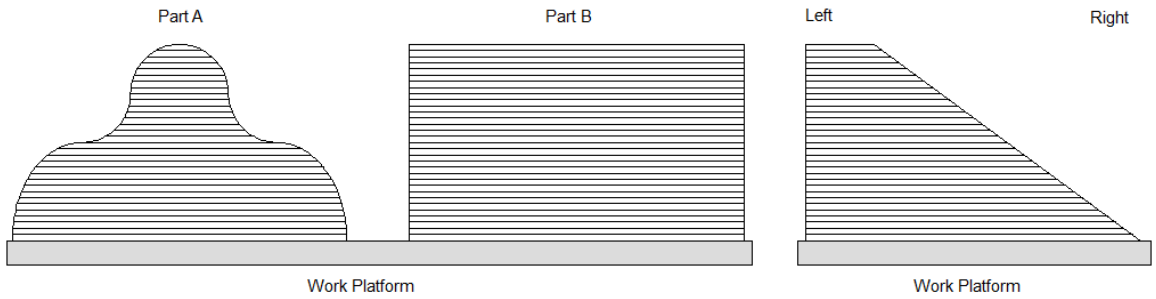

Fig. 3.6 A common problem with the basic adaptive slicing

Increasing the efficiency of slicing also could be a part of the adaptive slicing. Identifying the significance of the slicing process, Tata et al. [117] developed a high speed and accurate slicing engine capable of recognising and retaining key characteristics and graphically representing slices. The slicing engine first uses the Facet Processor to sub-group facets and then based on the Key Characteristics Identifier locates the features on the .stl file. A thickness calculator also was introduced to vary the thickness of layers based on cusp height, maximum deviation and chord length and finally, backtracking to handle sudden changes in complexities.

3.1.2 Advanced adaptive slicing based on .stl files

Adaptive slicing through basic methods as discussed above solve only part of the problem, and need more advanced approaches for the overall efficiency. A more advanced adaptive slicing was attempted by Sabourin et al. [86] by introducing the accurate exterior, fast interior method. In essence, the approach is to building parts with precise exterior and rapidly built interior regions as shown in Fig. 3.7. The finer exterior layers are filled with appropriate speeds while the interior regions are filled much faster and the algorithm was implemented on a Stratasys FDM 1600 system by using the code written in C++. Experiments showed that the fill rate in the interior region can be increased by a factor of five or more over the conventional material deposition rates to yield around 50-80 percent reduction in build time without affecting the surface quality or part integrity.

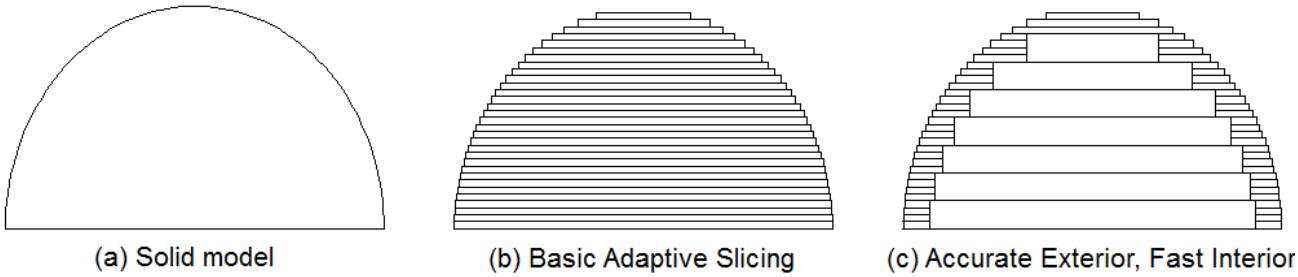

Fig. 3.7 Adaptive slicing using the accurate exterior, fast interior method

Tyberg and Bohn, presented a method of slicing each part and feature independently within the build envelope called local adaptive slicing [88]. Individual parts and part features are first identified and then an appropriate build layer thickness for each of them was determined separately as shown in Fig. 3.8. The result showed the elimination of most slices that do not effectively enhance the quality of the part surface and an additional time saving of 17-37 per cent over conventional adaptive slicing methods.

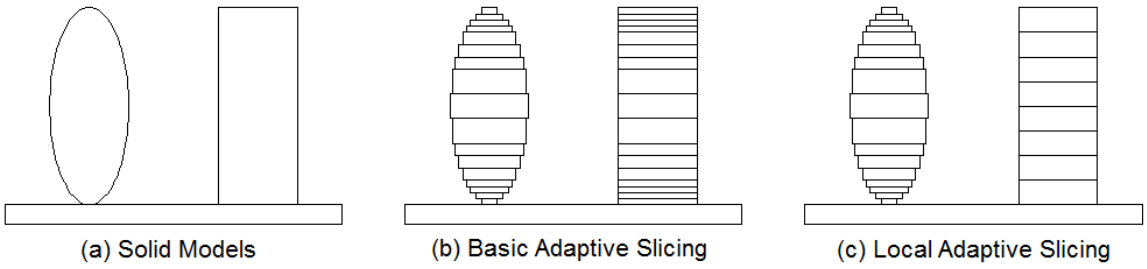

Fig. 3.8 Slicing results based on local adaptive slicing

Mani et al. [118] presented the region-based adaptive slicing which allows the user to specify distinct cusp height values for different surfaces of the CAD models. The model was decomposed into two regions; Adaptive Layer Thickness region and Common Interface Layer region, to be filled with adaptive and uniform thicker layers respectively, as shown in Fig. 3.9. They used an ACIS model as input rather than the STL file and the slice data was output in the Stratasys SLC format. Initial experimental results showed the time to manufacture the model reduce by 23% when region based adaptive slicing was used as opposed to basic adaptive slicing. It was also claimed that this method could be applied to heterogeneous objects by using different slice and layer generation strategies for different material regions.

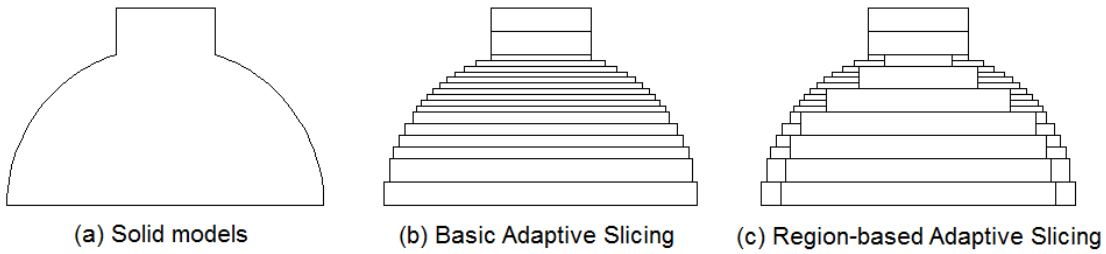

Fig. 3.9 Results of region-based adaptive slicing

3.1.3 Advanced adaptive slicing based on other format files

Jamieson and Hacker [98] used commercial software to produce the slices direct from the CAD model. Layers with a standard and a maximum thickness were considered first, and comparing the two, if the section of the part was not changed in a large interval, the maximum thickness would be used. Otherwise, a new slice halfway between the standard layer thickness and maximum thickness would be fit in for a further comparison. This process gets repeated until a

maximum allowable layer thickness is found. This showed that direct slicing could be a benefit while handling CAD models of different input formats.

Kulkarni and Dutta [85] developed an algorithm for determining a variable layer thickness for an object represented in the parametric form. The normal curvature in the vertical direction is used to determine the maximum allowable layer thickness for the surface at the referenced level with a pre-specified cusp height. The algorithm was implemented and tested with two sample parts built by the Stratasys 3D modeller. The comparison with uniform slicing showed that when the cusp height was constant, the adaptive slicing took a lesser time to manufacture. Chen et al. [119] also used the commercial software, PowerSHAPE, to create solid models for direct slicing and the results are lines, arcs, and Bezier curves, which are more precise and easy to use on a additive manufacturing system. Kumar et al. [90] presented a method that approximates the outer wall between two successive contours by a series of taut cubic spline patches. Ma et al. [95] developed an algorithm using which, a non-uniform rational B-spline (NURBS) surface model was directly sliced with adaptive slicing in order to obtain an accurate and smooth part surface. A selective hatching strategy was also implemented, which is similar to the region-based adaptive slicing, to further reduce the build time. A direct method was developed for computing skin contours for all tolerance requirements. The experimental results showed that adaptive slicing was effective for any complex model with freeform surfaces and the selective hatching strategy was most effective for general freeform parts with thick walls.

Another approach to adaptive slicing was through the use of the point cloud data. Qiu et al. [101] noticed that direct slicing of point cloud data was an effective way to integrate reverse

engineering and rapid prototyping but failed to handle complex shapes when multi contoured slices existed. They developed a method to extract topological structure from the point cloud data and applied to it a moving-least square (MLS) surface-based direct slicing. Two modified topology extraction methods were developed to improve the efficiency and stability of the process; (1) a variation of the traditional projection-based MLS surface and (2) a 2D contour generation rectification algorithm. Case studies showed improvements in the efficiency of the algorithm. Zeng et al. [96] developed another adaptive slicing approach based on a Layer Depth Normal Image (LDNI) method to achieve a compromising solution for the Constructive Solid Geometry (CSG) models. The adaptive Boolean operation was first applied to the 1D segment of the adaptive LDNI solids and then layered loop construction was applied to the Boolean LDNI solid consisting of a layered ordered point cloud.

While the foregoing discussion gives an impression of the developments in adaptive slicing, it may be noted again that most of these are mere mathematical algorithms and for most part had not been implemented in practice. The temperature of the filament and that of the substrate and the speed at which filaments are deposited will have critical roles to play in the inter-road and inter-layer diffusion and bonding. Further, the mechanism and mechanics of material consolidation greatly affect the mesostructure, together with the layer thickness and the rate of printing. These aspects need specific attention in order to be able to understand the real effects of varying layer thicknesses. A further insight into the mechanics of material consolidation in FDM is considered next so that the effects of varying layer thickness on the final part characteristics can be evaluated.

3.2 Mechanism of material consolidation and critical factors in FDM

A further discussion of the mechanism and mechanics of material consolidation in FDM is necessary now, in continuation to the preliminary discussion presented earlier. As mentioned in the previous chapter, FDM parts are constructed by first filling with semi-molten filament and then consolidating the filaments with thermal energy. During the consolidation process, the material cools, solidifies and bonds with the surrounding material. However, unlike injection modelling, the material is only partially bonded and forms a typical meso-structure as shown in Fig. 3.10. This type of meso-structure significantly influences the final part characteristics and as mentioned in the previous chapter investigated and reported by different researchers [35-37, 73]. It is important at this stage to understand the means of formation of the meso-structure and the critical parameters that play significant roles in the process.

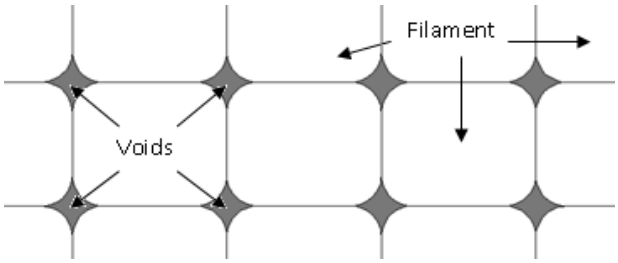

Fig. 3.10 General meso-structure of an FDM part

During material consolidation, the thermal energy drives the semi-molten strands in FDM to form the inter-road bonds. Bellehumeuar et al. [33] divided this process into three different stages; (1) surface contacting, (2) neck growth, and (3) molecular diffusion at interface and randomization, as shown in Fig. 2.7, and a slightly different version is reproduced in Fig. 3.11 for better understanding. Considering observations by different researchers, and as already noted

in chapter 2, the inter-road and inter-layer bonding process in FDM can be analysed based on sintering or diffusion mechanisms. While both sintering and diffusion models have their own strengths and limitations, the time spent on the unit length cannot be ignored. Further, the diffusion model does not take the shape of the contact area into consideration, which leaves it far from reality. Relatively, the sintering model simulates the bonding process in FDM close to the reality and will be used in the current analysis [33].

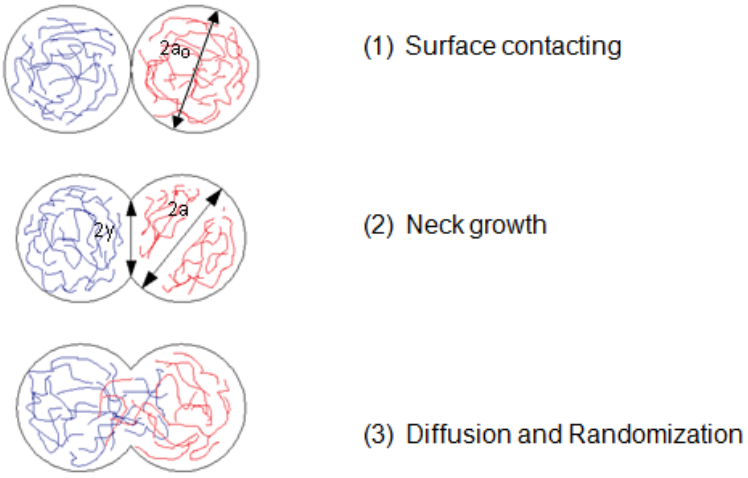

Fig. 3.11 Bond formation process between two filaments: (1) surface contacting (2) neck growth (3) molecular diffusion at interface and randomization

Sintering is the coalescence of particles under the action of the surface tension. Frenkel [120] derived the first analytical model describing the rate of the coalescence occurring by viscous flow for two identical spherical particles as:

$$\frac{y}{a} = \left(\frac{3}{2}\frac{\Gamma t}{\mu a_0}\right)^{\frac{1}{2}} \qquad (Eq.3.9)$$

where a, a_0, t, y, μ and Γ are the particle radii, sintering time, sintering neck radius, viscosity, and surface tension of the material respectively as shown in Fig. 3.11. However, Eshelby found that the continuity equation for an incompressible fluid was violated in the development of Frenkel's model and proposed corrections, subsequently referred to as the Frenkel-Eshelby Model, as given in Eq. 3.10.

$$\frac{y}{a} = \left(\frac{\Gamma t}{\mu a_0}\right)^{\frac{1}{2}} \qquad (Eq. 3.10)$$

Hopper [121-123] proposed an exact analytical solution of the Navier-Stokes equations for a two-dimensional viscous flow driven by capillary forces acting on the free surface and analyzed the capillary flow for two cylinders having an inverse ellipse at their cross section and presented the following sintering models [121, 123]:

$$\frac{y}{\alpha_f} = (1-\alpha)(1+\alpha^2)^{-\frac{1}{2}} \qquad (Eq. 3.11)$$

$$\frac{\Gamma t}{\mu a_0} = \frac{\pi}{4}\int_{\alpha^2}^{1}\left[\beta(1+\beta)^{\frac{1}{2}}K(\beta)\right]^{-1} d\beta \qquad (Eq. 3.12)$$

Where α_f is the final particle radius and α is the parameter of the inverse ellipse. Pokluda et al. [61] further developed (Eq. 2.1) the Frenkel-Eshelby model assuming two spherical particles sintering into each other and finally becoming a single sphere. However, this model cannot be directly applied to sintering across cylindrically shaped strands.

Although all sintering and diffusion models currently available suffer from limitations to be able to simulate the physics of material consolidation in FDM close to the reality, there is one common parameter of interest in all of them; the sintering time. Bellehumeuar et al. [33] experimentally evaluated the typical time-dependent coalescence evolution of ABS P400 cylindrical particles. The projected areas of the particles and the variation of the diameter of the neck formed between them were measured based on a series of photographs taken at different time intervals as shown in Fig. 3.12. The shape of the particles is similar to the theoretical prediction shown in Fig. 3.11. The dimensionless quantity y/a represents the ratio between the neck radius and the particle's radius. After prolonged exposure for sufficient time and temperature, the overall contour in the plan view became irregular and the particles started to merge into each other. Other than semi-solid droplets, powder particles also proved the sintering time to have significant effects on the consolidation process [124].

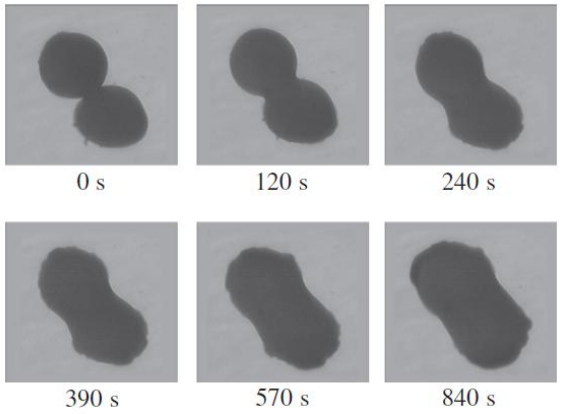

Fig. 3.12 Neck growth evolution for ABS P400 at constant temperature (200˚C) (Image source: Bellehumeur et al. [33])

Sintering temperature is also another critical parameter influencing the final mechanical properties of the FDM part. Li et al. [125] presented both theoretical and experimental results

showing that the neck growth for ABS P400 is negligible at temperatures below 200˚C. In their theoretical model, lumped-capacity analysis was applied to model the cooling process. They also assumed a uniform temperature distribution throughout the cross-section and the cooling process was simplified into a one-dimensional transient heat transfer model as shown in Fig. 3.13. For the differential element, the energy balance is as follows:

$$\rho CAv\frac{\partial T}{\partial x} = A\frac{\partial\left(k\frac{\partial T}{\partial x}\right)}{\partial x} - hP(T - T_{\infty}) \qquad (Eq.3.13)$$

with $T = T_o$ at $x = 0$ and $t \geq 0$

and $T = T_{\infty}$ at $x = \infty$ and $t \geq 0$

P and A are the filament perimeter and cross-section area. h covers the effects of both heat convection with air and conduction with foundation. P and A are defines as:

$$P = \pi(a + b)\left(\frac{64 - 3\lambda^4}{64 - 16\lambda^2}\right) \text{ where } \lambda = \frac{a - b}{a + b}$$

$$A = \pi ab$$

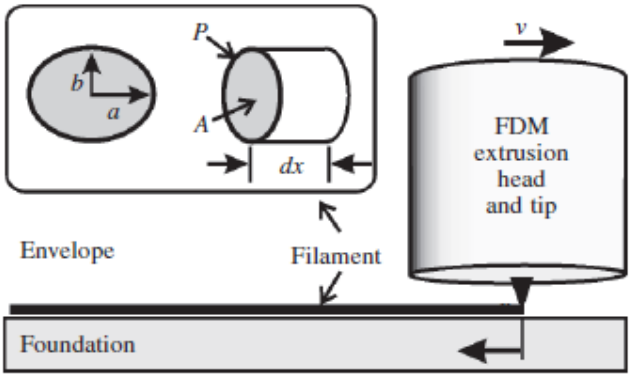

Fig. 3.13 Schematic of deposition and cooling of a filament in FDM process ((Image source: Bellehumeur et al. [33])

Fig. 3.14 shows the predictions on the neck growth between strands based on their model. It can be seen that most of the neck growth between the polymer filaments occurs within seconds following the extrusion of the polymer and deposition on the foundation. The rate and level of wetting that can be achieved between polymer filaments are highly dependent on the extrusion temperature. Furthermore, material viscosity and surface tension are all temperature dependent.

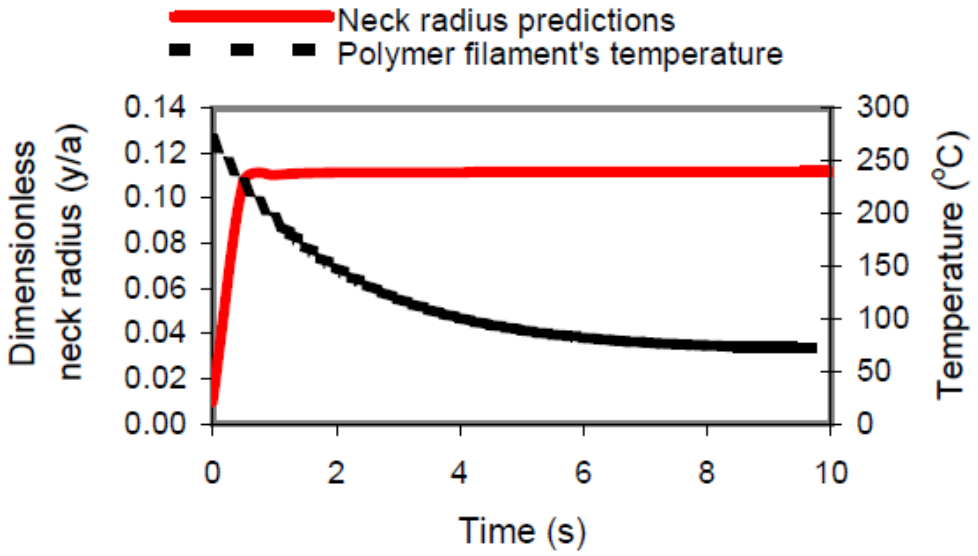

Fig. 3.14 Model predictions for the dimensionless neck growth profile for ABS P400 (Image source: Li et al. [125])

Based on the foregoing discussion, it can be concluded that both sintering time and temperature are critical parameters of the consolidation. However, these two parameters are not independent of each other. The sintering temperature is the first prerequisite while sintering time is the second. Only when the material reaches the sintering temperature, the neck growth initiates

together with the coalescence between roads or layers and if the sintering time is insufficient, poor bonding or a complete lack of bonding might occur. Again, in the actual deposition process, both sintering time and temperature cannot be directly controlled. The sintering temperature is mostly dependent on the temperature in the extrusion head and quickly changes depending on the envelope or the substrate temperature, while the sintering time is directly related to the print speed. In other words, the print speed and the extrusion temperature will have control over the meso-structure and in turn on the mechanical properties of the FDM part. However, all the past research reviewed so far only considers effects of sintering temperature and time in the context of uniform layers and there is little evidence of the role of adaptive layers evaluated so far. The next section attempts this by applying the consolidation mechanics to adaptive slicing in FDM.

3.3 Analytical modelling of the role of adaptive slicing

It is commonly believed that adaptive slicing dramatically reduces the build time both in slicing and depositing, while maintaining the surface quality. However, only a few researchers actually attempted to envisage the plausible effects of adaptive slicing on the mechanical properties of the parts processed with layers of varying thicknesses. The main reason is that most of the earlier research is focussed around mathematical algorithms and software implementations of the adaptive slicing, and practical implementation and testing is very limited, considering the numerous difficulties with the hardware. Commercial FDM systems work like black boxes and allow no freedom to play with basic settings and in practice, it is very difficult to achieve programmatically controlled and varied layer thickness from a single nozzle set-up. Ma et al. [95] implemented layers of varying thicknesses while printing a hollow model using a Stratasys

modeler with the thickness of the layers varied from 0.178mm to 0.508mm, but the print speed effects were not segregated while evaluating the effects on the consolidation process. Another interesting belief in FDM is that finer layers produce parts of better mechanical characteristics, presumably due to finer voids and better meso-structures. Again, there is very little practical evidence to support this too, considering that most attempts were actually made printing layers of thicknesses beyond normal sizes. This necessitates evaluation of whether uniform thin layers always give better mechanical properties. An analytical model is built from the first principles here to evaluate the true role of adaptive slicing followed by experimental validation of the same.

The first step of the analysis is the choice of a certain mechanical attribute to serve as a benchmark for the comparative evaluation of the role of the layer thickness. Flexural strength, which is defined as a material's ability to resist deformation under load, is one of the common mechanical properties and represents the highest stress experienced within the material at the point of rupture. It is often tested by three-point bending and does not require a dog-bone shaped test piece and is used as a means of testing for the analytical and experimental work done here. The flexural strength is the same as the tensile strength in an ideal case for which the material is homogeneous, but in FDM, the meso-structure dominates the internal structure and will affect the final properties of the part.

A flat piece specimen of dimensions 50 mm X 20 mm X 4 mm is considered as the basis for all analytical and experimental investigations carried out as part of the work presented in this chapter. Assuming pure bending and constant flexural strength, the equation for the stress from the elementary principles of solid mechanics is:

$$\sigma = -\frac{Md}{I}$$

where M is the bending moment, d is the distance from the neutral axis, and I is the second moment of area. In this equation, the moment of inertia, I is dependent on the cross-sectional shape of the test part, which in turn varies with the filament size and inter-road coalescence and will be used as a basis for the analytical evaluation of the flexural behaviour of multi-layer FDM samples. Considering that the deposited filaments partly fuse into one another, an exact cylindrical road is far from reality and the actual shape of each filament depends on the rate of coalescence. In order to establish the maximum flexural strength of the specimens, the raster orientation is taken to be axial for all test pieces. Different researchers had tried different geometries to simulate cross-sectional areas of filaments partly fused to varying degrees. Thomas and Rodriguez [126] assumed rectangular filaments, while Bellehumeur et al. [33] considered elliptical sections. In the current work, a mixture of both is considered to be more appropriate and the resulting shape of the cross section is a square with elliptical fillets and when used to construct multilayer models, the overall cross-section looks as shown in Fig. 3.15

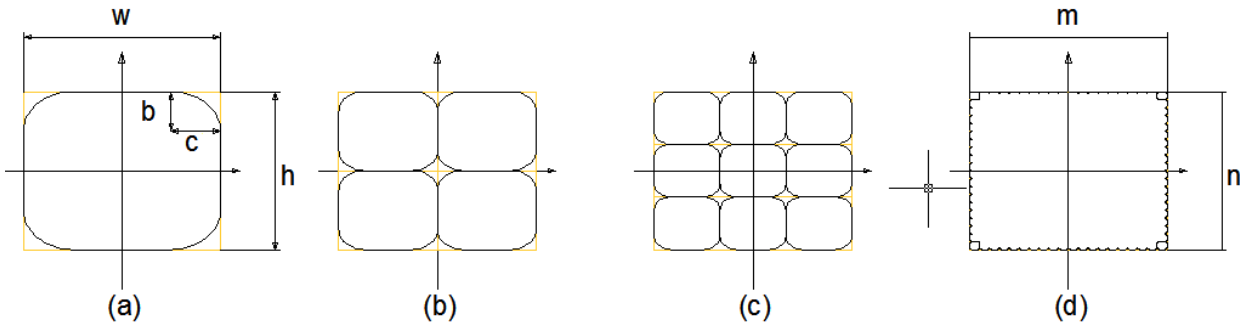

Fig. 3.15 Cross-sectional area of a square shape with precise filling: (a) Single layer, (b) Two layers, (c) Three layers, and (d) Multi layers

For this model, the second moment of area and the area of the single layer (a) are:

$$I_1 = \frac{h^3 w}{12} + \left(\frac{\pi}{4} - 1\right) bch^2 + (2 - \pi) b^2 ch + \left(\frac{5\pi}{4} - \frac{4}{3}\right) b^3 c \qquad (Eq. 3.14)$$

$$A_1 = hw + (\pi - 4)bc \qquad (Eq. 3.15)$$

For the multi-layer model, the equations become:

For each of the areas

$$I_{ns} = \frac{1}{mn^3} I_1 \qquad (Eq. 3.16)$$

$$A_{ns} = \frac{1}{mn} A_1 \qquad (Eq. 3.17)$$

For a model with m rows and n layers the MI of the whole area is:

$$\begin{cases} I_n = nmI_{ns} + 2mA_{ns} \sum_{i=1}^{k} \left[\frac{h}{2n} + \frac{h}{n}(i-1)\right]^2 & when\ \ n = 2k, k \in N \qquad (Eq. 3.18a) \\ I_n = nmI_{ns} + 2mA_{ns} \sum_{i=1}^{k} \left[\frac{h}{n}(i-1)\right]^2 & when\ \ n = 2k+1, k \in N \qquad (Eq. 3.18b) \end{cases}$$

After simplification and substituting for I_{ns} (Eq. 3.16) and A_{ns} (Eq. 3.17), these equations become,

$$\begin{cases} I_n = \frac{1}{n^2} I_1 + \frac{A_1 h^2}{n^3} \frac{(2k-1)k(2k+1)}{6} & when\ n = 2k, k \in N \qquad (Eq. 3.19a) \\ I_n = \frac{1}{n^2} I_1 + \frac{A_1 h^2}{n^3} \frac{k(2k-1)(k-1)}{3} & when\ n = 2k+1, k \in N \qquad (Eq. 3.19b) \end{cases}$$

The final equation for the moment of inertia of the model with m rows and n layers is:

$$I_n = \frac{1}{n^2}\left(I_1 - \frac{A_1 h^2}{12}\right) + \frac{A_1 h^2}{12} \qquad (Eq.3.20)$$

This equation also depicts the upper limit of the Moment of Inertia for the FDM part in accordance with the mathematical expression:

$$I_\infty = \lim_{n\to\infty} \frac{1}{n^2}\left(I_1 - \frac{A_1 h^2}{12}\right) + \frac{A_1 h^2}{12} = \frac{A_1 h^2}{12}$$

Substituting I_1 (Eq. 3.14) and A_1 (Eq. 3.15), Eq. 3.20 can be expanded as follows:

$$I_n = \frac{1}{n^2}\left[\frac{2}{3}\left(\frac{\pi}{4} - 1\right) bch^2 + (2-\pi)b^2 ch + \left(\frac{5\pi}{4} - \frac{4}{3}\right) b^3 c\right] + \frac{h^2}{12}[hw + (\pi - 4)bc] \quad (Eq.3.21)$$

This is the general equation for the second moment of area for a multi-layer and multi-strand rectangular object based on geometrical considerations. However, this needs to be considered together with the inter-road and inter-layer coalescence now. As already mentioned, the Frenkel-Eshelby model could be used to predict the inter road sintering phenomena in FDM and will be applied here. If the print speed is kept constant, time elapsed for a unit length of deposition is the same. Viscosity and surface tension of the material are temperature sensitive material properties, but if the same material is used with different thicknesses, Eq. 3.10 can be written as:

$$C = \left(\frac{\Gamma t}{\mu a_0}\right)^{\frac{1}{2}} = \frac{y}{a} = \frac{w - 2c}{w} = \frac{h - 2b}{h} \qquad (Eq.3.22)$$

where C is constant here and for an ideal case, $0 < C < 1$.

Further,

$$b = \frac{h(1-C)}{2} \qquad (Eq.3.23)$$

$$c = \frac{w(1-C)}{2} \qquad (Eq.3.24)$$

Substituting b (Eq. 3.23) and c (Eq. 3.24) in Eq. 3.21,

$$I_n = \frac{h^3 w}{n^2}\left[\frac{1}{6}\left(\frac{\pi}{4}-1\right)(1-C)^2 + \frac{1}{8}(2-\pi)(1-C)^3 + \frac{1}{16}\left(\frac{5\pi}{4}-\frac{4}{3}\right)(1-C)^4\right] + \frac{h^3 w}{12}\left[1 + \right.$$

$$\pi 4 - 11 - C2 \qquad Eq.3.25$$

In order to better understand the model, viscosity and surface tension of the material, which is ABS in this case, need to be considered. For this, the viscosity and surface tension data for ABS P400, as reported by Bellehumeur et al. [33] can be used in Eq 3.22. The speed at which the filament is printed must be the same as the speed at which it is extruded and it must allow the smallest of the filaments to coalesce. Considering a specific print speed, v, Eq. 3.22 can be rewritten as:

$$C = \left(\frac{\Gamma \dfrac{mnl}{vmnl}}{\mu \dfrac{h}{n}}\right)^{\frac{1}{2}} = \left(\frac{\Gamma n}{\mu h v}\right)^{\frac{1}{2}} \qquad (Eq.3.26)$$

Where ***n***, ***m***, ***l***, and ***h*** are the number of layers, number of roads, part length and part height respectively.

This equation for C allows predicting the influence of speed of printing on the rate of coalescence between adjacent strands and also on the second moment of area, when used in Eq. 3.25, considering different filament sizes, for a multilayer component. In this case, the sintering

time becomes a function of print speed and the number of layers. With the print speed kept constant, if the number of layers is increased (layer thickness decreased), the total time of printing the sample of given dimensions increases and so also the time for inter-road and inter-layer coalescence at any given geometrical location.

Fig. 3.16 depicts variations in C and I with varying number of layers for a given speed of printing; 60 mm/s. While printing with a fixed speed, the higher the number of layers, the higher is the coalescence and the better the second moment of area due to the excess time available. For a test piece of given dimensions, as fixed earlier in this section, the filament size varies with the number of layers. As the filament size varies, the deposition head needs to adjust the extrusion speed and the X-Y gantry of the FDM system needs to match the printing speed, to keep the speed of printing the same.

This result indicates that adaptive slicing with finer slicing results in better part strength, apart from improved surface quality due to reduced stair-step effects, as reported in the literature. After a certain number of layers, the inter-strand voids become much smaller, giving almost a full dense material structure and the coalescence approaches unity. As the coalescence increases, the second moment of area reaches its upper limit as mentioned above and the curve representing the variation of I becomes almost asymptotic with the horizontal axis as dictated by the overall dimensions of the part. Alternatively, for the same part with the same dimensions, printing by thicker layers with the same fixed speed would result in an overall reduction of the total time of printing. This leads to lesser inter-road sintering times and consequent loss of mechanical properties.

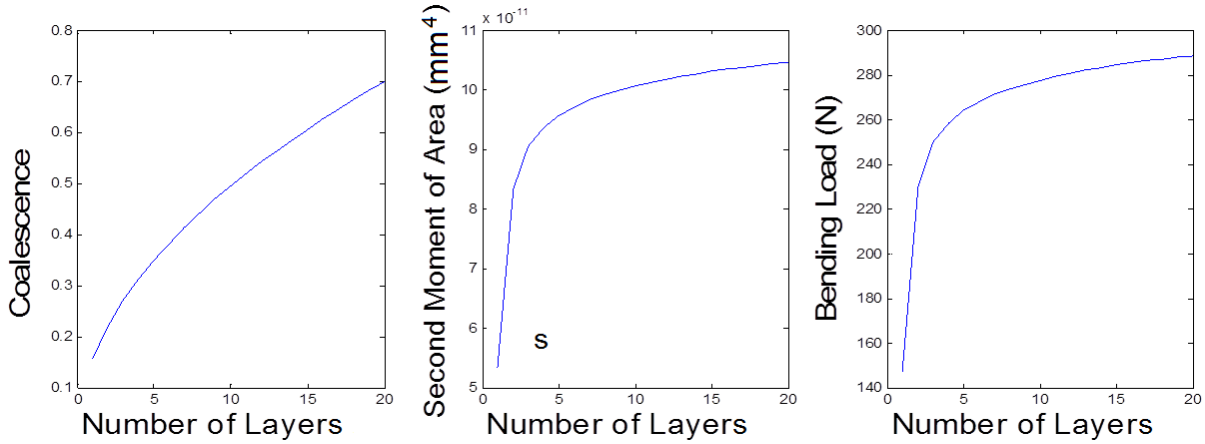

Fig. 3.16 Coalescence, second moment of area, and bending load vs. number of layers based on the model for print speed effects (Speed of printing = 60mm/s)

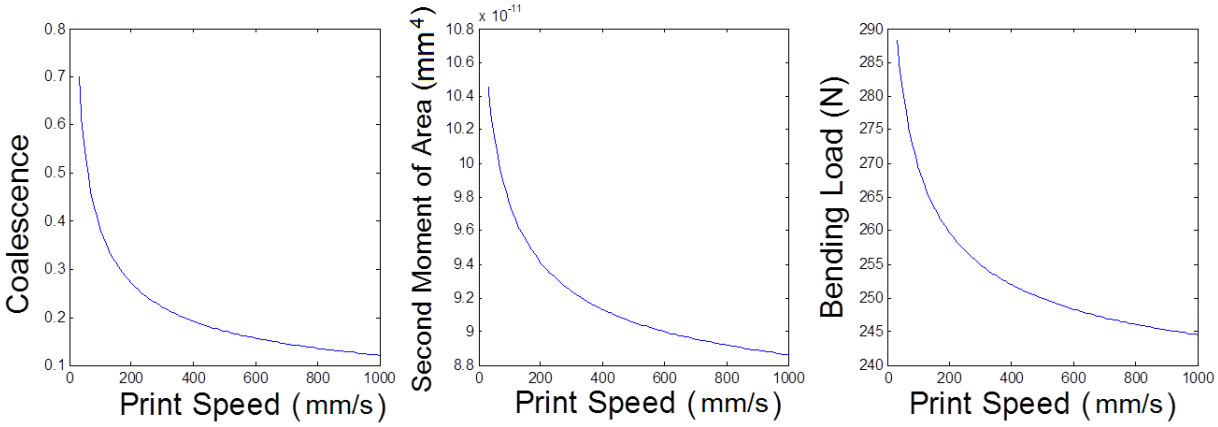

Fig. 3.17 Coalescence, second moment of area, and bending load vs. print speed based on the model for print speed effects (No. of layers = 10)

The same equations are now used to ascertain the effects of speed explicitly. Fig. 3.17 predicts variations in C and I with increasing speed of printing, for a given filament size. In this case, the filament size corresponds to the diameter needed to make the standard test specimen with 20

layers, which is equal to 0.2 mm in this case. As evident, with the given filament size, C and consequently I decrease with increasing print speed. Evidently, the higher the speed, the lesser is the time available for a unit length of the filament to coalesce with the adjacent filaments and the lesser is the value of C.

In the FDM process, the temperature of the filament remains above the glass transition temperature for a relatively long period of time. Under such conditions, the intermolecular diffusion occurring across interfaces is an important mechanism to consider. The interface between filaments gradually disappears and mechanical strength at the interface develops. This phenomenon was mentioned by Thomas and Rodriguez [126]. A macroscopic recovery function (normalized fracture toughness), $R(t)$, is defined for isothermal conditions in terms of the convolution between an intrinsic healing function for wetting and diffusion, $R_h(t)$, and a wetting distribution function, $\phi(t)$:

$$R(t) = \int_0^t R_h(t-\tau)\frac{d\phi(t)}{dt}d\tau = \frac{K(t)}{K_\infty} \qquad (Eq.3.27)$$

Where $K(t)$ is the interface toughness after time t seconds at some constant temperature T, and K_∞ is the fracture toughness of the original material. The convolution integral represents bonding as the sum of wetting and diffusion processes initiated at different times. The intrinsic healing function $R_h(t)$ is given by:

$$R_h(t) = R_{0+}(1-R_0)\left(\frac{t}{t_\infty(T)}\right)^{\frac{1}{4}} \qquad (Eq.3.28)$$

Where R_0 is the normalized toughness that develops on wetting and $t_\infty(T)$ is the reptation time as a function of temperature, T.

Although healing influences the mechanical properties of the final FDM part, it is essentially the inter-road and inter-layer coalescence that has a predominant role. If the neck formation is insufficient or improper, bonding with thicker layers is also weaker even when the healing time is infinite. In other words, the neck growth and associated coalescence are mainly responsible for the mechanical properties of the FDM part and calescence in turn depends on the sintering time between roads and layers. This theoretical model proves that thicker layer deposition will weaken the bonding of the FDM part if they are printed with the same speed as the thinner layer. As a conclusion of this section, the adaptive slicing method employed using thicker layers in specific zones helps reduce the total build time, but results in inferior mechanical properties.

3.4 Time-dependent analytical modelling of the role of adaptive slicing

Based on the geometry of the meso-structure together with the coalescence considerations, it was evident that thicker layers, while reducing print time, might lead to inferior mechanical properties, while thinner layers may result in better properties, if the speed of printing of a unit length of the filament is the same in both cases. It is pertinent to point out that inter-road and inter-layer coalescence depends on both sintering time and temperature. The sintering temperature is the result of the envelope temperature and the temperature of the freshly formed layer, which will eventually be fixed at a particular value, depending on the fused material system. If this temperature is too low, both neck-growth and sintering will be adversely affected and if too high, surface tension forces will not allow formation of proper meso-structures. In

other words, this parameter cannot be independently varied greatly, and depending on the material system, needs to be fixed at a certain level, though in actual practice, there may be variation over a narrow range. On the other hand, sintering time is an independent parameter that can be controlled by varying the print speed. The overall impression from the previous section is that the part strength is better with higher sintering times.

However, it should be noted that the print speed does not necessarily remain constant while printing an adaptively sliced object. In other words, a part with thicker layers can be printed slower compared to printing the same with thinner layers, and depending on the total time of printing, the end result in terms of the part strength may be in favour of any of the two approaches. Eq. 3.10 is now modified using the total time required for printing a unit length of the filament of a given size:

$$C = \frac{y}{a} = \left(\frac{\Gamma \frac{t_{total}}{lmn}}{\mu \frac{h}{n}} \right)^{\frac{1}{2}} \qquad (Eq. 3.29)$$

According to Agarwala [110] and based on the popular belief, the roller speed and the filament feed rate are determined by layer thickness, road width and the speed of movement of the extrusion nozzle. This may prove to be true with relatively thin layers, but with thicker layers, the thermal energy associated with the filament also needs to be taken into consideration. The geometrical and process conditions used should allow the filament to absorb enough thermal energy to ensure that all particles reach the sintering temperature, which requires the thermal properties of the material to be given due consideration. In other words, once the heating element is fixed, and a specific material is selected, the roller speed and consequently the print speed are

fixed, and there is limited freedom to change the layer thickness, without altering the internal thermal energy conditions. This was one of the reasons adaptive slicing was not effectively implemented in practice in the past.

Considering the internal mechanism of material processing of the deposition head in FDM, the speed of extrusion and the flow velocity of the filament need to be synchronised in order to achieve a given speed of printing. Considering two nozzles with diameters d_1 and d_2 as shown in Fig. 3.18, assuming that the material is fed by the same motor with the same speed (extrusion speed), the volume of material displaced by the piston is the same for a total given time.

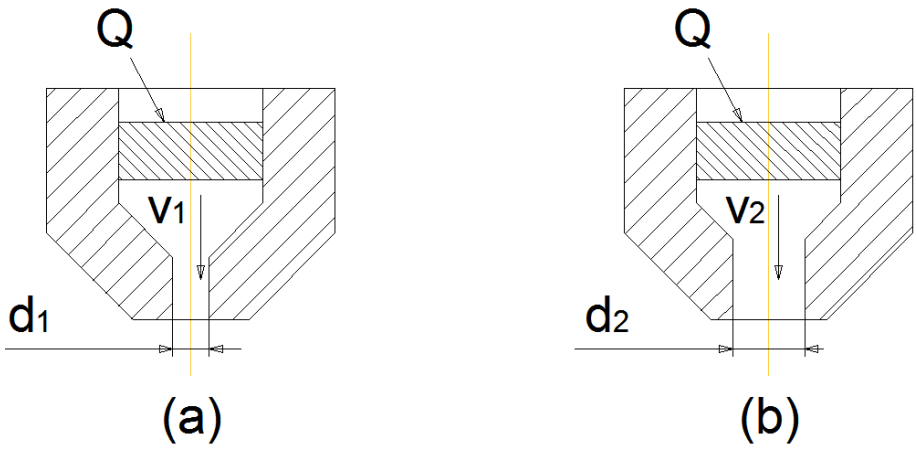

Fig. 3.18 Two nozzles with different diameters

The relationship between the volume of the material, extrusion speed in the tip to the nozzle and the nozzle diameter can be described as:

$$Q = \frac{\pi {d_1}^2}{4} v_{e1} = \frac{\pi {d_2}^2}{4} v_{e2} \qquad (Eq. 3.30)$$

Where Q is the volume of the unit flow, d_1, and d_2 are nozzle diameters in (a) and (b), and v_{e1} and v_{e2} are extrusion speeds at the tip of the nozzle.

Then the relation between the extrusion speeds with different nozzle diameter is:

$$\frac{v_{e1}}{v_{e2}} = \frac{{d_2}^2}{{d_1}^2} \qquad (Eq. 3.31)$$

Based on the volume continuity,

$$A_{p1}v_{p1} = \frac{\pi {d_1}^2}{4} v_{e1} = Q = A_{p2}v_{p2} = \frac{\pi {d_2}^2}{4} v_{e2} \qquad (Eq. 3.32)$$

where v_{p1}, v_{p2}, A_{p1} and A_{p2} are the print speed and the cross-sectional area of the road respectively in Fig. 3.18 (a) and (b).

In order to simulate variations of filament forms close to reality, the shape of the cross-sectional area of the road was assumed to be as shown in Fig. 3.19. The width and the thickness of the cross-sectional area in Fig. 3.19 (a) are in the same linear portion to their counterparts in Fig. 3.19 (b). Assuming that the ratio of the two cross-sectional areas to be equal to *l*, as earlier, the relationship between v_{p1} and v_{p2} becomes:

$$\frac{v_{p1}}{v_{p2}} = \frac{v_{e1}}{v_{e2}} = \frac{{d_2}^2}{{d_1}^2} \qquad (Eq. 3.33)$$

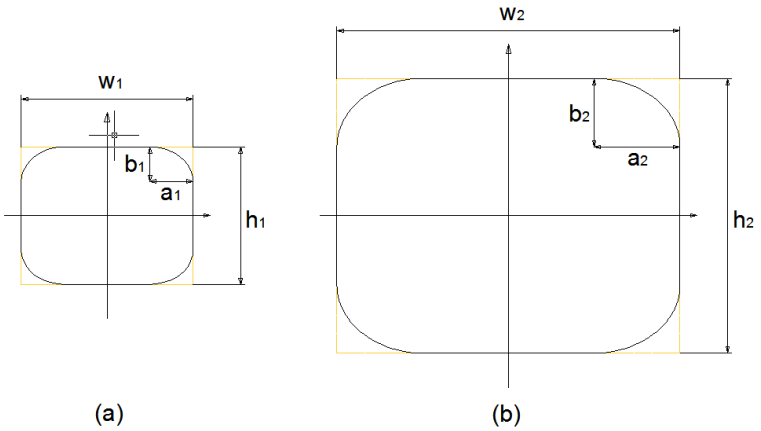

Fig. 3.19 Road shape of each cross-sectional area in two different nozzle settings

When a number of strands are used to constitute the cross-section, the ratio number of rows to number of columns is taken as j,

$$\frac{m}{n} = j \qquad (Eq. 3.34)$$

In order to understand the influence of the time factor, the mathematical model developed earlier needs to be revisited now. Previously, C is assumed to be constant based on the time t spent on the unit length of the road to be the same. The expression for the total time is as follows:

$$t_{total} = lmnt = ljn^2 \qquad (Eq. 3.35)$$

The expression for C derived as a function of the total time in Eq. 3.29 is simplified as given in Eq. 3.36. For a given part dimensions, with a fixed total time, the time for printing a unit length and consequently the print speed will change as the filament size varies.

$$C = \frac{y}{a} = \left(\frac{\Gamma t_{total}}{\mu jhn}\right)^{\frac{1}{2}} \qquad (Eq. 3.36)$$

Further, the expression for the second moment of area as a function of C will take the same form as Eq. 3.20, and is repeated below for convenience:

$$I_n = \frac{h^3 w}{n^2}\left[\frac{1}{6}\left(\frac{\pi}{4}-1\right)(1-C)^2 + \frac{1}{8}(2-\pi)(1-C)^3 + \frac{1}{16}\left(\frac{5\pi}{4}-\frac{4}{3}\right)(1-C)^4\right] + \frac{h^3 w}{12}\left[1 + \left(\frac{\pi}{4}-1\right)(1-C)^2\right] \quad (Eq.\,3.37)$$

These equations allow evaluation of effects of varying total time and filament sizes on the values of C and the moment of inertia. First, considering the variation of number of layers, Fig. 3.20 shows both C and I decreasing with increasing number of layers, for a given total time of printing the test piece which is 75 second in this case. The total time being fixed, the speed of printing increases with increasing number of layers, allowing lesser time for a unit length of deposition, and lesser coalescence. It may be noted, this trend is an almost reversal of that shown in Fig. 3.16. Thus, while contradicting each other, the time factor and the speed of printing also interact with the filament size.

It is also interesting to note the influence of the total time with the filament size fixed at a particular level. Fig. 3.21 presents variation of *C* and *I* with increasing total time of printing, with the number of layers fixed at 10. For a given filament size, the more the time given to complete a part of given dimensions, the lesser are extrusion and print speeds, and the better will be the inter road coalescence and the moment of inertia. This result is again a reversal of the trend shown in Fig. 3.17, where increasing print speed has an adverse effect on the coalescence.

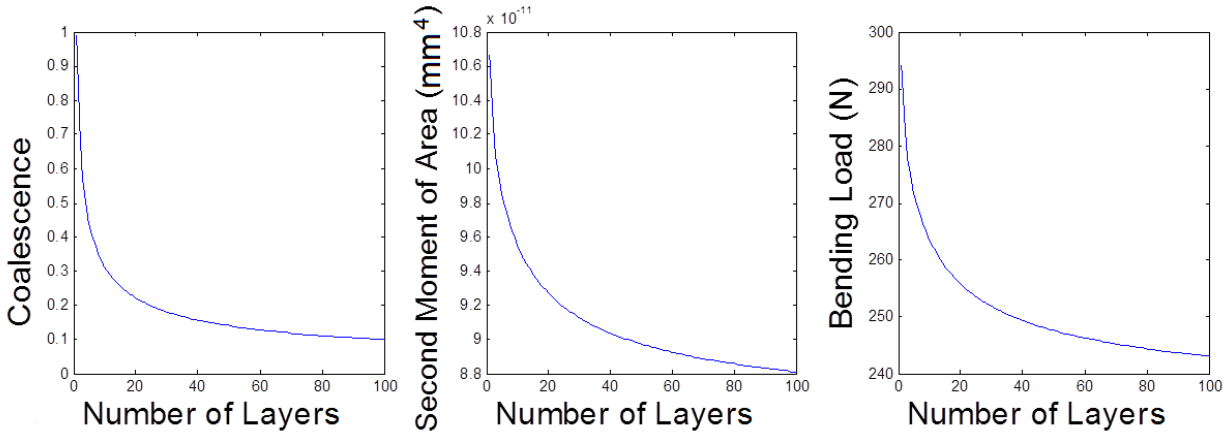

Fig. 3.20 Coalescence, second moment of area, and bending load vs. number of layers based on the model for print time effects (Total print time = 75s)

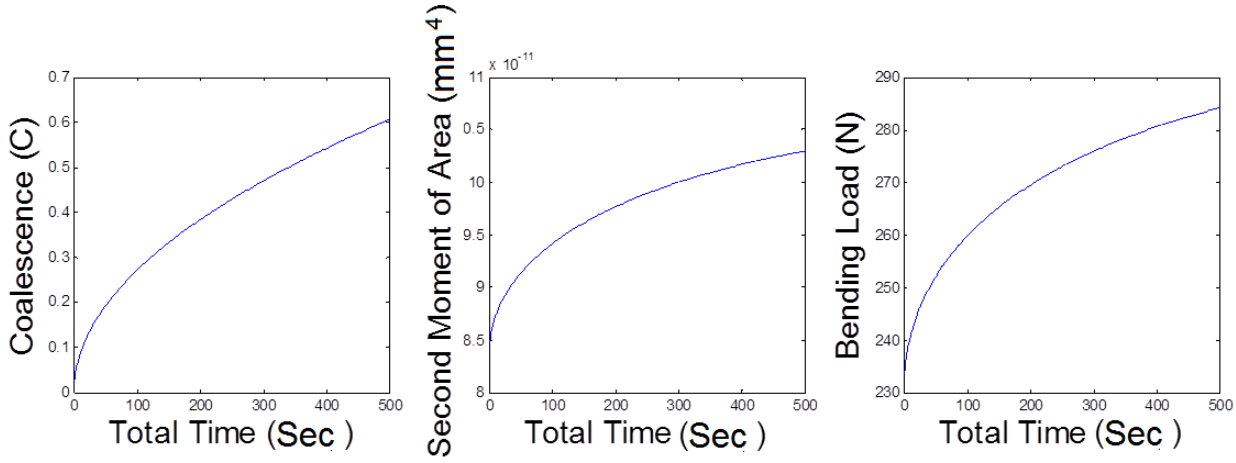

Fig. 3.21 Coalescence, second moment of area, and bending load vs. total time based on the model for print time effects (Number of layers =10)

Based on predictions from analytical models, it is evident, the print speed, time of printing and the filament size have compounding effects on the final strength of the part, when varied together. The end result evidently depends on the actual combination of these parameters for a given part. The existing literature only talks about the possible improvements in the surface

quality with adaptive slicing, neglecting significant effects on other aspects such as the part strength. From the observations of the results of the analytical models developed here, it is apparent that true benefits of adaptive slicing can only be realised by properly adjusting the three process parameters so as not to compromise on the mechanical characteristics.

Evidently, the modified analytical model precludes the direct influence of speed and allows highlighting the significance of printing time. The total printing time is a function of both print speed and the length of the deposition path. For a fixed total printing time, it is clear that thick layers result in better mechanical properties compared to thinner layers, much against the popular belief in adaptive slicing literature. However, the analytical models need some form of experimental validation at this stage and the next section presents results of three point bending tests designed for this purpose.

3.5 Experimental evaluation of adaptive slicing

Three point bending tests are designed to validate the analytical models presented in the previous section. Test pieces for three point bending need to be printed with varying speed and total build time of printing, to be able to provide direct experimental support of the analytical models. As already mentioned, a true practical implementation of adaptive slicing involves synchronising the rate of extrusion of the polymer from inside the hot chamber with the X-Y motion while simultaneously changing the nozzle heads to achieve deposition strands of different diameters. Considering hardware limitations to programmatically achieve this, experiments are mainly designed to establish influences of layers of varying thicknesses printed at different speeds.

While allowing for almost no freedom to adjust process parameters, commercial FDM machines also do not allow the layer thickness to be more than 0.5mm. Make-shift test facilities could be built, but will have limitations on the quality of controlling the parameters. After trying a couple of options, a Makerbot cupcake CNC kit [127] was finally procured and assembled. It uses a heated metal plate as the platform for printing, allowing for the temperature of the substrate to be controlled. The injection head draws ABS feed rod of 3 mm diameter to extrude through a heated nozzle of selected size. The arrangement of the print head and the heated platform is shown in Fig. 3.22. Without a closed enclosure, the healing process [62] might affect the internal bonding of the meso-structure to some extent, but healing is also a function of time and depends on the coalescence. With speed of printing the same, if parts printed with thicker layers perform better than the thin layered ones, it would mean that the theoretical predictions are correct in capturing the influences of time-dependent coalescence.

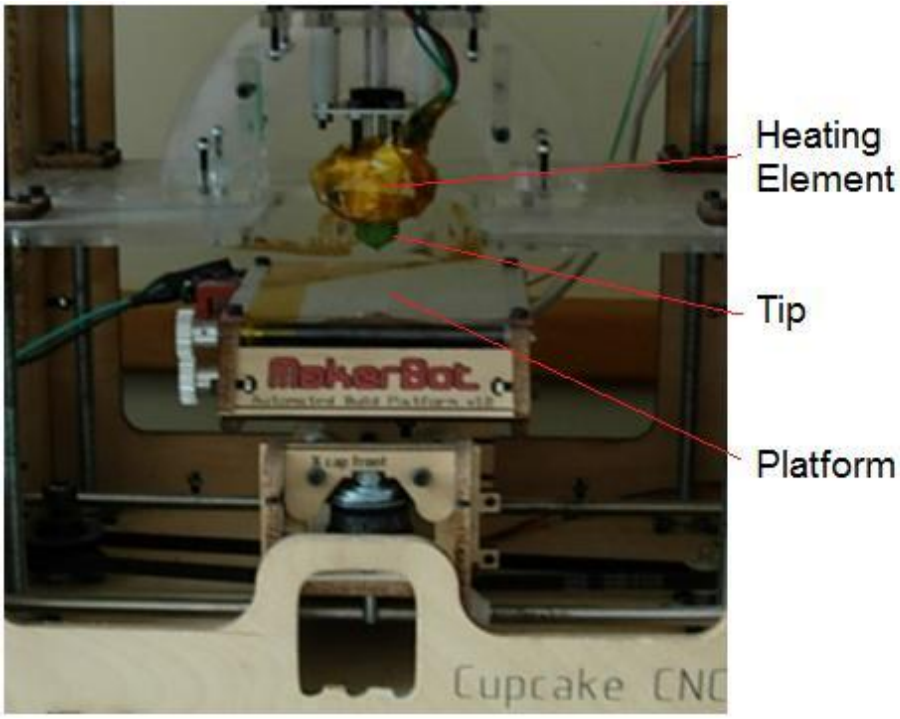

Fig. 3.22 The experimental setup

In order to be able to satisfy the thermal energy requirements, the extrusion speed is set constant at a rotational speed of 255 rpm for the main feed drive motor, regardless of the diameters of the nozzle. This is equivalent to an extrusion speed of 7 mm/s for the filament. The temperature for the heating element was set at 225˚C and tested to be at 215˚C to 220˚C at the tip. This temperature is the recommended setting for the Makerbot system and is also in accordance with the test results by Bellehumeuar et al. [33], stating that the coalescence process would stop if the temperature is under 200˚C with ABS P400. The temperature of the heated platform is set at 100˚C and is tested to be actually varying from 100˚C to 110˚C. This is to ensure that the FDM test pieces stay just above the glass transition temperature and provide a soft substrate for subsequent layers to be effectively coalesced into one another. This will also minimise the shrinkage of the bottom layers and allow for better attachment of the test pieces to the heating platform. Without the heating platform, the shrinkage difference between the layers would cause shear stresses and lead to the corner lifting phenomenon. In order to be close to the commercial use of the technology, natural ABS polymer is used as the test material with mechanical properties as shown in Table 3.1.

Table 3.1 Mechanical properties of the test material (ABS)

Physical Properties	Metric	Comments
Density	1.03 g/cm^3	ASTM D792
Tensile Strength, Yield	37.7 MPa	ASTM D638
Elongation at Break	30.0%	ASTM D638
Tensile Modulus	2.46 GPa	ASTM D638
Flexural Modulus	2.14 GPa	ASTM D790
Flexural Yield Strength	60.7 MPa	ASTM D790

Nozzles of two different diameters are used in this experiment; 0.5 mm and 1.0 mm, allowing for the thinner and thicker versions of layers. For each printing trial, the nozzle of the appropriate diameter is fixed to the extruder tip and the DC motor is driven with a pre-set constant speed to keep the thermal energy evenly dissipated to heat the polymer particles inside and produce the semisolid filament with consistent mechanical and thermal characteristics. The inter-road gap is set to provide a 10% overlap in order to minimize the voids and also increase the degree of sintering. The first step is to establish the significance of speed of printing on the resulting mechanical characteristics and verify the results presented in Fig. 3.17. There are two critical speeds that can be controlled in FDM; the extrusion speed, which is internal to the deposition head and then the actual printing speed, which depends on the speed of movement of the X-Y gantry. Both of them need to be controlled and synchronised in order to achieve a given print speed, as the continuity of material flow needs to be maintained. Test pieces of the same dimensions as used in the analytical models (50 mm X 20 mm X 4 mm rectangular specimens) are printed with the print speed varying from 35 mm/s to 75 mm/s with the 0.5 mm filament and 13 mm/s to 15 mm/s with the 1 mm filament.

Three-point bending tests are implemented on a Tinius Olsen tester, on which test specimens are horizontally placed between two triangular supports spanned at 44 mm. Compressive load is applied at a constant rate of 10mm/min until the maximum load is reached. While testing, all specimens are observed to exhibit similar deformation characteristics; the bottom most surfaces begin to bend and the colour of the area opposite to where the load is applied changes to dull white from ivory. Both the deflection and change of colour increase with the load, until the test piece finally fails. Two types of fracture are observed; some specimens showed obvious cracks

in the dull white area while others exhibited continuous dull white strands. The maximum compressive load is considered as the point of failure and the results of these bending tests are discussed next.

The variations of the average compressive loads under three point bending tests with thin layer samples produced with varying print speeds are recorded as shown in Fig. 3.23 to 3.28 while the maximum compressive loads are further consolidated in Table 3.2. The average compressive load may be observed to decrease with increasing print speed due to decreasing time allowed for inter-road coalescence. Average values of maximum compressive loads obtained for various printing speeds and times listed in Table 3.2 are then used for the plots shown in Fig. 3.29, with the corresponding graphs based on analytical models juxtaposed, for a direct comparison. Due to practical limitations with the experimental setup, the print speed could only be varied within a narrow range.

The maximum compressive load taken by a sample gradually decreases with increasing speed, as inter-road and inter-layer sintering reduce. A comparison of the two results in Fig. 3.29 reveals close correlations between analytical predictions and experimental results within the ranges of experimental factors. However, the experimental values tend to deviate much from the predictions by the analytical model at lower total time settings, or higher print speeds, which is probably due to problems associated with the synchronization of the extrusion and the actual print speeds; a limitation of the current test setup, using a relatively low torque DC motor, which came along with the Makerbot machine, to drive the polymer extrusion. Also, varying thermal conditions might be playing specific roles, though sufficient care is taken to keep thermal variation at a minimum.

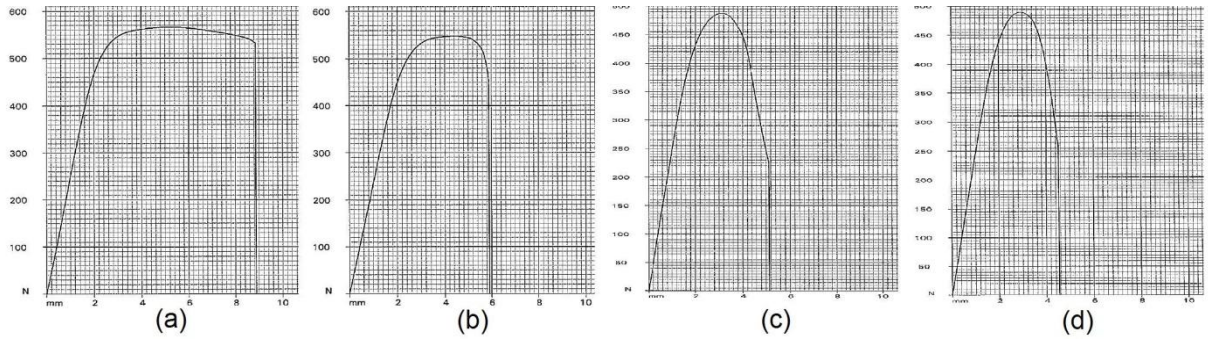

Fig. 3.23 Load deflection diagrams from three point bending tests of thinner layer parts with print speed at 35 mm/s

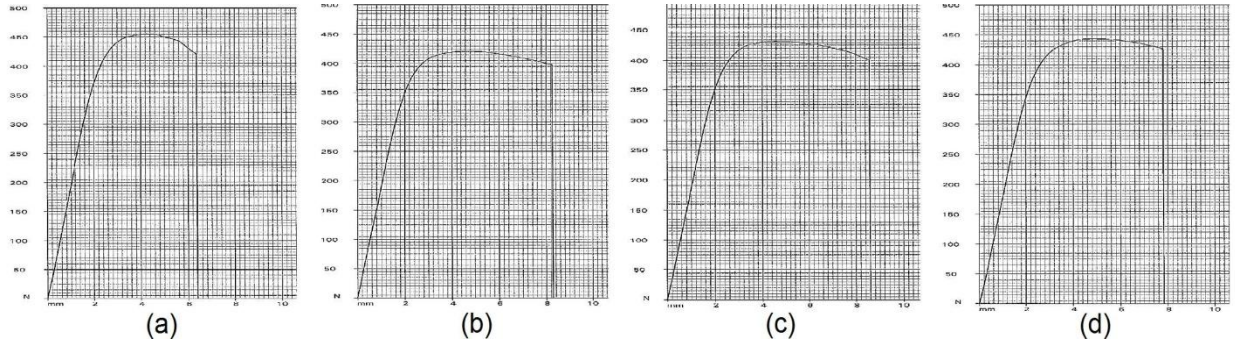

Fig. 3.24 Load deflection diagrams from three point bending tests of thinner layer parts with print speed at 40 mm/s

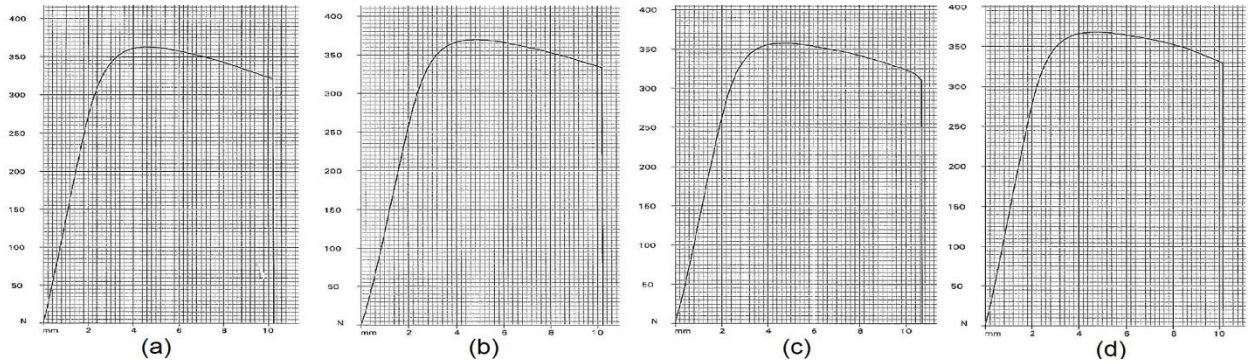

Fig. 3.25 Load deflection diagrams from three point bending tests of thinner layer parts with print speed at 45 mm/s

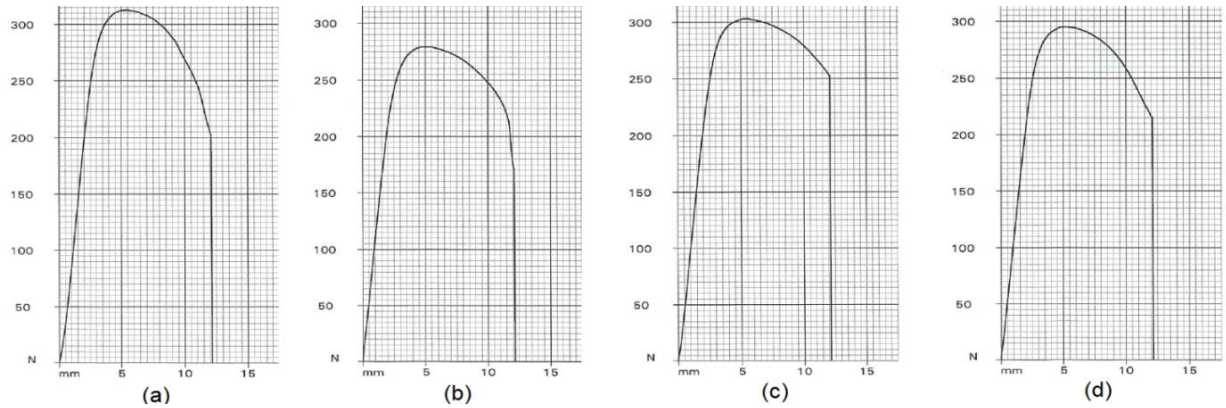

Fig. 3.26 Load deflection diagrams from three point bending tests of thinner layer parts with print speed at 50 mm/s

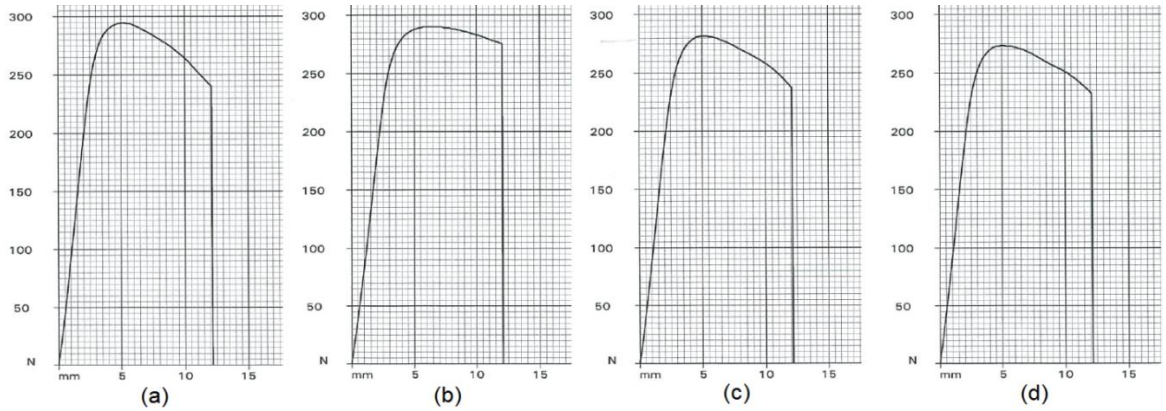

Fig. 3.27 Load deflection diagrams from three point bending tests of thinner layer parts with print speed at 55 mm/s

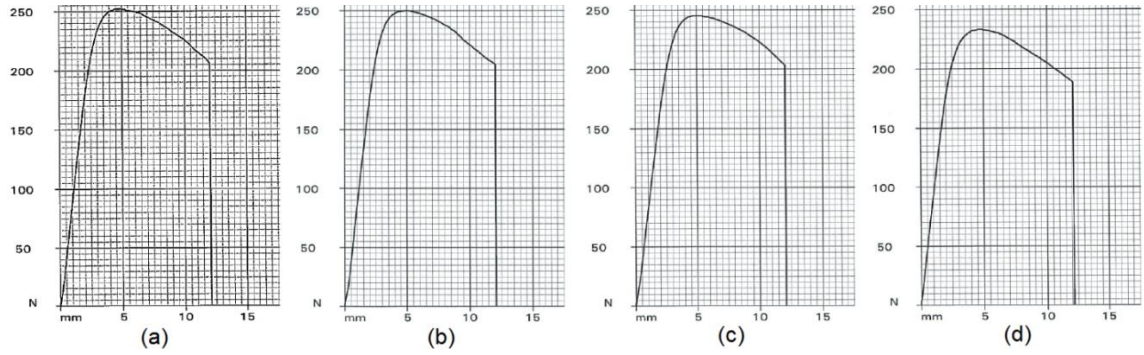

Fig. 3.28 Load deflection diagrams from three point bending tests of thinner layer parts with print speed at 60 mm/s

Table 3.2 Results from three point bending tests on specimens produced with thin layers of 0.5 mm thickness

Print Speed (mm/s)	Maximum Compressive Load (N)				Average (N)	Equivalent Load (N)	Standard deviation	Build Time (sec)
	Part 1	Part 2	Part 3	Part 4				
35	566.666	490.333	487.666	548.333	523.250	263.937	20.31	507
40	421.333	432.666	456.000	443.000	438.250	272.7986	9.20	452
45	363.000	369.666	357.666	368.000	364.583	263.952	3.92	407
50	313.000	279.333	303.333	295.000	297.667	280.580	13.58	374
55	294.666	290.333	282.000	273.666	285.166	276.303	9.28	339
60	252.000	250.000	245.333	233.000	245.083	241.515	8.40	313

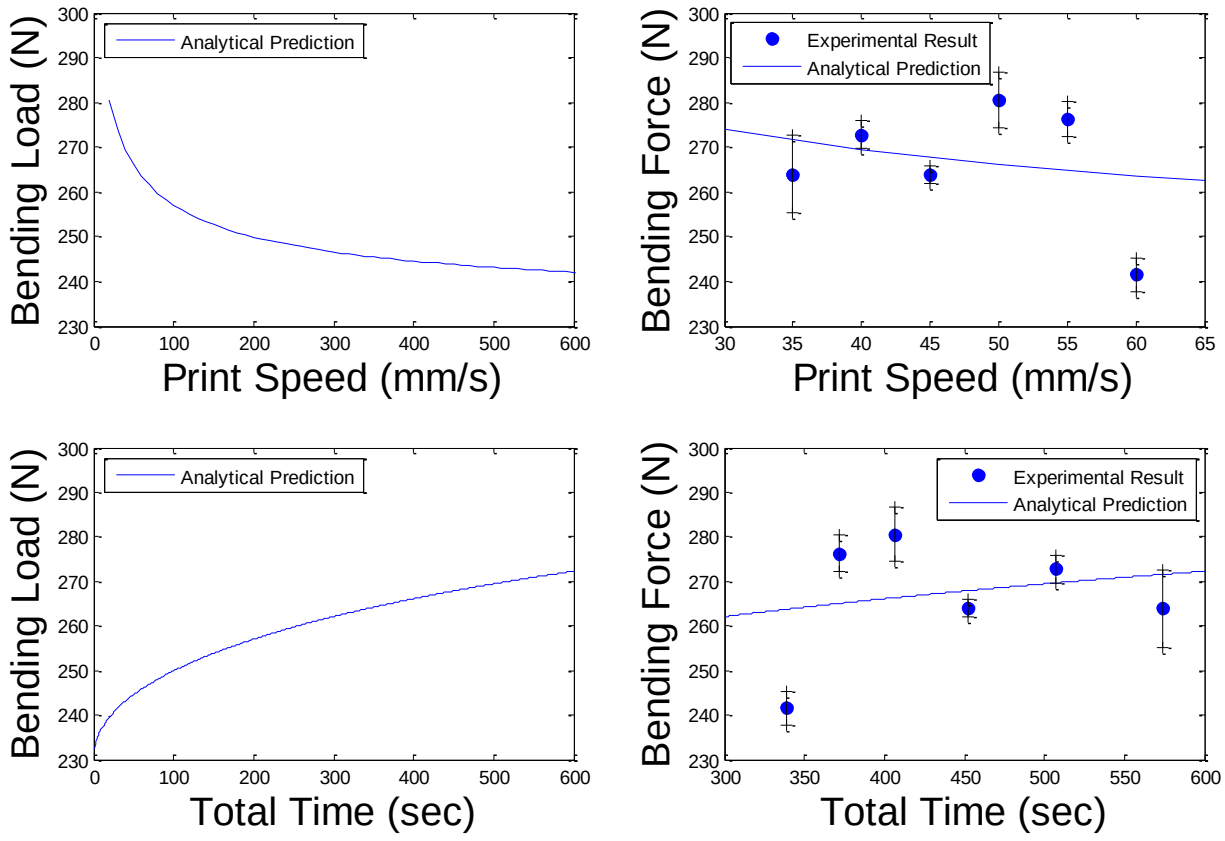

Fig. 3.29 Comparison between analytical predictions and the experimental results using thinner layer printing (layer thickness of 0.5 mm)

Three point bending test results based on thick layer specimens are obtained similarly as depicted above and the results are consolidated in Table 3.3. As in the case of the thin layer samples, it is evident that the higher the speed of printing, the lesser is the average compressive load. Further, the analytical predictions and the experimental results with thick layer samples also closely correlate, as shown in Fig. 3.30.

Table 3.3 Results from three point bending tests on parts produced with thick layers of 1.0 mm thickness

Print Speed (mm/s)	Maximum Compressive Load (N)				Average	Equivalent Load (N)	Standard deviation	Build Time(sec)
	Part 1	Part 2	Part 3	Part 4				
9	373.666	378.666	347.000	344.000	360.833	276.502	13.81	576
10	318.333	286.333	295.333	316.333	304.083	274.301	14.21	514
13	294.666	321.666	321.000	317.666	313.750	298.658	12.24	386
15	273.666	255.666	269.333	265.000	265.916	268.602	7.77	343

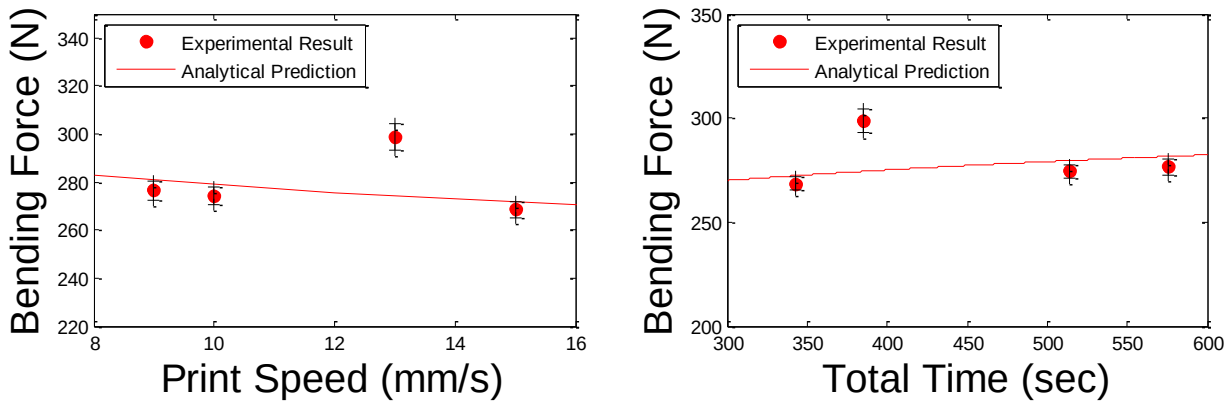

Fig. 3.30 Comparison between analytical predictions and the experimental results using thicker layer printing (layer thickness of 1.0 mm)

The experimental data developed can also be used to ascertain the time-based model within narrow ranges. For this, the average compressive load data for specific print conditions from the above tests is collated and presented in Table 3.4. It may readily be observed that the average performance of thick layer samples is slightly better than the thin layer samples for a given build time, which is in accordance with the analytical results discussed earlier. This proves the hypothesis that print speed and time dependent coalescence must be considered together, while ascertaining the roles of alternative printing and slicing strategies in FDM.

Table 3.4 Comparative performance of thin and thick layer samples with different build time settings

Build Time 510 sec				
Layer Thickness (mm)	**Equivalent Load (N)**	**Flexural Yield Strength (MPa)**	**Print Speed (mm/sec)**	**Actual Time (sec)**
0.5	263.937	54.44	35	507
1.0	276.502	57.03	10	514
Build Time 380 sec				
Layer Thickness (mm)	**Equivalent Load (N)**	**Flexural Yield Strength (Mpa)**	**Print Speed (mm/sec)**	**Actual Time (sec)**
0.5	276.303	56.99	55	374
1.0	298.658	61.60	13	386
Build Time 340 sec				
Layer Thickness (mm)	**Equivalent Load (N)**	**Flexural Yield Strength (Mpa)**	**Print Speed (mm/sec)**	**Actual Time (sec)**
0.5	241.515	49.81	60	339
1.0	268.602	55.40	15	343

Further to experimental validations of both models proposed, the general trend in the variations of the bending stress with both speed of printing and total time of printing are depicted in Fig. 3.31. For a given speed of printing, thin layers lead to longer times and better coalescence but the

total build time would be high. For a given total time, which is the combined result of the length of the tool path and the speed of printing, thicker layers mean longer sintering time and better coalescence. Both models have their merits, it is necessary to use the most appropriate one, to provide meaningful explanations in a given situation.

While using uniform flat layers, the speed based analytical model could be used to predict the proper print speed setting for given levels of mechanical properties. When adaptive slicing is used, for example, as suggested by Sabourin et al. [86], with thinner layers for the exterior and thicker layers for the interior, the total time of printing can be utilized to predict the overall part quality and achieve optimum settings for the best surface quality together with a minimum print time, without compromising much on the mechanical attributes.

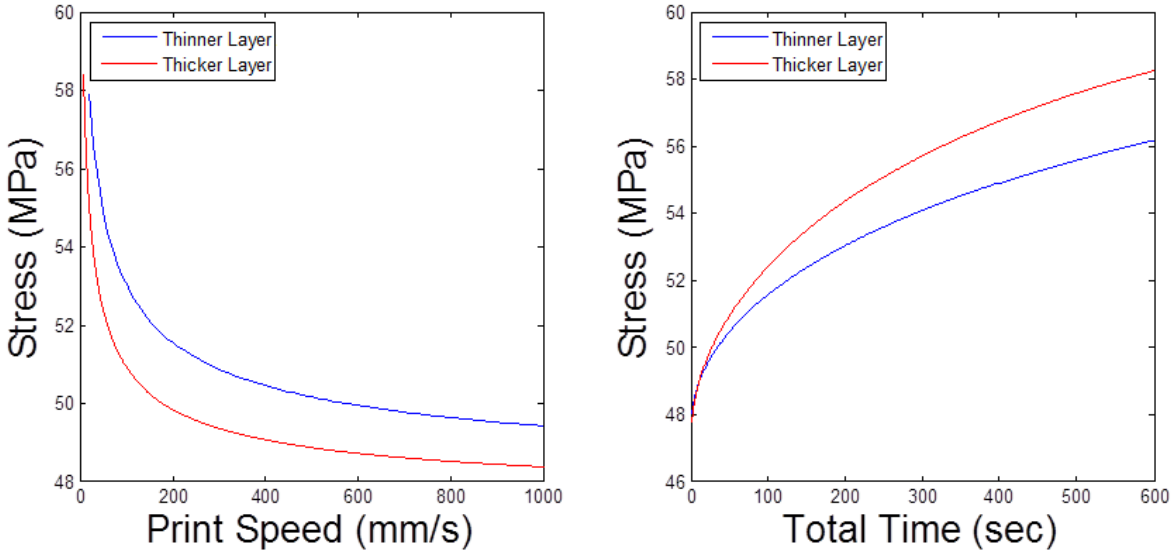

Fig. 3.31 Stress vs. print speed and print time on prediction produced with layers of thickness 0.5 mm and 1.0 mm (part size 50mm X 20mm X 4mm)

In conclusion, numerous adaptive slicing schemes targeting better parts are reviewed in this chapter, but identified to be mere mathematical models, with very little or no theoretical or experimental substantiation. The coalescence model for the inter-strand bonding condition is reviewed and two important factors influencing the bonding inside the FDM components are identified; sintering temperature and sintering time. Mathematical models based on moments of inertia of cross sections of specimens used in three point bending tests are developed giving due consideration to the meso-structures. Effects of adaptive slicing are evaluated with the time dependent variation of the inter-road coalescence. Analytical models predict the moment of inertia and consequently the bending strength of parts to decrease with increasing print speed and increase with increasing total print time, for a given filament size. Experimental results also confirmed the analytical predictions. With the time dependency of coalescence considered, it is evident that thicker layers actually give better mechanical properties, for a given total print time. Overall, adaptive slicing has a definite role in influencing the final part characteristics, but the true significance can only be realized by giving due consideration to the speed of printing, the time dependency of inter-road coalescence and the overall meso-structure.

Chapter 4 Raster orientation effects in FDM

4.1 The role of the raster angle in FDM

Unlike an injection moulding part with an isotropic structure as in Fig. 4.1(a), the common internal structure of a FDM part is anisotropic in nature, as depicted in Fig. 4.1(b). As already mentioned, the final mechanical properties of the FDM component are significantly influenced by the internal meso-structure. Experimental evaluation of the influence of the mesostructures showed significant influences on the stress-strain responses. Coalescence between adjacent filaments was analysed using the classical Frenkel-Eshelby model together with appropriate thermal models. With general FDM, it was observed that the extruded filaments are not usually at the required temperatures long enough for the coalescence between adjacent strands to be complete. Experimental results showed the moduli and strength values to be lower than those of the ABS monofilaments as well as the injection moulded parts. Gray et al. [128] reported the effects of fibre orientation on the stiffness and strength of ABS and a novel fibre reinforced polypropylene (short thermotropic liquid crystalline polymer fibres), processed through FDM. Tensile modulus values of ABS monofilament and ABS processed through fused deposition modelling were reported to be 2.07 GPa and 1.55 GPa respectively with a 0˚ fibre alignment.

The actual mechanism through which the internal meso-structure influences the characteristics of a FDM part is complex and involves both individual and combined effects of different parameters. Several attempts were made in the past to identify the most important parameter affecting the meso-structure, considering the deposition strategies and process parameters. The

most significant of all these is the raster orientation. Five important control parameters primarily determine the strength of a FDM processed component; layer thickness, part build orientation, raster angle, road width and air gap. As mentioned in Chapter 2, the anisotropy properties are caused by the polymer molecules aligning themselves with the direction of flow, formation of pores in preferred orientations and weak interlayer bonding. It is confirmed that the part strength is affected by the raster orientation while the fracture of the part is controlled by either weak interlayer bonding or porosity, or both, based on three-point bending and impact tests [119]. Other research results [37, 47, 52, 78, 80, 111] also confirm that the raster angle plays a more significant role in controlling the mechanical properties, compared to other parameters, such as layer thickness, road width, speed, temperature, air gap etc.

Fig. 4.1 Process-dependent material structures (a) injection moulding part and (b) FDM part

Evidently, the raster angle plays an important role in influencing the meso structures and eventually, the mechanical properties. As a result, the choice of the raster angle in a given layer is important, as also the variation of raster orientations across different layers. Typically,

alternate layers are built with raster directions at 90˚ to one another. Such a strategy maximises the material packing while minimising the number of voids between roads and layers. Depending on the complexity of a given closed loop feature in a layer, there may be more than one raster segment. Considering the plausible complexities, the analysis presented here is confined to a single raster segment for each layer and parallel raster orientation patterns in successive layers.

Ahn et al. [111] developed the anisotropic failure model of ABS parts produced by the FDM process mainly considering the effects of the raster angle. The Classical Lamination theory was used to calculate stresses in the material for given loads assuming a thin plate as shown in Fig. 4.2 to be in plane-stress. Using plane stress conditions in the lamina together with Tsai-Wu Failure Criterion a mathematical model was developed to predict the failure of the FDM parts under tension. The stiffness matrix derived constitutes of three parts; the extensional, coupling, and bending stiffness matrices. They treated the layer as a homogeneous solid medium, ignoring the coalescence effects. Based on experimental validation, this anisotropic model was reported to be reasonably well in predicting the failure of FDM parts.

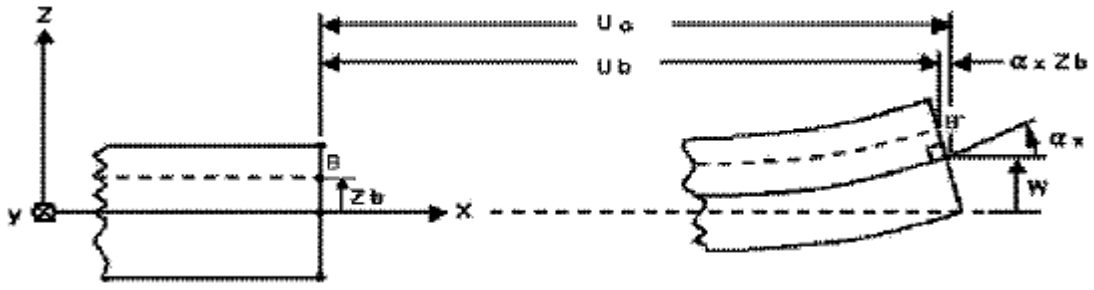

Fig. 4.2 Definition of coordinates in a plate (Image source: Ahn et al. [111])

In similar lines, Li et al. [78] also used the classical lamination theory to find the relationship between the raster angle and mechanical properties. The tensile modulus of the FDM part was used as the criterion and considered the ply orientation to be symmetric about the centreline of the laminate. The effect from the ply above the mid plane would be cancelled by the identical ply below the mid plane. In this case, the coupling stiffness matrix *B* equals to zero and there is no extension-bending coupling. Therefore,

$$\begin{bmatrix} \varepsilon_x^o \\ \varepsilon_y^o \\ \gamma_{xy}^o \end{bmatrix} = [A^{-1}] \begin{bmatrix} N_x \\ N_y \\ N_{xy} \end{bmatrix} \qquad (Eq\ 4.1)$$

For a uniaxial tensile load applied in the x direction and laminate thickness h , $N_x = h\sigma$, $N_y = 0$ and $N_{xy} = 0$. Thus, the mid plane Young's modulus along the x direction can be determined as,

$$E_x = \frac{1}{[A^{-1}]_{11} h} \qquad (Eq\ 4.2)$$

The FDM parts were also considered as composites of partially bonded ABS filaments and voids and a new set of equations were proposed to calculate the elastic constants, by gathering the elastic modulus, Poisson's ratio and shear modulus along longitudinal and transverse directions, as follows:

Longitudinal tensile modulus

$$E_1 = (1 - \rho_1)E \qquad (Eq\ 4.3)$$

Transverse tensile modulus

$$E_2 = \zeta(1 - \rho_2)E \qquad (Eq\ 4.4)$$

In plane shear modulus,

$$G_{12} = \zeta'(1 - \rho_2)G \qquad (Eq\ 4.5)$$

In plane Poisson ratio,

$$\upsilon_{12} = \upsilon \qquad (Eq\ 4.6)$$

where E and G is the Young's modulus and shear modulus of the plastic filament, ρ_2 and ρ_1 are the area void density in the plane normal to filaments and the linear void fraction along the transverse direction, ζ and ζ' are the empirical factors equal to 0 to 1.

E_1, E_2, G_{12} and υ_{12} were tested by strain gauges set at different orientations. The relationship between the resultant tensile modulus $E_x^{45^\circ}$ in the x direction the tested parameters were obtained as:

$$G_{12} = \frac{1}{\frac{4}{E_x^{45}} - \frac{1}{E_1} - \frac{1}{E_2} + \frac{2\upsilon_{12}}{E_1}} \qquad (Eq\ 4.7)$$

This relationship was considered as the theoretical model to predict the variation of the tensile modulus with the raster angle. Experimental evaluations were also done using four different raster angles: [0˚/90˚], [30˚/-60˚], [45˚/-45˚] and [15˚/-75˚] and the results are in close correlation with the theoretical predictions as shown in Fig. 4.3.

Evidently, there is a definite relationship between the raster angle and the mechanical properties of FDM parts. Though experimental and theoretical results were obtained and correlated, the lamination theory applied to a stack of layers with criss-cross orthographic raster orientations across successive layers may not be truly representative of the actual role of raster orientation. Further, the above model assumes symmetrical raster patterns and layer structures on either side

of the central plane. Considering the highly anisotropic nature of the composite material constituted of partly coalesced intricate network of polymer strands interspersed with air gaps, this appears to be over simplifying the problem. The analytical approach followed in the current research is based on the hypothesis that elastic and shear moduli of the material structures resulting from extrusion 3D printing vary with varying raster angles and coalescence ratios. Also, the model by Li et al. [78] uses moduli established from two extreme directions (mesostructure-based material properties), to predict the effects of raster variations. Ideally, the mathematical model should be able to predict the effect of varying raster angles from the known properties of a mono filament. This is attempted in this chapter by applying the elastic plane stress theory to a single strand with different orientations.

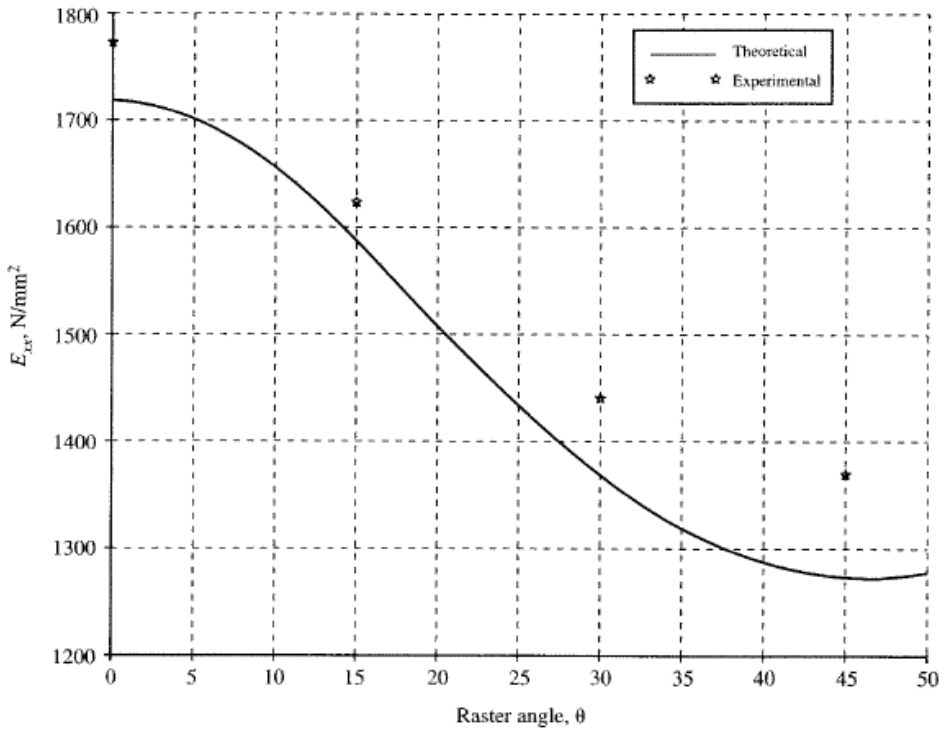

Fig. 4.3 Tensile modulus vs. Raster angle orientation (Image source: Li et al. [78])

4.2 A preliminary experimental assessment of the role of raster angle

Before delving deeper into the raster angle mechanics, a simple experiment is devised to understand the actual role of raster angle on the mechanical characteristics of FDM parts. All commercial FDM systems employ either orthographical cross, or unidirectional (either 0˚ or 90˚) raster settings. Such restricted settings limit the research freedom and for similar reasons, the theoretical models developed by Li et al. [78] ignored the coupling and bending stiffness matrices. This is tantamount to ignoring the inter-layer torsional effects, but as the raster angle varies, torsional effects become more significant and obvious. In order to capture the actual role of the raster angle, specimens are printed with the same raster angle in all the layers of the test specimens of the current experiments. Ideally, single layer samples would best suit to capture the influences of raster angles, but there are practical difficulties like over-filling at the ends of raster paths and insufficiently connected strands, apart from the difficulties in extracting the samples from the printer base, without disturbing the fragile strand structure of a single layer sample.

Different materials testing standards were employed earlier for testing FDM samples. While Croccolo et al. [58] used the common ASTM D638 with the dog bone shaped specimens, considering the close resemblance to the structure of a composite material, Ahn et al. [47] suggested ASTM D3039, requiring rectangular test pieces. Based on similar considerations that FDM parts will have both ABS material and the air gaps interspersed, giving a typical internal mesostructure and also the ease of printing, ASTM D3039 07 [129] is employed as the standard procedure for the current experiments involving tensile testing of ABS samples printed by FDM. The test specimen selected is a 50mm X 20mm X 4mm rectangular block. The CAD file of the specimen is created and then converted into a .stl file, which is subsequently processed using a

MATLAB program to develop uniform flat layer slices and the deposition path data with specific raster angles. Tool paths are generated with raster angles 0˚, 15˚, 30˚, 45˚, 60˚, 75˚, and 90˚ as shown in Fig. 4.4(a). The layer thickness is set as 0.4mm while the road width is 0.5mm. The extrusion nozzle diameter is 0.5mm. The diameter of the extruded strand expands slightly and measures around 0.55 mm, due to the swelling phenomenon, as mentioned by Bellini [38]. This provided the overlapping between roads and is equivalent to an air gap setting of -0.03 mm. This also increases the contact area for the inter-road coalescence. Test specimens with all selected raster angles are built on a FDM test setup based on the modified Makerbot CNC system described in the previous chapter and the samples printed with 10 layers each are as shown in Fig. 4.4(b).

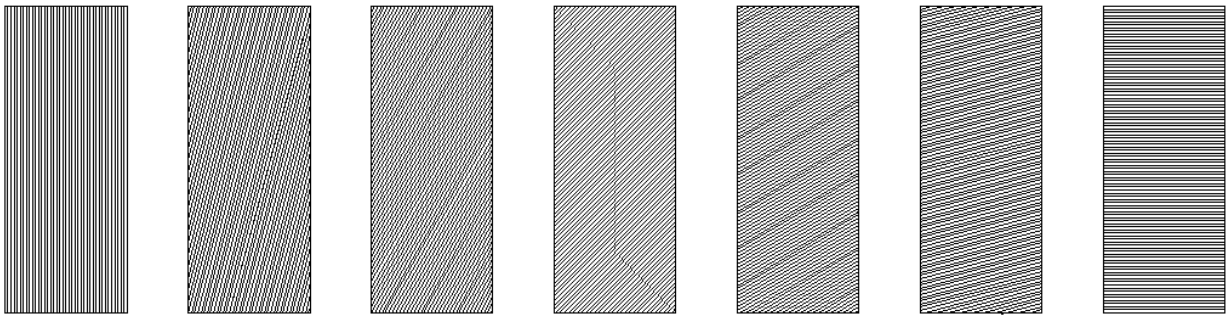

(a) CAD models

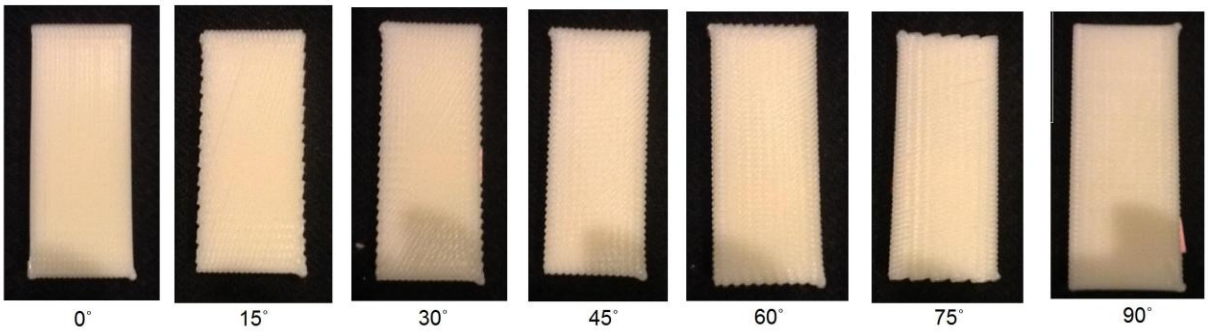

(b) Printed test specimens

Fig. 4.4 Test specimens with unidirectional orientation

Based on the experimental conditions stated above and using Eq. 3.36, the coalescence for the test samples was calculated to be between 56 and 62 per cent. Further, SEM photographs are taken as in Fig. 4.5, to show the meso-structure of the test pieces made and also indicate the time-dependent coalescence and inter-strand diffusion as reported by Rodriguez et al. [126]. Using the photomicrograph of Fig. 4.5, the inter-road coalescence could be estimated to be around 55 to 60 per cent, which is close to the theoretical value calculated using Eq. 3.36.

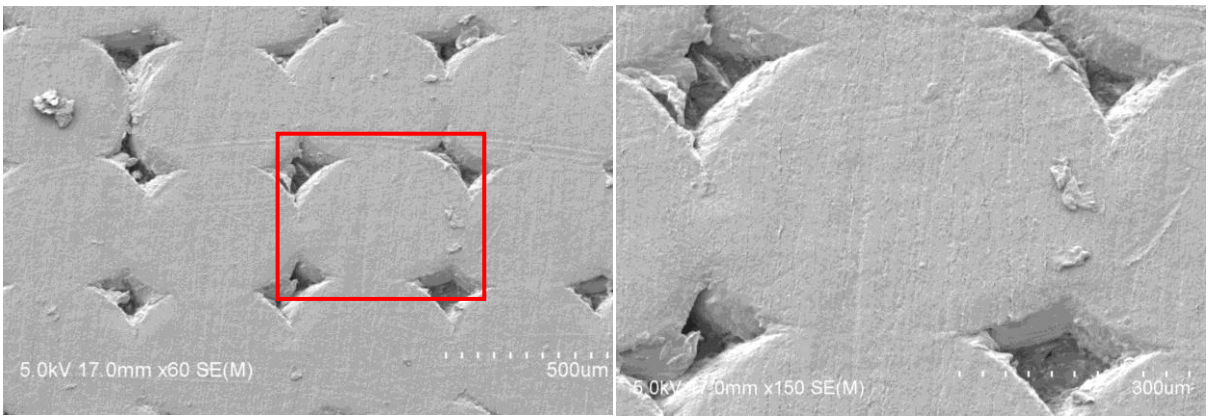

Fig. 4.5 meso-structure of the FDM test specimen

Tensile tests are conducted on the test pieces produced using a Tinius Olsen tensile testing equipment. Specimens are clamped with suitable vices as shown in Fig. 4.6 at either end and slowly pulled at a velocity of 0.1 mm/s until fracture or the maximum possible loads are reached. Ultimate tensile strength is the target response from these tests, and so, only load-elongation curves are generated. After the tensile test, two phenomena are commonly observed; first, the crack usually follows the raster angle direction except for 90˚, but the location of the crack varied randomly in similar lines to Ahn's failure model [111]. This is probably direct experimental evidence in support of the hypothesis that the raster angle affects the mechanical

properties of FDM parts. Second, there is no obvious necking phenomenon occurring in most test specimens before fracture. The load elongation plot as in Fig. 4.7 also shows that it is mostly elastic deformation almost until the ultimate point, with no strain hardening region in the curve. The small kink in the curve at around 600 N is possibly due to a few snapped strands of the test specimen. Otherwise, this trend is similar to the typical stress-strain curve of an ABS injection moulded part [130].

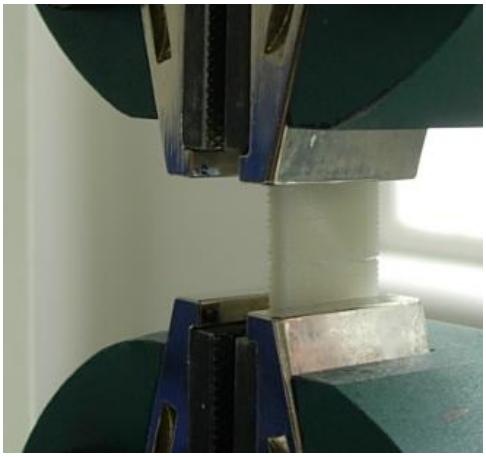

Fig. 4.6 Experimental setup during a tensile test

Ultimate tensile load results obtained with different specimens of varying raster angles are listed in Table 4.1. The ultimate strength decreased with increasing raster angles. The maximum and minimum loads are 2476.67 N and 806.67 N obtained with 0˚ and 90˚ raster angles, respectively. However, the ultimate load plot against the raster angle, as shown in Fig. 4.8(a), is not linear; the gradient is low from 0˚ to 30˚, very steep between 30˚ and 60˚ and then lowers again at still higher raster angles. The ultimate strength vs raster angle plot shows a similar trend as depicted in Fig. 4.8(b). The maximum and minimum stresses are 30.79 MPa and 10.08 MPa obtained at 0˚ and 90˚ respectively, resulting in a reduction from 81% to 26% of the ultimate strength of the

ABS properties as shown in Table 3.1. While the ultimate load and stress as depicted in Fig. 4.8 (a) and (b) clearly establish the significant role of raster orientation on critical mechanical attributes, it is interesting and important to understand the mechanics of these effects through a theoretical formulation as attempted next.

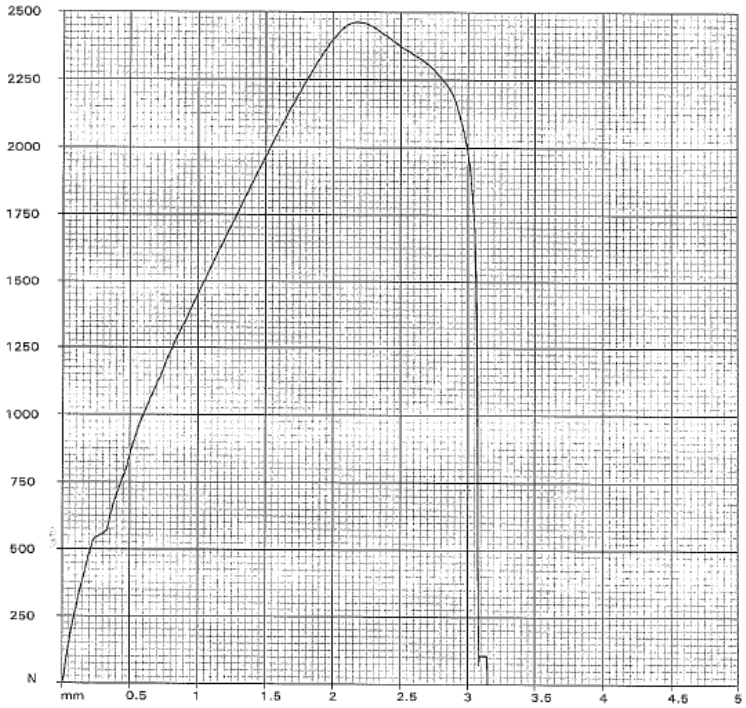

Fig. 4.7 Load-elongation curve from the tensile test

Table 4.1 Tensile test result for different raster orientation

Raster Angle	Specimen 1 (N)	Specimen 2 (N)	Specimen 3 (N)	Average Load (N)	Stress (MPa)
0˚	770.000	848.333	801.666	806.666	10.08
15˚	833.333	805.000	1155.000	931.111	11.64
30˚	1110.000	1120.000	1015.000	1081.667	13.52
45˚	1318.333	1513.333	1568.333	1466.666	18.33
60˚	2053.333	2040.000	2106.667	2066.667	25.83
75˚	2235.000	2448.333	2360.000	2347.778	29.35
90˚	2496.667	2470.000	2463.333	2476.667	30.96

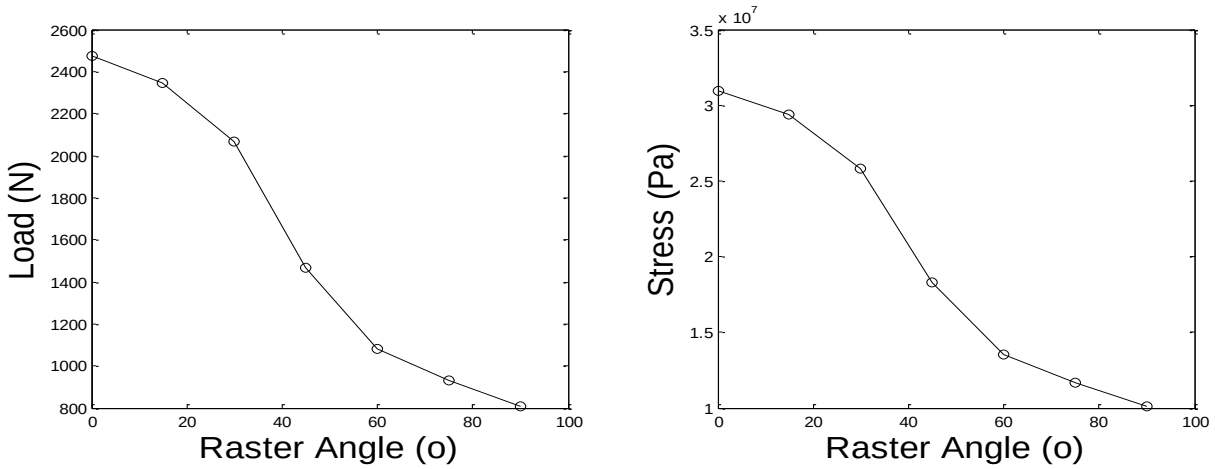

Fig. 4.8 Raster angle results (a) Load versus raster angle and (b) Stress versus raster angle

4.3 Tensile modulus vs. raster angle; an analytical model

The internal meso-structure of the FDM part is the result of a set of parallel filaments used to print the part. The rate of coalescence and angle of these parallel filaments determine the mechanical properties of the FDM part. Tensile modulus is a measure of the stiffness of an elastic material and is a quantity used to characterize materials. Bellini et al. [38] conducted tensile tests on FDM specimens with different raster angles and found the Hooke's Law to be still valid. It was also reported that the tensile modulus will not be influenced considerably by the extrusion process. Based on these observations, a couple of assumptions are made to serve as the basis for the models developed:

- Definite relationships exist between the raster angle and the ultimate strength and tensile modulus values of FDM parts.
- Tensile modulus of the FDM part is only affected by the raster angle for a given coalescence.

Based on the test specimens used for the experiments discussed above, the internal meso-structure of the FDM part is depicted as shown in Fig. 4.9 (a). Each layer of the FDM part is filled with parallel filaments and these filaments are formed with the same raster angle as shown in Fig. 4.9(b). In order to build the analytical model capturing the mechanics of the internal changes due to resultant loads, a small section is chosen for evaluation as shown in Fig. 4.9(c). Assuming that a single layer is subjected to external forces only from two directions, a random section is assumed to be under the internal resultant forces as shown in Fig. 4.9(d).

Considering Fig. 4.9(d), all forces are assumed to be in the same plane, or otherwise, resulting in plane stress conditions. For an infinitesimal case, the effect of surface area on the internal resultant forces can be ignored by assuming the small section to be a block. However, the surface area might affect the FDM plane stress state due to the coalescence condition. Ideally, if the coalescence between two roads is 100%, all voids are completely eliminated. However, in the actual case, internal voids exist between the roads and layers due to the incomplete filling and inconsistent material flow [31]. This partially bonded meso-structure makes the raster angle a more significant parameter together with the percentage of coalescence.

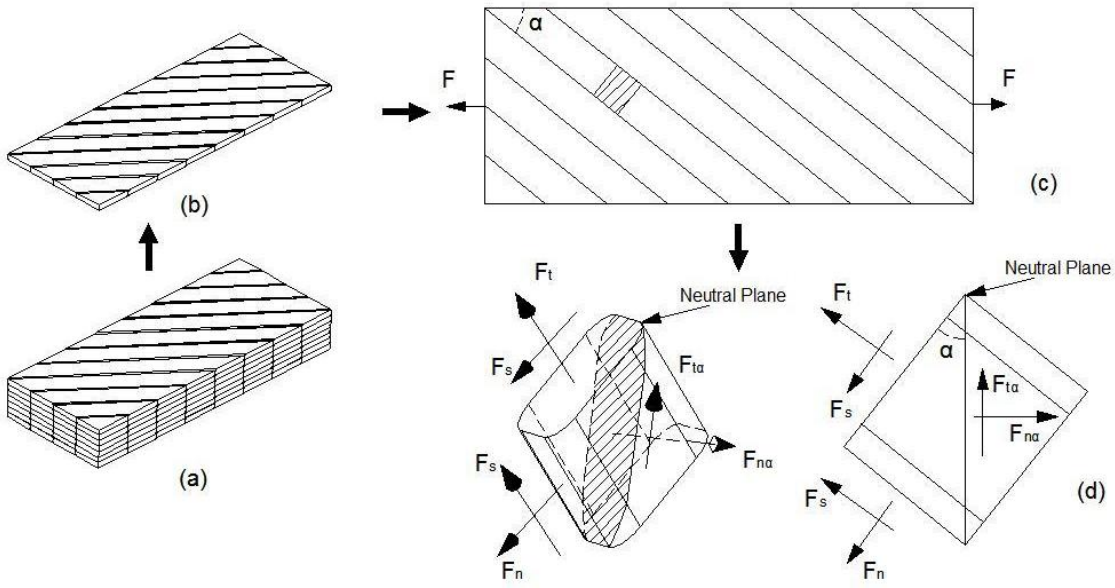

Fig. 4.9 Force system in multi-strand component of a specific raster angle

A single layer of the meso-structure is considered next for establishing the relationship between the raster angle and the mechanical properties assuming the layer to be under tensile load from both sides. One random small section of a filament is selected next for analysing the internal resultant forces. The 2D force system acting on an infinitesimally small section is as shown in Fig. 4.10(a). Considering all forces and the geometry of the small section, plane stress state can be used in this situation as shown in Fig. 4.10(b). Further, the force equilibrium equations can be written as follows:

$$\sum F_{x\alpha} = 0$$

$$\sigma_y A_y \cos\alpha + \tau_y A_y \sin\alpha + \tau_x A_x \cos\alpha + \sigma_x A_x \sin\alpha = \sigma_\alpha A_\alpha \qquad (Eq\ 4.8)$$

$$\sum F_{y\alpha} = 0$$

$$-\sigma_y A_y \sin\alpha + \tau_y A_y \cos\alpha - \tau_x A_x \sin\alpha + \sigma_x A_x \cos\alpha = \tau_\alpha A_\alpha \qquad (Eq\ 4.9)$$

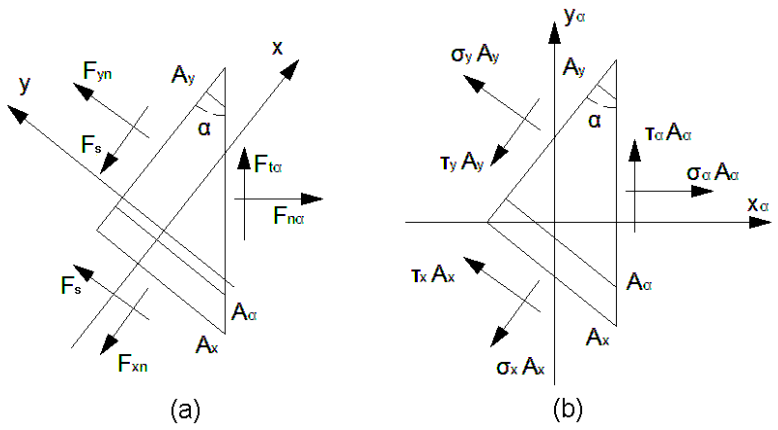

Fig. 4.10 Internal resultant forces exerted on a FDM road section

Considering that the deposited filaments partly fuse into one another, an exact cylindrical road is far from the reality and the actual shape of each filament depends on the rate of coalescence. For practical reasons, the shape of each filament, which was shown in Chapter 3, is used again here and considered as a square with elliptical fillets and multilayer models are constructed as shown in Fig. 4.11.

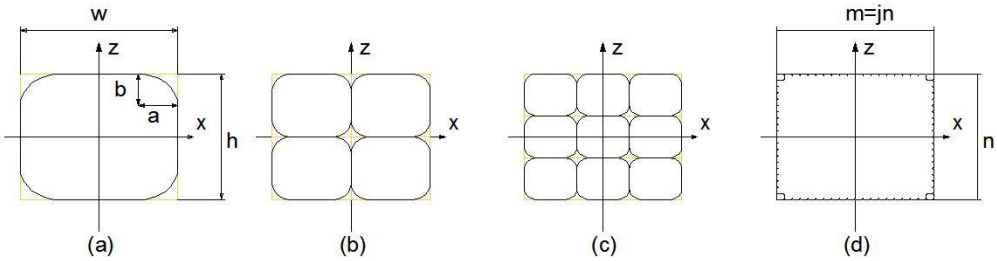

Fig. 4.11 Cross-sectional area of a square shape with precise filling; (a) Single layer, (b) Two layers, (c) Three layers, and (d) Multi layers

With these considerations, the area of application of the resultant forces needs to be recalculated in a proper manner. In this case, the random section in Fig. 4.9(d) is used to calculate the components of resultant force areas A_x, A_y and A_α of the single layer shown in Fig. 4.12, as:

$$A_x = w \tan\alpha \, (h - 2 \cdot b) \qquad (Eq\ 4.10)$$

$$A_y = hw + (\pi - 4)bc \qquad (Eq\ 4.11)$$

$$A_\alpha = \frac{A_y}{\cos\alpha} = \frac{hw + (\pi - 4)bc}{\cos\alpha} \qquad (Eq\ 4.12)$$

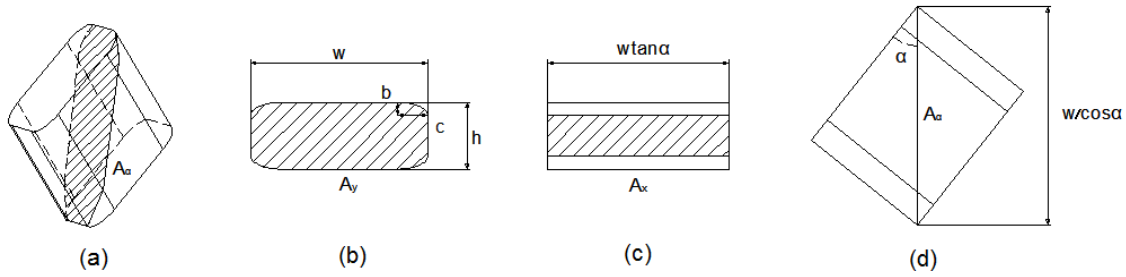

Fig. 4.12 General dimensions and areas of FDM section; (a) Isotropic view area A_α , (b) front view area A_y, (c) side view area A_x , and (d) top view A_α

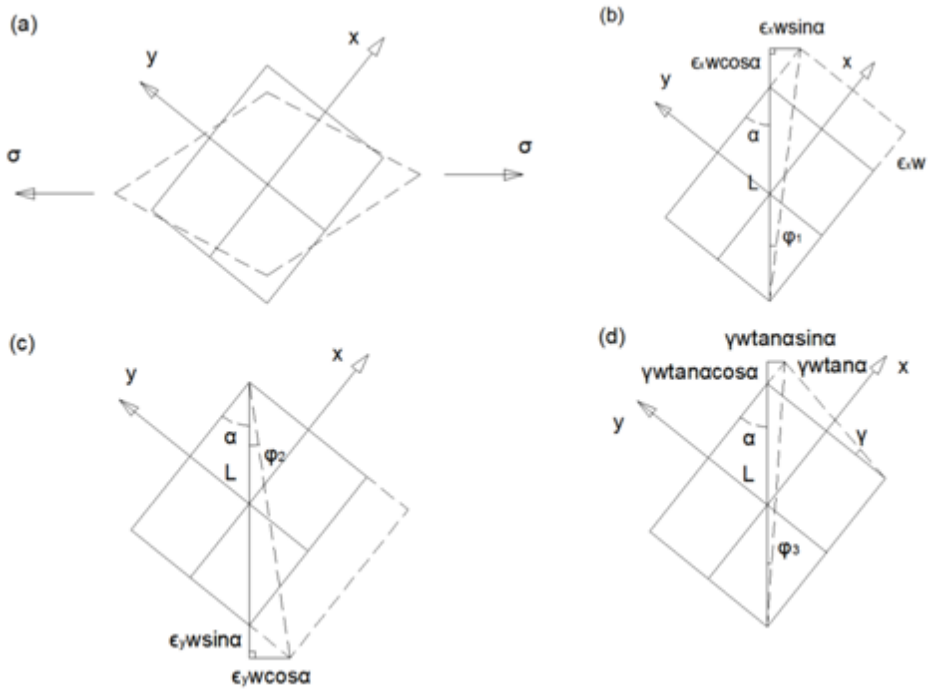

Fig. 4.13 General deformation of the FDM section; (a) normal stress on the random section, (b) strain in the x-direction, (c) strain in the y-direction, and (d) shear strain

Initially, for a given longitudinal load, all strands are stretched under pure tension, and shear stresses and strains gradually build up depending on the internal structure resulting from the structure of the strands. The net effect of the forces acting on the section under consideration is a deformed section as shown in Fig. 4.13(a). The deformed section is subjected to tensile loads and the total strain in the tensile load direction needs to be calculated. As all the layers are with matching raster patterns, the twist or torsion between layers is negligible and consideration of plane stress conditions is justified. The total strain could be considered as a combination of the strain along x (Fig. 4.13(b)) and y directions (Fig. 4.13(c)) and rotation (Fig. 4.13(d)). The random section of a road undergoes different deformations based on the raster angle. Also, these deformations are affected by the coalescence. Hence, the infinitesimal strain model, which ignores the areas, cannot be used directly in this case and the contact area needs to be considered.

In the random section of a road, strain deformations occur in both axial and transverse directions. As shown in Fig. 4.14, the transverse and axial directions are assumed as x and y axes respectively. The random section of the road could be used to apply the finite strain theory because the strand could be considered as a continuum body and the internal structure is homogenous. Haddow's et al. [131] mentioned three configurations for an initially homogenous body; the initial unstrained and unstressed configuration at the uniform reference temperature, the unstressed plastically strained configuration at the reference temperature and the stressed elastic-plastic configuration. Considering the current tensile test at room temperature, the unstressed, plastically strained configuration at the reference temperature could be ignored. The cause of strain here is based on the initial unstrained and unstressed configuration and the

stressed elastic-plastic configuration and hence the analytical model could use the Cauchy or engineering strain:

$$\epsilon = \frac{\Delta L}{L}$$

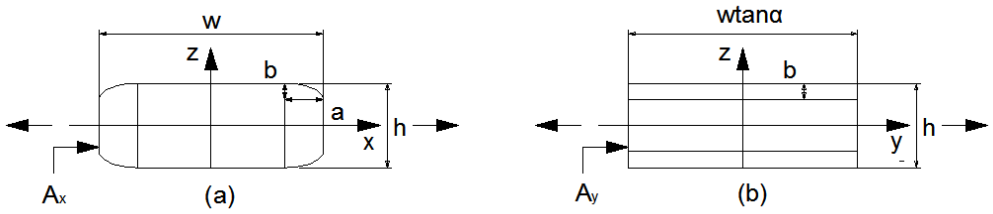

Fig. 4.14 Strain in transverse and axial direction; (a) transverse and (b) axial

Equations for normal strains in x and y directions are different as the load area and the length of the section are different. The load area for the x axis is varied based on the coalescence and the raster angle orientation, while the length along the y axis varies with the raster angle orientation. Hence the equations for the x- and y- strains need to be obtained individually.

In the x-direction, strain is affected by the coalescence and the raster angle orientation as shown in Fig. 4.13(a). The random road section suffers loads form both axial and transverse directions; hence, the strain in each direction is composed of three terms. The first term is due to the normal stress along the specific axis, which is the obvious strain. The second term is generated by the transverse strain effects along y axis, as all the surfaces of the section of the road are contracted. Considering this, the strain equations along x- and y-axes are expressed as follows:

$$\epsilon_x = \frac{\partial u}{\partial x} = \frac{(\sigma_x - \nu\sigma_y)A_x}{Ew^2 \tan\alpha} \int_0^w \frac{1}{x} dx$$

$$\epsilon_x = \frac{\partial u}{\partial x} = \frac{\sigma_x - \nu\sigma_y}{Ew^2 \tan\alpha}\left(\int_0^c \frac{1}{x}dx + \int_c^{w-c} \frac{1}{x}dx + \int_{w-c}^{w} \frac{1}{x}dx\right)$$

$$\epsilon_x = \frac{\partial u}{\partial x} = \frac{A_x}{Ew^2 \tan\alpha} C1\left(\sigma_x - \nu\sigma_y\right) \qquad (Eq\ 4.13)$$

Where

$$C1 = \frac{w - 2c}{h} + \frac{2hc}{b\sqrt{h - 2b}\sqrt{h + 2b}} \tan^{-1}\sqrt{\frac{h + 2b}{h - 2b}} - \frac{c\pi}{2b}$$

E and ν are the tensile modulus and Poisson's ratio of ABS, respectively.

Similarly, in the y direction, strain is affected by raster angle orientation as shown in Fig. 4.13(b), and can be expressed as,

$$\epsilon_y = \frac{\partial v}{\partial y} = \frac{1}{E}\left(\sigma_y - \nu\sigma_x\right) \qquad (Eq\ 4.14)$$

Shear strain here is not caused by the shear stress but is the result of the normal stress. The normal stress pushes the strand, which deforms in lines similar to the deflection of a beam fixed at the end. Hence, the beam deflection theory is used here to represent the shear strain. The x-and y- shear strain components are evaluated as follows:

$$u = \int \epsilon_x\, dx = \int \frac{\partial u}{\partial x} dx$$

$$\frac{\partial u}{\partial y} = \frac{\partial\left(\int \frac{\partial u}{\partial x} dx\right)}{\partial y} = \left[\frac{A_x}{Ew^2 \tan\alpha} C1\left(\sigma_x - \nu\sigma_y\right)\right]\frac{1}{\tan\alpha} \qquad (Eq\ 4.15)$$

$$\frac{\partial v}{\partial x} = \left[\frac{1}{E}\left(\sigma_y - \nu\sigma_x\right)\right]\tan\alpha \qquad (Eq\ 4.16)$$

Then the total shear strain is described as:

$$\gamma_{xy} = \frac{\partial v}{\partial x} + \frac{\partial u}{\partial y} \qquad (Eq\ 4.17)$$

Following the plane stress theory,

$$\epsilon_\alpha = \epsilon_x \sin^2 \alpha + \epsilon_y \cos^2 \alpha + \gamma_{xy} \sin \alpha \cos \alpha \qquad (Eq\ 4.18)$$

$$\gamma_\alpha = (\epsilon_x - \epsilon_y) \sin 2\alpha + \frac{\partial u}{\partial y} \cos^2 \alpha - \frac{\partial v}{\partial x} \sin^2 \alpha \qquad (Eq\ 4.19)$$

The tensile and shear moduli can be obtained using the Hooke's Law:

$$E_\alpha = \frac{\sigma_\alpha}{\epsilon_\alpha} \qquad (Eq\ 4.20)$$

$$G = \frac{\tau_\alpha}{\gamma_\alpha} \qquad (Eq\ 4.21)$$

As already discussed in Chapter 3, the modified Frenkel-Eshelby model can be used to predict the inter road sintering phenomena in FDM. Eq. 3.19 to 3.21 are repeated here for convenience:

$$C = \left(\frac{\Gamma t}{\mu a_0}\right)^{\frac{1}{2}} = \frac{y}{a} = \frac{w - 2c}{w} = \frac{h - 2b}{h} \qquad (Eq\ 3.22)$$

where C is constant here and for an ideal case $0 < C < 1$.

and,

$$b = \frac{h(1 - C)}{2} \qquad (Eq\ 3.23)$$

$$c = \frac{w(1-C)}{2} \qquad (Eq\ 3.24)$$

Substituting Eq. 3.20 and 3.21 into Eq. 4.10 to 4.12,

$$A_x = hwC \tan\alpha \qquad (Eq\ 4.22)$$

$$A_y = hwC3 \qquad (Eq\ 4.23)$$

$$A_\alpha = \frac{hwC3}{\cos\alpha} \qquad (Eq\ 4.24)$$

Where $C3 = 1 - \frac{(1-C)^2}{4}$

For the sake of simplifying the equations, let

$$C1 = \frac{w}{h}\left(C + \frac{2}{\sqrt{1-\left((1-C)\right)^2}}\tan^{-1}\sqrt{\frac{2-C}{C}} - \frac{\pi}{2}\right) = \frac{w}{h}C2 \qquad (Eq\ 4.25)$$

where $C2 = C + \frac{2}{\sqrt{1-\left((1-C)\right)^2}}\tan^{-1}\sqrt{\frac{2-C}{C}} - \frac{\pi}{2}$

Substituting Eq. 4.13 to 4.16 into Eq. 4.8 and 4.9, they become:

$$\sigma_\alpha = \sigma_y \cos^2\alpha + \left(\frac{\partial u}{\partial y} + \frac{\partial v}{\partial x}\frac{C}{C3}\right) G \sin\alpha\cos\alpha + \sigma_x \frac{C}{C3}\sin^2\alpha \qquad (Eq\ 4.26)$$

$$\tau_\alpha = \left(\sigma_x \frac{C}{C3} - \sigma_y\right)\sin\alpha\cos\alpha + G\frac{\partial u}{\partial y}\cos^2\alpha - G\frac{\partial v}{\partial x}\frac{C}{C3}\sin^2\alpha \qquad (Eq\ 4.27)$$

Then substituting Eq. 4.32 to 4.34 into Eq. 4.28 and 4.31, they become:

$$\epsilon_\alpha = \frac{\partial u}{\partial x}\sin^2\alpha + \frac{\partial v}{\partial y}\cos^2\alpha + \left(\frac{\partial v}{\partial x} + \frac{\partial u}{\partial y}\right)\sin\alpha\cos\alpha \qquad (Eq\ 4.28)$$

$$\gamma_\alpha = \left(\frac{\partial u}{\partial x} - \frac{\partial v}{\partial y}\right)\sin 2\alpha + \frac{\partial u}{\partial y}\cos^2\alpha - \frac{\partial v}{\partial x}\sin^2\alpha \qquad (Eq\ 4.29)$$

$$E_\alpha = \frac{\sigma_y \cos^2\alpha + \left(\frac{\partial u}{\partial y} + \frac{\partial v}{\partial x}\frac{C}{C3}\right)G\sin\alpha\cos\alpha + \sigma_x\frac{C}{C3}\sin^2\alpha}{\epsilon_x\sin^2\alpha + \epsilon_y\cos^2\alpha + \left(\frac{\partial v}{\partial x} + \frac{\partial u}{\partial y}\right)\sin\alpha\cos\alpha} \qquad (Eq\ 4.30)$$

$$G_\alpha = \frac{\left(\sigma_x\frac{C}{C3} - \sigma_y\right)\sin\alpha\cos\alpha + G\frac{\partial u}{\partial y}\cos^2\alpha - G\frac{\partial v}{\partial x}\frac{C}{C3}\sin^2\alpha}{\left(\epsilon_x - \epsilon_y\right)\sin 2\alpha + \frac{\partial u}{\partial y}\cos^2\alpha - \frac{\partial v}{\partial x}\sin^2\alpha} \qquad (Eq\ 4.31)$$

However, stresses σ_x and σ_y vary with areas A_x and A_y. For instance, if both areas suffer the same amount of load but one side has a smaller area, it would reach the ultimate stress before the other and fracture begins. From the experimental results and based on literature, σ_α equals σ_x or σ_y, when the section of the strand considered aligns with the axial or transverse directions. In both cases, there will be no shear stress and the normal stress could reach up to the ultimate stress internally.

It is evident from Eq. 4.13 to 4.16 that the theoretical strain depends only on stresses and the areas. Based on this, an interesting analogy develops; considering that the FDM part is made of a single strand and the loads are exerted on the strand as shown in Fig. 4.15. The shear load and stress are assumed to be the by-products of the normal loads. In the very beginning, there is no shear load or shear strain as mentioned above. Only normal loads along axial or transverse directions constitute the external loads. The force balance equation is of the form:

$$F_x \sin\alpha + F_y \cos\alpha = F_\alpha \qquad (Eq\ 4.32)$$

Which becomes,

$$\sigma_x \frac{C}{C3} \sin^2\alpha + \sigma_y \cos^2\alpha = \sigma_\alpha \qquad (Eq\ 4.33)$$

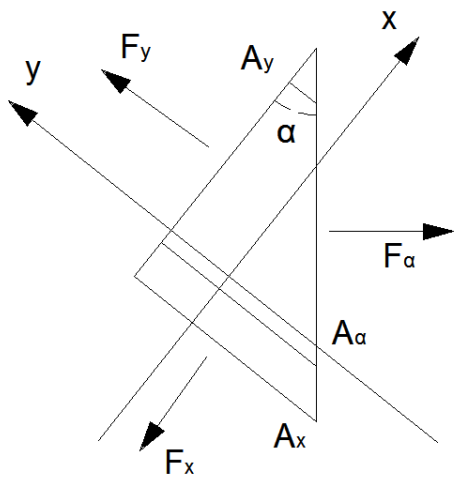

Fig. 4.15 Resultant forces on a single strand of the FDM part

With increasing σ_x and σ_y, the normal strain and the shear strain continue to increase, until they reach the ultimate values and then the balance is established just before the fracture. At this point, the stresses in X and Y directions are assumed to be reaching the ultimate stress values and substituted into Eq. 4.26 to 4.31, which become:

$$\sigma_\alpha = \sigma \cos^2\alpha + \sigma \left(\frac{\partial u}{\partial y} + \frac{\partial v}{\partial x}\frac{C}{C3}\right) G \sin\alpha \cos\alpha + \sigma \frac{C}{C3} \sin^2\alpha \qquad (Eq\ 4.34)$$

$$\tau_\alpha = \sigma\left(\frac{C}{C3} - 1\right)\sin\alpha\cos\alpha + G\frac{\partial u}{\partial y}\cos^2\alpha - G\frac{\partial v}{\partial x}\frac{C}{C3}\sin^2\alpha \qquad (Eq\ 4.35)$$

$$\epsilon_\alpha = (1-\nu)\left[\left(\frac{C2\cdot C\sigma}{E}\sin^2\alpha + \frac{\sigma}{E}\cos^2\alpha\right) + \left(\frac{\sigma}{E}\tan\alpha + \frac{C2\cdot C\sigma}{E\tan\alpha}\right)\sin\alpha\cos\alpha\right] \qquad (Eq\ 4.36)$$

$$\gamma_\alpha = (1-\nu)\left(\frac{C2\cdot C\sigma}{E} - \frac{\sigma}{E}\right)\sin 2\alpha + (1-\nu)\left[\frac{C2\cdot C\sigma}{E\tan\alpha}\cos^2\alpha - \frac{\sigma}{E}\tan\alpha\sin^2\alpha\right] \qquad (Eq\ 4.37)$$

$$E_\alpha = \frac{\sigma\cos^2\alpha + \left(\frac{\partial u}{\partial y} + \frac{\partial v}{\partial x}\frac{C}{C3}\right)G\sin\alpha\cos\alpha + \sigma\frac{C}{C3}\sin^2\alpha}{(1-\nu)\left[\left(\frac{C2\cdot C\sigma}{E}\sin^2\alpha + \frac{\sigma}{E}\cos^2\alpha\right) + \left(\frac{\sigma}{E}\tan\alpha + \frac{C2\cdot C\sigma}{E\tan\alpha}\right)\sin\alpha\cos\alpha\right]} \qquad (Eq\ 4.38)$$

$$G_\alpha = \frac{\sigma\left(\frac{C}{C3} - 1\right)\sin\alpha\cos\alpha + G\frac{\partial u}{\partial y}\cos^2\alpha - G\frac{\partial v}{\partial x}\frac{C}{C3}\sin^2\alpha}{(1-\nu)\left(\frac{C2\cdot C\sigma}{E} - \frac{\sigma}{E}\right)\sin 2\alpha + (1-\nu)\left[\frac{C2\cdot C\sigma}{E\tan\alpha}\cos^2\alpha - \frac{\sigma}{E}\tan\alpha\sin^2\alpha\right]} \qquad (Eq\ 4.39)$$

Considering the ABS material inside the small section as a homogeneous, isotropic linear material, the shear modulus could be determined as $G = \frac{E}{2(1+\nu)}$,

4.4 Results and discussion based on the analytical models predicting the raster angle mechanics

The analytical models developed are processed using MATLAB and the results obtained with varying coalescence and raster angles are plotted in Figs. 4.16 to 4.21. Generally, normal stress σ_α, normal strain ϵ_α and tensile modulus E_α are expected to decrease with increasing raster

angles based on experimental results as shown in Fig. 4.8 and the theoretical models for normal stress also prove this to be true in the low to mid-range of values of the coalescence as evident from Fig. 4.16. At higher coalescence values such as 0.8 and above, normal stress decreased initially, until around 30˚ and then increased until 50˚ and then decreased again, with further increase in the raster angle. This might have been caused by the shear strength from the rotational effects, increasing the total stress. Normal strain, as shown in Fig. 4.17, also follows a similar pattern, but the central peak is observed at relatively lower values of coalescence. While varying effective area of cross section is one of the plausible causes for the central peak, a dominant load in the x direction superimposed on the load in the y-direction could also be causing this variation. At higher values of coalescence, there is also a possibility for spinning in the strands as a result of the axial load, which might be resulting in the higher strain values. The normal stress and strain variations result in the graphs for the elastic modulus as shown in Fig. 4.18 which look like cosine curves. The elastic modulus values remained more or less constant and almost at the peak as the raster angle is varied from 0˚ to 10˚. With further increase in the raster angle, the elastic modulus values decreased, attained a minimum and then increased through varying degrees. It is important to note that the modulus of elasticity is not a bulk material property in this case, and varies with the meso-structure which in turn changes with the raster orientation. The variation is also significantly affected by the rate of coalescence and at relatively higher coalescence rates, the minimum elastic modulus values correspond to 45˚ raster orientations.

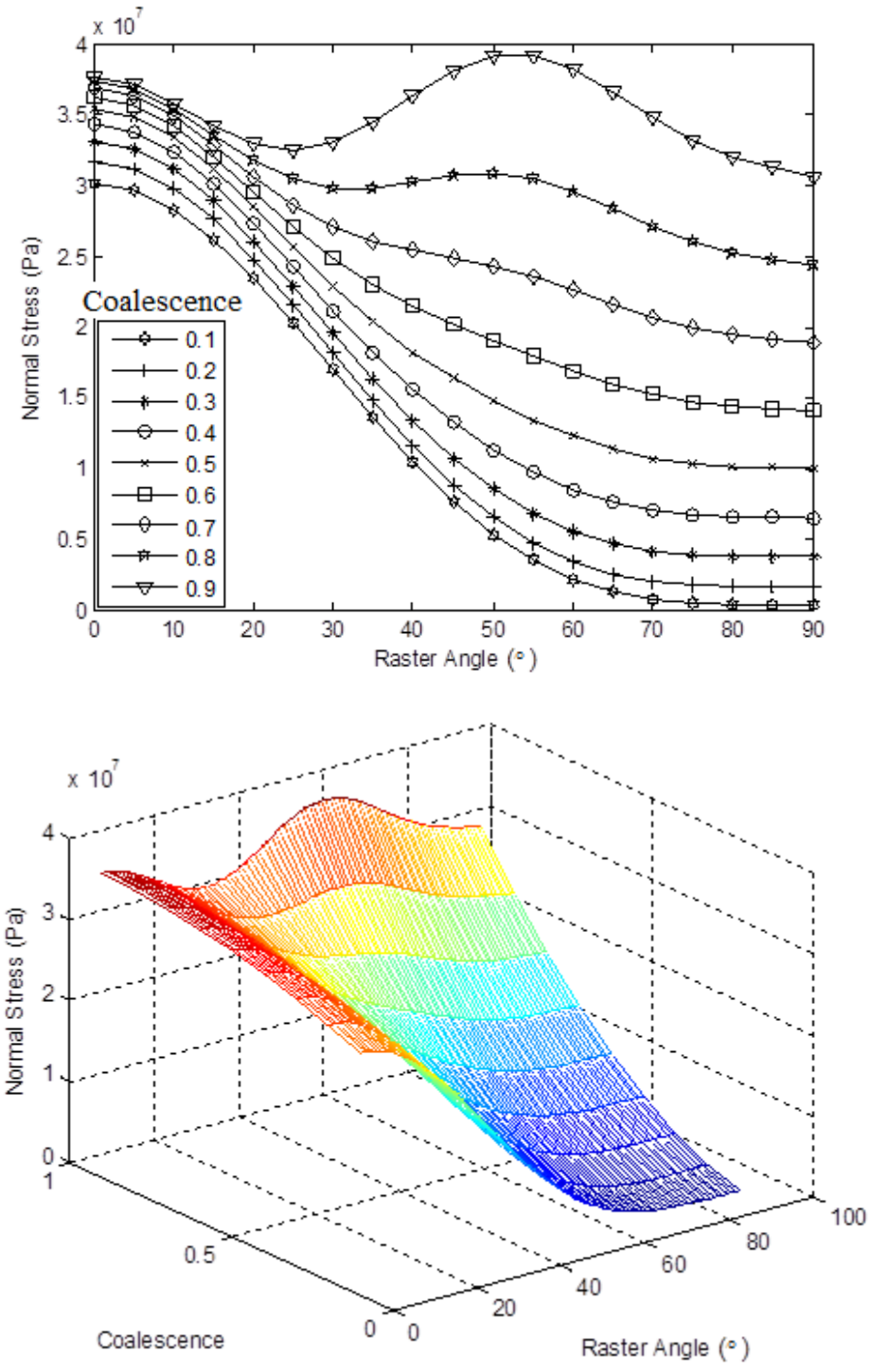

Fig. 4.16 Theoretical normal stress versus raster angle

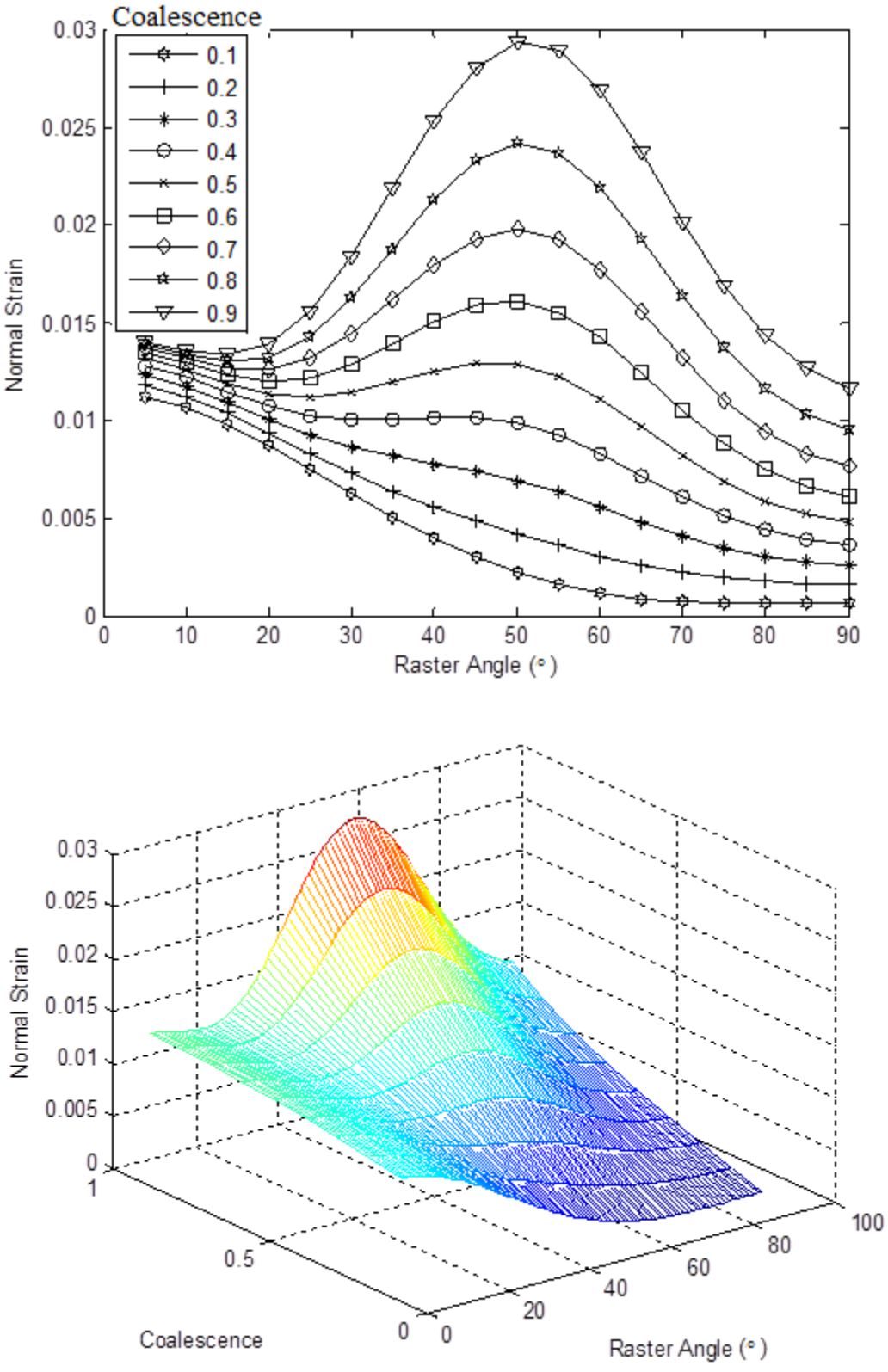

Fig. 4.17 Theoretical normal strain versus raster angle

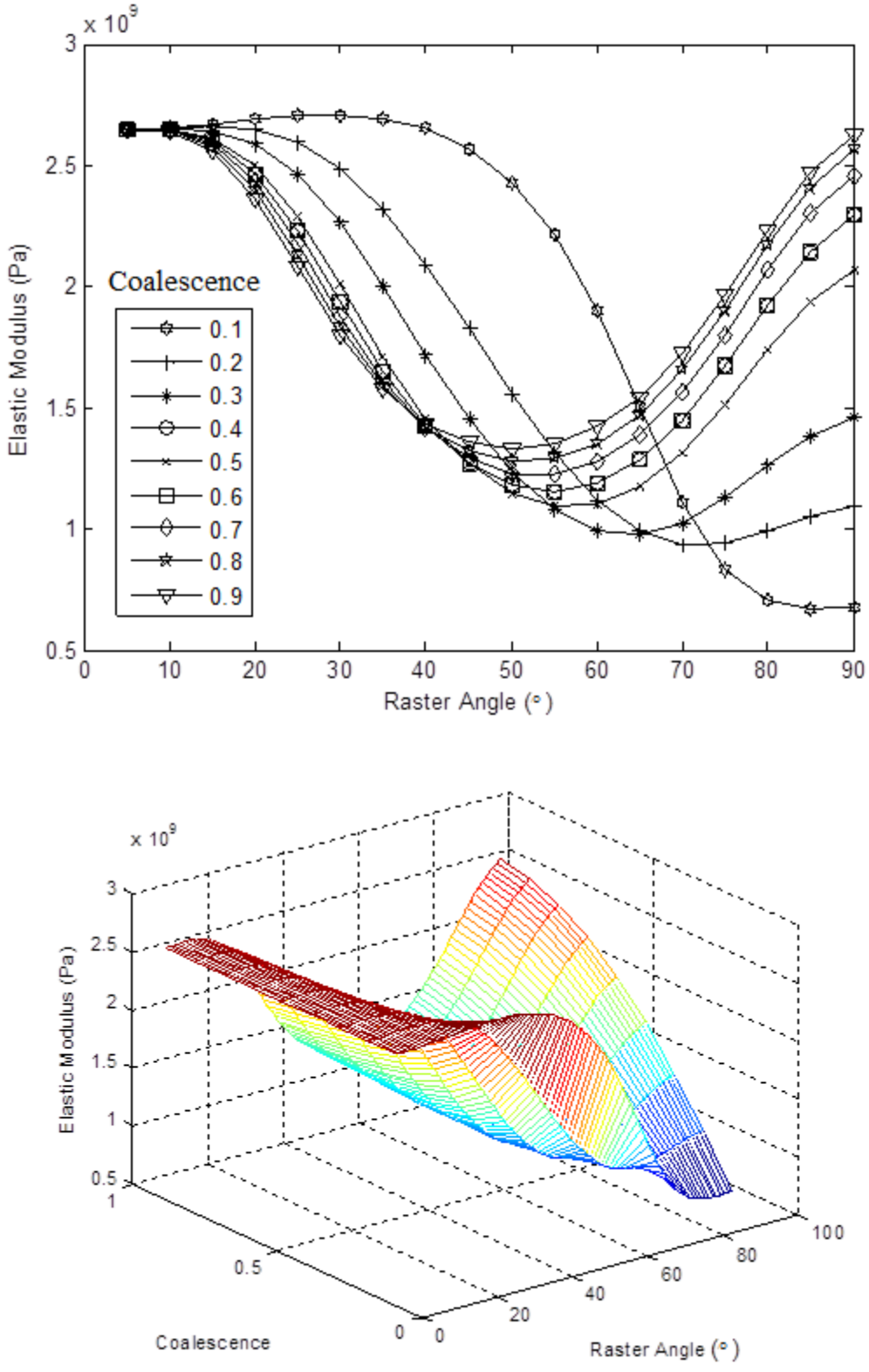

Fig. 4.18 Theoretical tensile modulus versus raster angle

For a given coalescence, the initial decrease in the modulus of elasticity with increase in the raster angle may be attributed to the relatively higher strain which is a combination of longitudinal, transverse as well as torsional strains generated. However, beyond a certain value of the raster angle, the strands gradually get aligned normal to the direction of loading, and will only depend on lateral strains across the inter-road joints resulting from coalescence. With higher values of coalescence, the modulus of elasticity is higher as the situation is closer to applying loads on a fully packed material structure with a uniform rectangular cross section, and all the strands being aligned across the load direction, there is relatively lesser strain for given stress levels, resulting in higher modulus of elasticity values. It is important to note that the modulus of elasticity is not a bulk material property in this case, and varies with the meso-structure which in turn changes with the raster orientation. The variation is also significantly affected by the rate of coalescence and at relatively higher coalescence rates, the minimum elastic modulus values correspond to 45˚ raster orientations.

Fig. 4.19-4.21 show the effects of raster angle on shear stress, strain, and shear modulus values with varying rates of coalescence. According to the shear stress theory, the maximum shear stress exists at around 45˚ raster angle, if the part is under pure shear stress state. In the present case, the maximum shear stress (negative) points vary between 30˚ to 60˚ depending on the coalescence rate. The shear stress increases with increasing raster angle and reaches the maximum value and subsequently decreases as raster angle is increased as evident from Fig. 4.19. The negative sign is indicative of the direction of the shear stress. With higher coalescence, the maximum and minimum shear stresses correspond to 30˚ and 60˚ respectively. Ideally, the shear stress is zero corresponding to 90˚ raster angle, but in some cases a small residual error

from calculations is observed, but overall, the shear stress values are close to zero. A similar trend is also obtained with shear strain variation, as shown in Fig. 4.20. The shear modulus variation evaluated based on the shear stress and strain variations are presented in Fig. 4.21. Past research on shear modulus evaluation was mainly based on fibrous composite material [132] or fibre reinforced composite material [78] models, neglecting the meso-structure. However, it is evident from the current models that the shear modulus values change with varying raster angles. It may be observed from Fig. 4.21 that the shear modulus values remained constant for most part of the variation of the raster angle and gradually reduce to a minimum at around 70˚-85˚, depending on the coalescence factor.

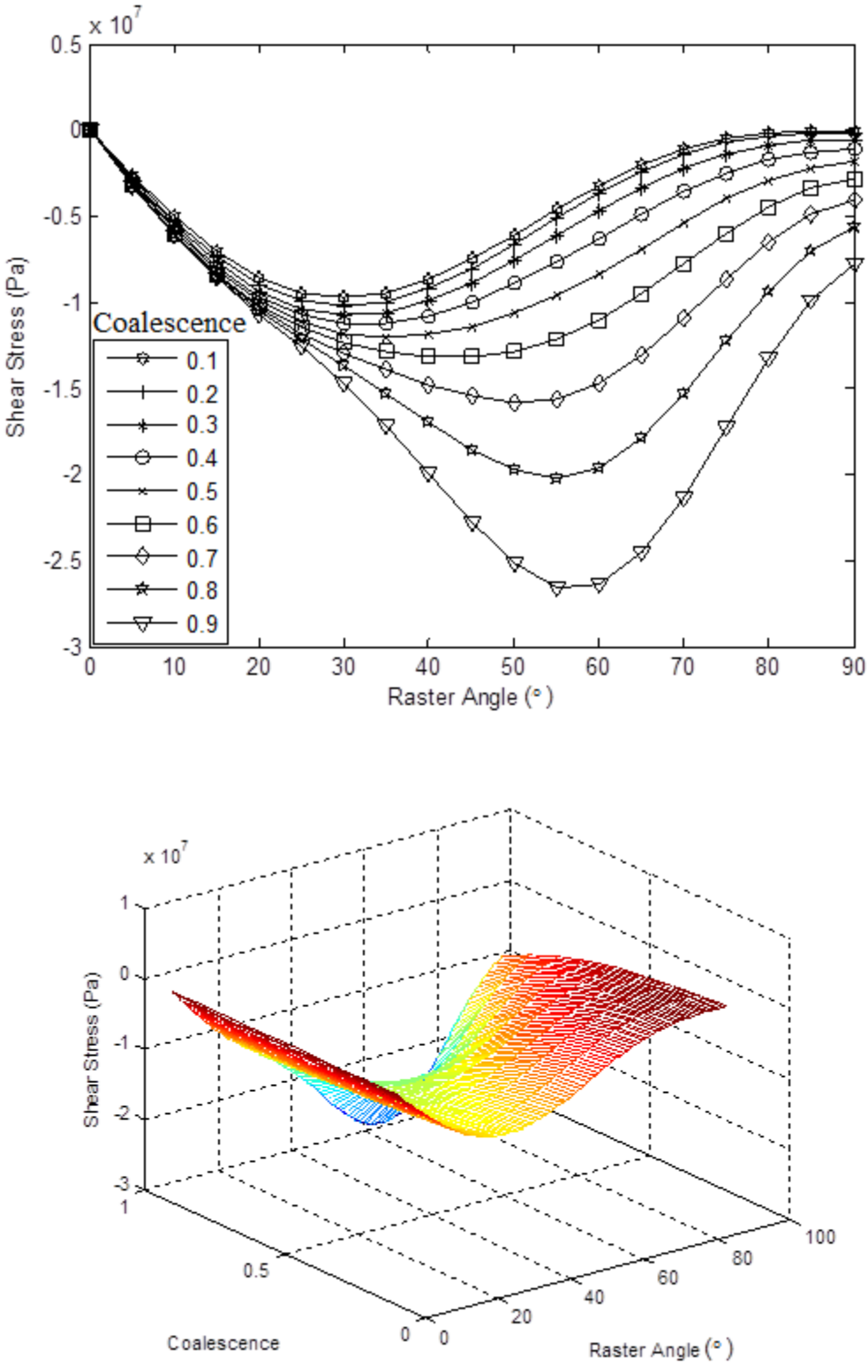

Fig. 4.19 Theoretical shear stress versus raster angle

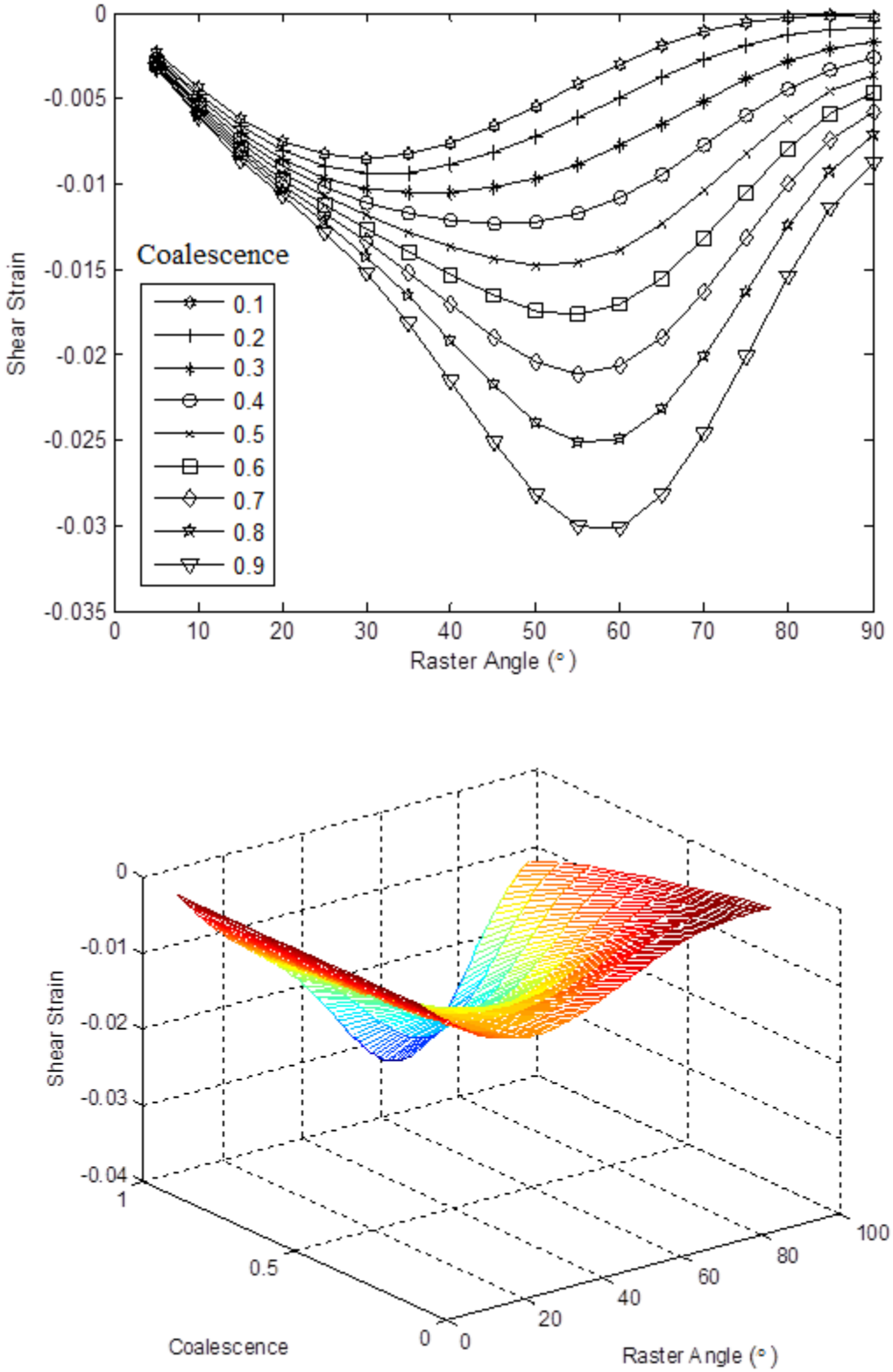

Fig. 4.20 Theoretical shear strain versus raster angle

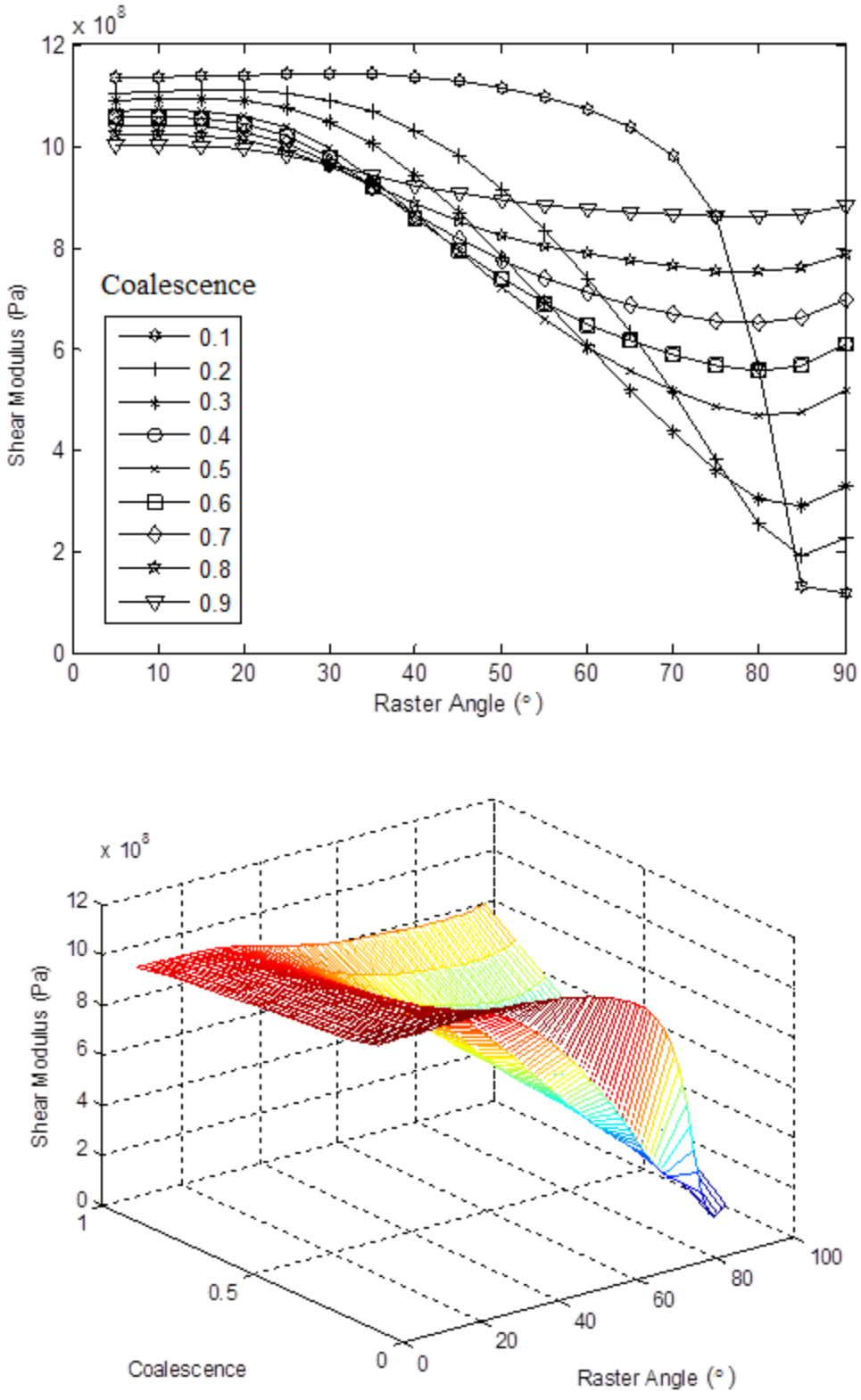

Fig. 4.21 Theoretical shear modulus versus raster angle

4.5 Correlation between analytical and experimental results

A comparative evaluation of the experimental and analytical results is essential now. As already stated, based on the coalescence models in Chapter 3, and also further ascertained by the experimental evidence through the SEM photomicrographs presented in Fig. 4.5, a coalescence value of 0.6 can be attributed to the samples used for the experiments at the beginning of this chapter. Now, using a coalescence value of 0.6, Eq. 4.38 predicts the variation of the tensile stress with the raster angle as shown in Fig. 4.22.

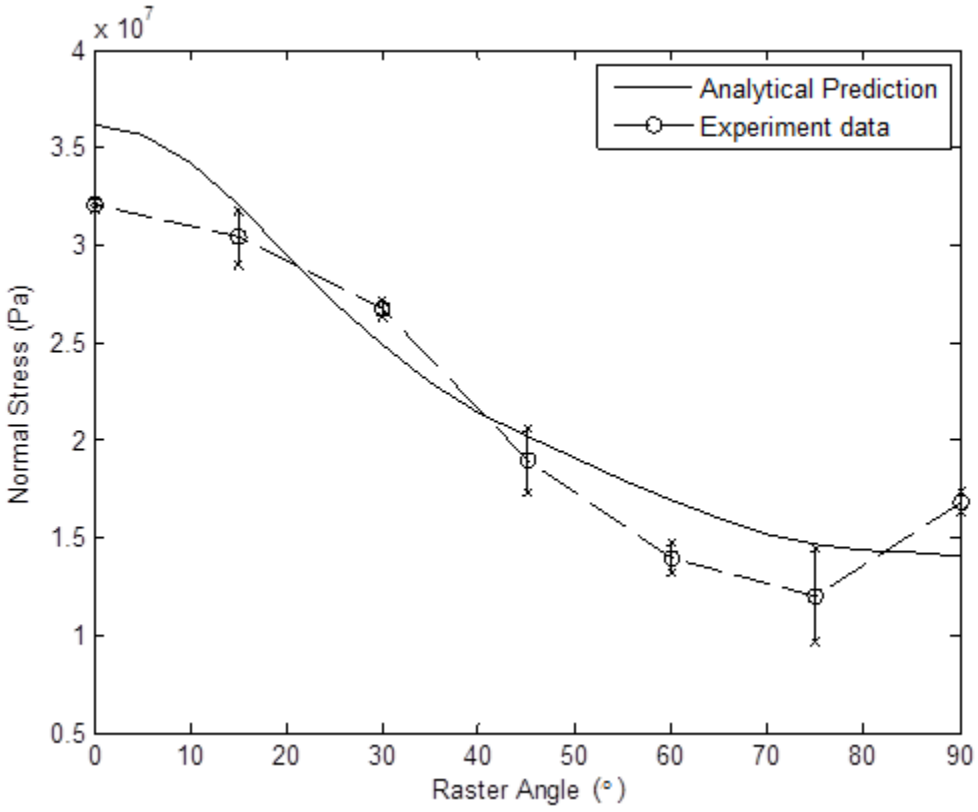

Fig. 4.22 Correlation between experimental analytical values of normal stress

Superimposing the experimental results, it may be observed that the theoretical and experimental predictions are closely correlated, giving strength to the validity of the model developed. This result also correlates quite well with the analytical and experimental results reported by Rodriguez et al. [132], which is reproduced here in Fig. 4.23. This gives strength to the assumption set above that the stress from axial and transverse directions reach the ultimate strength at the same time before facture occurs as in Eq. 4.44. Further, the tensile modulus variation is calculated using Eq. 4.48 and plotted as shown in Fig. 4.24 This trend is again in close correlation with the results reported by Li et al. [78] which is reproduced as shown in Fig. 4.3 .

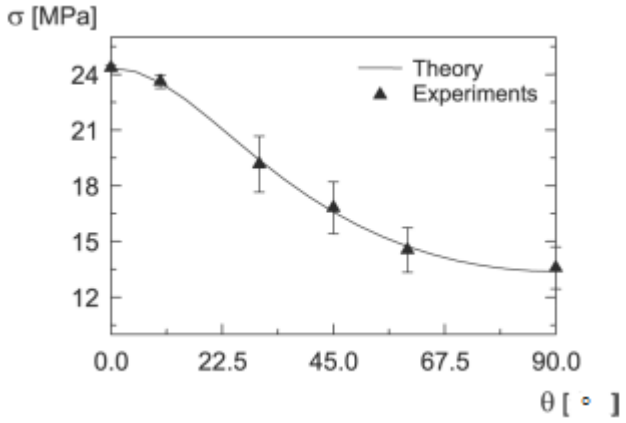

Angle (°)	S (MPa)
0	24.4 ± 0.1
10	23.6 ± 0.4
30	19.2 ± 1.5
45	16.8 ± 1.4
60	14.5 ± 1.2
90	13.6 ± 1.1

Fig. 4.23 Strength of unidirectional ABS material with aligned configuration against raster angle reported by Rodriguez et al. [132]

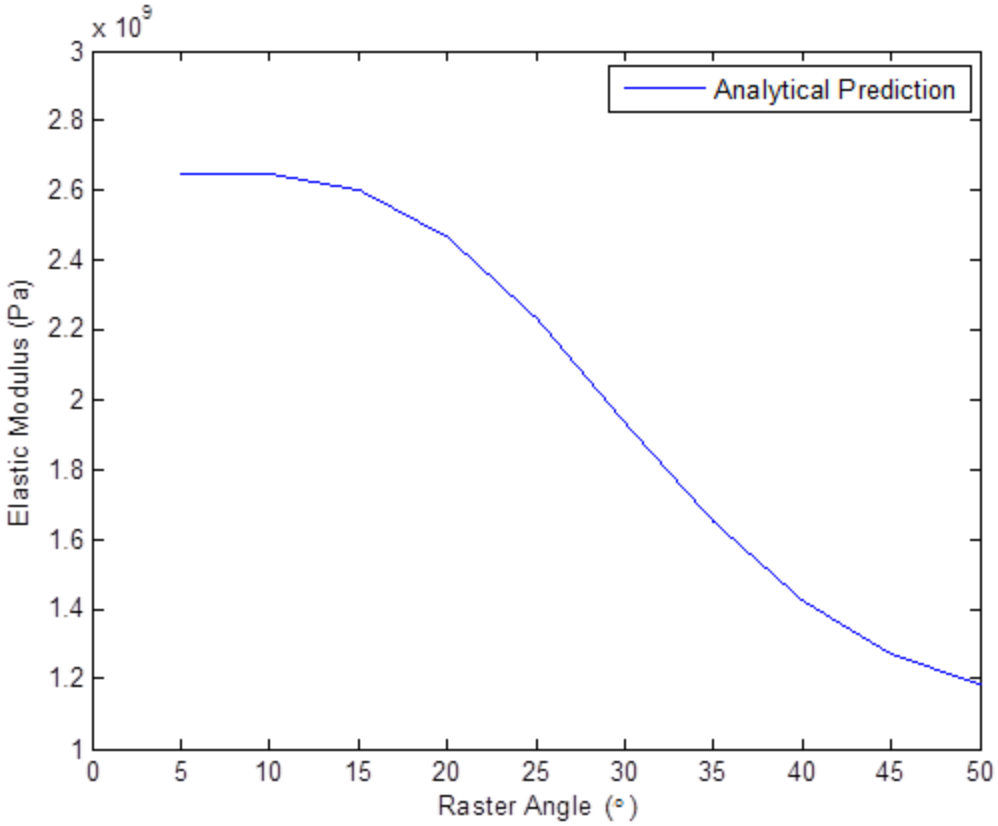

Fig. 4.24 Correlation between experimental and analytical values of normal stress

Considering that the analytical models are close to experimental results and the results from the literature, these models are now extended to understand certain related phenomena. Poisson's ratio cannot be evaluated by using the standard relationship between tensile and shear moduli, considering the anisotropic nature of the FDM material and so is evaluated using the basic definition. For the FDM parts, the transverse strain can be calculated using the relationship;

$$\epsilon_t = \epsilon_x \sin^2 \alpha + \epsilon_y \cos^2 \alpha + \gamma_{xy} \sin \alpha \cos \alpha \qquad (Eq\ 4.40)$$

Eq. 4.46 and 4.50 can be used to evaluate the Poisson's ratio according to the basic definition;

$$\nu = -\frac{\epsilon_t}{\epsilon_\alpha}$$

The variation in the Poisson's ratio as predicted by the theoretical model is presented in Fig. 4.25 for varying raster angles and coalescence rates. At relatively higher coalescence values, the Poisson's ratio remains more or less constant initially, and begins to rise from about 10˚to 20˚ and attains a peak at around 50˚ and subsequently reduces with increasing raster angles. At lower coalescence values, the trend is the other way around. With higher coalescence values, as the raster angle increases, the rotational effects creep in, resulting in the reduction of the lateral strains. However, when the raster angle is beyond the 50˚ mark, the strands begin to get aligned perpendicular to the direction of loading, and so the lateral strain becomes predominant, leading to a reduction in the Poisson's ratio. The reversal in the trend with lower coalescence values is probably due to the breaking up of the weak links between adjacent strands and their gradual alignment in the direction of the longitudinal loading. It is interesting to note that at lower coalescence values, there is a possibility to have a material structure that induces a zero Poisson's ratio as is evident with the curve corresponding to 0.2 coalescence rate.

Part rotation, also known as plastic spin, is another aspect that can be modelled based on the analytical models presented above. Part rotation considers the rotation of individual strands under the action of tensile or compressive loads and is defined as follows [133]:

$$\omega = \frac{1}{2}\left(\frac{\partial v}{\partial x} - \frac{\partial u}{\partial y}\right) \qquad (Eq\ 4.41)$$

Each strand undergoes not only tensile deformation but also rotation following the direction of the tensile load. Based on the analytical model, the variation in the plastic spin is evaluated for

varying process conditions and plotted in Fig. 4.26. In each case, the part rotation increases initially, attains a peak and further decreases as raster angle increases. The higher the coalescence, the higher is the peak value of rotation and the reason for the relatively lower values of rotation at lower coalescence is the fact that the inter-strand bonds are broken before any consolidated rotation takes place. This again proves the fact that proper meso-structure resulting from a combination of raster angle and rate of coalescence will help improve the mechanical characteristics of FDM parts under a given tensile loading.

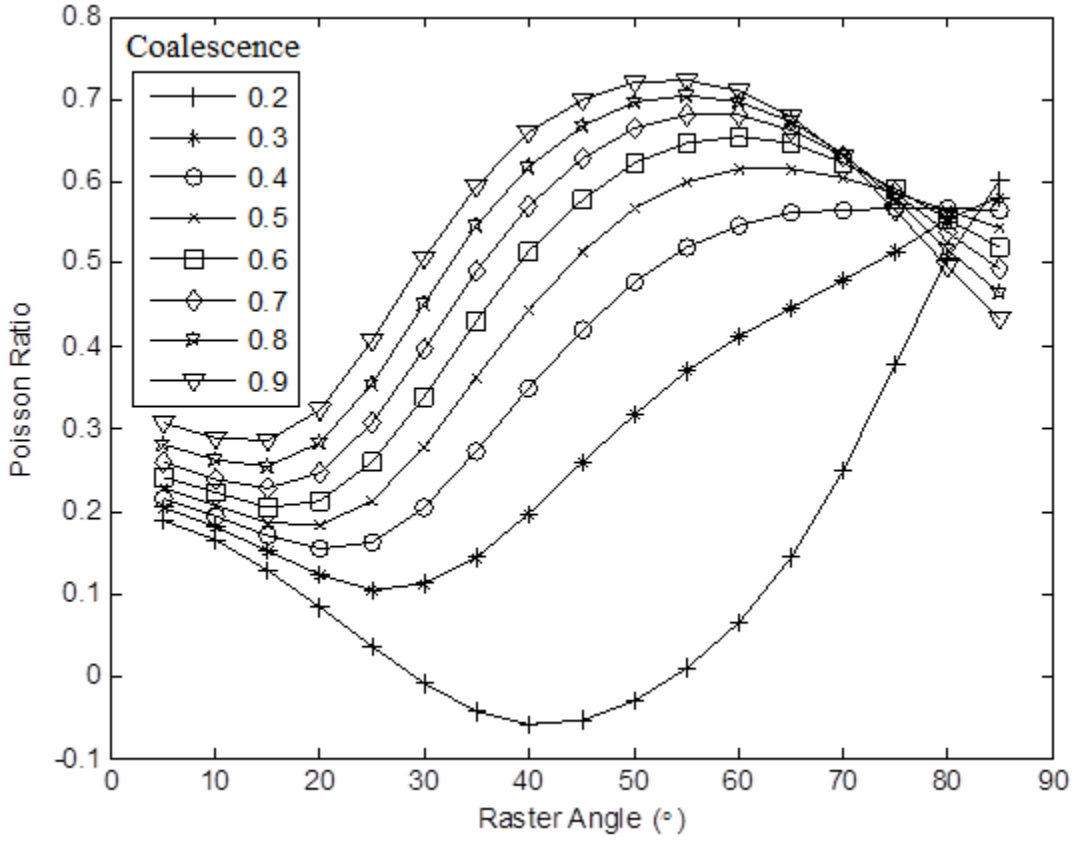

Fig. 4.25 Theoretical prediction of the variation of Poisson's ratio with varying raster angle and coalescence

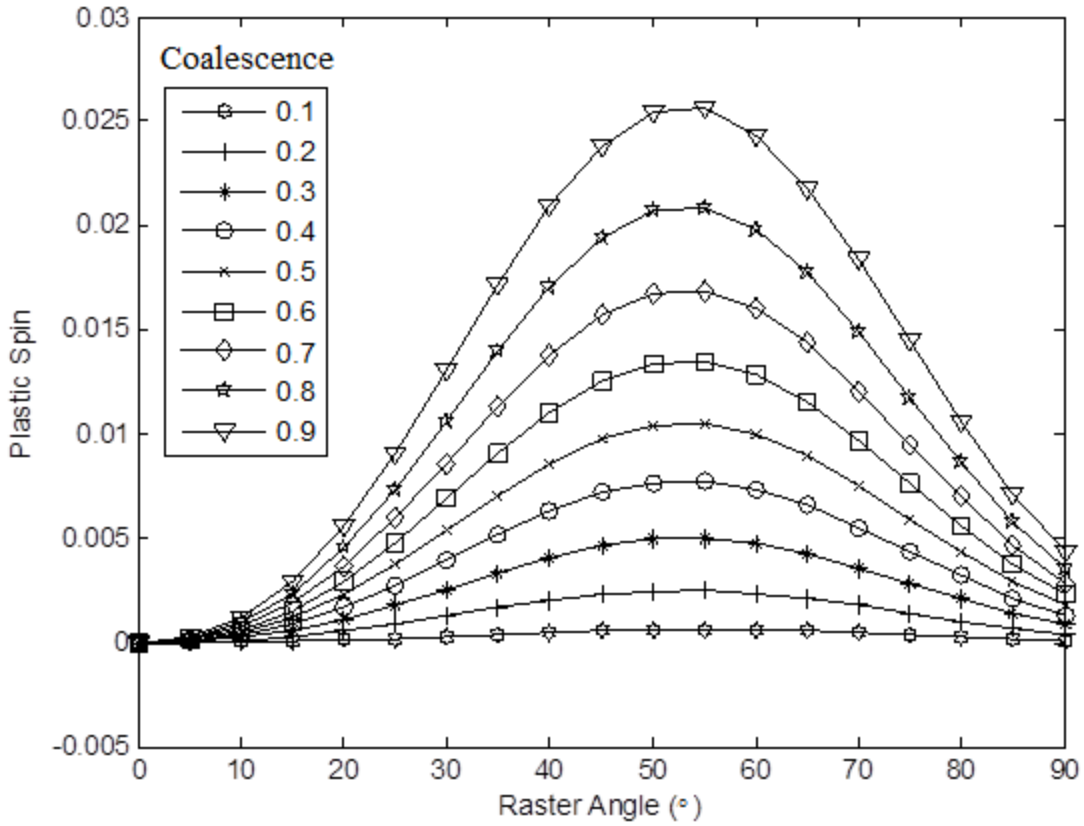

Fig. 4.26 Plastic spin versus raster angle with varying coalescence

Overall, this chapter is aimed at investigating the influence of the raster angle on the mechanical characteristics of the FDM part. The hypothesis that material constants are sensitive to varying meso-structures resulting from varying process conditions in fused deposition modelling is tested by experimental and analytical means. Tensile test results of samples built with varying raster angles showed the ultimate tensile stress gradually decreasing with increasing raster angle. Analytical models are developed for elastic stress, strain and moduli using the plane stress approach. A good correlation was observed between experimental results and analytical predictions in the case of the ultimate strength, thus validating the models. The elastic modulus

decreased with increasing raster angle and attained a minimum at around 50˚ to 60˚, depending on the magnitude of coalescence, which is also in good agreement with other results from the literature. The shear modulus remains stable at lower raster angles, but gradually decreases beyond 45˚ at varying rates depending on the magnitude of coalescence. Analytically, the Poisson's ratio is observed to vary widely with varying coalescence and raster angles and the possibility of achieving zero values is noted. The plastic spin is found to peak at around 45˚ raster angle, for different levels of coalescence.

Chapter 5 Curved Layer Slicing for FDM

5.1 Flat layer slicing; some shortcomings

Flat Layer Fused Deposition Modelling was made commercially available since the early nineties and had undergone a continuous improvement in materials and product quality. Hardware and software solutions evolved over time to be able to generate various prototype models and parts with different materials. Current slicing algorithms can handle all models of any complexity, in any orientation. However, the urge to develop improved, more effective and efficient mathematical algorithms for flat layer slicing of CAD models has been never ending, and adaptive slicing introduced in Chapter 3 is one of the significant developments.

Based on the results of the analytical and experimental investigations of Chapter 3, it is evident that adaptive slicing, while improving surface quality, could also influence the mechanical properties through variations in the internal meso-structures. Significant time savings are possible, while achieving specific mechanical attributes at the same time. However, all these advantages are geometry-specific, and are effective mainly in the case of solid parts or parts with thick solid walls. Parts with specific features such as aerodynamic shapes, or thin shell-like constructs, may not be benefiting much from adaptive slicing.

For example, a typical thin shell-type structure as shown in Fig. 5.1 is sliced with flat layers and built upwards from the bottom-most layer, in conventional FDM processing. Evidently, there is fibre discontinuity in this approach, in addition to the obvious stair-step effects. Very thin

uniform flat layers or even adaptive flat layers may resolve the stair-step effects to some extent, but the fibre discontinuity and resulting loss of mechanical strength are still at large. Further, both approaches will require considerably high processing times eventually. Apart from the relatively weak bonding across filaments and layers resulting from shorter interfaces as discussed earlier, the fibre discontinuity is likely to develop points of stress concentration and structural weakness.

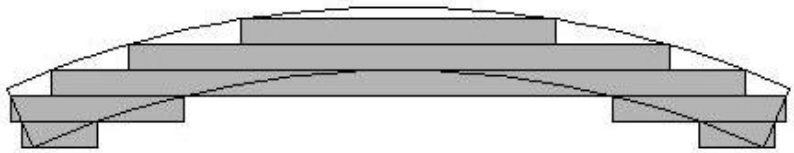

Fig.5.1 Fabricating a thin shell type part in FDM

Considering the surface quality, adaptive slicing might help minimize the stair case effects by means of reducing the user-defined cusp height and use of thinner layers. There are limitations to this approach too, and as shown in Fig. 5.2, however small the cusp height is, there is still some residual stair-step effect as the layers cannot assume infinitesimally small thicknesses, due to practical limitations. This leaves the flat layers ineffective in fully resolving the surface quality issues, even with the adaptive slicing approach.

Fig. 5.2 Fabricating a slight curved part in FDM

Proper build orientation is an alternative approach to reducing stair-case effects and as pointed out by Xu et al. [112], the ability to evaluate and determine the best build orientation is important for additive manufacturing processes to achieve a satisfactory part/prototype within the limits of the manufacturing time and cost. Due to the specific process characteristics of layer-by-layer construction, different sets of geometric features may get differently affected based on the build direction and proper part-specific print orientations are expected to improve the part quality and reduce the build time. Hu et al. [134] developed an algorithm to determine the optimal direction of a hybrid rapid-prototyping process by considering both the CNC machining process attributes and the deposition process attributes. However, the optimum build orientation approach might not be effective in all cases, and again, the thin shell type hemispherical or bi-directional curved part as shown in Fig. 5.3 will suffer from serious surface and other problems. Considering mainly the geometrical features, it appears, a completely different slicing and printing approach is needed to circumvent the inherent weaknesses of uniform or adaptive flat layers in handling the surface and structural shortcomings.

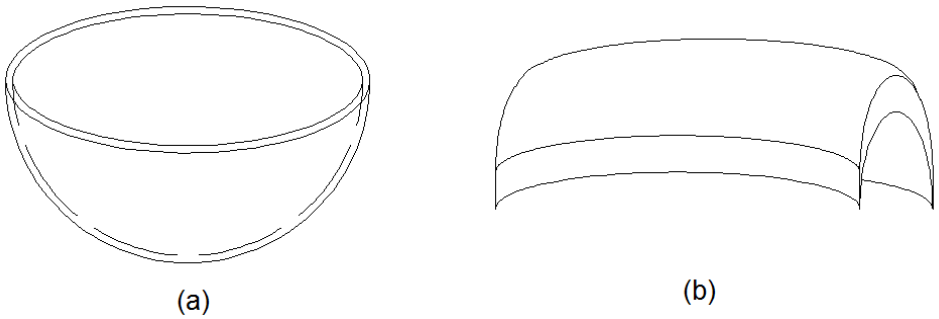

Fig. 5.3 Geometrical forms that cannot be handled even with the best-build orientation method: (a) thin shell hemispherical shape and (b) bi-directional curved part

5.2 Curved layer slicing

A closer look at the problem of losing surface and other qualities while making thin shell-type parts by flat layers indicates a plausible solution through use of curved layers following the profiles of the external surfaces. This requires the part to be sliced using curved planes. Klosterman et al. [104] observed that maintaining surface fibre continuity is critically important to thin shell-type structures and developed the first curved layer slicing approach; the Curved Layer Laminated Object Manufacturing (CLLOM) method. In addition to the technical incentives, implementing a curved layer build style also offers economic incentives in terms of saved time.

Although curved layer LOM overcomes certain limitations of the flat layer LOM, software and hardware amendments became necessary. The matched tool to support the curved layers needed to be fabricated before the LOM processing. Hence, the support tool geometry from the .stl file was to be generated. Heuristic algorithms were formulated to remove undesired features on the support structure and the height grid approach was used to approximate the actual top surface with successive curved layers. New CLLOM machine components including material sheet feeding and rotating mechanism, curved layer bonding apparatus and curved surface laser cutting were developed to fabricate the CLLOM part. All these developments demonstrated the new approach to overcome some of the inherent limitations of the flat layer LOM. However, there are limitations too, and eventually, the practical application of curved layer LOM was limited.

Nevertheless, the curved layer slicing and building a part by adding a series of curved layers one over the other seems to be a promising solution to some of the difficulties associated with FDM.

For example, to produce the thin shell-type shape shown in Fig. 5.4 (a), the conventional FDM deposits the material as shown in Fig. 5.4 (b), or by working on the side view of the product and resulting in a poor quality, due to stair-step effect and discontinuity of filaments across the section. If curved layer FDM is made possible through hardware and software developments, the same part could be built by depositing materials in a curved layer fashion, as shown in Fig. 5.4(c) for the thin shell-type shape. This will result in reduced stair-step effects, increased strength of parts and reduced number of layers, the significance of which may be readily seen in applications such as skull bone replacements.

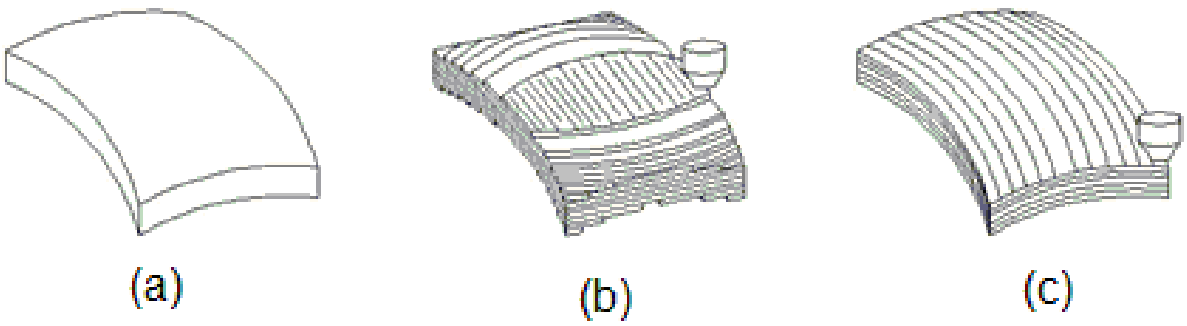

Fig. 5.4 The concept of Curved Layer deposition: (a) A curved model, (b) flat layers, and (c) Curved layers

Chakrabory et al. [105] first proposed the Curved Layer FDM or CLFDM and analytically modelled and tested the approach based on freeform surfaces. Higher strength and better surface quality were envisioned by employing long and continuous filaments or roads and obtaining curved intermediate layers of relatively larger areas. Using a parametric surface represented by $\mathbf{P}(u, v)$ the offset surface could be obtained using:

$$\mathbf{P}_{\text{off}} = \mathbf{P}(u, v) + \mathbf{n}\alpha \qquad (Eq. 5.1)$$

Where α is the surface offsetting distance and n is the unit normal vector for the surface **P** that can be calculated as:

$$\mathbf{n} = \frac{\mathbf{P}_u \times \mathbf{P}_v}{|\mathbf{P}_u \times \mathbf{P}_v|} \qquad (Eq. 5.2)$$

$\mathbf{P}_u$ and $\mathbf{P}_v$ are partial derivatives of P with respect to u and v respectively. A work coordinate system moving along each curve considered within the envelope of filament paths is used to derive the parametric equation of the surface representing the envelope. At each point on the filament curve, y_w and z_w axes are considered tangential and normal to the curve respectively and the third axis x_w is considered perpendicular to the osculating plane and following the right hand rule. Considering the parametric representation of the splined path of the filament at different locations, they represented the unit vectors $\mathbf{i}_w$, $\mathbf{j}_w$ and $\mathbf{k}_w$ along the three mutually perpendicular axes as follows [105]:

$$\mathbf{k}_w = \mathbf{n} \qquad (Eq. 5.3a)$$

$$\mathbf{j}_w = \frac{\mathbf{FLC}'(t)}{|\mathbf{FLC}(t)|} \qquad (Eq. 5.3b)$$

$$\mathbf{i}_w = \mathbf{j}_w \times \mathbf{k}_w \qquad (Eq. 5.3c)$$

FLC'(t) (filament location curve) is the first derivative of the function of filament location curve representing the gradient along the tangential direction at different points.

However, this research was mainly theoretical and had never been implemented practically. The current research takes off from this point and after a review of other existing solutions, moves to more effective algorithms for Curved Layer Slicing and the practical implementation of the same for curved layer fused deposition modelling. It involves the development of both hardware and software solutions and their integration into a working system with critical steps being the development of suitable algorithms for curved layer slicing and the practical implementation of the same for CLFDM.

5.3 Current mathematical algorithms for curved layer slicing

As already mentioned, the analytical approach to curved layer FDM by Chakraborthy et al. [105] was based on the parametric representations of free form surfaces. Apart from offsetting curved layers, deposition path patterns need to be developed, together with the implementation schemes. This involves an understanding and subsequent modelling of the 3D surface, setting data points and fitting a surface model, developing an offsetting scheme, development of offset surfaces, evaluation of curved deposition patterns and finally practical implementation on a FDM system. The author developed some preliminary solutions as part of the master's research [106] done earlier.

In all curved layer slicing algorithms, gathering the key point data from a specific top surface is the fundamental task. Chakraborthy et al. [105] used parametric surfaces for this purpose, but the method is too theoretical, and in more practical situations, parametric surfaces form only a part of the representation of a solid, and there may be other non-parametric surfaces too, like for

example, polygon surfaces. Although there are options to convert information in other formats to parametric forms, data loss may result during conversion, as it happens even between two different parametric surfaces [135], for example, as is the case with the conversion of a sphere represented by a parametric expression to a B-spline surface. Appropriate construction of the subsequent curved layers is dependent on the accuracy of data points from the initial top surface. In the author's previous research [106], the surface data was generated predominantly by both G&M (These are codes used in CNC software to represent coordinates and other spindle movements) code method and the parametric representation of surfaces based on Bezier models, in lines similar to Chakraborthy et al. [105].

A thin curved part, as shown in Fig. 5.5(a), was used as the basic shape for testing the proposed curved layer slicing algorithm, and the first step was to create a solid model. The CAD model was then transferred to the CAM module of any solid modelling software. For the given orientation of the model, the CAM software identifies the top surface and generates the G&M codes automatically for the CNC cutter paths with its own or user defined patterns. A ball cutter of size equal to the deposition nozzle diameter was used in the tool path generation, in order to replicate the motions of the deposition nozzle when run on the FDM machine. Fig. 5.5(b) shows the cutter paths developed using the G and M code data generated by the Manufacturing Module in UniGraphics for the top surface of the model.

When using different CAD software, the formats of the CAD models may vary from one to the other. Further, when they are transferred to the CAM software, the mathematical equations or descriptions might be lost. It is necessary to exercise caution while gathering the data points

from the surfaces, especially the ones required to be machined or deposited in this case. The CAD files may be stored in the IGES or other similar format, for compatibility between different platforms. The reason for using G and M codes here is to record the x, y and z coordinates of the points defining the surface topology. When the G&M codes are generated, the x, y and z coordinates of the surface points are recorded by the computer program and saved as a text file for subsequent use as the input for the slicing program. The other method using a Bezier surface and the deposition path lines generated subsequently in MATLAB are shown in Fig. 5.6.

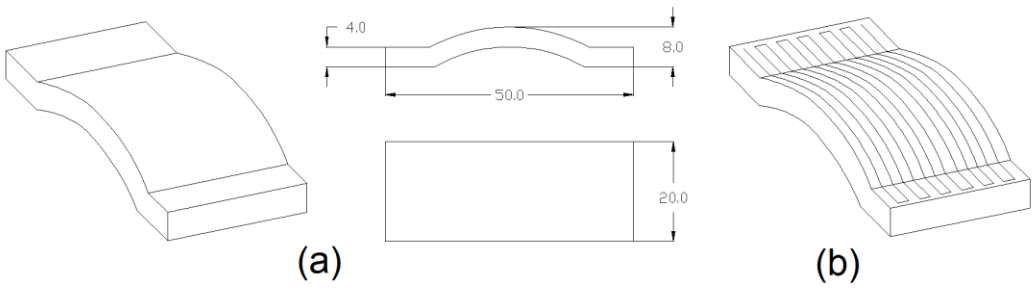

Fig.5.5 Solid model of the test part and cutter path data: (a) Solid model and (b) Top surface cutter path data

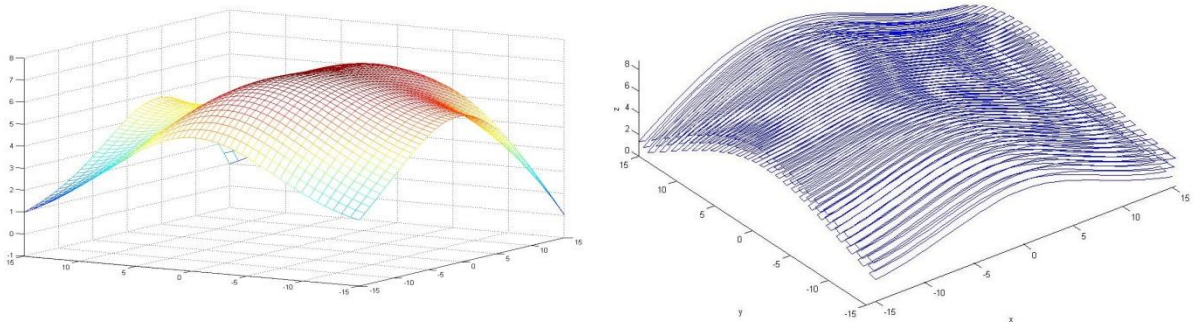

(a) Bezier surface (b) Deposition path data

Fig. 5.6 Deposition path data based on a free form surface

The cutter/deposition path data thus generated is used to develop the point cloud data representing the top surface of the part. Curved layer slicing is employed next by means of offsetting the top surface points, rather than direct slicing, using a series of planes, as is the case with flat layers. After attempting a vertical surface offsetting method and then a two-vector cross product approach, a four-vector cross product solution was found to produce good results with minimum deterioration of offset surfaces. This was further modified employing two vectors on the surface and one auxiliary vector at each surface point, to construct the cross product vectors. This approach as depicted in Fig. 5.7 was found to be computationally less intensive and very effective in capturing the local surface variations. After loading the input data into the slicing program, two vectors $\mathbf{V}_1$ and $\mathbf{V}_2$ are constructed by $\mathbf{P}_{i,j,k}$, $\mathbf{P}_{i-1,j,k}$ and $\mathbf{P}_{i,j,k}$, $\mathbf{P}_{i+1,j,k}$ respectively, whilst the auxiliary vector $\mathbf{V}_3$ is perpendicular to the vertical plane J from $\mathbf{P}_{i,j,k}$.

Two cross product vectors $\mathbf{V}_{13}$ and $\mathbf{V}_{23}$ are constructed following the right–hand rule based on vectors $\mathbf{V}_1$, $\mathbf{V}_2$, and $\mathbf{V}_3$. The magnitudes of all the cross product vectors are equal to the thickness of the curved layer. The governing equations of $\mathbf{V}_{13}$ and $\mathbf{V}_{23}$ are:

$$\mathbf{V}_{13} = \text{thickness} \cdot \frac{\mathbf{V}_1 \times \mathbf{V}_3}{|\mathbf{V}_1 \times \mathbf{V}_3|} \qquad (Eq.5.4)$$

$$\mathbf{V}_{23} = \text{thickness} \cdot \frac{\mathbf{V}_3 \times \mathbf{V}_2}{|\mathbf{V}_3 \times \mathbf{V}_2|} \qquad (Eq.5.5)$$

As shown in Fig. 5.7, $\mathbf{V}_5$ is based on $\mathbf{V}_{13}$ and $\mathbf{V}_{23}$, The equation of angle α is:

$$\alpha = \cos^{-1} \frac{\mathbf{V}_{13} \cdot \mathbf{V}_{23}}{|\mathbf{V}_{13}| \cdot |\mathbf{V}_{23}|} \qquad (Eq.5.6)$$

And the equation of $\mathbf{V}_5$ is:

$$\mathbf{V}_5 = \frac{\text{thickness}}{\cos\frac{\alpha}{2}} \cdot \frac{\mathbf{V}_{13} + \mathbf{V}_{23}}{|\boldsymbol{V}_{13} + \boldsymbol{V}_{23}|} \qquad (Eq.5.7)$$

Then, the location to which $\mathbf{V}_5$ directs is the point of the offset curved surface. Therefore, the final equation is:

$$\mathbf{P}_{i,j,k+1} = \mathbf{P}_{i,j,k} + \mathbf{V}_5 \qquad (Eq.5.8)$$

$\mathbf{P}_{i1,j,k+1}$ is the new point on the offset curved layer and the process is repeated at all points of the first surface to generate the point cloud data of the first offset layer. Further, the entire process is repeated to create as many curved layers as necessary for a given part.

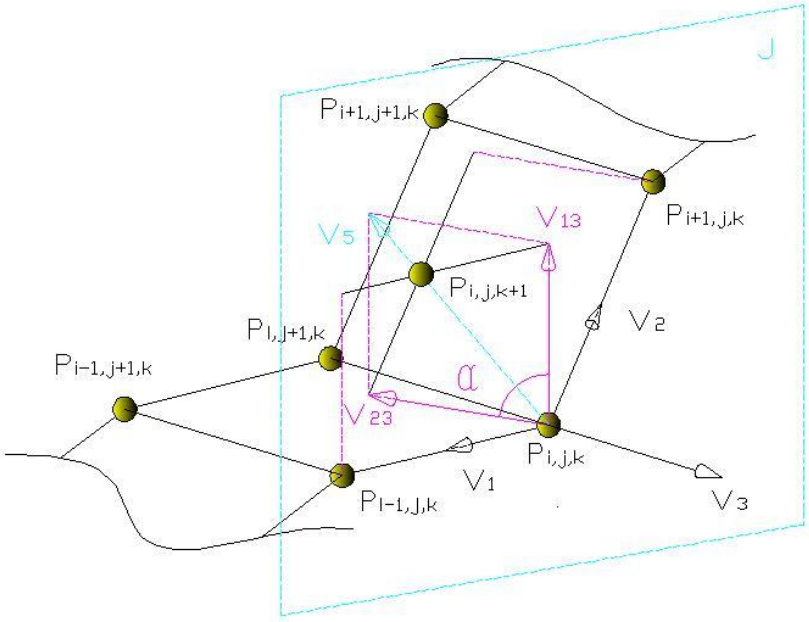

Fig. 5.7 Modified cross product method considering nodes on a vertical plane

For most curved parts, a support structure is usually needed, the shape of which depends on the art geometry. Generation of the support structure follows the geometry of the part and depends

on the nature of the overhanging features. The support structure requirement is associated with the shape of the bottom surface. Out of all triangular elements representing the bottom surface, the facets at the lowest level, at z=0 for the case as shown in Fig. 5.8 (a), need to be discarded, and the rest of the facets are grouped together as shown in Fig. 5.8 (b). The critical triangular facets identified thus are used to construct the triangulated shape of the support structure as shown in Fig. 5.9 (a). A series of flat horizontal layers at appropriate levels are then used to slice this shape into a set of flat layers which are subsequently used to generate the deposition path data as shown in Fig. 5.9 (b).

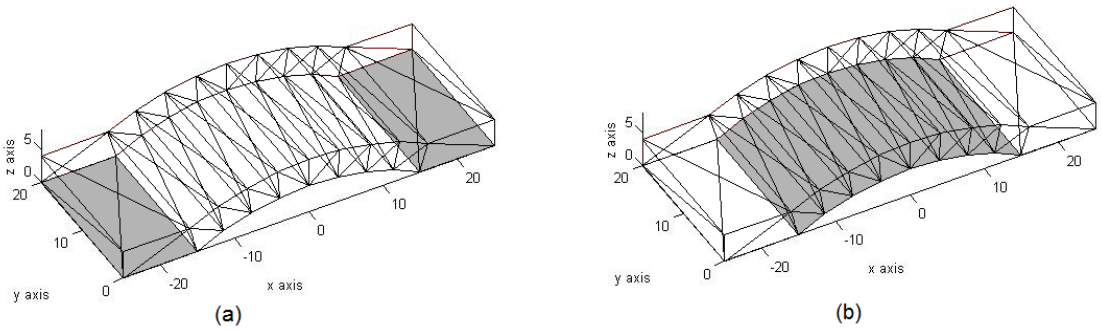

Fig. 5.8 Selection of surface facets for the support structure

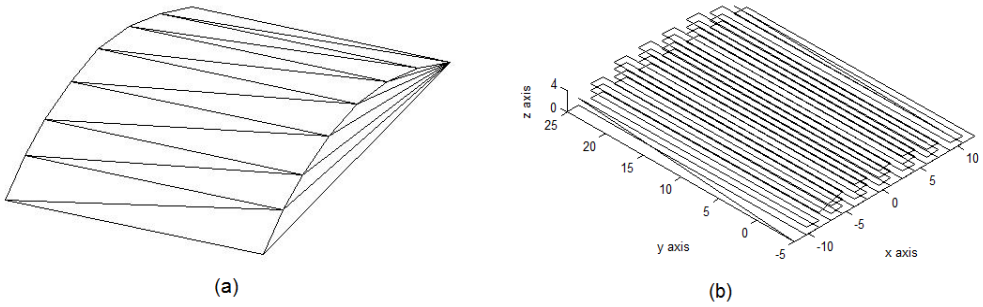

Fig. 5.9 Support structure deposition path generation

5.4 Enhanced curved layer slicing models

The modified method using three vectors and their cross products in pairs presented above works fine for curved layer slicing, but there are specific shortcomings. Self-intersection and multi-point interference are two major issues that occur mostly with concave shapes. A self-intersection elimination algorithm and a multi-point interference elimination algorithm were developed by the author earlier [106], to eliminate these defects, but the processing time usually is high, especially when the total number of points representing a given surface is large. Further, this algorithm does not allow much control over the meso-structure, as the deposition path patterns in all successive slices are replicated from the top reference surface. A more flexible and better curved layer slicing scheme needs to be developed.

In general, solid models for slicing could be in the form of CAD models or tessellated CAD models. The tessellated CAD model normally refers to the .stl format file, but more recently, the .amf format file [136] is being used, which follows the same structure as the .stl format file in geometry specification, but carries further details such as colour and materials and allows optional curved triangles to improve the surface representation. Both .stl and .amf file formats could be used as the input for curved layer slicing. However, most commercial AM systems still use the .stl format files as the input and identification of different materials is not a primary concern yet. Considering these aspects, the .stl format is employed in the current research for the curved layer algorithms, though the .amf format has advantages in terms of closely defining complex details. Based on the .stl format files, a new curved layer slicing algorithm is developed which essentially consists of three steps; (1) Collecting surface data, (2) Offsetting surface data and (3) Generating in plane disposition path ways.

Surface data collection from .stl format file

The .stl file model can be created using any available 3D software, especially 3D engineering software. As .stl format files are in binary form and it is hard to implement further operations, like gathering the point cloud data. An open source MATLAB program, written by Doron Harlev [137], is used for gathering the coordinates of the vertices of the triangular facets. The surface data obtained from this program is saved in data files in the form of four matrices containing X, Y, and Z coordinates and the colour of each facet. At this stage, though information pertaining to all surface triangles representing the solid model is identified, the data is still in the raw form and the specific triangles forming the top surface, based on a given print orientation need to be bundled together next.

After ascertaining the print orientation, the first step is to establish the top surface based on the .stl format file. In order to avoid complications, the top surface is assumed to be continuous and uniform in the current work, without any sharp variations in form. In the .stl file, each facet has its own vertices and a normal, which allows determination of the facet orientation as the angle between the normal and the z-axis. This angle, representing the orientation of the facet in the 3D space is used as the criterion to decide whether a certain facet belongs to the top surface or not. Generally, both top and bottom surfaces are horizontal in the most ideal case, while vertical facets usually form side surfaces. In the current algorithm, all facets with the normal making 0 to 30˚ with the vertical are considered belonging to the top surface and those satisfying this condition are segregated and grouped together. The facets on the bottom surface get singled out due to a change of orientation of the outward normal.

Again, it may be realised that the top surface data is very critical in curved layer slicing, including the facets, vertices and normal directions. After collecting the top-surface facet data, some further processing may become necessary as it may not always be a single continuous surface as in Fig. 5.10(a). In reality, the top surface may be split into a number of segments as shown in Fig. 5.10(b) or (c).

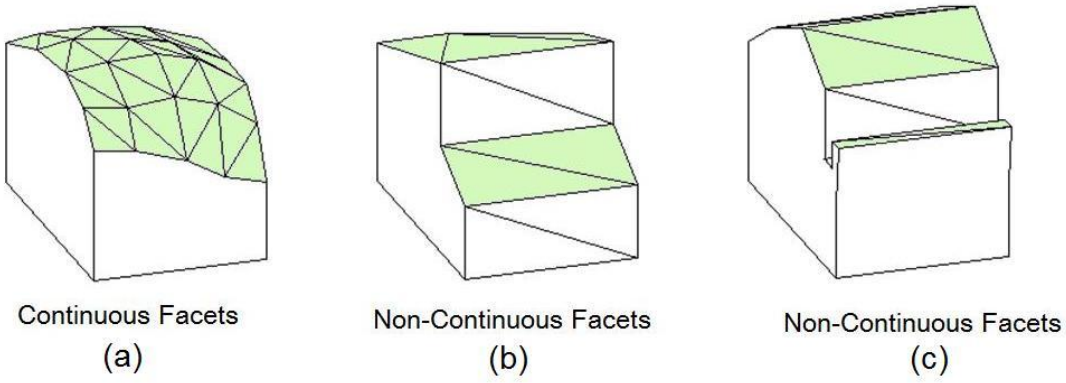

Fig. 5.10 Continuity of the top surface

The algorithms developed as part of the current research cannot handle multiple surface sets simultaneously, as it gets quite complex while deciding the curved layer slicing strategies. As a result, further to identifying the top-surface facets, a facet-grouping algorithm is used to identify the highest segment of the marked areas as the true top surface for initiating the curved layer slicing. The facet-grouping procedure is as follows:

- Identify the facets defining the top surfaces of the part for the selected orientation using the angle criterion.
- Locate the highest point of all the top surface facets and make it as the reference point.

- Identify all triangular elements of the top surface that have this highest point as one of the corners. This will result a set of triangles around the highest point as depicted in Fig. 5.11.
- Use each of the other corners of this initial set of triangles and repeat the above step to further expand the collection of top surface triangles.
- Repeat this procedure until all connected triangles are located and grouped together as shown in Fig. 5.11.
- The process can also be repeated with other segments of the top surface if any, but in this chapter, the algorithm is limited to identifying the highest top surface segment and using it for curved layer offsetting.

This algorithm is applied to the simple curved shape shown in Fig. 5.5. After triangulation and the selection of the print orientation as shown in Fig. 5.12, the shaded elements are identified as the top-surface by the algorithm implemented in MATLAB.

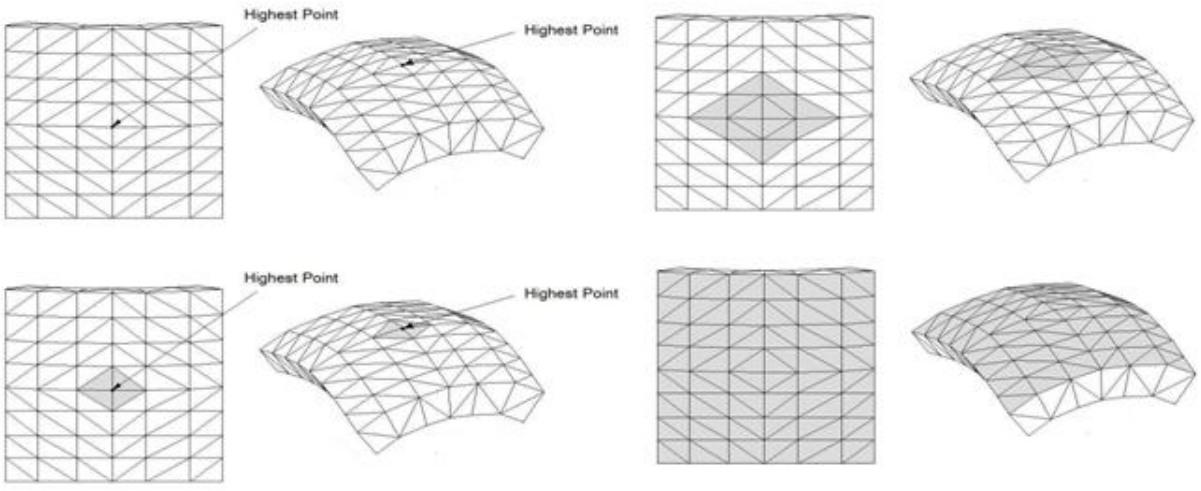

Fig. 5.11 Facet grouping procedure

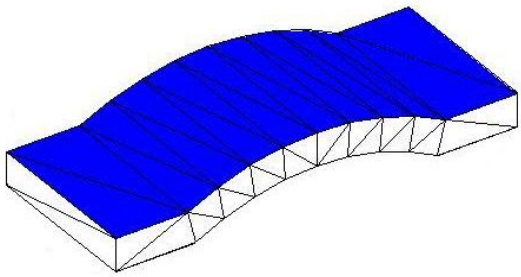

Fig. 5.12 Top facet grouping

Surface data offsetting

Chakraborthy et al. [105] attempted curved layer slicing by offsetting every point on the reference surface along the normal by an amount equal to the slice thickness. The methods developed by the author earlier also employed marching along the normal direction, but using a vector cross product scheme based on the point cloud data representing the top surface of the part. Both these approaches essentially achieve offset surfaces based on a number of points usually generated along the deposition pathways developed on the base surface. The data files used for additive manufacturing, whether in .stl or .amf format are approximate representations of the original CAD model, and often, the surface data is partially lost. Employing point cloud data generated using deposition pathways based on .stl files for offsetting often results in further deterioration in successive layers. The curved layer surface generation scheme used here is an adaptation of the method developed by Qu et al. [138], based on whole facet offsetting.

The top surface of the part selected as the original reference surface for curved layer offsetting is as shown in Fig. 5.13, and assumed to be continuous and uniform, without any sharp variations in forms. The nodal data is gathered from individual triangular facets representing the

geometrical form of the surface. The order of the nodes must follow the sequence vertices of each triangle as dictated by the .stl format, so that the normal to the facet points outwards from the reference surface.

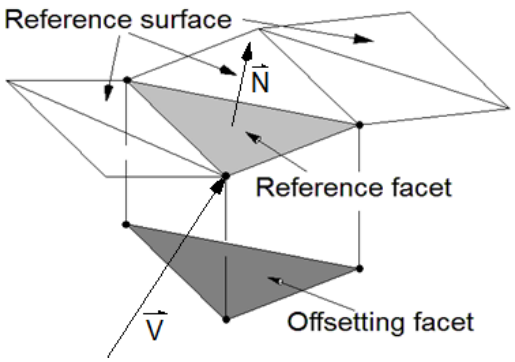

Fig. 5.13 Reference surface on the CAD file and facet offsetting for curved layer slicing

The first step in the offsetting procedure is to gather the element connectivity. This is essential as common points on adjacent elements would be displaced after each facet is offset individually along its own normal direction resulting in discontinuities in the element structure eventually. The plane-offset algorithm was developed to generate inward or outward offsets for the entire surface of a .stl model. The approach is to offset a control point on the triangular facet instead of offsetting numerous individual points along curves generated on freeform surfaces. Each facet belonging to the top surface is chosen to be the reference spatial plane which can be described as:

$$ax + by + cz + d_o = 0$$

where *a*, *b* and *c* is the normal of the facet, *x*, *y* and *z* is the points on the facet, d_0 is the intercept distance of the facet.

This equation could also be written in the vector format, as:

$$\vec{\boldsymbol{N}}_o \cdot \vec{\boldsymbol{V}}_o = -d_o \qquad (Eq.5.9)$$

where $\vec{\boldsymbol{N}}_o$ is the normal of the origin reference face, (a, b, c), $\vec{\boldsymbol{P}}_1$ is the coordinate vector of the origin reference point, (x, y, z), and d_o is the constant of the Cartesian plane equation.

The vertices of each triangular facet are then offset one after the other, using the three-plane algorithm [119]. Each vertex is represented as the unique point of intersection of three planes with different normal directions. The equations of the three planes represent the intersection point, which can then be moved to obtain the offset point. While the triangular facet constitutes the base plane, two auxiliary planes are needed to obtain the vertex point and further offset the same. Based on the location of a given facet, selection of auxiliary planes arises three possible scenarios; (1) Two imaginary vertical auxiliary planes, (2) One adjacent linked facet and an imaginary vertical auxiliary plane, or (3) Two adjacent linked facets, as shown in Fig. 5.14.

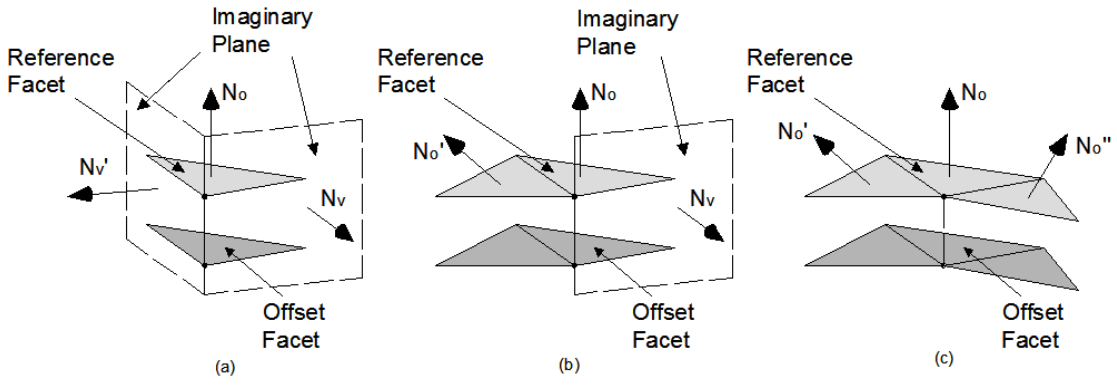

Fig. 5.14 Typical situations in the offsetting procedure; (a) Two imaginary vertical auxiliary planes, (b) One adjacent linked facet and an imaginary auxiliary vertical plane, and (c) Two adjacent linked facets

The first situation normally occurs in the case of facets having one of the vertices representing the corner of a solid. In this case, two auxiliary imaginary planes perpendicular to the reference facet plane need to be constructed. While selecting the top surface elements, the nodal connectivity of each facet is recorded, and in this case, the vertex is linked to no other elements. The first imaginary vertical auxiliary plane should be a plane parallel to the normal of the top facet and going through the vertex and one of the edges of the triangular facet as shown in Fig. 5.16. The normal of this imaginary auxiliary plane can be calculated by using the cross product of the non-overlapping edge and the facet normal. However, the direction of this imaginary auxiliary plane should be selected in such a way that the normal points outwards. Hence, the cross product of the edge and the facet normal is:

$$N_v = \frac{\vec{\boldsymbol{L}}_1 \times \vec{\boldsymbol{N}}_o}{\left|\vec{\boldsymbol{L}}_1 \times \vec{\boldsymbol{N}}_o\right|}$$

where $\vec{\boldsymbol{L}}_1$ is the vector on the edge, which is calculated as:

$$\vec{\boldsymbol{L}}_1 = \vec{\boldsymbol{P}}_2 - \vec{\boldsymbol{P}}_1$$

where $\boldsymbol{P}_2$ is the next point in the triangular facet following the counter clock wise numbering. Once the normal of the imaginary auxiliary plane is ascertained, the intercept of the imaginary auxiliary plane, d_v, is calculated as:

$$d_v = -\vec{\boldsymbol{N}}_v \cdot \vec{\boldsymbol{P}}_1$$

Then, the equation of the first imaginary auxiliary plane becomes:

$$\vec{\boldsymbol{N}}_v \cdot \vec{\boldsymbol{V}}_o = d_v \qquad (Eq.5.10)$$

Similarly, the second imaginary auxiliary plane based on the other non-overlapped edge is evaluated as:

$$\overrightarrow{\boldsymbol{N'}_v} \cdot \vec{\boldsymbol{V}}_o = d'_v \qquad (Eq.5.11)$$

Considering the offsetting distance as equal to the layer thickness, the offset facet is shifted following the direction opposite to the normal of the facet and the equation of the offset facet becomes:

$$\vec{\boldsymbol{N}}_o \cdot \vec{\boldsymbol{V}}_o = d_o - t \qquad (Eq.5.12)$$

Considering a matrix [$\boldsymbol{N}$], where $[\boldsymbol{N}] = \left[\vec{\boldsymbol{N}}_o \quad \vec{\boldsymbol{N}}_v \quad \overrightarrow{\boldsymbol{N'}_v}\right]^T$, and a vector [$\boldsymbol{D}$], where $[\boldsymbol{D}] = [d_o - t \quad d_v \quad d'_v]^T$, the equation in the matrix form is:

$$[\boldsymbol{N}][\boldsymbol{V}] = [\boldsymbol{D}] \qquad (Eq.5.13)$$

where [$\boldsymbol{V}$] is the coordinate vector and $\vec{\boldsymbol{N}}_o \cdot \vec{\boldsymbol{N}}_v = 0$, $\overrightarrow{\boldsymbol{N}}_o \cdot \overrightarrow{\boldsymbol{N'}}_v = 0$ and $\left|\vec{\boldsymbol{N}}_v - \overrightarrow{\boldsymbol{N'}}_v\right| \neq 0$. $\vec{\boldsymbol{N}}_v$, $\overrightarrow{\boldsymbol{N'}_v}$ are the normals of two imaginary planes and d_v and d'_v are constants. This makes sure that the matrix [$\boldsymbol{N}$] is full rank and can be inversed, so that the equation will have a unique root. Then the new offsetting point is:

$$[\boldsymbol{V}] = [\boldsymbol{N}]^{-1}[\boldsymbol{D}] \qquad (Eq.5.14)$$

The second situation normally occurs in facets with one of the sides representing an edge of the solid. In this case, the offsetting point is linked to two triangular facets on the top surface. During the offsetting process, these two triangular facets need to be offset at the same time and only one imaginary plane needs to be constructed. Hence, matrix [$\boldsymbol{N}$] and vector [$\boldsymbol{D}$] need to be modified

as $[\boldsymbol{N}] = \left[\overrightarrow{\boldsymbol{N}_o} \quad \overrightarrow{\boldsymbol{N'}_o} \quad \overrightarrow{\boldsymbol{N}_v}\right]^T$ and $[\boldsymbol{D}] = [d_o - t \quad d'_o - t \quad d_v]^T$, where $\overrightarrow{\boldsymbol{N'}_o}$, $\overrightarrow{\boldsymbol{N'}_v}$ d'_o and d_v are the normal of the adjacent linking facet, the normal of the imaginary vertical plane, the intercept of adjacent linking facet, and the intercept of the imaginary vertical plane respectively. Further, there is a possibility that those two facets share the same normal. In order to make matrix [$\boldsymbol{N}$] full rank, extra criteria need to be satisfied for adjacent facet selection, such as; $\overrightarrow{\boldsymbol{N}_o} \cdot \overrightarrow{\boldsymbol{N}_v} = 0, \overrightarrow{\boldsymbol{N'}_o} \cdot \overrightarrow{\boldsymbol{N}_v} = 0$ and $\left|\overrightarrow{\boldsymbol{N}_o} - \overrightarrow{\boldsymbol{N'}_o}\right| \neq 0$. If the two facets share the same normal, the offsetting procedure will be similar to the first situation.

Similarly, matrix [$\boldsymbol{N}$] and vector [$\boldsymbol{D}$] also need to be modified before fitting into Eq. 5.14 for the third situation, which occurs in the central region of the reference surface. As an imaginary plane is not necessary, matrix $[\boldsymbol{N}] = \left[\overrightarrow{\boldsymbol{N}_o} \quad \overrightarrow{\boldsymbol{N'}_o} \quad \overrightarrow{\boldsymbol{N''}_o}\right]^T$ and $[\boldsymbol{D}] = [d_o - t \quad d'_o - t \quad d''_o - t]^T$. If three facets have different normals, which means $\left|\overrightarrow{\boldsymbol{N}_o} - \overrightarrow{\boldsymbol{N'}_o}\right| \neq 0, \left|\overrightarrow{\boldsymbol{N}_o} - \overrightarrow{\boldsymbol{N'}_o}\right| \neq 0$ and $\left|\overrightarrow{\boldsymbol{N'}_o} - \overrightarrow{\boldsymbol{N''}_o}\right| \neq 0$ for the adjacent facets selected, then Eq. 5.14 can be used to calculate the offset point. If two facets share the same normal and the third one has a different normal, the offsetting procedure would search for another facet to satisfy the full rank matrix requirement. If all the facets have only two different normals, the offset procedure turns back to the second situation. Further, if all the facets have the same normal, the procedure will be the same as in the case of the first situation.

The facet-based offset procedure will be repeated with every facet on the top surface and all offset points form the new curved layer, which will become the reference surface for the next offsetting iteration. The procedure is repeated until the object is filled with the required number of curved layers as shown in Fig. 5.15, for the solid model depicted in Fig. 5.5 (a). This method

of curved layer offsetting is computationally less intensive, and works better than the other existing methods [105, 106, 138] in terms of capturing and preserving the original surface profiles.

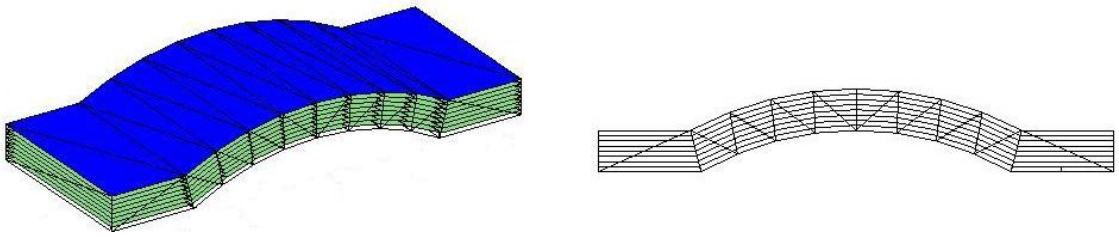

Fig. 5.15 Curved layer slicing based on facet-offsetting

Curved layer offsetting; some difficulties

To further test the abilities of the proposed algorithm, two slightly different models are processed next. The first case is the same basic shape as above, but with the side surfaces slightly slanting inwards. The actual curved layers generated using the algorithm proposed on this model are presented in Fig. 5.16. The second case is a more general form as processed and depicted in Fig. 5.17. In both cases, the top surface used as the basis for all calculations is shown shaded. While the method works reasonably well with most common arrangements of elements, there are problems such as discontinuities as shown in Fig. 5.18 resulting from specific facet configurations. Qu et al. [138] noted that discontinuities may arise if more than three normal directions exist at a given vertex, based on the local facet structure.

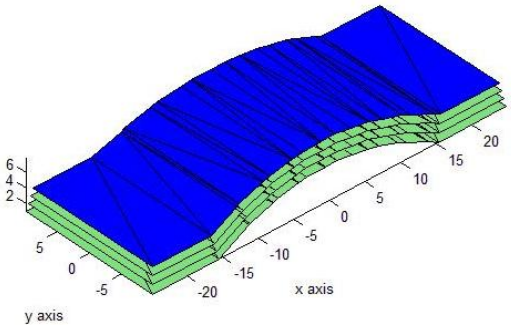

Fig. 5.16 Curved slicing of the model with slanted side surfaces

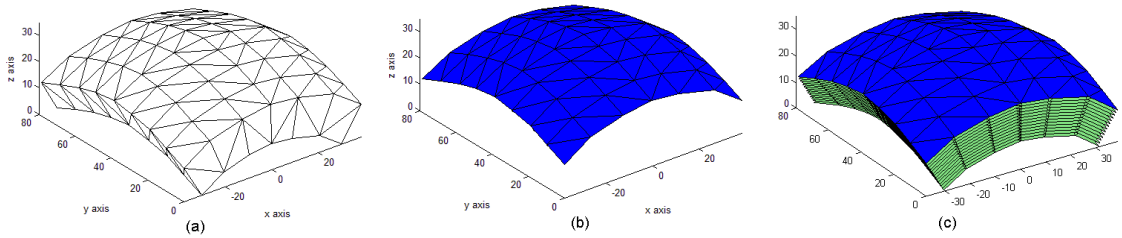

Fig. 5.17 Curved layer offsetting based on the top reference surface

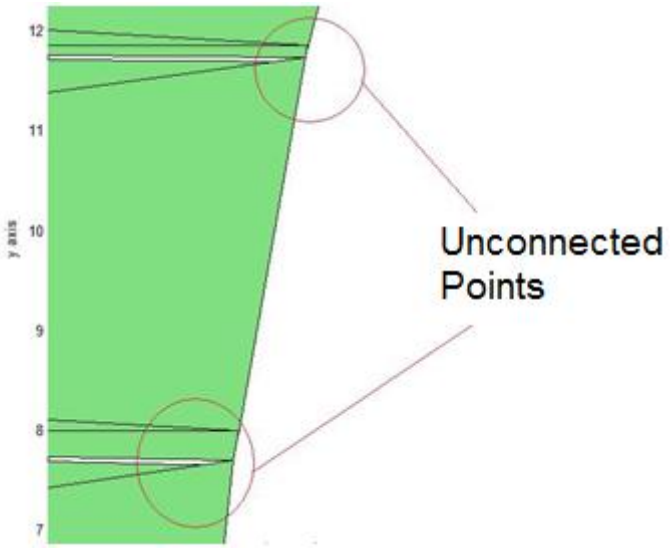

Fig. 5.18 Unconnected points after offsetting

Analytically, unconnected points arise as follows:

For instance, a point X_1 can be represented by two matrix equations:

$$A_1 X_1 = D_1$$

$$A_2 X_1 = D_2$$

After offsetting,

$$D_1^{'} = D_1 + C$$

$$D_2^{'} = D_2 + C$$

Where C is (t, 0, 0) T,

$$A_1 X_1^{'} = D_1^{'}$$

$$A_2 X_2^{'} = D_2^{'}$$

$$X_1^{'} = A_1^{-1} D_1^{'} = A_1^{-1}(D_1 + C) = X_1 + A_1^{-1} C$$

$$X_2^{'} = A_2^{-1} D_2^{'} = A_2^{-1}(D_2 + C) = X_1 + A_2^{-1} C$$

If A1 equals A2, the offset points will connect together; otherwise, the point gets offset into multiple points. The point approximation method suggested by Qu et al. [138] is slightly modified and employed here to resolve the problems with multiple offset points. Considering the three-plane method used for curved layer slicing, any three facets could have different offset points from the same vertex. The approximation method uses the arithmetic mean to replace the individual points if the differences among these are not very large. But if the differences are

large, one or more new facets are constructed with these points on the offset layer. For the curved layers generated currently, the differences among offset points are not large as the original surface is relatively smooth; hence mean locations are evaluated to merge multiple points.

Deposition path generation

Unlike the deposition path profiles in fixed directions as used by Chkraborthy et al. [105] and the author in the previous work [106], additional freedom is allowed to vary the raster orientations in the current work. The raster angle could be defined by the user or automatically generated to be crisscross in successive layers, in order to minimize the isotropic properties of the FDM components, similar to the flat layer FDM. After all coordinates of the vertices are located and saved in matrices, points on each layer are connected in proper sequences to develop triangulated surfaces. Then selected vertical planes are used to slice the surfaces in the .stl format, as shown in Fig. 5.19, where a simple wedge shape is used to demonstrate the method.

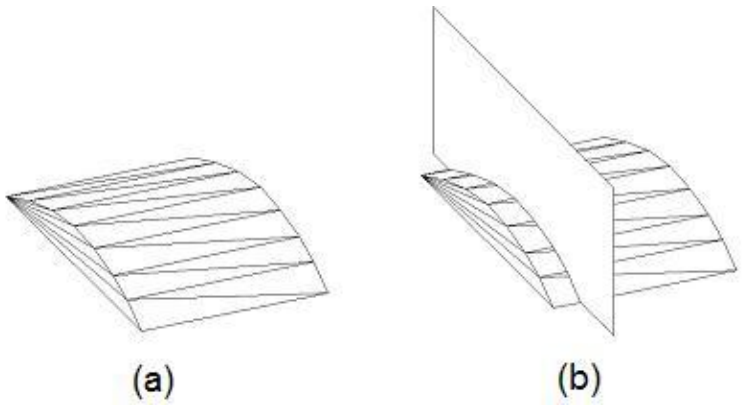

Fig. 5.19 Deposition path generation; (a) a standard .stl file and (b) slicing a triangulated object

In order to provide the flexibility to alter the raster orientations, deposition path generation begins with a vertical slicing plane making a specified angle with the x-z plane considered at the leftmost (or the rightmost) point on the .stl file. Then this plane is offset to generate a number of parallel vertical slicing planes up to the point of the other extreme, generating the intersection points with each plane. However, with each slicing plane, only a set of the triangular facets are intersected. The distances between the vertical slicing plane and the vertices of each triangular facet are used as the criteria to judge which triangular planes are getting intersected by a given vertical slicing plane. The equation of the distance between the slicing plane and a vertex is:

$$D = \frac{ax_0 + by_0 + cz_0 + d}{\sqrt{a^2 + b^2 + c^2}} \qquad (Eq. 5.15)$$

Three such distances D_1, D_2 and D_3 will be generated with the three vertices of a given triangular facet. If all of them are either greater than zero or less than zero, then the triangular facet is not intersected by the slicing plane under consideration. Otherwise, there exist a couple of intersection points that can be established. This procedure will eliminate evaluation of non-existent intersection points and improves the slicing efficiency. Eq. 5.16 also helps determine start and end points of slicing as follows:

$$\begin{aligned} P_{start} &= \min_{\mathrm{i}}\{D_{1i}, D_{2i}, D_{3i}\} \\ P_{end} &= \max_{\mathrm{i}}\{D_{1i}, D_{2i}, D_{3i}\} \end{aligned} \qquad (Eq. 5.16)$$

The parallel vertical planes cut the facets on the curved surfaces and allow construction of intersection lines. The intersection lines from each curved layer are then linked together in a proper sequence to form the deposition path ways within layers. This process is repeated with all other curved layers, but the raster angle can be changed as desired from one plane to the other.

The algorithm is coded in MATLAB and deposition path data from successive layers is appropriately connected at the end and stored in a text file in reverse order, to facilitate printing on a FDM system from the bottom upwards. Fig. 5.20 shows the tessellated model of the simple solid used throughout this work, curved layer slices developed and deposition path lines generated with a 45˚ raster angle.

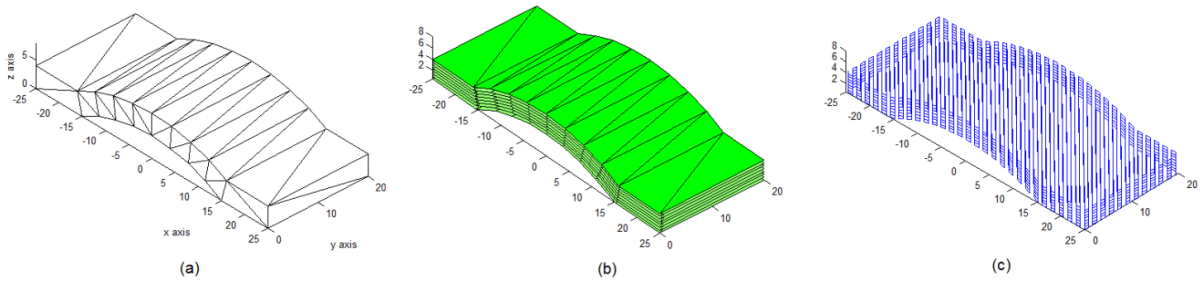

Fig. 5.20 An example of how the .stl file is sliced and tool path generated for CLFDM; (a) .stl Model, (b) Curved layer slicing, and (c) deposition path generation

5.5 Implementation and experimental evaluation of CLFDM

Test beds of varying capabilities are usually developed by researchers to test modified approaches in RP, and the Fab@Home FDM machine developed by Evan Malone of Cornell University [139] was first employed in the author's previous research for the initial testing of the mathematical algorithms developed for CLFDM. This has a standard syringe type deposition tool which consists of a disposable syringe. This system is initially tried for the physical implementation of the curved layer models developed here and the output from the MATLAB code is a text file that contains deposition path data to control the machine for printing various models in curved layers.

For initial trials and proof of concept, SILAFLEX RTV Silicone is employed as the fused material. Text files containing support structure data as well as the curved layer data are loaded on the printer one after the other for printing test pieces. It is evident that the parts, though following the required deposition pattern as per the outcomes of the CLFDM scheme, suffer from defects due to either the absence of a certain strand or the overriding of the nozzle due to the inherent difficulties with the test facility. Next, FabEpoxy [140], a special 2 part epoxy formulated for Fab@Home by Kraftmark Company of Spring City, PA, USA is tried for testing the mechanical characteristics of parts produced. It was much easier to work with Fabepoxy, as it had better extrusion as well as post extrusion characteristics. This may be evident in the simple curved object printed using both flat and curved layers as shown in Fig. 5.21(a) and (b), respectively. For the initial examination for comparing the mechanical properties between flat layer and curved layer, a three point bending test conducted with the specimens loaded as shown in Fig. 5.22 revealed that the curved layer part fails at 152 N, as against the maximum load of 70 N supported by the flat layered part.

Fig. 5.21 Parts printed using Fabepoxy: (a) Flat layers and (b) Curved layers

The curved part remained mostly intact until failure in the end, which was a sudden fracture from the bottom upwards, almost at the middle of the length of the part. The continuous fibres fused together very well, reducing the gap structure, and the cured polymer seemed to have formed a well integrated molecular structure across the filaments as well as layers. The flat layered part on the other hand, gradually gave in at almost half the load, due to a shear slip across the layers. Failure seemed to have initiated at the junction of the curved and flat portions of the part, where there was a possible stress concentration, and finally the weak interlayer bonds gave away for a shear failure, allowing successive flat layers to slide against one another.

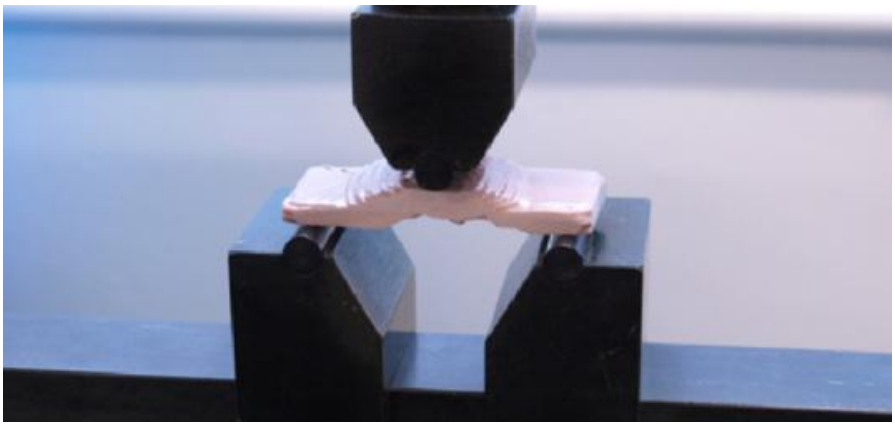

Fig. 5.22 Test part loaded for 3-point bending test.

The Makerbot kit [127] introduced in chapter 3 is employed next for a more significant testing of the influence of employing curved layers for thin shell-type parts. The actual printing was implemented in a semi-automatic way considering that the extrusion speed has difficulties to match with the print speed. These difficulties developed from both the thermal history of the

process and the mechanical limitations of the 2.5D printing as against the 3D printing essential in this case.

Like any commercial FDM machines, the Makerbot kit also provides effective control over the X- and Y-motions, and so, the extrusion speed is set to match the print speed on x and y axes. The system considers the motion along the Z-direction as auxiliary and independent of the other two axes. While this works reasonably well with flat layer FDM, problems arise with curved layer FDM, as all three axes need to be synchronised to some degree. This might lead to a slowing down of the motion along X- and Y- axes in order to be synchronised with the Z-motion. However, the extrusion speed which is dependent on the heating element will be difficult to control. Some other researchers assumed a seamless variation of the extrusion speed as is the case with any other process parameters, but in reality, the extrusion speed has a fixed relationship to the heating element. If the extrusion speed is too high, the filament might not be able to heat the polymer sufficiently and the partly fused polymer might block the nozzle. On the other hand, a too slow extrusion speed might result in overheating and excessive plasticity. If the extrusion speed is too low, the filament might be over heated. Hence, the test could only be conducted in a semi-automatic way.

Generating the support structure in the Makerbot machine raises yet another difficulty. Support structures are needed based on the shape of the solid model, and in the current case, with the thin shell type part, the central arch shape requires bottom support to be built initially. Normal FDM machines build the support structure with a different material that can be easily dissolved and removed further to printing. With Makerbot, as there is a single deposition head, it is not

possible to achieve this. Instead, the current support structure is built controlling the temperature of the extrusion nozzle at 220˚C and the heated platform at around 100˚C. This allows a relatively coarse support structure that can be easily removed later. Further, a base raft is also introduced to avoid incorrect dimensions due to the uneven build platform. In order to get the maximum mechanical properties for the test pieces, a 0˚ raster angle is employed, so that the deposition paths are aligned along the longitudinal axis. The final deposition path patterns of the FDM part together with the support structure and the raft are shown in Fig. 5.23 and the actual part printed on the Makerbot machine with a nozzle of diameter 1mm is shown in Fig. 5.24.

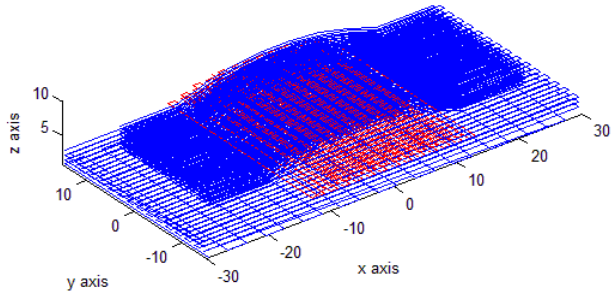

Fig. 5.23 Combined tool path of FDM part, support structure and raft

Fig. 5.24 The test piece printed by curved layer FDM on the Makerbot system

The actual test consists of printing four samples each of the same basic shape as earlier, using both flat and curved layer FDM. The flat and curved parts printed are shown in Fig. 5.25(a) and (b), respectively, and the surface quality is distinctly better in CLFDM. A view of the back side of the CLFDM part as shown in Fig. 5.25(c) clearly shows the continuous filaments stacked parallel to one another. Fig. 5.26(a) and (b) present scanned copies of the load-deflection diagrams obtained from the 3-point bending tests performed on the two sets of samples together with photographs of deformed samples. The experimental data in terms of the maximum compressive load in each case is compiled in Table 5.1 for a statistical evaluation of the comparative performance of flat and curved layer FDM. The average compressive load in the case of flat layered components falls short by almost about 100 N compared to the curved layer parts, clearly indicating a much better mechanical performance by CLFDM. The standard deviation in both cases is relatively small and very close, indicating consistency and the experimental error with a 95% confidence level is approximately ±11 N.

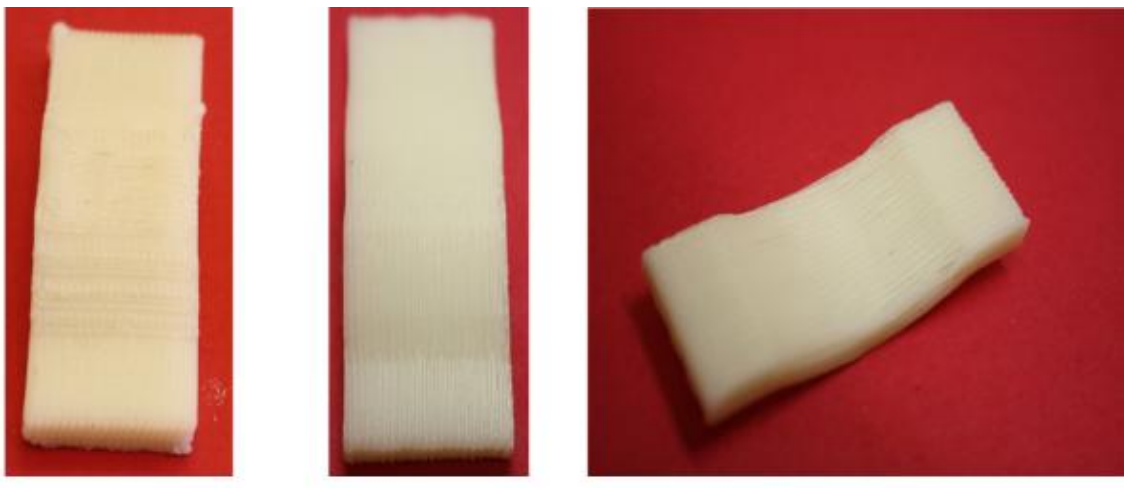

Fig. 5.25 Flat and curved parts printed using ABS polymer; (a) Flat layer part, (b) Curved layer part, and (c) continuous filaments in CLFDM

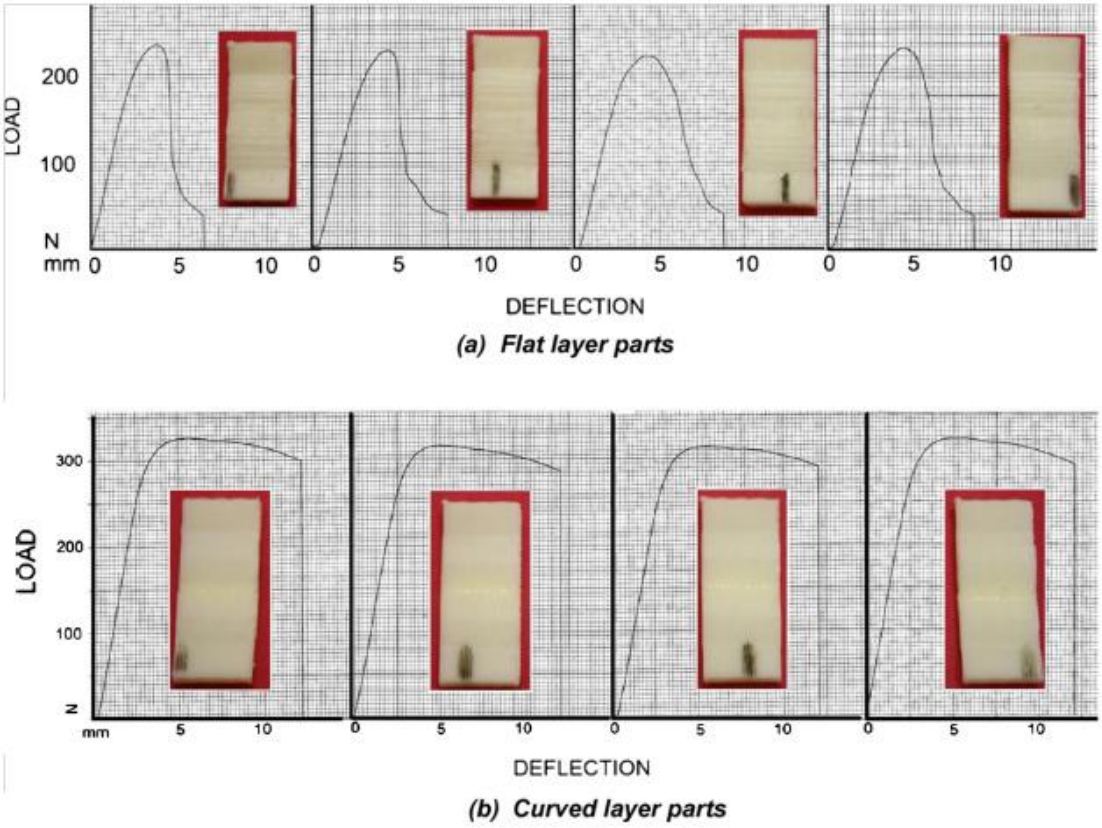

Fig. 5.26 Load deflection diagrams from tensile tests: (a) Flat layer parts and (b) Curved layer parts

Table 5.1 Results of three-point bending tests for different deposition strategies

Build style	**Maximum compressive Load (N)**					
	Part 1	Part 2	Part 3	Part 4	Average	Standard deviation
Flat layer	220.000	233.666	227.000	228.333	227.250	5.63
Curved layer	326.666	316.666	314.000	322.666	319.999	5.73

5.6 Role of Curved Layer Slicing and significant observations

Fig. 5.27 (a) and (b) shows the bottom surfaces of the compressed flat and curved layer specimens respectively close to the deformation and fracture zones. It is evident that all the flat layer parts are severely stressed and cracked almost uniformly at the central zones of the bottom layers, while the curved parts seem to have only undergone some stretching and local distortion, with the continuous filament structure still intact. A closer look at the critical zones of deformation in both cases as shown in Fig. 5.28(a) and (b) reveals initiation of cracks at the bottom most layers and subsequent growth across the width in the case of the flat layered components. Possible reason for this could be the stress concentration on the ill formed filament structure leading to a snapping of individual strands and subsequent gross failure due to the propagation of the shearing action across layers. The same action on the curved parts could only result in a localised distortion as a number of parallel filaments, sufficiently fused into one another act together to resist deformation, crack formation, and growth.

Further evidence of the differences in the two fracture modes is obtained through SEM photographs as shown in Fig. 5.28. In the case of flat layer samples, as obvious from Fig. 5.28 (a), individual strands opposite to the point of application of the compressive load are fractured at multiple locations, disrupting the filament continuity as well as the general strand structure. Contrary to this, the curved layer sample shows a continuous strand structure, which is still intact even after the part is stretched beyond the normal elastic limits. In the case of the flat layers, certain strands are loaded beyond the maximum limits probably due to an unfavourable meso-structure leading to an uneven distribution of the internal stresses. There is also evidence of the

inter-road bonds being disrupted in the fracture zones. In the curved layer sample, the strands being continuous and sufficiently coalesced across roads and adjacent layers, resulted in a better internal meso structure and a more uniform distribution on the internal stresses. The overall material characteristics are superior and also the stress concentration points are avoided.

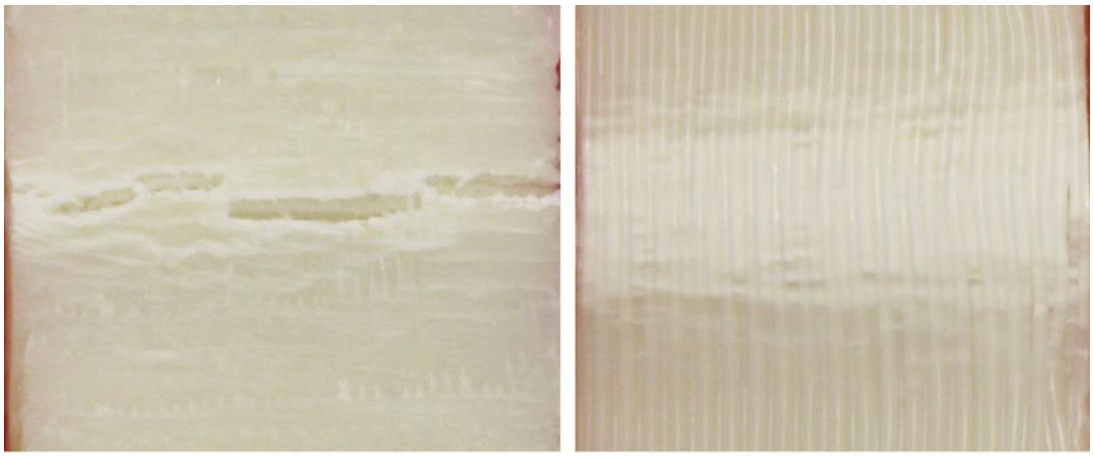

Fig. 5.27 Close-up views of deformation patterns: (a) Flat layer FDM and (b) Curved layer FDM

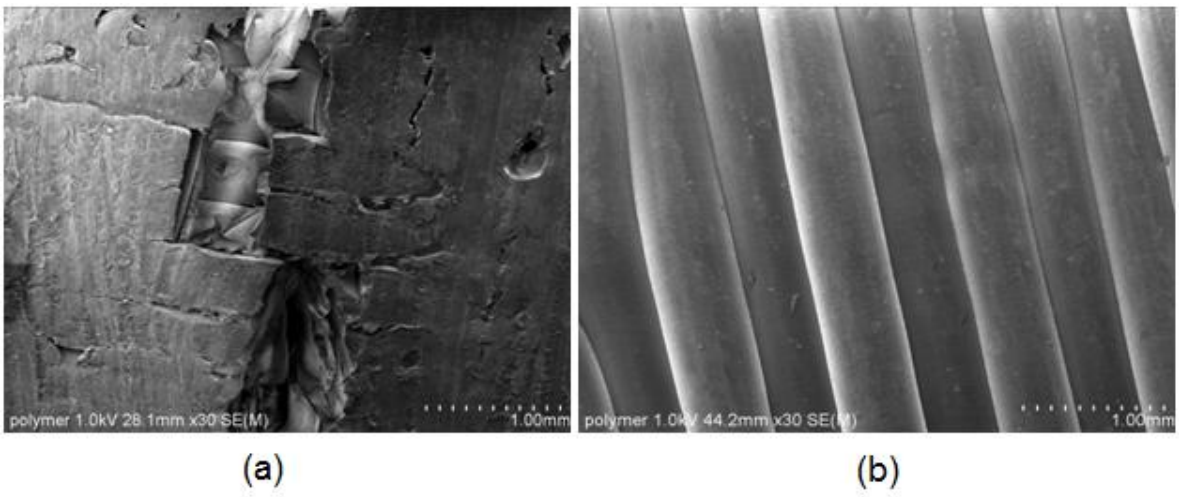

Fig. 5.28 SEM photos of factures: (a) Flat layer FDM and (b) Curved layer FDM

To conclude, curved layer FDM is envisioned to be a promising solution to overcome the stair-step and fibre-discontinuity problems in the case of thin shell-type parts. The existing curved layer slicing models are reviewed; an enhanced algorithm is developed and successfully implemented. Curved layer FDM is successfully implemented and physical parts are generated using both Fabepoxy and ABS polymer. Curved layer specimens exhibited better surface qualities as well as mesostructures resulting from long continuous fibres with improved inter-road and inter-layer coalescence.

Experimental results also indicate better mechanical performance by parts produced using curved layer FDM. The average fracture compressive load of curved layer parts under three point bending was raised almost by 40%, compared to that of the flat layer counter parts. While this could be attributed to the improved meso-structure, fracture zones clearly indicated greater structural integrity due to continuous fibres resulting from CLFDM. Overall, the work done as part of the research presented in this chapter allowed to develop improved curved layer slicing algorithms, better implementation schemes and a comparative evaluation of flat and curved layer slicing by experimental means. The results clearly indicate curved layer FDM to be better for thin shell-type parts. However, there are other opportunities to further enhance these benefits, either by combining the adaptive slicing discussed earlier and curved layer slicing to build adaptive curved layers or by mixing both flat and curved layer slicing together to process different regions of a given part differently, as will be elaborated in the next chapter.

Chapter 6 Integrated alternative slicing and deposition strategies for FDM

6.1 Alternative slicing and deposition strategies; a retrospective

The literature review of Chapter 2 envisioned the deposition strategies and styles and the overall sintering environment to critically influence the eventual mechanics of material consolidation in FDM. Varying raster orientations, adaptive and curved layer slicing are significant approaches attempted often to control the deposition parameters by alternative means. Adaptive layer deposition and the ensuing interactions with time and speed of printing are evaluated in Chapter 3. The role of varying raster angles in influencing the mechanical behaviour of FDM parts is experimentally and analytically evaluated in Chapter 4. Curved layer slicing algorithms and experimental evaluation of the true significance of curved layer deposition in specific cases are presented in Chapter 5. Each of these approaches is proved to be significant in its own way in influencing the mechanics of material consolidation in FDM. However, it is interesting to evaluate how they work together in different combinations.

The effective consolidation of the material in FDM is predominantly governed by the inter-strand and inter-layer sintering induced by the molecular migration. Sintering is in turn a time and temperature dependent phenomenon. Temperature control is a more complex aspect in FDM and a controlled variation is rather more difficult to achieve and is not attempted in the current research. All aspects investigated in Chapters 3 to 5 consider a constant sintering temperature

and in the experimental work, this is achieved by the use of a hot plate printing base and through a proper control of the temperature of the extruded filament. However, the sintering time is an integral aspect of all alternative FDM approaches attempted and cannot be assumed to be fixed and will also interact with the speed of printing. These aspects are effectively evaluated through the analytical models of Chapter 3 in the context of varying layer thickness and Chapter 4 considered the same with raster orientations. While the eventual sintering conditions, consequent material structures and resulting properties can be controlled through properly adjusting the print speeds in the case of printing with varying layer thicknesses, optimum raster angles could be identified for each printed layer based on the observations from Chapter 4.

The curved layer slicing and printing approach evaluated in Chapter 5 proved to be effective in improving the surface quality and also increasing the part strength in thin-shell type structures as a result of the fibre continuity. Experimental evidence clearly indicated curved layer samples to perform better under mechanical loading and the fracture modes demonstrated the marked improvement in the material behaviour resulting from the fibre continuity and the elimination of points of stress concentration.

Thus, all aspects investigated individually point to the effective control of the material deposition system and ensuing time dependent coalescence as possible means of achieving better part quality in FDM. At the same time, for a given part, it is also readily evident that it may be necessary to combine two or more of these in different regions in order to achieve the best material consolidation. For example, a part with a light-curved surface at the top and a solid base is best printed with curved layers up to some depth at the top and then the rest with uniform flat

layers. Further, if the same part has some intricate details in the bottom solid part, then adaptive flat layer slicing may become necessary. The same is also true if the top curved part has intricate details, as it may better be processed employing adaptive curved layer slices. All these aspects require sufficient attention in terms of developing specific algorithms, integration of individual solutions into an overall scheme and evaluation of the mixed mode approaches in specific case studies. This chapter focuses on these issues, but first, some further attention is paid to the evaluation and practical implementation of an adaptive slicing scheme, as this aspect was not done in Chapter 3.

6.2 Adaptive flat layer FDM; a practical implementation

Although coalescence effects are mentioned in the previous chapters and flat layer adaptive slicing (FLAS) was studied by other researchers, practical application was limited and as a result, most solutions tend to be too theoretical, and often suffer from specific shortcomings. Generally, cusp height shown in Fig. 6.1 (a) is the most significant criterion used in conjunction with the surface roughness requirements to judge the suitable thickness of a layer in adaptive slicing. The region with high slope or small radius of curvature will be less affected from cusp height problems, while the region with slight slope or large radius of curvature will suffer more, and in turn, will have more obvious stair-step effects. Further problems arising out of slice thickness include missing finer details on surfaces perpendicular to the direction of slicing as shown in Fig. 6.1(b) and negative and positive errors developed as shown in Figure 6.1(c). The offsetting distance is based on the thickness of the layer and not directly related to the features or details on the surface of the CAD file. Further, a slight difference in the angle with a slice of a

given thickness also leads to loss of geometrical features as shown in Figure 6.1(d). All these aspects are likely to adversely affect the surface quality of FDM parts and adaptive slicing evolved as a possible means of resolving some of these issues.

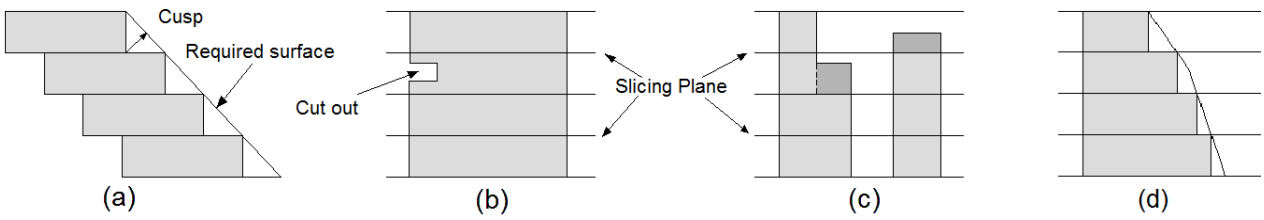

Fig. 6.1 Issues arising out of uniform flat layers; (a) cusp height, (b) missing features, (c) negative error (Left) and positive error (Right), and (d) missing surface profile

Adaptive slicing algorithms need to be sufficiently robust to cover all the issues mentioned above. The algorithm proposed by Dolenc and Makela [115] uses the cusp height to develop adaptive layers using the equation:

$$\beta = \cos^{-1}\left(\frac{h_c}{t}\right) \qquad (eq.6.1)$$

where β is the included angle between the surface facet and the horizontal slicing plane, h_c is the cusp height, and t is the layer thickness as shown in Fig. 6.2.

The main problem with this approach is that it assumes a continuous variation of layer thickness, as generated by the mathematical algorithm. In actual practice, there can only be a few layer thickness options available, based on the FDM system used. The .stl or .amf files are already approximations of the original CAD model, involving data loss during the conversion of the

format. More data losses are likely to occur, with further format conversions, deteriorating the internal or external details of the component. A feature detection model also needs to be incorporated. The algorithm proposed by Dolenc and Makela [115] is revisited here considering all these aspects and is practically implemented in specific cases as follows. Four specific layer thicknesses, 0.1 mm, 0.2 mm, 0.5 mm and 1.0 mm, are used covering all necessary thicknesses from the lower limits as per the specifications of one of the commercial FDM systems, Stratasys Fortus 360mc [141], while the upper limit is based on the available extrusion nozzle of the Makerbot Machine.

In this case, the cusp height is a user-specified parameter and it must be within the tolerance limits of either the surface roughness or a part dimension, depending on the requirements. Substituting pre-set thicknesses into Eq. 6.1, the ranges of included angles can be calculated for given values of cusp heights. With these considerations and for a given cusp height of 0.1 mm, when the above algorithm is implemented for the form with varying surface angles as shown in Figure 6.3, layers of varying thicknesses as shown will result, while the angle and layer thickness values vary as shown in Table 6.1.

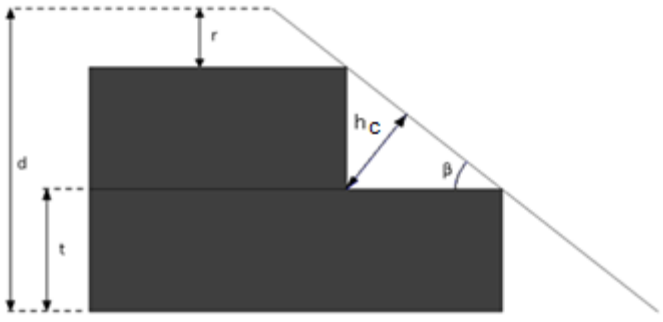

Fig.6.2 Layer thickness and cusp height geometry

Table 6.1 layer thicknesses and ranges of angles

Included angle range	Layer thickness
[0˚, 65˚)	0.1mm
[65˚, 79˚)	0.2mm
[79˚, 85˚)	0.5mm
[85˚, 90˚]	1.0mm

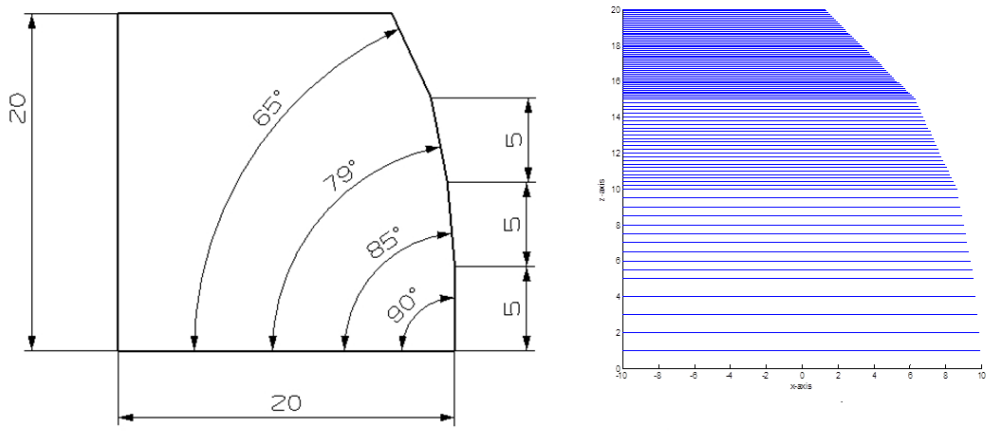

Fig. 6.3 Adaptive slicing based on the cusp height criterion

This adaptive slicing procedure based on the cusp height can handle most situations, but fails in handling minor variations in shapes, such as the ones shown in Fig. 6.1(b), (c) and (d). A further modification involving the consideration of the residual height after creating every slice is proposed and implemented here to overcome these shortcomings. The tessellated format file describes the geometrical features by triangles. The boundaries of triangular facets cover all the small features. The slicing process usually proceeds from the bottom upwards, along the vertical

axis. When developing a slice at a given height, all the triangular facets that are intersected by a horizontal plane considered at that height are collected, as shown by the shaded triangles in Fig. 6.4(a). The set of triangles thus gathered as in Fig. 6.4(b) are sliced with the horizontal plane at the current height and the slice shape is developed based on the intersecting points. The process is repeated with other layers using equal increments, in the case of uniform layers, or at the appropriate increments as decided by the above algorithm in adaptive slicing. The need to modify the basic adaptive slicing algorithm considering the residual height h_r, the distance between the top of the current layer and the lowest apex of the triangular facet as shown in Fig. 6.4(c) is realised and implemented in this work.

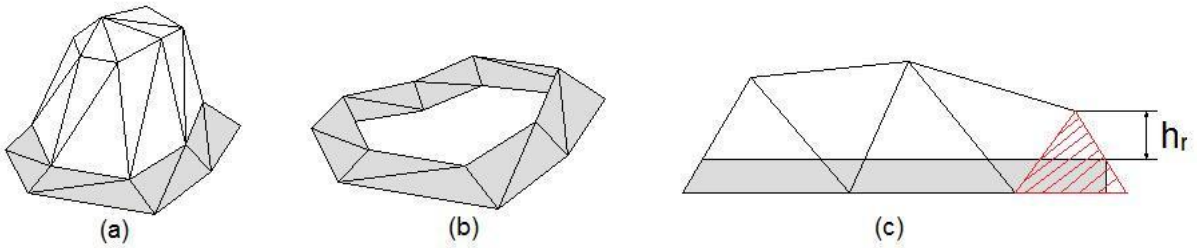

Fig. 6.4 Evaluation of the residual height; (a) tessellated .stl file, (b) sliced facets grouped together, and (c) the residual height consideration

The residual height varies with different situations, depending on the configuration of the triangular mesh. The equation of the residual height can be written as:

$$h_{ri} = \max(z_j) - H_{total} \qquad (eq.6.2)$$

Where h_{ri} is the residual height within the critical triangular facet, z_j is the z coordinate of each vertex on the triangular facet and H_{total} is the total height of the stacked layers.

The residual height to determine the next layer thickness is:

$$h_r = \min\{h_{r1} \quad \dots \quad h_{rn}\} \qquad (eq.6.3)$$

Once the residual height h_r is confirmed, the slicing algorithm will choose a layer of appropriate thickness to fill the gap from the thickness options available. Based on the residual height considerations, the combinations of included angle and layer thickness for a given cusp height of 0.1 mm as used earlier will change as shown in Table 6.2.

Table 6.2 Included angle and layer thickness combinations together with residual heights

Included angle range	Residual Height (h_r)	Layer thickness
[0˚, 90˚]	[0, 0.2)	0.1mm
[65˚, 90˚]	[0.2, 0.5)	0.2mm
[79˚, 90˚]	[0.5, 1.0)	0.5mm
[85˚, 90˚]	[1.0, ∞)	1.0mm

The algorithm is converted into a MATLAB code and implemented in different cases. Two specific examples are shown in Fig. 6.5 (a) and (b) depicting the effectiveness of employing the residual height considerations in the adaptive slicing scheme. In both cases, the left part is the layer pattern obtained with normal adaptive slicing and the right part is the layer pattern obtained with adaptive slicing together with the residual height. It is readily evident that the residual height consideration is very effective in capturing finer details and surface variations.

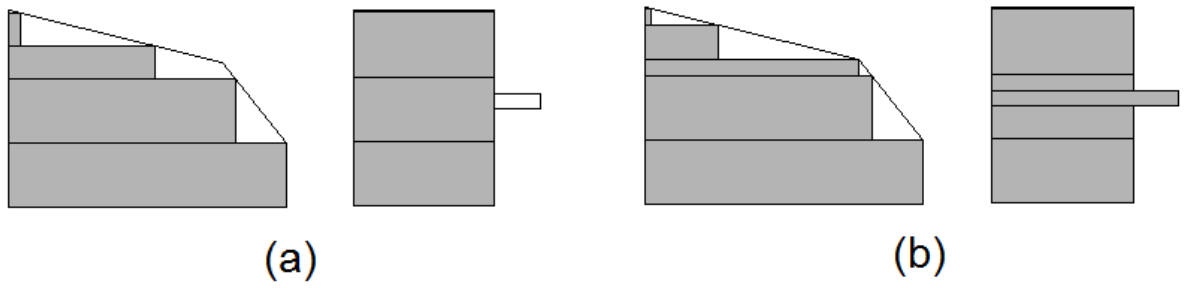

Fig. 6.5 Adaptive slicing using (a) cusp height criterion alone and (b) both cusp and residual height criteria

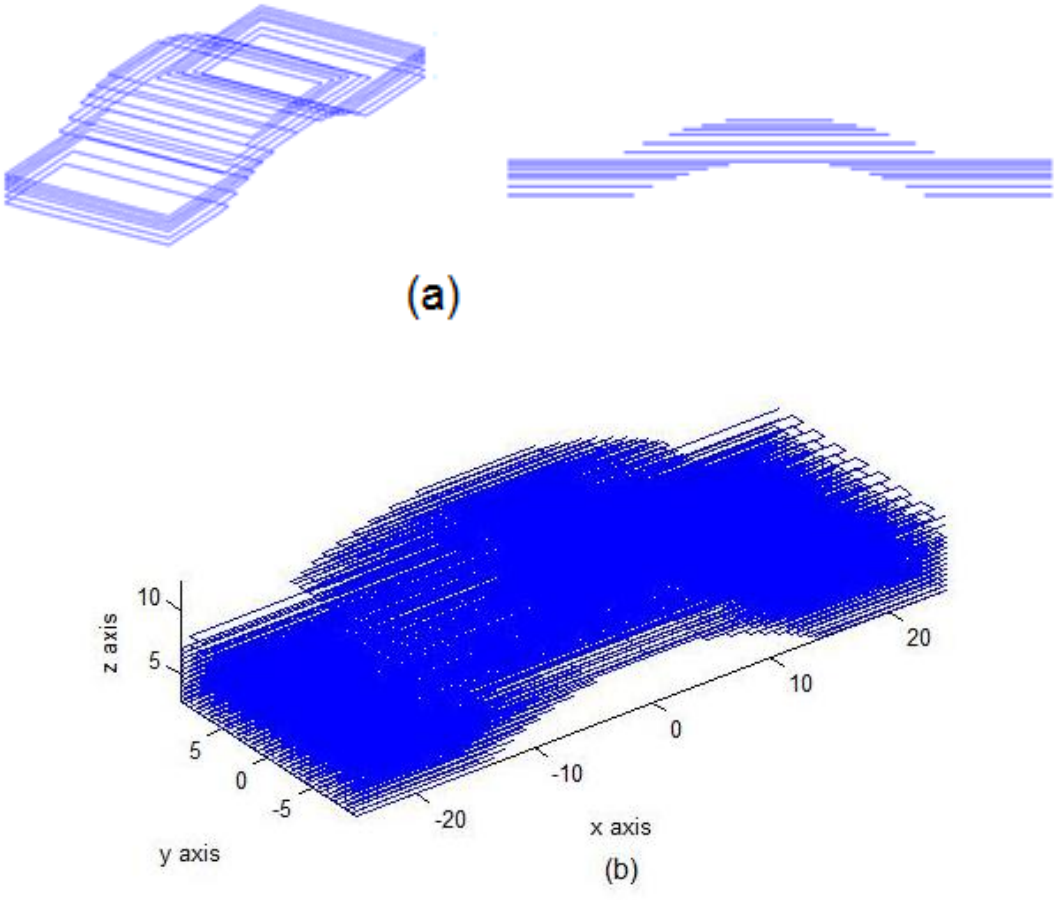

Fig. 6.6 Adaptive flat layer slicing applied to the light-curved part; (a) adaptive slices and (b) raster paths

The light-curved part used for all the experimental work presented in Chapter 5, is again considered here, but with the thickness increased to 6 mm. It is then sliced using the MATLAB code, implementing the modified adaptive slicing algorithm. The isometric and the side views of the adaptive layers obtained are shown stacked in Fig. 6.6 (a). It may be observed that varying external surface profiles at the top of the arch and at the point where curved and flat surfaces meet resulted in layers of finer thicknesses. Fig. 6.6 (b) is the continuous print path pattern needed for the actual printing as discussed in the next section.

The nozzle size used for printing in this case is 0.5 mm and two different filament sizes 0.5 mm and 1.0 mm are generated for printing, the actual mechanism of achieving this will be discussed more in detail in section 6.3. The effects of print speed and time on coalescence together with varying filament sizes are modelled and discussed in Chapter 3. With print speed being the same, thicker layers use lesser time than thinner layers and so suffer from a loss of coalescence. When these observations are applied to the adaptively sliced specimen here, it is obvious that different material characteristics result in different zones, if the speed of printing is the same for both thick and thinner layers. In order to achieve the same level of coalescence and mechanical characteristics throughout the volume of this test piece even with the use of layers of varying thicknesses, appropriate print speeds must be established for the two filament sizes. For this, Eq. 3.33, discussed in Chapter 3 can be used. With the thicker and thinner layers at 1.0 mm and 0.5 mm for the present case, based on Eq. 3.33, it can established that the thinner layers must be printed at four times the speed of printing of the thicker layers to achieve similar coalescence and mechanical characteristics. However, there will also be further effects due to the size of the

filament, variations in the latent heat and so on, but these minor variations are neglected in the current work.

6.3 Adaptive flat and uniform curved layer slicing; a comparison

A comparative evaluation of the adaptive and curved layer slicing schemes is undertaken now in order to be able to establish the relative merits in actual practice. For completeness, uniform flat layer, adaptive flat layer and curved layer slicing are considered together for evaluating the relative significance of each method. The modified Makerbot system introduced in Chapter 3 is again used for printing test samples of the same shape as in Fig. 6.6.

The uniform and adaptive flat layer and curved layer deposition schemes are implemented on the upgraded Makerbot system. The .stl format file of the basic test piece shape is processed using different MATLAB modules developed to generate the slices and deposition path ways in different approaches. The uniform flat layer slices and the integrated deposition path data generated are presented in Fig. 6.7 (a) and (b) while similar data for the adaptive slicing and curved layer slicing cases are already presented in Fig. 6.6 and 5.25 respectively. Test pieces printed with uniform, flat, adaptive flat and curved layer slices are shown in Fig. 6.8. The layer thickness is 0.5 mm in both uniform flat and curved layer cases.

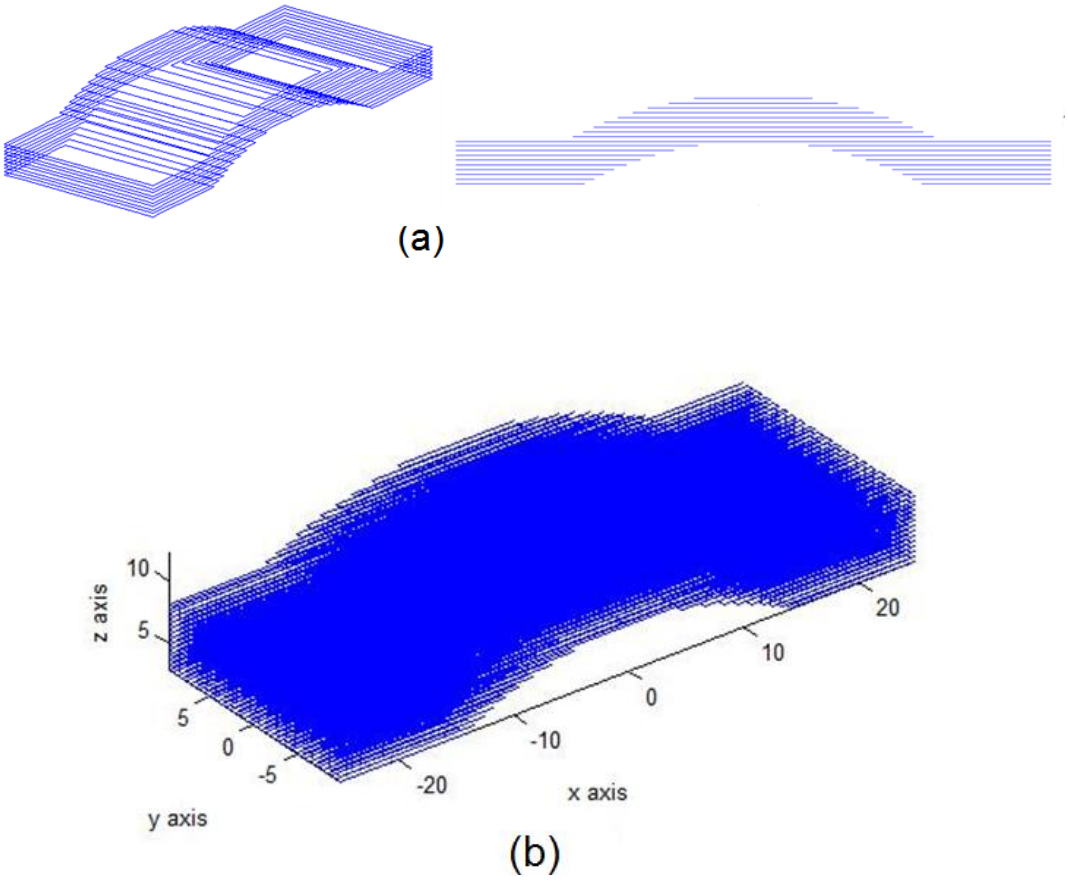

Fig. 6.7 Uniform flat layer slicing and raster path generation for the light-curved part

For better comparison and in order to achieve the maximum strength under uniaxial compression, all three specimens are printed with a 0˚ raster orientation, based on the analytical and experimental results of Chapter 4. Four specimens are printed for each case and tested for three-point bending performance. The experimental data in terms of the maximum compressive load in each case is compiled in Table 6.3 for a statistical evaluation of the comparative performance of the three FDM deposition strategies. The average compressive load in the case of conventional flat layered components falls short by 140 N compared to the adaptive layer parts, while the adaptive flat layer parts scored almost 200 N below the curved layer counterparts.

Though curved layer slicing appears to be scoring better, considering the experimental difficulties, these results may have limitations, as also indicated by the widely varying standard deviation values. It may also be noted that the results with the curved layer samples presented in Chapter 5 are different from the current results as thickness values of samples are different between the two experiments.

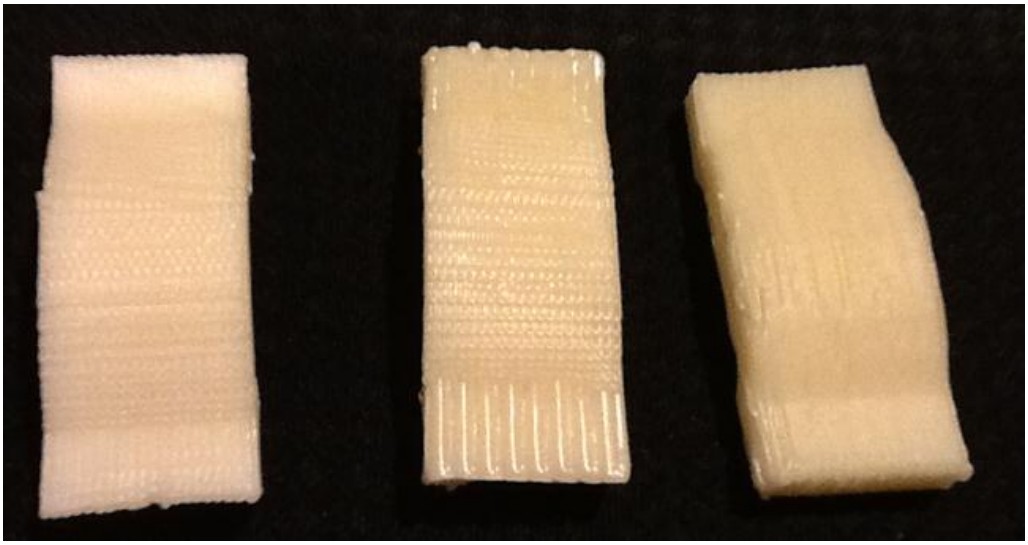

Fig.6.8 Uniform and adaptive flat layer and uniform curved layer parts printed with ABS polymer

The average fracture compressive load under three-point bending of curved layer parts increased almost 28% and 42% compared to that of the adaptive and conventional flat layer parts respectively. Eventually, all these results are in effect the consequences of varying internal mesostructures. The total print time with curved layer slicing is slightly more at 16 minutes as against the average 14 minutes time required for the other two cases.

Table 6.3. Three point bending results comparing uniform and adaptive flat layer and uniform curved layer slicing

Deposition Strategies	Maximum Compressive Load (N)				Average (N)	Standard deviation (N)	Time (sec)
	Part 1	Part 2	Part 3	Part 4			
Uniform Flat layer slicing	582.666	582.333	691.666	649.333	626.500	46.476	840
Adaptive Flat layer slicing	806.000	702.333	863.000	687.333	764.666	72.876	840
Curved layer slicing	963.000	926.333	986.000	930.333	951.417	24.515	960

6.4 Curved layer adaptive slicing

While curved layer slicing eliminates stair-step effects and enhances fibre continuity in light-curved parts, adaptive slicing mainly allows for finer details to be captured more effectively. Evidently, a combination of both is expected to result in better part characteristics and reproduction of detail. This section presents the method of combining the curved and adaptive layer slicing together and the outcomes of implementing the same in a couple of applications.

The process of identifying the reference surface to be offset is similar to the curved layer slicing algorithm. The adaptive curved layer slicing comes into effect when the side surfaces are inclined beyond a certain limit or when there are certain projecting details to be captured. Finer details such as projections or recesses on side surfaces are processed relatively easily by the residual height criterion as explained earlier. However, the slanting surfaces need specific attention through a proper evaluation of the included angles of the facets. This means, apart from the top surface, a part of the side surface also needs to be considered to be able to implement the

curved layer adaptive slicing approach. Based on Eq. 6.1, a user-defined cusp height is the local control parameter to differentiate between the top and side surfaces.

After fixing the part print orientation, the facet data is gathered from the .stl format file. The algorithm uses the cusp height based on Eq. 6.1 to identify the top surface as well as develop adaptive layers. Once the included angle is defined, the top original reference surface (surface to be offset) and the side surface (non-offsetting surface) can be easily identified for subsequent offsetting. However, it may be noticed here that the adaptive curved layers generated need to be stretched to meet the inclined surfaces. This requires identification of both the top surface and parts of side surfaces of the model. The .stl format file defines six specific areas; top and bottom, front and back, left and right as shown in Fig. 6.9 and for the sample test piece considered in this research, various areas are defined as follows:

Top, bottom and side facets are defined by the angle between the normal vector and z axis.

Top: $0° < angle \leq 45°$

Side: $45° < angle \leq 135°$

Back: $135° < angle \leq 180°$

Front, back, left and right facets are defined by the angle between the normal and x axis following the counter clockwise direction.

Front: $-45° < angle \leq 45°$

Left: $45° < anlge \leq 135°$

Back: $135° < angle \leq 225°$

Right: $225° < angle \leq 315°$

Using this data, the top reference surface (surface to be offset) and the side surfaces (non-offsetting surfaces) can be easily identified for subsequent offsetting, similar to the curved layer slicing algorithm presented in Chapter 5.

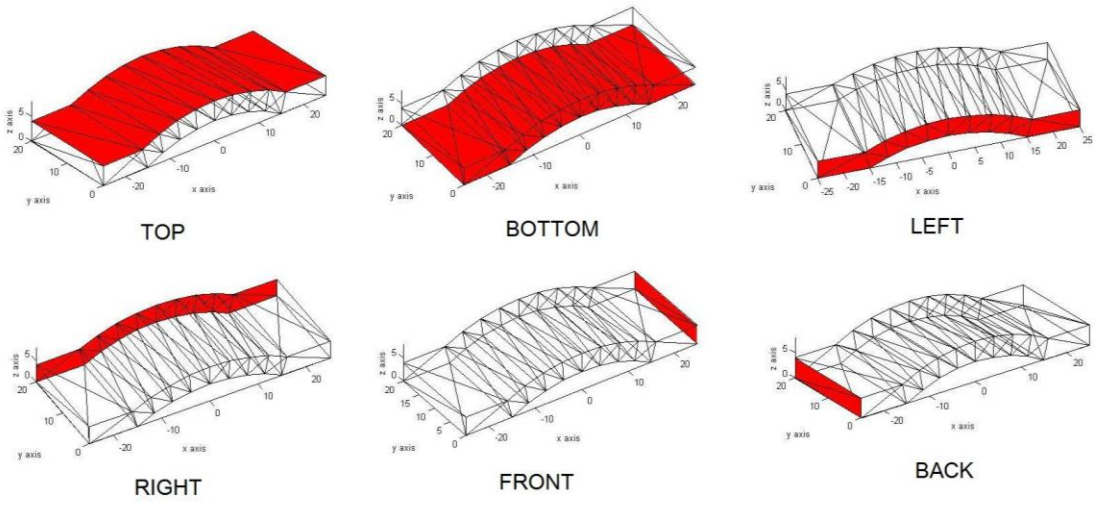

Fig. 6.9 Area definitions for a .stl format file

First, based on the .stl file as shown in Fig. 6.10(a), the top surface to be offset is selected. Using the coordinates of the points on the selected surface, the upper and the lower limits are defined passing through the points with the maximum and the minimum Z-coordinates respectively, as shown in Fig. 6.10(b) which result in an offsetting zone. The facets from the side surface sliced by the offset zone are detected next and grouped to form the adaptive slicing zone as shown shaded in Fig. 6.10(c). From the selected set of facets, the presence of specific features or slopes will allow to determine the offsetting distance as shown in Fig. 6.10(d), using the cusp and residual height calculations.

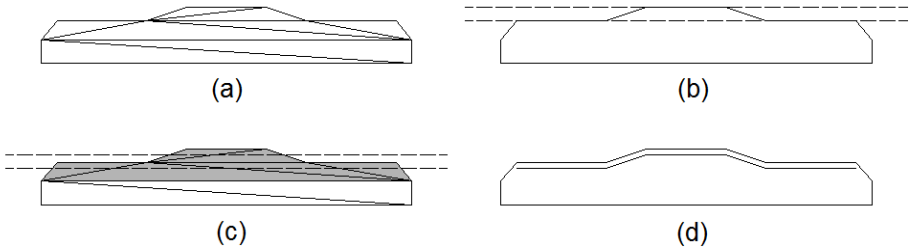

Fig. 6.10 Offsetting adaptive curved layers; (a) .stl file, (b) upper and lower limits of the top surface, (c) offset zone, and (d) offset curved layer

Once the offset distance is determined, the offsetting procedure begins gathering the vertices on the reference surface, followed by the calculation of offset vectors similar to the curved layer offsetting method discussed in Chapter 5 with three possible scenarios; (1) two side facets (2) one adjacent linked facet and a side facet, or (3) two adjacent linked facets. The auxiliary planes used here are replaced by the side facets. Eq. 5.14 in Chapter 5 will still be used in curved layer adaptive slicing, based on different situations to choose the matrix [***N***] and the vector [***D***]. While the third case is similar to the normal curved layered slicing, the other two situations could lead to displaced nodes, if offset by imaginary vertical planes. To eliminate this, the actual side facets are used in the three plane algorithm, as against using the imaginary vertical planes, but, it might lead to additional difficulties, violating certain basic rules of formation of facets in the .stl format files, as depicted in Fig. 6.11(a), (b), and (c).

When overhanging features are involved, flipped elements are likely to result with surfaces sloping upwards or downwards as shown in Fig. 6.11(a) and (b). This is the result of one or two vertices offset inwards, which will also lead to a flipped normal. To eliminate this, the resulting normal is compared with the normal from the reference facet and if the two directions are not the

same, the facet will be deleted. Multi offsetting points (multi nodes) result, when a given vertex is connected to more than one facet, as shown in Fig. 6.11(c). This problem is resolved by forming new offset facets as shown in Fig. 6.11(d), making use of the extra points generated in the process.

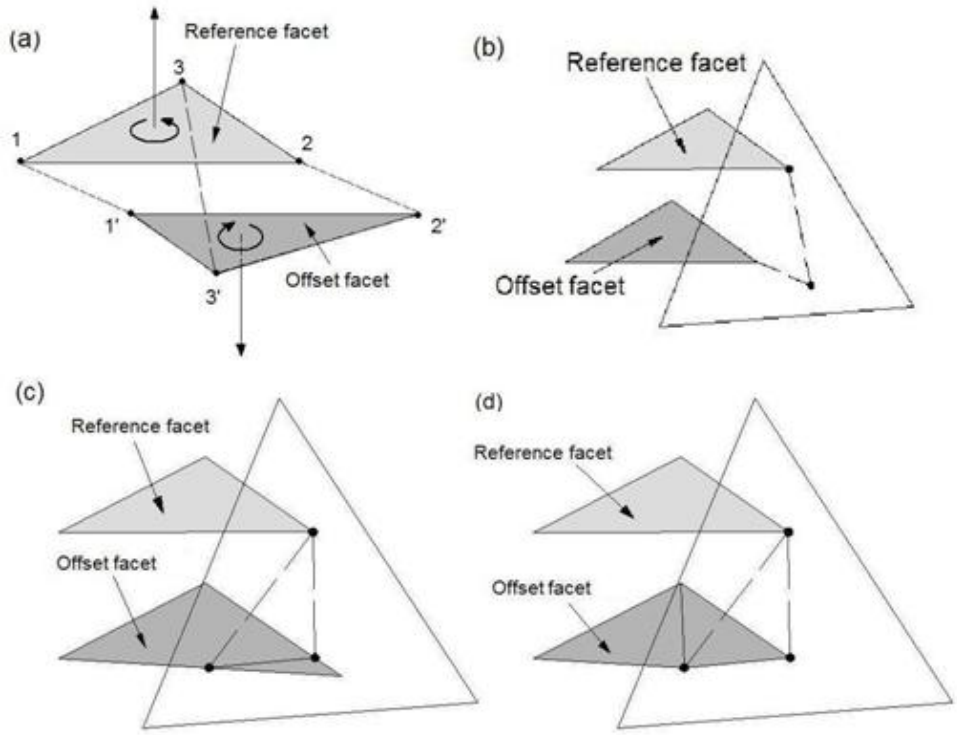

Fig. 6.11 Curved layer adaptive slicing issues; (a) upside-down offsetting, (b) unconnected points, (c) multi nodes, and (d) facet reconstruction

Deletion of offset facets from overhanging features often gives rise to either voids or interference between the offset facet and the bounding surfaces, as shown in Fig. 6.12. These issues can be resolved either by extending or by trimming the critical facets. The points where the extended offset facet intersects with the side surfaces are first obtained by using the three plane algorithm as explained in Chapter 5. No correction is necessary, if these points match with the nodes of the

offset facet. Otherwise, the element connectivity will be changed eliminating either unfilled areas or unwanted interference.

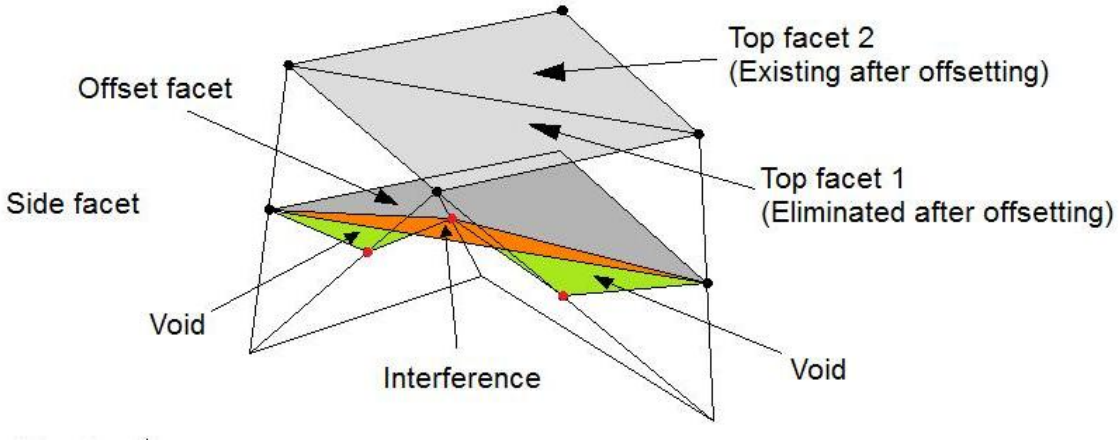

Fig. 6.12 Voids or interference caused by deleted facets

The overall scheme of the curved layer adaptive slicing algorithm is depicted as a flow chart in Fig. 6.13, developed using the standard symbols as exemplified by Hayasi and Asiabanpour [142]. The algorithm is applied to two specific cases as shown in Fig. 6.14 and 6.15. Both are essentially based on a light-curved shape, but the part in Fig. 6.14 has bevelled end faces, while that in Fig. 6.15 has a fine projecting feature. As shown in Fig. 6.14 (b), the curved layer adaptive slicing algorithm sensed the variation in the slopes of the end faces and developed curved layers of two different thicknesses. Similarly, the fine projected detail is captured by means of two finer curved layers as shown in Fig. 6.15(b).

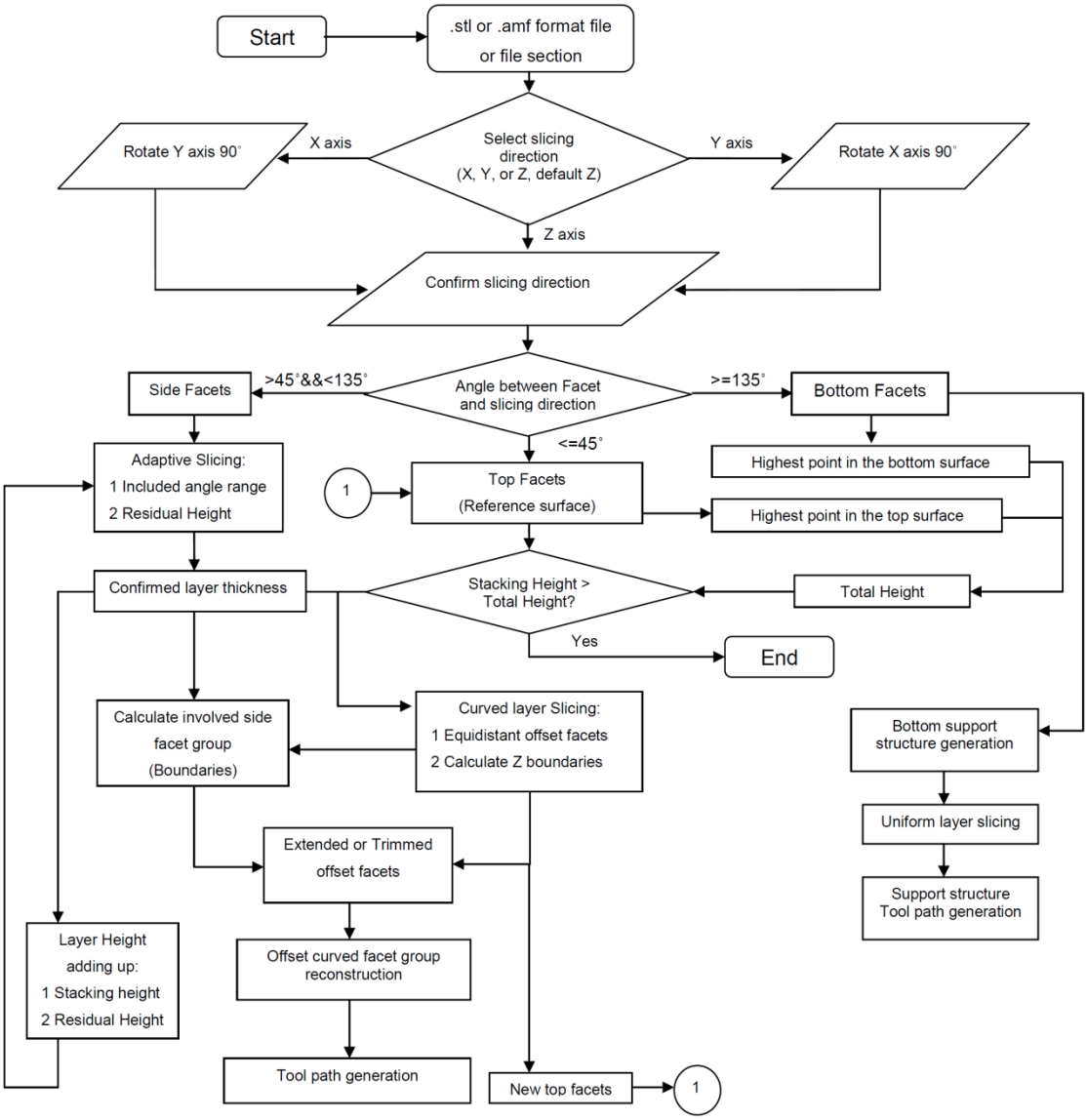

Fig. 6.13 overall scheme of the curved layer adaptive slicing algorithm

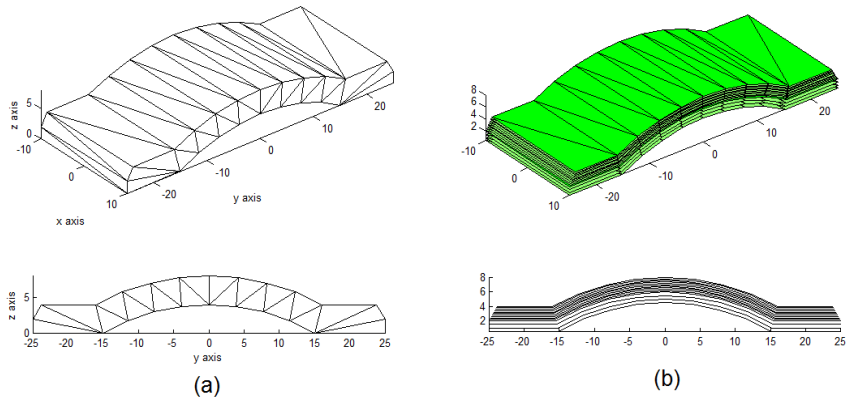

Fig.6.14 A light-curved part with bevelled end faces

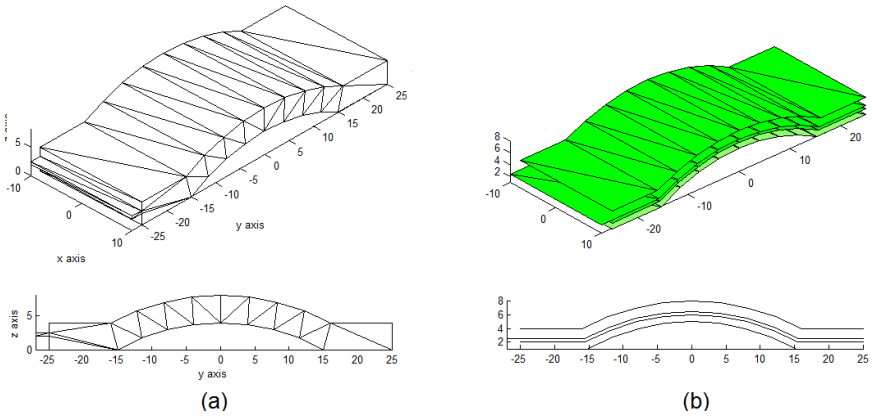

Fig. 6.15 A light-curved part with a fine projecting feature

The earlier curved layer FDM algorithms essentially used only 0˚ raster angles for the deposition path ways. Tool path generation for adaptive slicing has been attempted by other researchers with boundary contour and internal filling [143]. However, for practical testing of the mechanical properties of curved layer adaptive slicing of FDM parts, the internal filling pattern is more important. Hence, the tool path generation is only focused on the internal filling pattern in this research. This requires a relatively sharp response in change of motion in both the Z-direction as well as the internal drive mechanism of the deposition head considering the steep

rise along the curved path. From past experiences, the author realised that a 45˚ raster orientation makes it much easier to synchronise the two motors. Also, considering the isotropic nature of FDM parts, a criss-cross raster pattern with varying raster angles is beneficial but in the current cases a 45˚ raster angle is uniformly applied in all layers. The tool path generation algorithm used here is capable of these considerations. Parallel equidistant vertical planes are used at the selected raster angles to slice the top surface. Properly ordered intersection points with the corresponding facets form the point cloud data for building the raster paths. The raster paths are then connected in a proper sequence to develop the deposition path for building the part from the bottom upwards. Fig. 6.16 shows the simple curved part, adaptive curved layer slices and the raster paths generated for the final deposition scheme.

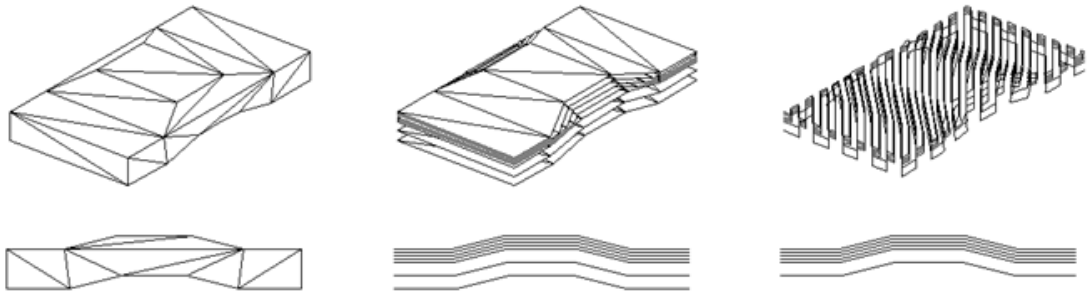

Fig.6.16 Adaptive curved layer slicing of a .stl format file and raster path generation

Theoretical and experimental investigations done on flat layer adaptive slicing were presented in Chapter 3. An experimental implementation of the adaptive curved layer slicing is attempted here to understand the influence of varying curved layer thickness on the mechanical characteristics. The modified Makerbot cupcake machine is the test bed again, with ABS polymer as the raw material in the filament form. Implementation of varying layer thicknesses in the same part calls for a multi-head extrusion system. However, the strand from the tip of the

extrusion nozzle swells due to sudden release of pressure at the exit [38], which allows for a means of achieving different road diameters with a single extrusion head. According to Agarwala et al. [110], the following relationships are valid amongst road width, thickness, nozzle diameter and the extruder motor speed

$$Q = W \cdot T \cdot v \qquad (eq. 6.4)$$

$$H = \frac{4F \cdot Q}{\pi d^2} \qquad (eq. 6.5)$$

$$n = \frac{H}{2\pi r} \qquad (eq. 6.6)$$

where W, T, v, Q, d, r and n are road width, thickness, extrusion nozzle movement speed, volumetric flow rate, filament diameter, roller groove radius and roller speed. F is the friction factor between the rollers and the filament. Ideal gripping and feeding requires F to be equal to 1. If F > 1, then the filament is crushed by the rollers and if F <1, then the filament slips between the rollers. Based on Eq. 6.6 to 6.6, provided the roller speed is fixed or similar, different layer thicknesses can be achieved by changing the road width and the speed of printing. The relationship between thickness, road width and speed of printing is

$$\frac{v_{d1}}{v_{d2}} = \frac{W_2 T_2}{W_1 T_1} = \frac{{d_{n2}}^2}{{d_{n1}}^2} \qquad (eq. 6.7)$$

Appropriate use of these equations together with the settings on the test bed allowed achieving different layer thicknesses effectively from a single nozzle. For example, a faster extrusion rate coupled with a relatively slower print speed results in an accumulation of excess material for a given length of the printed strand, and will result in a larger filament diameter. However, there is

only a narrow range of variation in diameters possible by this means, as too much of material accumulation results in a wavy strand and too less of extruded material results in unnecessary stretching and perhaps a variation in the internal molecular structures. Commercial FDM systems also use similar approaches to achieve filaments of varying diameters from the same deposition head. In the current experiments, a 1 mm nozzle is used and by programmatically varying process conditions, three different layer thicknesses 0.8 mm, 1.2 mm and 2.4 mm are obtained. It may be noted that these thicknesses are different from those used for the mathematical models earlier, for the same practical constraints as stated here. Four specimens of the light-curved part shown in Fig. 6.16 are printed with overall dimensions 50mm X 20mm X 4 mm with each of the three strand sizes. The top and bottom surfaces were processed with 45˚ raster lines and the layers in between are filled with 0˚ raster lines. The curved parts defined by the .stl format files are sliced with layers of different thicknesses and the deposition paths are generated as shown in Fig. 6.17(a), (b), and (c) using MATLAB programs. The tool path data generated from MATLAB is converted into G and M codes and then transferred to the RepG 24 interface of the FDM test bed to physically build the specimens. Considering the limitations of the make-shift experimental setup, three specific cases are considered; the space between the top and the bottom layers is filled by three, two, and single curved layers as shown in Fig. 6.17(d), (e), and (f) corresponding to the use of layers of thickness 0.8mm, 1.2 mm and 2.4 mm respectively. Fig. 6.18 presents photographs of physical specimens built with the three different curved layer configurations.

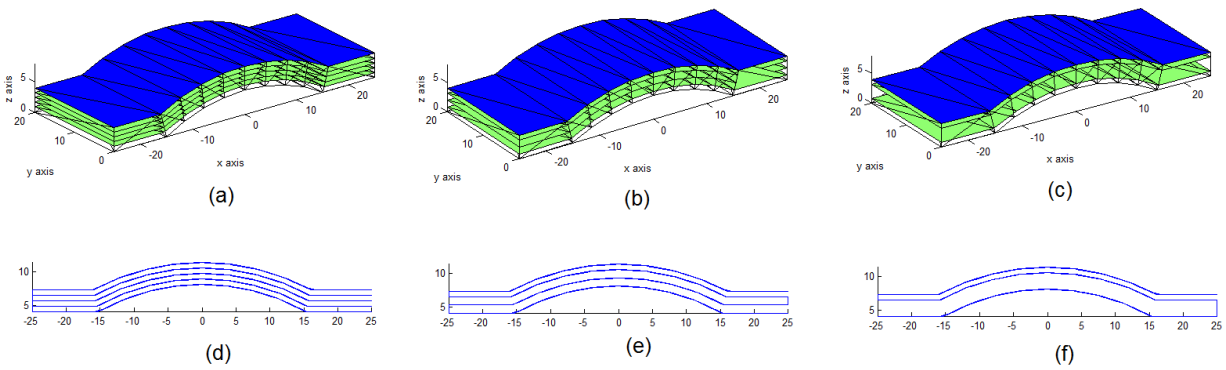

Fig.6.17 Adaptive curved layer slicing and deposition path generation; (a) three-central-layers, (b) two-central-layers, and (c) one-central-layer

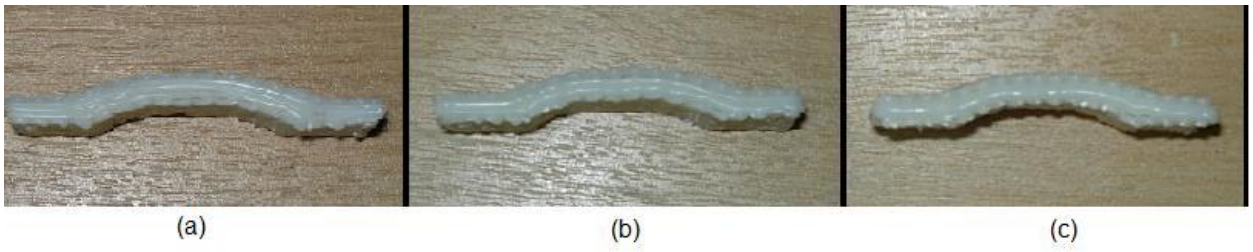

Fig. 6.18 Adaptive curved layer specimens printed; (a) three-central-layers, (b) two-central-layers, and (c) one-central-layer

The specimens produced are tested under three point bending loads as in Chapter 3. The curved specimens are placed on two supports with a 44mm central distance and the compressive load is applied centrally. All specimens initiated fracture cracks at the bottom surfaces at 45˚ inclinations, due to the 45˚ raster angle orientation used. Maximum compressive loads withstood by different samples, together with other results are given in Table 6.4.

Table 6.4 Results of three point bending tests on specimens produced with adaptive curved layer printing

3-central layer specimen	Time (sec)	Speed (mm/s)	Width (mm)	Thickness (mm)	Testing Load (N)	Equivalent Load (N)	Equivalent Flexural Stress (MPa)	Average Equivalent Load (N)	Average Flexural Stress (MPa)
1	474	12	19.98	4.91	350.666	232.962	32.5	225.419	30.9
2	474	12	20.06	4.95	318.666	207.4648	27.2		
3	474	12	20.02	4.92	357.333	235.9548	33.1		
4	474	12	19.56	4.67	300.333	225.2944	30.9		
2-central layer specimen	Time	Speed (mm/s)	Width (mm)	Thickness (mm)	Testing Load (N)	Equivalent Load (N)	Equivalent Flexural Stress (MPa)	Average Equivalent Load (N)	Average Flexural Stress (MPa)
5	480	5.18	19.42	4.63	319	245.2051	35.3	231.640	32.2
6	480	5.18	19.42	4.7	308.333	229.9985	31.8		
7	480	5.18	19.52	4.67	289.666	217.7378	29.1		
8	480	5.18	19.3	4.65	304.666	233.6204	32.6		
1-central layer specimen	Time	Speed (mm/s)	Width (mm)	Thickness (mm)	Testing Load (N)	Equivalent Load (N)	Equivalent Flexural Stress (MPa)	Average Equivalent Load (N)	Average Flexural Stress (MPa)
9	485	1.28	20.04	4.42	322	263.1865	41.0	239.978	35.3
10	485	1.28	19.9	4.46	293	236.8617	34.3		
11	485	1.28	19.92	4.44	289.666	236.0436	34.2		
12	485	1.28	20.18	4.43	277	223.8212	31.5		

Evidently, the three layer sample gave the least average equivalent load and flexural strength. The two layer sample is in the middle of the range, and the single central layer sample gave the load and strength values at 239.978 N and 35.3 MPa respectively. Again, considering the wide experimental errors, and the variations within narrow zones, the inferences from these results must be considered with some caution. Based on the observed trends, adaptive curved layers appear to influence the mechanical characteristics, with thicker layers performing slightly better under mechanical loading. This trend is in accordance with the theoretical and experimental results obtained by evaluating adaptive flat layer slicing in Chapter 3. Thicker filaments experience better inter-road coalescence due to more time and more favourable thermal

conditions resulting from higher residual energy in each strand. A thicker layer also reduces the chances of discontinuities. While the print speeds for the top and bottom layers are the same at 12 mm/s, the intermediate layers with thicknesses 0.8 mm, 1.2 mm and 2.4 mm are printed with speeds 12 mm/s, 5.18 mm/s, and 1.28 mm/s respectively in order to keep the total print time almost similar as given in Table 6.4. Realising that the print time is kept almost the same, the sample with the thickest layer should perform the best, as per the analytical model presented in Chapter 3 as Eq. 3.36, which is also readily evident from the experimental results listed in Table 6.4.

6.5 Mixed-mode slicing; combined flat and curved layer slicing

Evidently, curved layer FDM is a successful means of minimizing the stair-step effects. However, an interesting observation from Table 6.3 is that the total build time required for curved layer printing is more than that needed for flat layer printing. Though the difference in this case is relatively small, it may be much more in other situations; one of the primary reasons is the relatively inferior control on the Z-motion, rendering the FDM systems as two and a half axes systems rather than the expected 3-axes ones. Further, the total distance travelled by the extrusion nozzle is longer in curved layers for better representation of the geometrical shape of the test part, compared to the flat layers. As the application of FDM for manufacturing purposes increases in general, the total production time for a given part becomes quite important, and CLFDM approaches fail to fully satisfy this requirement. On the other hand, it is evident from Chapter 3, that adaptive slicing saves some build time, while maintaining or even improving the mechanical characteristics to some extent, notwithstanding the insufficiently resolved stair-step effects. Curved layer slicing is very effective in overcoming the stair-step effects and also

improves mechanical characteristics in thin shell type parts, but completely neglects the time-to-build aspects. Apparently, a better scheme of slicing and building FDM parts can be developed by appropriately combining both approaches together in a given part.

Inspired by the accurate external, fast internal slicing algorithm [86] and region-based adaptive slicing algorithm [118], a new slicing process combining both curved layer and adaptive flat layer slicing is developed. The basic approach is to slice the exterior with curved layers in order to capture finer details effectively as well as minimise the stair-step effects and use adaptive flat layers in the interior to optimise time and the mechanical characteristics of FDM parts. The first step of the proposed combined model involves an algorithm for dividing the CAD model into curved and flat layer regions. Appropriate curved layer and adaptive layer slicing schemes are developed next, together with the integrated deposition path generating algorithms.

6.5.1 Dividing the total volume into different sub-regions

Although different CAD format files could be used for subdividing a given model, the .stl format file is again used here for reasons already stated. The top surface data is critical, including the facets, vertices and normal directions. After collecting the top-surface facet data, some further processing as mentioned in Chapter 4 is used to bundle the linked facets into groups for the curved layer slicing. Once the top surface data is gathered, the next step is to divide the domain into curved and flat layer regions. Considering the required quality of the top surface, the curved layer slicing takes precedence over the other and should follow the shape on the top surface. Flat layers take over at some stage and it is necessary to establish the boundary between the two regions. The criterion used to decide this boundary is based on observations on the pattern of flat

layers deposited on supporting scaffold structures. Fig. 6.19 depicts flat layer filaments deposited on vertical scaffold structures of varying span. As evident from Fig. 6.19(a), the filament normally sags under its own weight and the associated plasticity. This effect can be eliminated by printing multiple layers on the same support structure as shown in Fig. 6.19(b) or by reducing the span length as shown in Fig. 6.19(c).

When curved layers are deposited over flat layers, the boundary condition between the two regions will be as shown in Fig. 6.20(a). Ideally, the curved layer is laid on top of the flat layers and represents the actual shape of the part, mostly using curves or splines. In the deposition system, all the curves or splines are converted to straight line segments, as shown in Fig. 6.20(b). In the actual deposition, the curved layer is a composite of strands. These strands are semi-melted and still soft when they are just extruded out of the nozzle. Therefore, they do not exactly represent the shape of the surface; instead, they will bend due to gravity, as shown in Fig. 6.20(c). Similar to the cusp height, a chordal height evaluation is used here to identify the boundary between curved and flat layer regions.

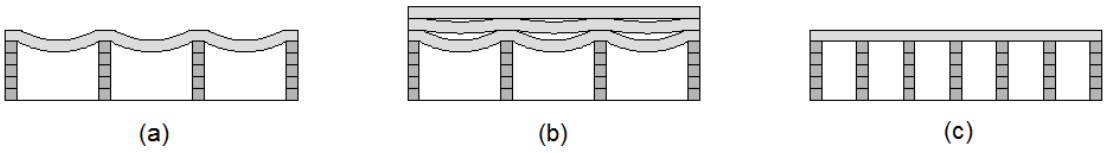

Fig. 6.19 Issues with flat layer deposition and solutions; (a) bending phenomenon during deposition, (b) Multi-layer solution, and (c) reduced gaps

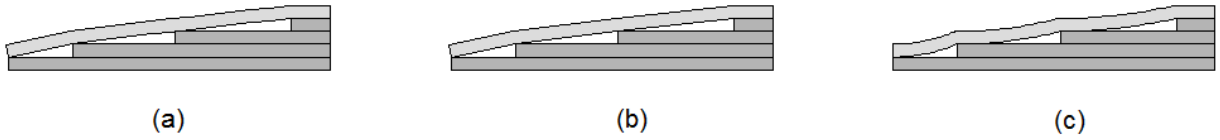

Fig. 6.20 Boundary connection between flat and curved layers; (a) ideal connection, (b) tool path connection, and (c) actual connection

Chordal error was mentioned in Chapter 2 describing the defects arising from piecewise linear segments used to represent a curved surface. The chordal height is used here as the criterion to determine the magnitude of the region to be filled with curved layers in order to eliminate the stair case effects based on the maximum allowed chordal error as defined by the end user. The amount of sagging in the plastic filament is taken into consideration to define the chordal error. Consider the deposited strand as a uniformly loaded simply supported beam, where the load comes from gravity. The deposited strand bends and a gap exists between the required shape and the actual deposition as shown in Fig. 6.21(a). The maximum deflection, which is assumed as the elastic deflection but irreversible, can be calculated as:

$$H_{chordal} = \frac{5qC^4}{384EI} \qquad (eq.6.8)$$

Once the first curved layer is deposited, the supports are wrapped around and the first layer offers a better support for the next layer, thus reducing the subsequent chordal height, as shown in Fig. 6.21(b). The relationship between the first and second chordal heights can be written as:

$$\frac{H_{chordal\ previous}}{H_{chordal\ current}} = \frac{{C_{previous}}^4}{{C_{current}}^4} \qquad (eq.6.9)$$

Where q is the uniform load per unit length due to gravity and depends on the angle α between the facet and the horizontal plane: $q = \rho A \cos\alpha \, dx$, ρ is the density of the material.

The geometrical relationship between $C_{previous}$ and $C_{current}$ is:

$$\frac{C_1}{C_{current}} = \frac{R_1}{R_{current}} = \frac{R_1}{R1 - Thickness}$$
$$\frac{C_{previous}}{C_{current}} = \frac{R_{previous}}{R_{current}} = \frac{R_{previous}}{R_{previous} - Thickness} \qquad (eq.6.10)$$

where $R_1 = \frac{\text{Thickness}}{2\sin^2\theta}$

Eq. 6.6 could also be used to determine the air gap for the support structure or help to determine the quantity of the layer to fit the current air gap in the support structure.

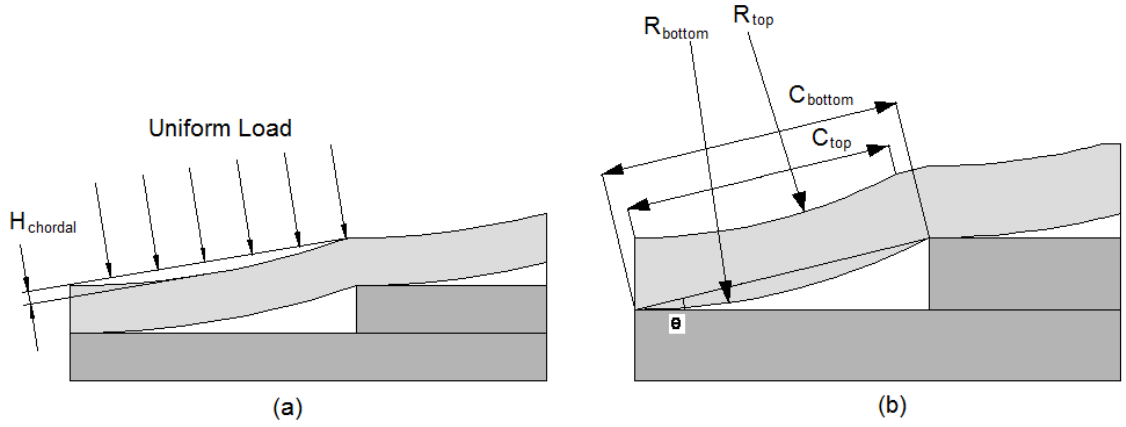

Fig. 6.21 Bending deposited strands; (a) uniform load forming a gap of deflection and (b) geometrical relationship of the chordal deflection between two consecutive layers

The chordal height is used as follows:

1. The angle of each facet on the top surface is noted and used with the minimum thickness of the layer to calculate the maximum span. Based on the angle between the facet and the horizontal plane where the maximum span is, the deflection is obtained as the initial chordal height, as shown in Fig. 6.21(a).
2. Once the initial chordal height is obtained, the top surface is offset to form the curved top layer as shown in Fig. 6.21(b). The chordal height from all the facets is calculated and used to get the maximum chordal height.
3. Then the maximum chordal height is compared with the user-defined chordal error. If the maximum chordal height is greater than the user-defined chordal error, extra curved layer needs to be used.
4. Repeat the same procedure until the chordal height meets the requirement and finalize the required number of curved layers.

Once the number of curved layers is finalized, the bottom layer needs to be offset once to become the top surface of the flat layer region.

6.5.2 Reconstruction of flat layer regions

Once the curved and flat layer regions are clearly distinguished, curved layer slicing is done using the methods discussed above. The flat layer part needs to be reconstructed back into the .stl format file, as conventional flat layers generated based on the whole volume are likely to interfere with the curved layers. This reconstruction could reduce the inaccuracy and could be

used for further subdivision. The reconstruction starts from restructuring the top surface of the flat layer region, which will also serve as the boundary between the curved and flat layer portions. The top of the flat layer is generated by offsetting the bottom-most curved layer through one layer thickness. The triangular facets on the side faces also may need restructuring, as most of them get distributed over the two regions, as shown in Fig. 6.22.

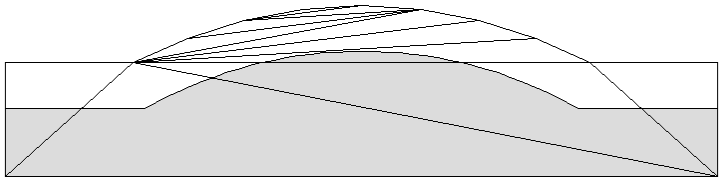

Fig. 6.22 Facets on the side face crossing the boundary between flat and curved regions

Two different methods of reconstruction are used, depending on the complexity of the shape. First, considering a simple solid shape with a curved feature as shown in Fig. 6.23(a), the flat layer portion is reconstructed into a new .stl file, by projecting the top nodes of all side facets on to the boundary surface between the curved and flat regions. Further, the element numbers and connectivity are carried forward from the original .stl file, as these will remain the same, even with the restructured shape of the flat layer portion. After the reconstruction, the coordinates of the top surface points are modified, and the stl form of the flat layer portion looks as shown in Fig.6.23 (b). However, this works well only when the offset surface and the top surface of the flat region parts are one and the same.

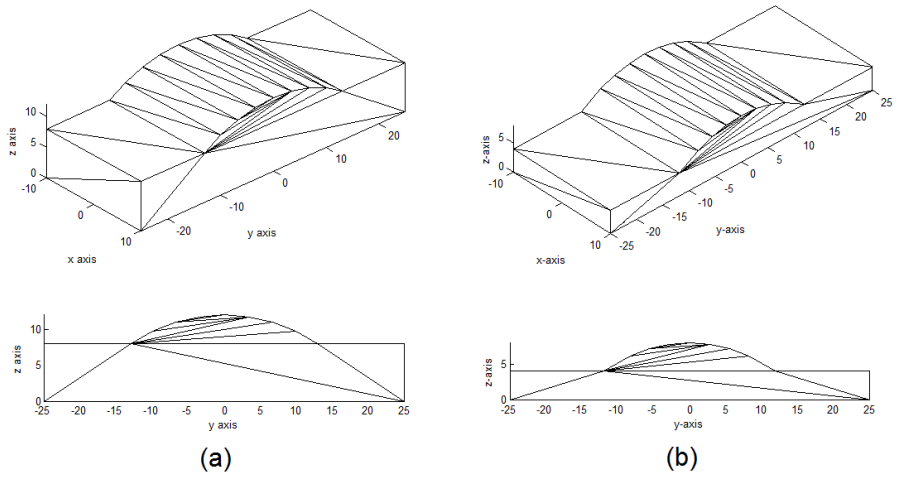

Fig. 6.23 Reconstruction of the flat layer region by offsetting points

When the offset surface is not the new reference top surface of the flat region, for example, as in the case of the slightly more complex shape shown in Fig. 6.24(a), an altogether new .stl format file needs to be built. The part shown in Fig. 6.24 has an irregularly shaped lateral hole, intentionally created to be able to test the effectiveness of the algorithm developed. The algorithm proposed is not a generalised scheme that can process any given shape, but will be able to handle a given solid part with a cavity of any shape inside. Based on a given range of normal directions, all faces of the given solid with a horizontal orientation are identified. In the case of the previous part, there are only two such surfaces, the curved one becomes the top surface and the flat one becomes the bottom surface. In the case of the part with a central cavity or hole, there are four such surfaces. The highest curved surface will be considered as the top surface for the whole part, and the bottom surface of the curved region will be differentiated from the actual bottom surface based on a check using the z-coordinates. Once this is done, the curved region is clearly identified, and the rest of the part becomes the region for flat layer slicing.

First, the points on the intermediate surface of the solid together with the points on the boundary between the curved and flat portions of the solid are marked, for example as points A, B, C,… in Fig. 6.25, as seen from the side view of the solid. Once the boundary points are identified, they are divided into two sets; the set that are freshly formed due to a partition between the curved and flat regions, such as points A, B, G, and H, and the set that are already existing in the original .stl file, such as C, D, E, and F. With the set of already existing points, there are triangular facets that are already defined and they will be used as they are. However, with the new set of boundary points, new facets are generated following the rules of triangulation. Further, the side facets also will be modified only where they are connected to the new points, while the existing facets are used with other points. For example, in the shaded portions on either side of the side view shown in Fig. 6.25, some of the existing facets are deleted and fresh connections are made joining points like A, B, G, and H to the bottom corner points, I and J. After implementing the algorithm, the curved and flat regions of the part with a central hole are separated and triangulated as shown in Fig. 6.24 (b).

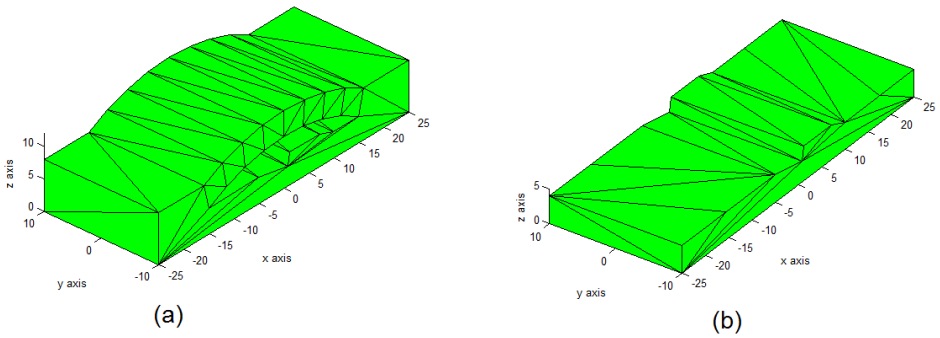

Fig. 6.24 reconstruction of flat layer region using the existing facets

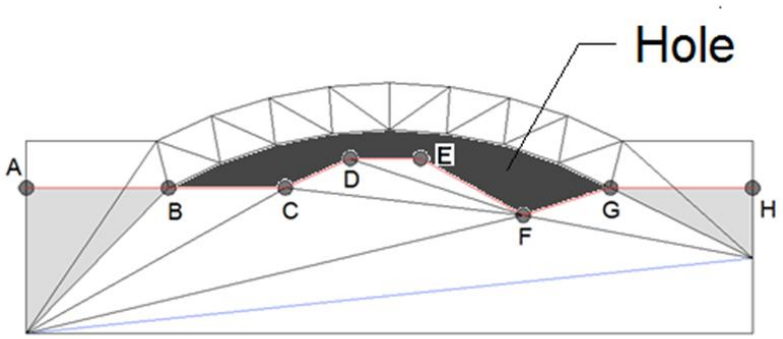

Fig. 6.25 Point-selection criteria for facet reconstruction

6.5.3 Combined flat and curved layer slicing

The mixed mode slicing techniques are implemented in MATLAB and tested for specific cases, first with uniform layers and then with layers of varying thicknesses. Fig. 6.26 (a) shows the .stl format file form and the combined curved and flat layer slices generated for the full solid part using the current algorithms. It may be seen that the top surface is modelled with curved layers, while the solid base part is filled with uniform flat layers. The maximum span is 6.995 mm and the chordal height based on Eq. 6.3 becomes 0.001mm. Considering a maximum deflection of 5% and using Eq. 6.5 and 6.6, it was found that a single curved layer satisfies the required error criterion. However, considering other practical problems, three extra curved layers are used, which will also allow for a shell of sufficient strength to envelop the flat layered core. Once the curved region is finalised, the boundary surface is generated, and the flat layer zone is reconstructed using offset vertices and facet reconnection approaches in this case, considering the relatively simple shape as shown in Fig. 6.26 (b).

Early research by Mani et al. [118] emphasises the need to properly sequence the deposition styles while using multiple deposition schemes. It may be realised that practical implementation of mixed curved and flat layers also requires some consideration and planning prior to actual deposition. Apparently, this part considered for the current investigation requires the flat layer portions to be deposited first, so as to serve as the basis for the curved layer deposition. Based on the slice data, the two sample parts are rasterised using 45˚ orientations as shown in Fig. 6.26(c), with the help of the deposition path generation algorithms implemented in MATLAB. The deposition path data is properly connected to form the appropriate sequence of deposition and converted into G and M codes. This information is further transferred to the Rep G 24 interface of the FDM test bed to physically build the test pieces. The model in Fig. 6.23 does not require a support structure and the bottom part is printed using flat layers. The upper curved form is built using curved layers as shown in Figure 6.26(d). Figure 6.26(e) shows the final part after the support structure is removed.

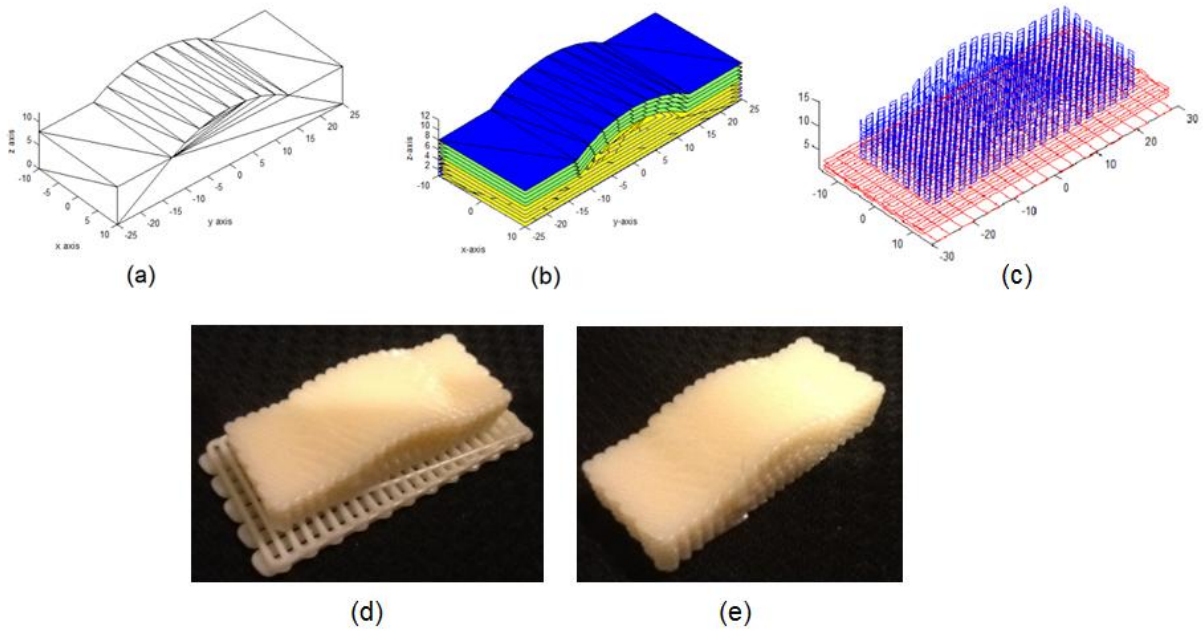

Fig. 6.26 Sample part with a curved surface; (a) .stl file, (b) subdivision into zones and slicing, (c) tool path generation, (d) actual printed part with support structure, and (e) final part

While uniform flat and curved layers need 946 and 1409 seconds respectively, it was noted that the combined curved and flat layer slicing is a good compromise, requiring 1187 seconds as given in Table 6.5, to build the whole part with better surface quality and internal structure.

Table 6.5 Comparative build times for different deposition strategies

Deposition Style	Build Orientation	Build Time
Flat Layer Deposition	90˚	946 s
Flat Layer + Curved Layer Deposition	90˚	1187 s
Curved Layer Deposition	90˚	1409 s

As already mentioned, the second test part is similar in shape, but has a lateral through hole of an irregular shape, as evident from the form depicted in Fig. 6.27(a) by the .stl format file. In this case, there are two distinctly different zones; one of thin shell type form and the other of a normal slab shape. As evident from Fig. 6.27(a), the algorithm picked up the thin shell type region to slice using curved layers. For the lower part, the boundary surface partly matches with the lower curved layer, while the central portion needs to be freshly constructed. A new parting surface is generated with extra facets and the lower part is rebuilt in the stl form and sliced using the uniform flat layer slicing algorithm. The mixed curved and flat layer slices created are shown in Fig. 6.27(b). For the tool path generation, the bottom flat layer part is to be printed first and then the sparse support structure, before laying out the curved layers. The deposition path data is generated accordingly and connected to form the appropriate sequence of deposition as shown in Fig. 6.27(c) and converted into G and M codes. The actual printed part and the final part are shown in Fig. 6.27 (d) and (e). Mechanical testing of this part is not feasible at this stage, but the resulting meso-structures are much better than those possible by the uniform flat layer means. Instead, further attention is paid in testing the effectiveness of these algorithms in more complex cases as presented next.

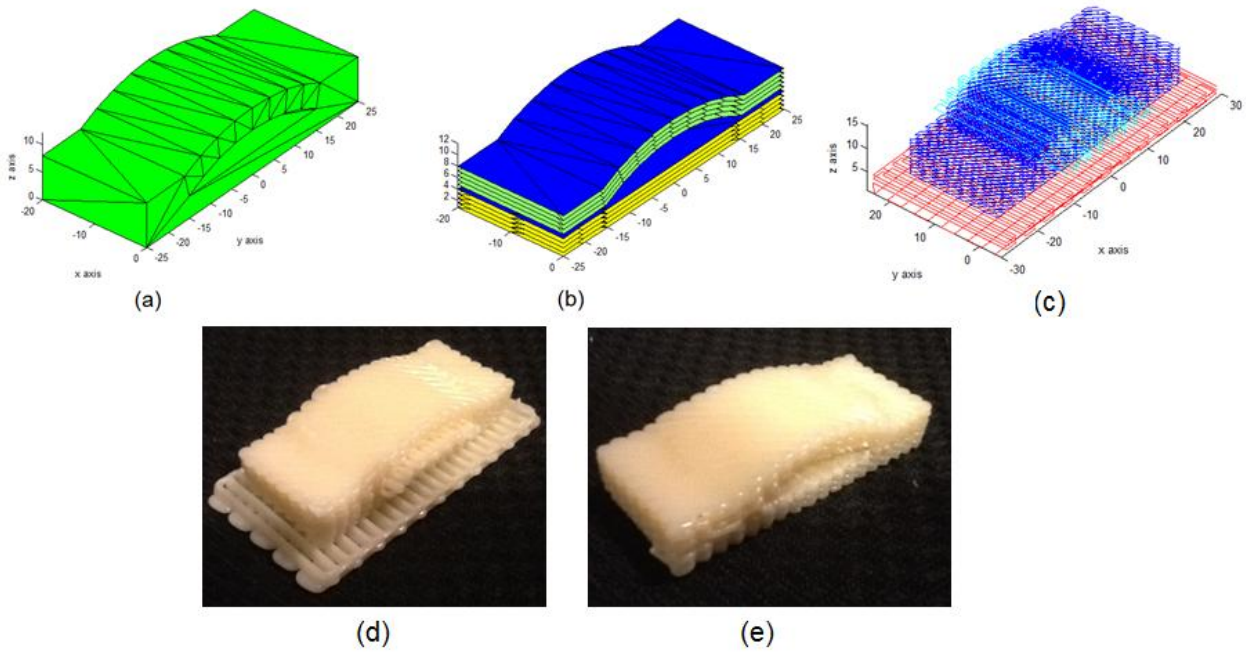

Fig. 6.27 Sample part with a curved surface and a cut out feature; (a) .stl file, (b) zone subdivision and slicing, (c) tool paths generation, (d) actual printed part with support structure, and (e) final part

6.6 Integrated alternative slicing and deposition; some case studies

The next step is to combine all forms of slicing and raster orientation aspects evaluated as part of this research into a multi-mode algorithm, to be able to identify the best solutions in different zones and build the best combination of slicing solutions for a given model. The uniform and adaptive flat and curved layer slicing schemes developed, together with the knowledge gained on the role of raster orientations are combined into a unified approach, referred to as the integrated alternative slicing. The algorithm is coded in MATLAB and allows processing any solid model and building appropriate layer and raster path patterns using the most suitable combinations of the alternative schemes available. It may readily be realised that a single solution cannot effectively handle all types of solid forms. A given part is usually divided into two or more

regions and the method to be used for this division varies depending on the overall geometry of the part. The flow chart of integrated alternative slicing is shown in Fig.6.28.

Three different approaches are developed here for resolving geometrical complications of varying degrees. The first method is a fully automated routine which segregates the curved and flat layer zones without any user intervention and can be used with parts of relatively simple shapes, as is the case with the examples presented for the combined flat and curved layer solution in section 6.5.3. The second approach is also fully automatic, but requires the user to specify a plane of separation for the two zones and in the absence of any specific input from the user, the central plane at mid-height will be used by default. The third method is for more complex cases and involves dividing the part domain into more than two zones and some user input prioritising different schemes based on specific attributes of each zone. The integrated alternative slicing and deposition scheme developed is now tested based on three typical cases requiring the three solutions mentioned. It may be noted that the following work is limited to verifying the effectiveness of the integrated schemes in altering the layer and deposition structures in specific situations. Except for case 1, practical implementation and testing of the other two relatively more complex parts could not be undertaken currently due to hardware limitations and will require better control of all three axes and in fact more degrees of freedom, such as perhaps five-axis CNC.

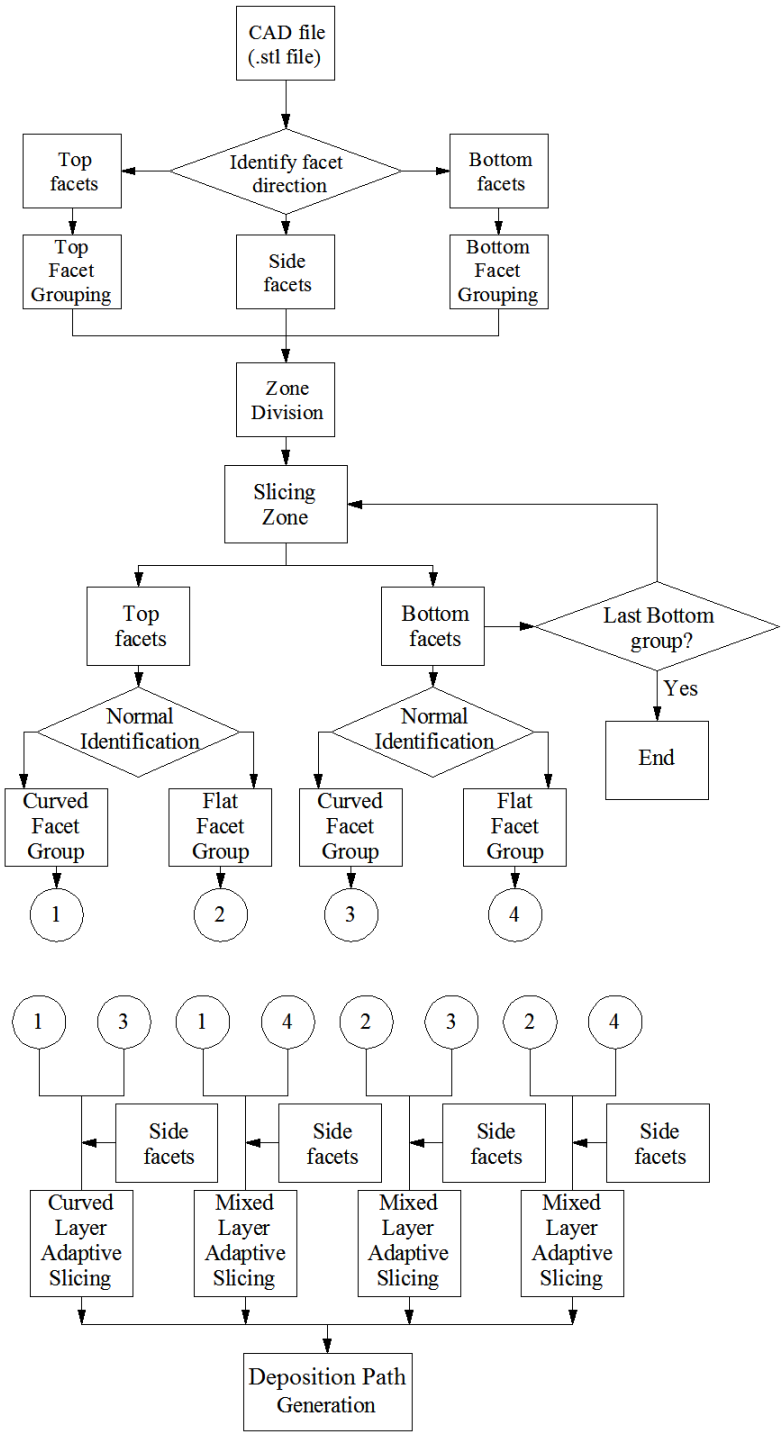

Fig. 6.28 overall scheme of the integrated alternative slicing scheme

Case 1

The first case is the same simple solid part as shown in Fig. 6.23, with the curved surface on the top and a flat bottom surface and is repeated again in Fig. 6.29(a). While the method used earlier is a simple combination of curved and flat layers to be filled in different regions, the integrated approach used here also adds the adaptive slicing capability. The part geometry being relatively simple, the whole process is fully automated and Figs. 6.29 to 6.31 depict different stages of slicing. The facets on the top surface are identified first and grouped together as shown shaded in blue colour in Fig. 6.29(a). This is followed by the identification of the region for curved layer slicing, considering the quantity of minimum layer thickness as shown in Fig. 6.29 (b). Once the curved slicing region is segregated, the adaptive curved layer slicing algorithm is employed to fill this zone with layers of two different thicknesses, 0.8 mm and 1.6 mm, as shown in Fig. 6.29(c). Subsequently, the bottom surface of the curved region and the rest of the .stl file are restructured as a new domain and considered as a different entity in .stl form as shown in Fig. 6.29(d). Adaptive flat layer slicing is then applied to this zone using layers of thicknesses 0.8 mm and 1.6 mm and the final adaptive flat and curved layer structure is as shown in Fig. 6.29(e).

Once the entire part is filled with adaptive flat and curved layers, the slice data is used to construct deposition paths employing two different raster orientations 30˚ and 90˚, as shown in Fig. 6.30. The deposition path data is then integrated into the G and M code format in order to be processed on the modified Makerbot Cupcake platform and build the physical parts as shown in Fig. 6.31. The mixed layer structure developed for the part together with the practical implementation prove the overall feasibility of the new integrated slicing approach developed as part of the current research. A mechanical testing of the physical parts is not carried out currently

but the overall approach is proved to be effective in terms of the most favourable distribution of the material in successive layers while overcoming surface defects such as stair-step effects.

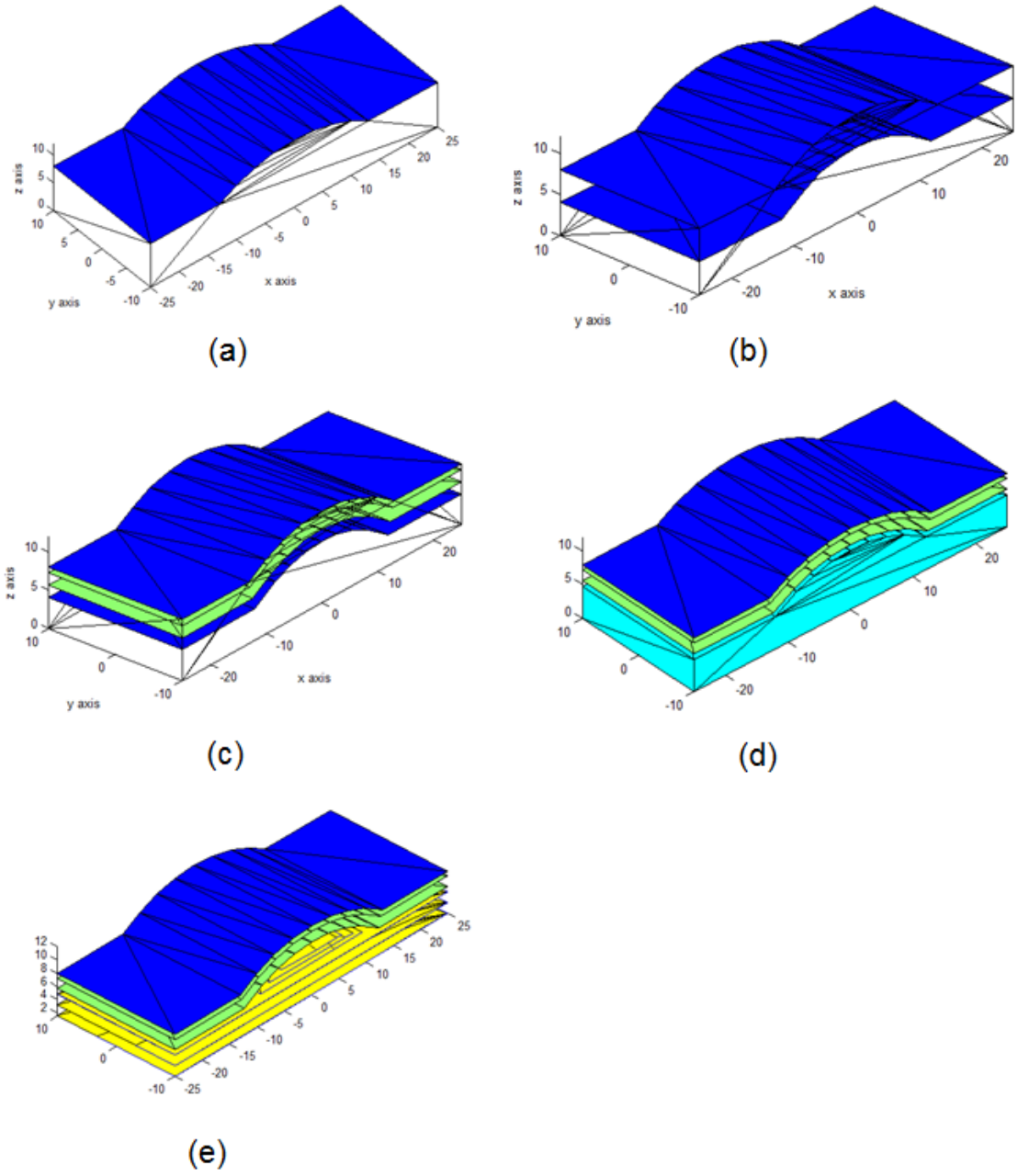

Fig. 6.29 Integrated slicing in Case 1; (a) identification of the top surface, (b) segregation of curved and flat layer zones, (c) adaptive curved layer slicing, (d) restructuring the flat layer zone in .stl form, and (e) adaptive flat layer slicing in the flat layer zone

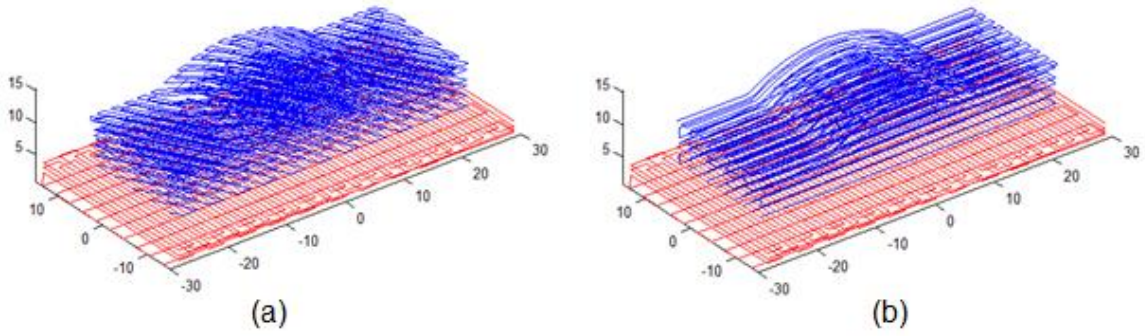

Fig. 6.30 Case 1; deposition paths generated; (a) 30˚ raster orientations and (b) 90˚ raster orientations

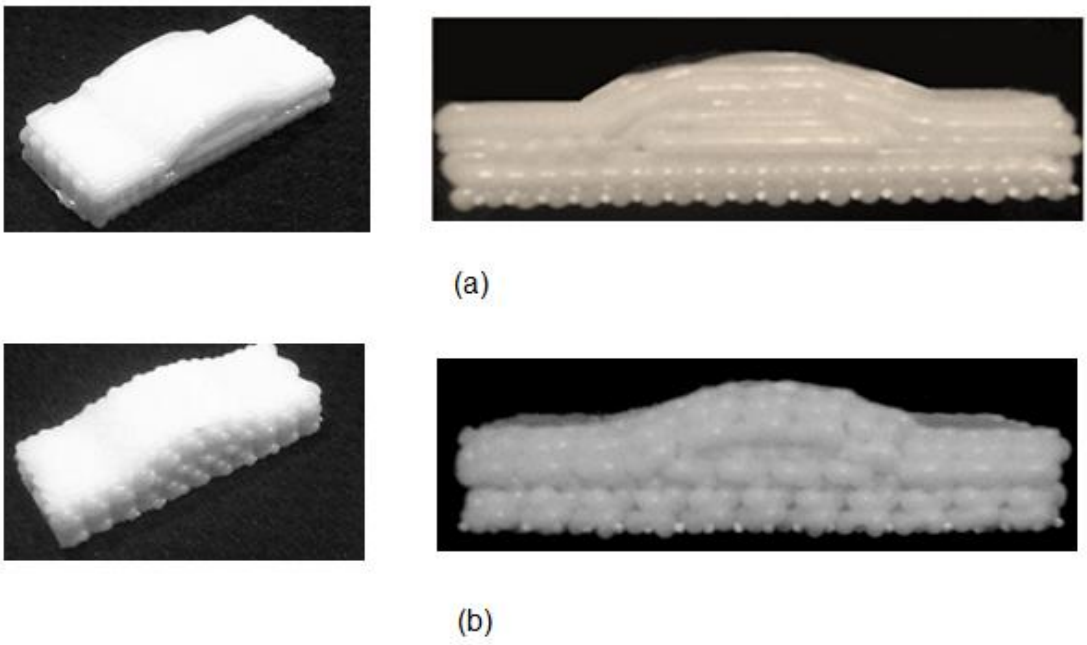

Fig. 6.31 Case 1; practical implementation (a) 30˚ raster orientation and (b) 90˚ raster orientation

Case 2

A more general case is then considered for testing the algorithm in two different versions as shown in Fig. 6.32 (a) and (b), with some slight variations in the minor detail at the top right hand corner. The CAD model is generated and triangulated using the SolidWorks software.

Both versions are processed using the second approach with a division of the part domain into two regions based on a default central plane or a plane of choice of the user. With more general cases such as these, it may also be noted that the identification of the top surface facets is not simple, as the vertical portions of the curved surface will be missed out to be a side surface. This is resolved by slightly modifying the algorithm used to identify the top surface and allowing the user to selectively choose the range of angles to be used to decide the top facets based on the specific part geometry.

Further to these modifications, the algorithm identifies both top and bottom surfaces first, and then proceeds with slicing from both directions, until the two fronts meet, where the boundary between the two zones is established. It may be observed that two sets of uniform curved layer slices are generated to be filled in the two geometrical regions for the case shown in Fig. 6.32 by the integrated slicing scheme. Considering the curved top surface and almost curved grove at the bottom, curved layer slicing is applied in both regions. The actual printing begins with the bottom region and gradually works its way upward into the upper regions, with curved layers deposited one over the other as depicted in Fig. 6.32. Further, comparing the results of Fig. 6.32 (a) and (b), the slant surfaces of the fine grove at the top right corner resulted in finer curved layer slices in the second case as the adaptive slicing algorithm picked up the difference. It is pertinent to point out here that the actual printing of surfaces of steep slopes or sharp curvatures as in this case is practically difficult to achieve on a 3-axis FDM system and require development of a 5-axis FDM in the future.

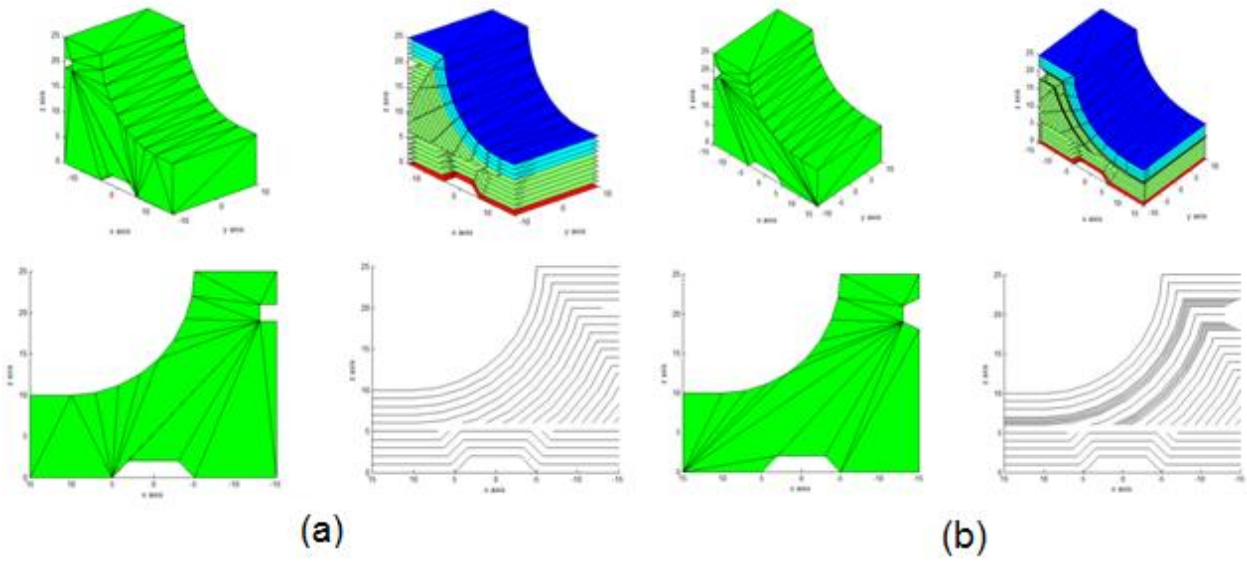

Fig. 6.32 Case 2; a more general solid model

Case 3

In order to test the integrated slicing algorithm using a more complex geometry, a bearing housing as shown in Fig. 6.33 is considered. The solid model of the bearing housing is developed in SolidWorks and exported into the .stl format file as shown in Fig. 6.33 (a). This case cannot be processed by a simple subdivision of the domain into two parts and requires further enhancements to be included. The first step is to identify the top and bottom surfaces of the part. When processed with the top-surface identification algorithm, the bearing housing will result in all the surfaces shown shaded in Fig. 6.33 (b). Overall, there are three top surfaces and two bottom surfaces identified in this case. The integrated slicing algorithm is further amended to use these multiple planes in pairs successively from the top and create the five sub-zones as shown in Fig. 6.34 (a) to (e).

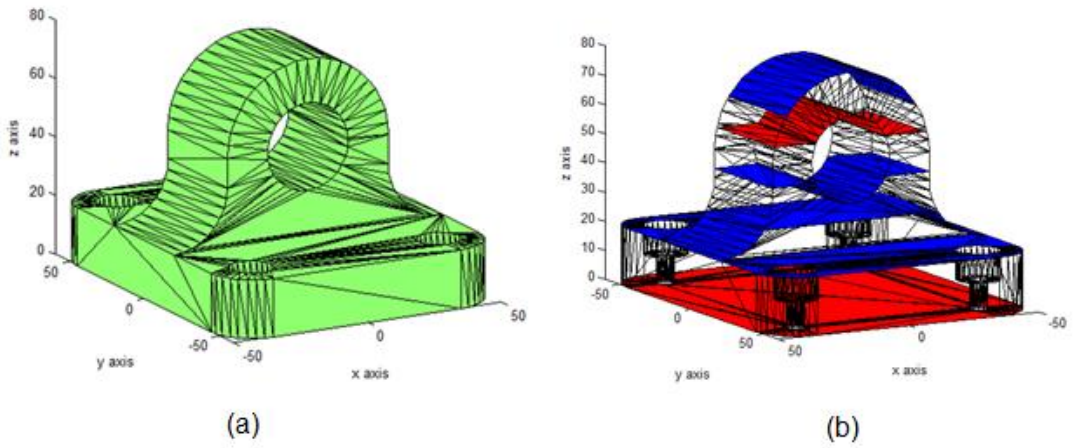

Fig. 6.33 A more complex solid model (bearing housing); (a) .stl format file and (b) top and bottom surfaces

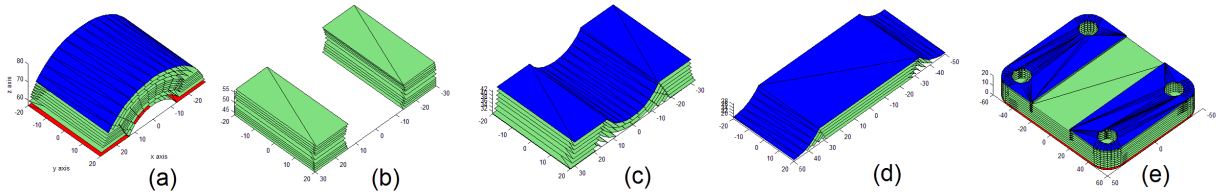

Fig. 6.34 Generation of sub-zones; (a) Zone A, (b) Zone B, (c) Zone C, (d) Zone D, and (e) Zone E

Each of these zones is considered next as an individual solid part and all these parts are further reformatted to be converted into .stl format files. Once this is done, each of these files is processed using the general integrated slicing software, but with specific constraints applied in different cases as discussed next.

Zone A

The solid model of zone A is presented in Fig. 6.34 (a) and the integrated algorithm processes this using the fully automated routine as in case 1 above. Both top and bottom surfaces are identified in this case, as shown by the surfaces shaded in blue and red respectively in Fig. 6.34 (a). The algorithm begins developing adaptive curved layers with the top surface first, and repeats the process until the boundary between the top and the bottom zones is identified based on the method explained in section 6.5.1. Uniform curved layers are generated by offsetting each curved plane by a layer thickness equivalent to the thinner layer. Further, considering the need to develop better surface quality at the top, the first of these layers is modelled with 45˚ raster paths as shown in Fig. 6.35 (a), while the subsequent layers are allowed 90˚ raster orientations as depicted in Fig. 6.35 (b).

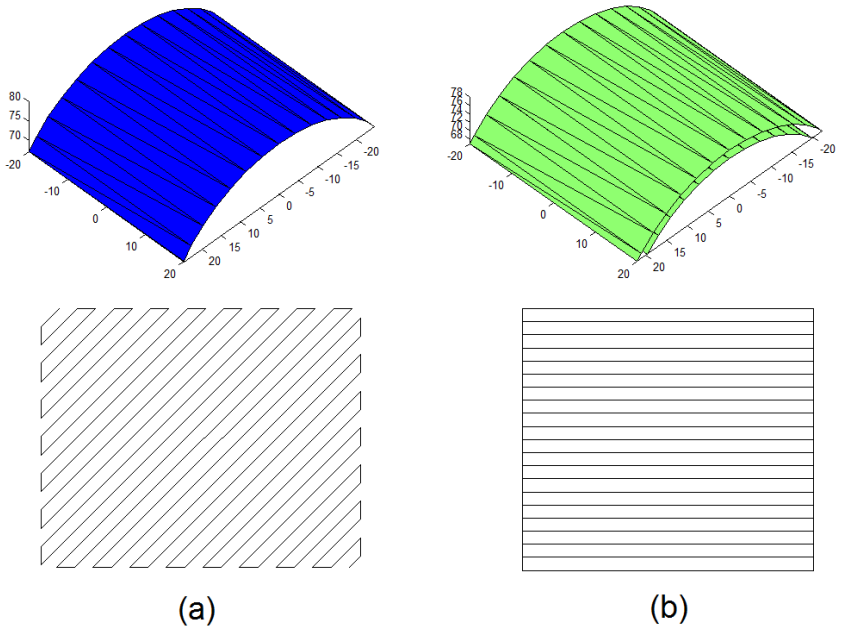

Fig. 6.35 Curved layer slicing and rasterisation in the upper part of zone A

Next, the bottom portion of this zone is sliced and considering that the existing bottom surface is a curved one, the algorithm processes this from bottom upwards, filling the volume with adaptive curved layers. It may however be noted that only the curved part of the bottom surface is so far identified and the two horizontal extensions on either side need to be added to the curved portion. A horizontal plane slices the part and obtains the intersection planes on either side of the central arch. The extended horizontal patches are then filled with triangular facets following the same outward normal direction as the central facets and then all of them are combined to form the full bottom surface representation for the lower part of zone A, as shown in Fig. 6.36 (a). Considering the need for a better surface quality, the bottom most layer is rasterised at 45˚ as shown in Fig. 6.36 (a), followed by a couple of thicker layers with 0˚ raster angles as shown in Fig. 6.36 (b). Subsequently, a number of thin curved layers are created due to the steeply varying slope of the curved surface with 45˚ criss-cross patterns as shown in Fig. 6.36 (b). While the 45˚ to 0˚ criss-cross pattern in the outer layers allows better meso-structures with layers of similar thicknesses, the 45˚ criss-cross pattern used with the thinner layers also gives the best meso-structure with the finer filament used for filling all around this zone as shown in Fig.6.36 (c).

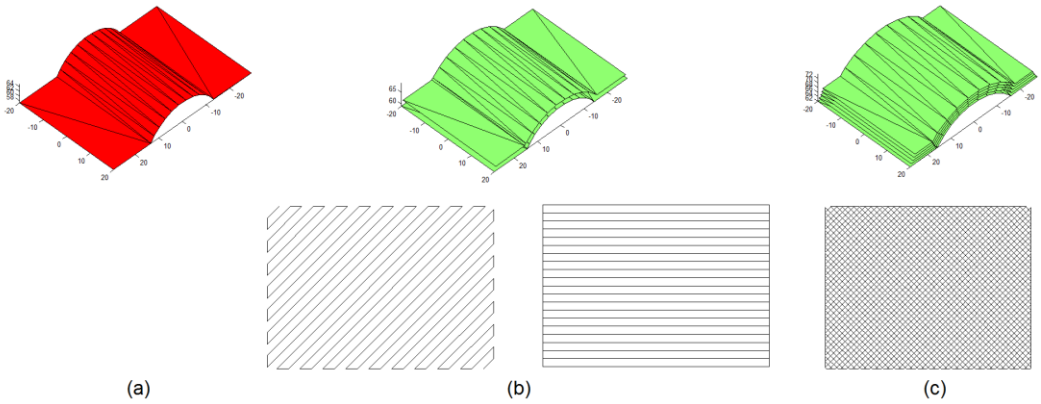

Fig. 6.36 Adaptive curved layer slicing and rasterisation in the bottom portion of Zone A

Zone B

Zone B consists of two vertical rectangular slabs as shown in Fig. 6.34(b) and is a typical flat layer case. When processed using the integrated slicing algorithm, adaptive flat layers are generated with five thinner layers from both ends and a couple of thicker layers at the centre due to the facet structure on the side face and the residual height considerations. Again, considering the mechanical strength required for this portion, all the thin layers are rasterised using 45˚ criss-cross patterns as shown in Fig. 6.37 (a) and (c) and the thick layers are employed with 90˚ raster directions as shown in Fig. 6.37 (b). According to the theoretical models of Chapter 3 depicting the mechanics of adaptive flat layer slicing, better and uniform part strength can be achieved, if the two central thick layers are printed at speeds slower than the speed used for thinner layer zones,

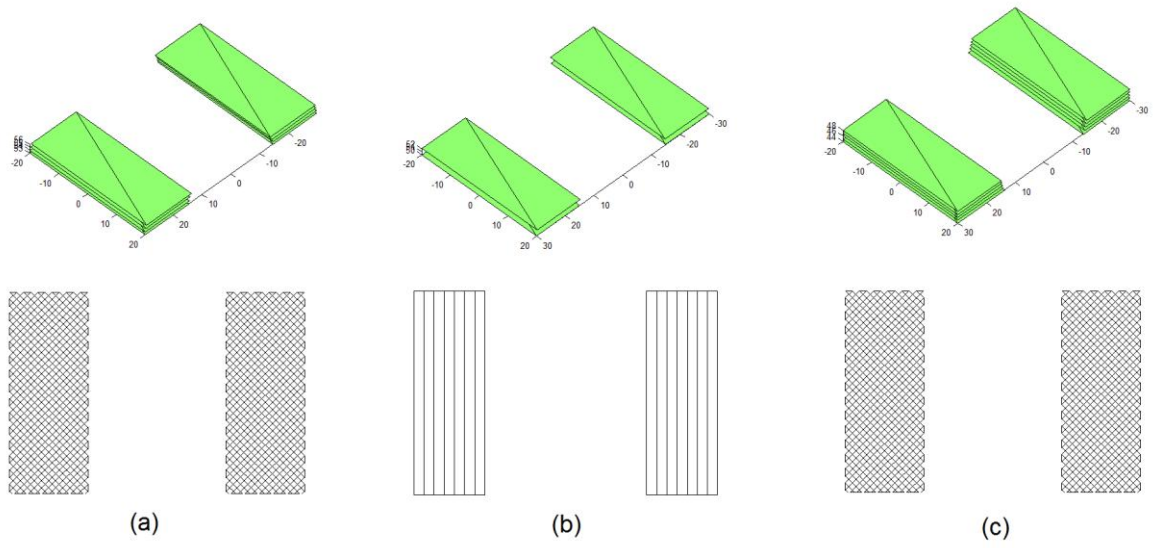

Fig. 6.37 Adaptive flat layer slicingin Zone B

Zone C

As shown in Fig. 6.34 (c), the top surface of zone C is the half-circular curved surface. While the bottom surface is generated by one of the intermediate critical planes at the top of the bottom square base of the bearing housing. Slicing by two horizontal planes, one at the top and the other one at the bottom of this zone will allow the reconstruction of the top and bottom faces, and restructuring of the .stl format file. Further processing by the integrated slicing scheme identified the zone to be suitable for adaptive curved layer slicing based on the top half-circular form and sliced the zone accordingly. However, considering that there are no drastic changes in the facets on the side surfaces, thick uniform curved layers are generated. Based on surface and strength considerations, the top surface is modelled with 45˚ raster patterns while the other layers are rasterised by 45˚ criss-cross patterns as shown in Fig.6.38.

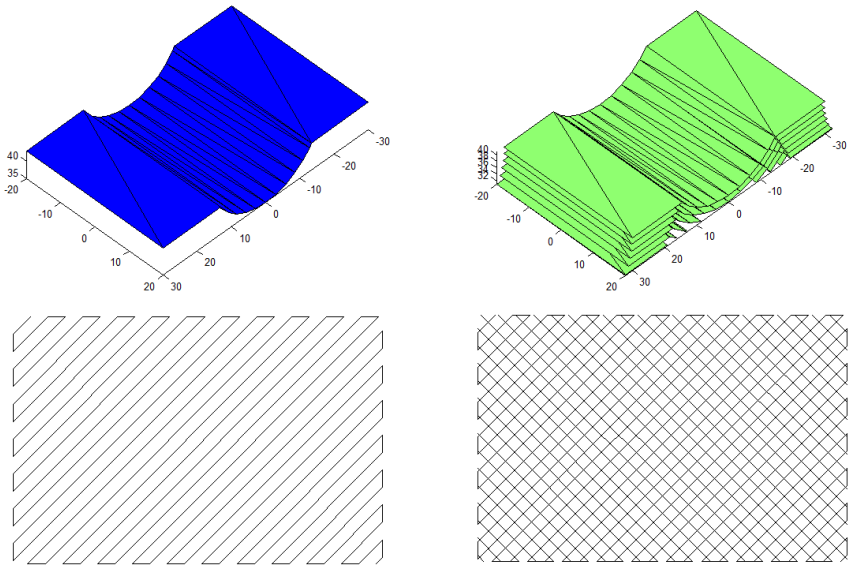

Fig. 6.38 Uniform curved layer slicing in Zone C

Zone D

Zone D is typically formed as the light-curved side shoulders on the vertical slab of the bearing housing are identified as possible intermediate critical top surfaces as depicted in Fig. 6.34(d). The other faces and the facet structure are non-existent initially. As with the other zones, the top and bottom horizontal planes are used to develop and tessellate the top and bottom surfaces. These surfaces are then integrated with the other facets already existing to complete the triangulation of the zone. Once this is done, the integrated slicing scheme easily identifies this as a typical flat layer case, but considering the slanting side surfaces, adaptive flat layers are generated as shown in Fig. 6.39 with 45˚ criss-cross raster patterns employed on all layers. Looking at the side view of the stacked curved layers, it may be observed that this layer configuration might cause a slight variation in dimension while actually printing. With each layer printed upon the previous one, an extra material deposition takes place both at the start and end of each raster line, thus increasing the depth slightly. To compensate for this, a corresponding recess needs to be chiselled out of the top surface of zone E, as discussed next.

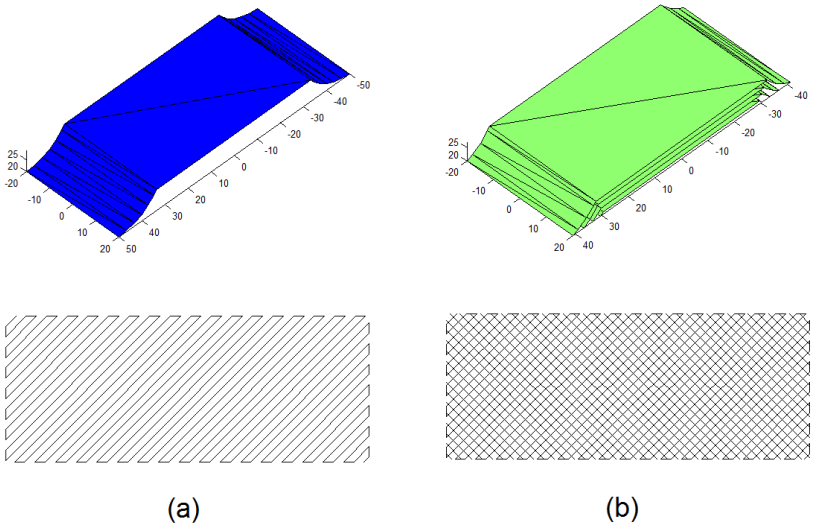

Fig. 6.39 Uniform curved layer slicing in Zone D

Zone E

Zone E as shown in Fig. 6.34(e) again is a typical flat layer domain. As mentioned above, a small recess of the size of the bottom surface of zone D needs to be developed on the top surface of zone E. The depth required for this recess actually varies between thicknesses of one to two layers, but based on calculations it is found to be equal to one layer thickness in the current case. Accordingly, the .stl file is restructured and re-triangulated for further processing. Zone E now requires being subdivided further using the same procedure as employed for the whole part. Once the set of top and bottom surfaces are identified and used to partition the volume of zone E, three subzones result as shown in Fig. 6.40 (a), (b), and (c). While Fig. 6.40 (a) is the result of the central recessed portion and the two side steps erected, Fig. 6.40(b) and (c) become necessary, as the holes in the baseplate are countersunk. Again, each of these zones is restructured and re-triangulated and processed using the integrated slicing algorithm. All zones are by far modelled with adaptive flat layer slicing; however, each of them achieved flat layers of uniform thickness. The first sub-zone shown in Fig. 6.40 (a) is modelled with thinner layers considering the relatively lesser depth and the raster angle is 45˚. The other two zones received uniform layers of the larger thickness, with criss-cross raster patterns, as shown in Fig. 6.40 (b) and (c).

Fig. 6.41 presents the sequence of printing and accumulation of the different zones to be able to construct the 3D form of the bearing housing. Within each zone, the layer structure and the intra layer raster path orientations follow the same schemes as discussed above. It may be noted that the last zone to be printed (zone A) would require the construction of a support structure using similar methods as presented in earlier chapters. Fig. 6.42 presents the overall and the side views

of the mixed layer structures developed for the bearing housing by the integrated alternative slicing scheme.

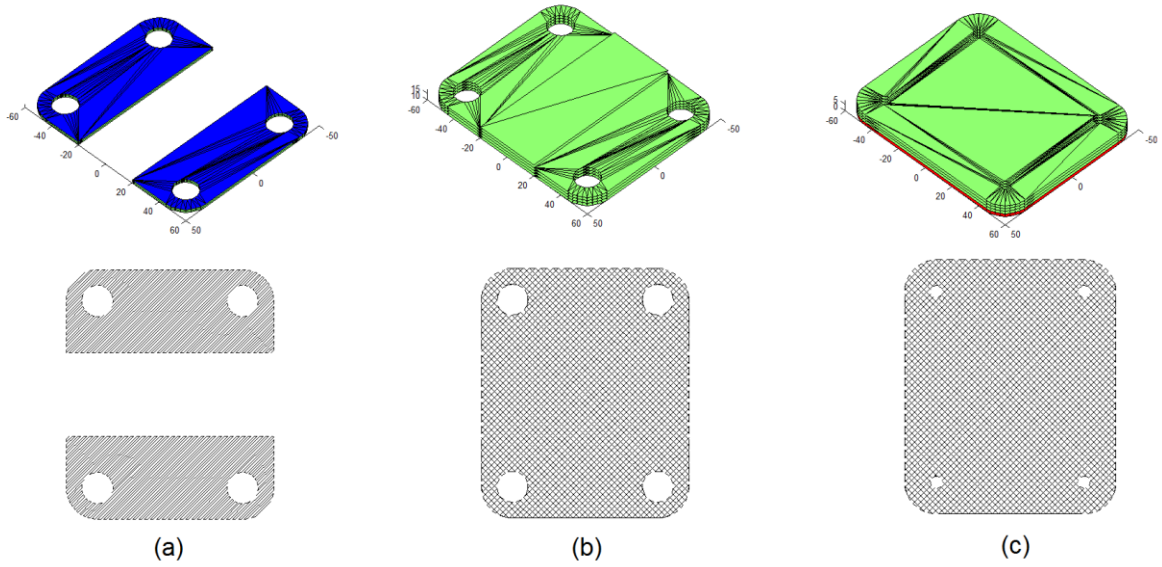

Fig. 6.40 Adaptive flat layer slicing in Zone E

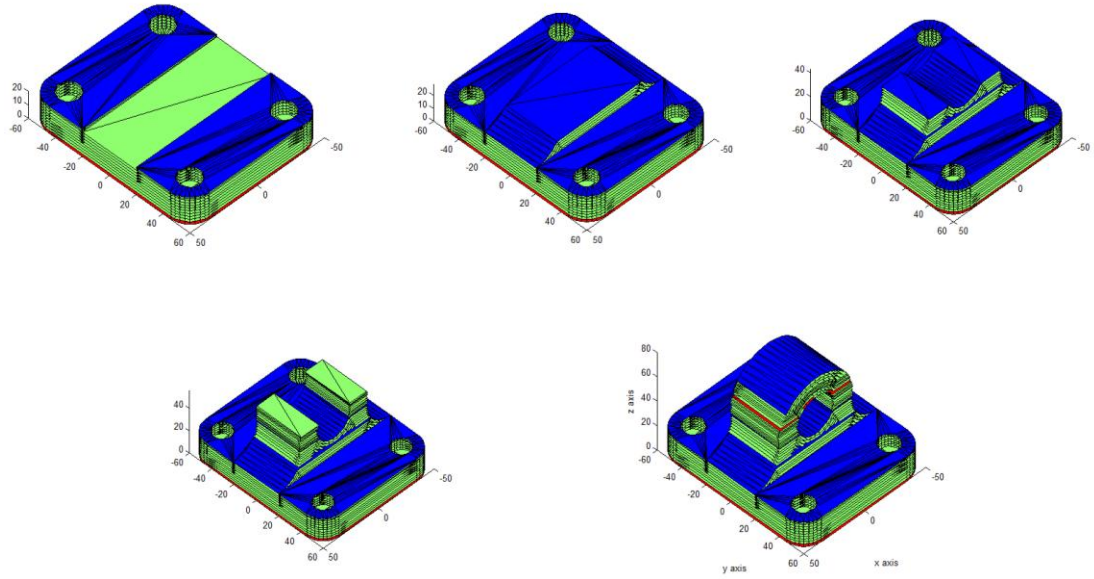

Fig. 6.41 Building the bearing housing from the bottom upwards

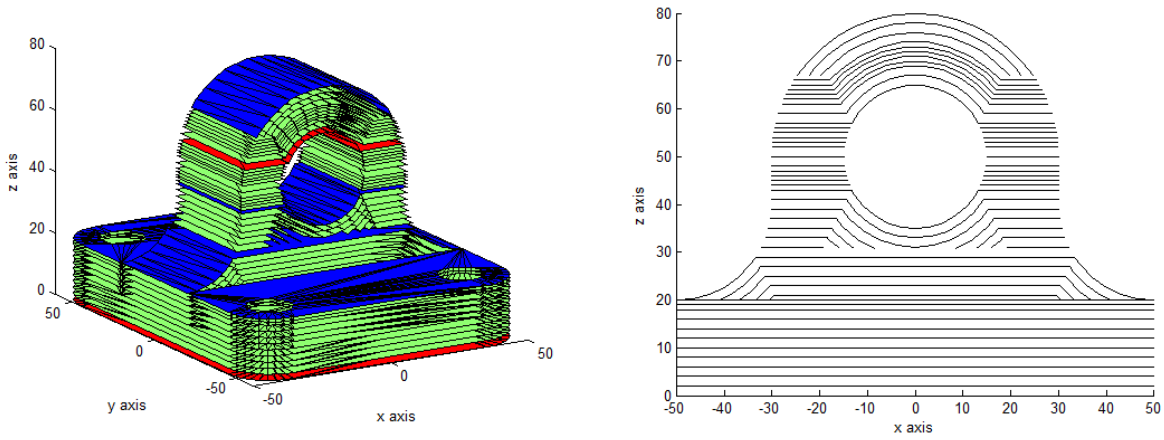

Fig. 6.42 Integrated alternative slicing scheme applied to the bearing housing

6.7 Discussion on integrated alternative slicing and deposition strategies and conclusions

The adaptive flat and curved layer slicing together with raster orientation are combined into a unified slicing approach referred to as the integrated alternative slicing scheme and applied to three different cases as discussed in the previous section. The overall performance of the integrated approach is evaluated discussing the critical results now.

For case 1, one of the samples printed with the integrated approach together with the same part printed with uniform flat layers are shown in Fig. 6.43 (a) and (b) respectively. The strand structure in Fig. 6.43 (a) clearly shows both curved and flat layers of varying thickness used in different zones, demonstrating the successful implementation of the proposed scheme. However, the strand structure looks a little ragged as the filament sizes used are relatively large (1.0mm, 2.0mm), considering the practical limitations of the make-shift FDM test bed. This appearance

will be much better when finer filaments are used on fully commercial systems under more controlled conditions of printing in the future.

Nevertheless, comparing the two specimens in Fig. 6.43, a striking difference is that the stair-case effect is sufficiently taken care of by the curved layers as evident from Fig. 6.43 (a). Further, the bead-like strands observed in Fig. 6.43 (a) are the result of adjusting the print speed conditions to achieve adaptive layers from the nozzle of a fixed diameter. These aspects can also be improved, if multi-head systems with multiple nozzles are used in the future.

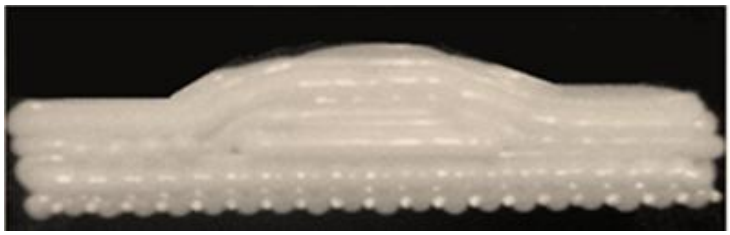

(a) Integrated slicing and printing

(b) Uniform flat layer printing

Fig. 6.43 A Comparative evaluation of printed samples in Case 1

The solid model of Case 2 is processed using both integrated alternative slicing and normal uniform flat layer slicing methods and the side-views of the CAD model and the layer structures obtained using both approaches are shown in Fig. 6.44 (a), (b), and (c) respectively. A sectional

view is generated at the same location for all these three objects and shown juxtaposed against each of them as shown again in Fig. 6.43 (a), (b), and (c). First, a comparison of the vertical dimension of the sectional views clarifies that the integrated slicing model allows an exact reproduction of the dimension as per the original CAD model. Whereas, the uniform flat layer model lost this dimension almost by about 6% due to the stair-step effect. In actual practice, this loss may be even more, depending on the part geometry and the curvature in the case of curved surface forms.

An interesting differentiation can be made using the mesostructural patterns shown in Fig. 6.44 (b) and (c). The black dots represent the location, number and relative sizes of air gaps obtained within the particular section with different slicing schemes. First, it may be noted that the total number of air gaps is lesser in the case of the domain processed using the integrated slicing scheme which is 165 as against a total of 225 holes obtained with the uniform flat layer slicing. Evidently, the sizes of these black dots representing the air gaps are larger in the case of the model sliced with the integrated alternative slicing scheme due to the angular orientation of the strand structure.

However, it may be noted that these shapes are only geometrical predictions, and when the part is actually printed, there will be time and temperature dependent coalescence and inter-strand neck growth and bonding, leading to a partial filling and reduction of size of each of these air gaps. Considering the appropriate choice of raster orientations and suitable print speed and time conditions, it is envisioned that the air-gap shrinkage will be more efficient with the integrated slicing approach. Eventually, it is the total number of these air gaps that will control the

mechanical properties, and the higher pin-hole porosity makes the uniform flat layer parts relatively weaker.

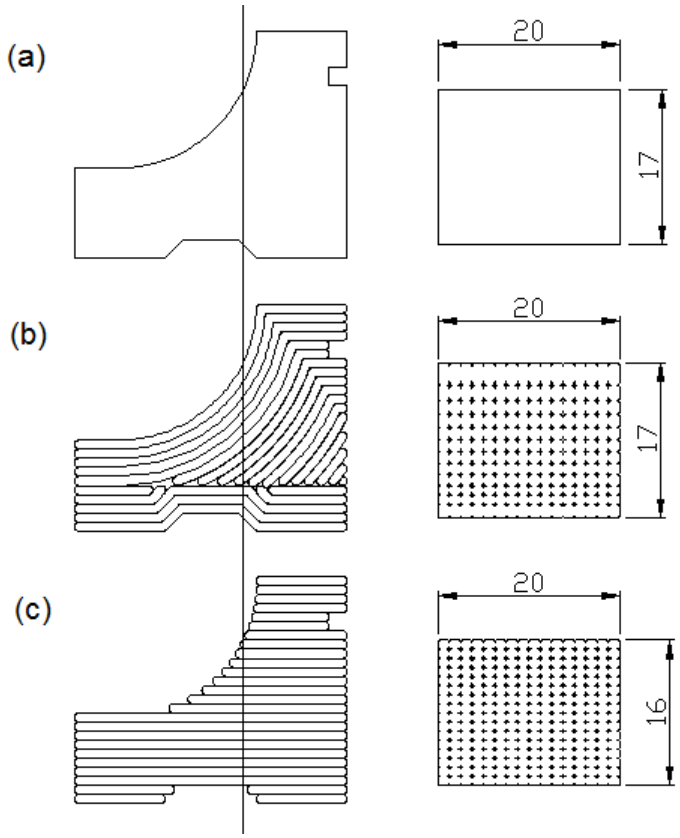

Fig. 6.44 A comparative assessment in case 2; (a) CAD drawing, (b) processed using integrated slicing, and (c) processed using uniform flat layer slicing

The bearing housing considered as Case 3 is now sliced using uniform thin flat layers, uniform thick flat layers and the integrated adaptive slicing approaches and the side views of the resulting layer structures at different locations are presented in Figs. 6.45 to 6.47. First, the general slicing patterns obtained with different approaches show marked variations in the overall layer

structures as observed in Figs. 6.45 to 6.47 (a). The top curved surface of the top arch suffered stair-casing effects to varying degrees as may be observed in Figs. 6.45 (b) and 6.47 (b). At the same time, the curved layer slicing allowed complete elimination of these defects at the top, as evident clearly, in Fig. 6.47 (b). Other than a couple of minor disturbances at the two extreme points, the rest of this zone is filled seamlessly with curved layers. However, while printing, there is always a dwell period both at the start and end of each deposited road resulting in a slightly excessive material deposition and will take care of the minor defects at the two extremities. Further, the most important aspect to be observed in this case is the distinct fibre continuity obtained with the integrated adaptive slicing approach as shown in Fig. 6.47 (b). Based on the experimental results of Chapter 5, it may be readily understood that the part strength with this layer structure is far better compared to the other two cases.

Again the central circular detail suffered great losses in surface quality in both cases of uniform flat layer slicing as seen in Figs. 6.46 and 6.47 (c). However, the loss of quality is much more pronounced in the thicker layer case presented in Fig. 6.46 (c). In fact, there is a long dash of layer missing both at the top and the bottom of the circular pattern as depicted in Fig. 6.45 (c). Again, the fibre continuity shown in the case of the integrated adaptive slicing method in Fig. 6.47(c) is far superior and a characteristic benefit resulting from the choice of curved layers.

Similar patterns can also be observed from the three cases presented in Figs. 6.45 to 6.47 (d). Stair-case effects resulted in a loss of surface quality with both thin and thick flat layer slicing, while the effects are more adverse with thicker layers, as may be expected. However, the integrated adaptive slicing scheme used both curved and flat layers in this zone. As may be

observed in Fig. 6.47 (d), the curved layer portion completely eliminated the stair-step effects, while there is some slight residual stair-casing in the flat layer part. It is pertinent to point out that the integrated schemes though effective in eliminating problems like stair-casing in most situations, cannot be expected to eliminate all problems completely from all zones. When the surfaces are too steep, curved layers cannot be used as it may require printing almost vertically, which is practically impossible to be achieved with 3 Axis printing.

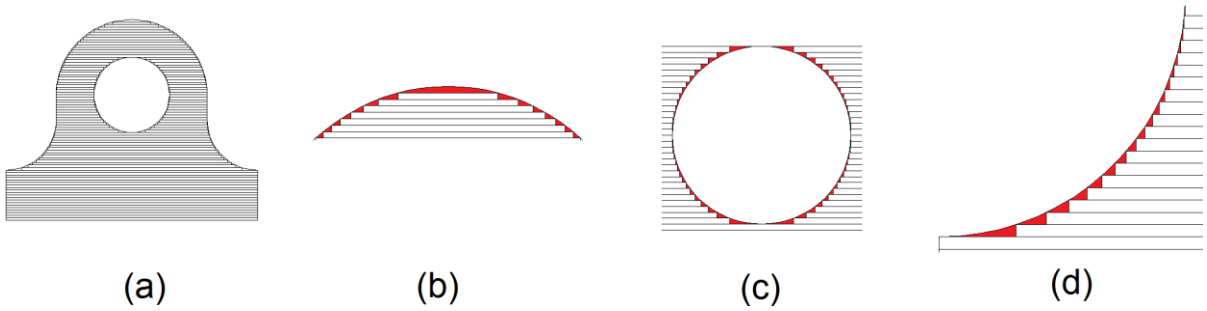

Fig. 6.45 Case 3: Uniform flat layer slicing with thinner layers (a) overall view, (b) top circular profile, (c) central hole, and (d) the curved side fillet

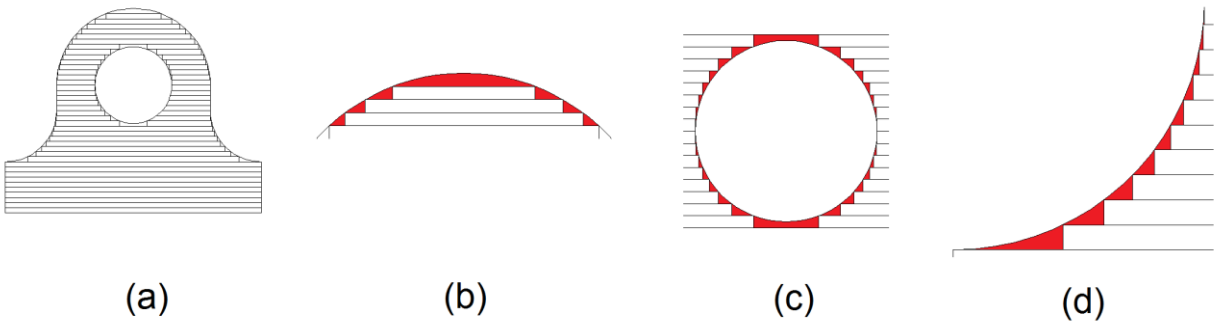

Fig. 6.46 Case 3: Uniform flat layer slicing with thicker layers (a) overall view, (b) top circular profile, (c) central hole, and (d) the curved side fillet

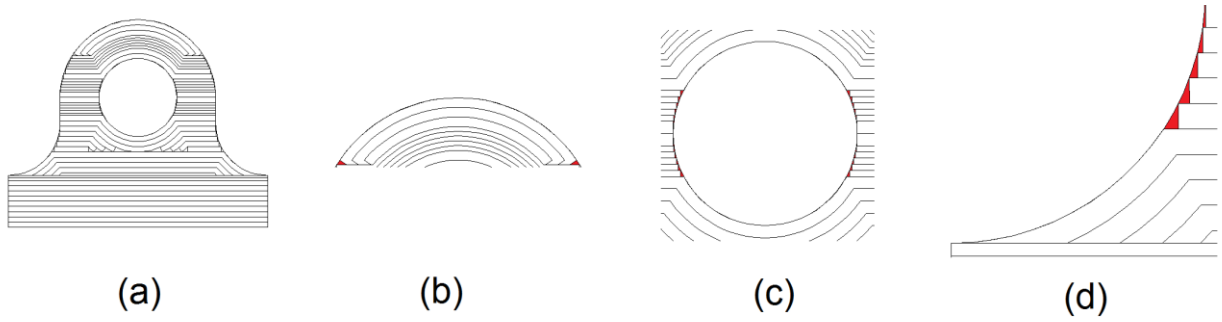

Fig. 6.47 Case 3: Integrated alternative slicing (a) overall view, (b) top circular profile, (c) central hole, and (d) the curved side fillet

In conclusion, an adaptive flat layer slicing scheme is identified, enhanced and practically implemented. A comparative experimental evaluation of uniform and adaptive flat layer slicing with uniform curved layer slicing is undertaken and the results proved the curved layer slicing to score the best in terms of flexural loads under three point bending. The curved layer slicing scheme is equipped with the adaptive layer option next, further enhancing the curved layer slicing algorithms. A couple of solid models analysed with the adaptive curved layer approach proved the algorithm to be effective in capturing sharply varying surface slopes or very fine details in solid models. Practical implementation of curved layer adaptive slicing proved thicker curved layers printed with the same total time to perform the best, thus validating the experimental and analytical models presented in Chapter 3 to be valid even with adaptive curved layers.

A region based sub-division method is developed next for combining flat and curved layer approaches together within the domain of a given solid model. Mathematical algorithms are developed based on .stl format files. The chordal error evaluation method was effective in

dividing the solid model domain into curved and flat layer regions. The mixed layer approach usually takes more time to print compared to the uniform flat layer approach, but the surface and internal meso-structures are much improved.

The adaptive flat and curved layer approaches together with schemes to choose proper raster orientations are combined into a unified approach, the integrated alternative slicing algorithm and coded in MATLAB. The algorithm operates in three possible routes; a fully automatic routine for relatively simple shapes, with a user-specified plane to divide specific solid forms into two distinct zones and finally, a more general approach involving multiple divisions, for more complex solid forms. Three case studies are considered and successfully processed, evaluating the effectiveness of the integrated slicing scheme. While the integrated slicing schemes are successful in handling different geometrical complexities, the layer patterns are observed to overcome typical shortcomings such as stair-step effects, while taking care of other aspects such as fibre continuity simultaneously in specific zones. The mesostructures are shown to be improved with the integrated scheme based on CAD models at specific sections and the benefits are envisioned to be equally good in all cases studied.

Chapter 7 Conclusions

7.1 Fused deposition modelling; some general observations

Several rapid prototyping technologies surpassed the initial stages of infancy and gradually became recognised as possible solutions for the direct manufacturing of end-use products in specific cases. Commonly referred to as additive manufacturing, this set of manufacturing processes is currently drawing wide attention and fused deposition modelling (FDM) is one of the significant techniques in this realm. In FDM, a polymer material in the form of a filament is heated and extruded through a nozzle, to be printed on a substrate as closely spaced strands or roads. Inter-road and inter-layer diffusion allow for bonding and consolidation of the material within and across layers to build 3D forms.

Within each layer, material deposition pathways are parallel and oriented in specific directions, referred to as the raster orientation. The overall layout of the stacked layers and the raster orientations, together with other process variables such as filament size, gap between filaments and time and speed of printing influence the final material structure; a composite of partially coalesced strands intertwined with air gaps. Literature also presented several possible defects in FDM parts, broadly classified into external and internal types. Overall, the internal meso-structure and external and internal defects if any will control the bulk material behaviour as well as the quality and performance of specific FDM parts. At a macro level, the process and geometrical parameters and their combinations will control the eventual mechanics of material consolidation and subsequent performance.

Closer to the point of adding the material point-by-point and line-by-line, the raster orientation plays a significant role. Varying raster angles will affect the quality of a single layer differently in different situations, while alternative raster orientations across successive layers further confound the mechanics. Uniform flat layers often result in shortcomings both in terms of stair-step effects and discontinuities in the fibre structure. While both are detrimental to the overall part quality, adaptive slicing emerged as a possible remedy, but is generally effective only to some extent, as fibre discontinuities are still at large, though stair-step effects are resolved. In addition, the adaptive slicing schemes involve variations in speed and time of printing which will add further complications to the sintering phenomena and associated material consolidation aspects.

Specific parts with curved external features and thin shell-like forms are more adversely affected with flat layer slicing and deposition. Stair-step effects are more pronounced and discontinuous fibres result in a profound loss of the internal structure and the integrity of the material. Curved layer slicing evolved as a plausible solution, but the solid modelling algorithms and practical implementation schemes are found to be inadequate and requiring further attention and enhancement. More intriguingly, curved layer deposition is effective in handling the surface quality, but requires additional adaptive layer enhancement to be able to handle the presence of finer details if any in the solid models processed. This leads to curved layer adaptive slicing and the time and print-speed interactions with the filament thickness and the resulting coalescence mechanics.

It is also apparent that both curved and flat layers have their own merits and limitations, and for any given part, the best possible solution is a suitable combination of both methods together with appropriate raster orientations. Based on these observations, the current hypothesis envisioned the final overall quality of FDM parts to be enhanced through proper utilisation of appropriate combinations of uniform, adaptive, flat, and curved layers and raster orientations. Validation of this premise required theoretical and experimental evaluation of the mechanics of raster orientation and adaptive slicing followed by mathematical algorithms developed for different slicing schemes and practical implementation in specific cases and development of an integrated slicing scheme combining different approaches into a unified algorithm. Typical achievements made in each of these directions, generic observations made answering critical research questions and the more specific conclusions made from analytical and experimental results are presented next.

7.2 Analytical and experimental investigations and generic conclusions

Adaptive slicing involves programmatically varying the layer thickness mainly as to change from relatively thicker layers to relatively thinner layers where surface quality or effective reproduction of finer details are of primary concern. Though a promising option, adaptive slicing could also lead to certain complications in physical reality. The print speed and time will interact with the filament size and affect the coalescence and in turn the mesostructures. The actual mechanics needs to be understood before making any meaningful adjustments. Analytical models are built based on moment of inertia calculations on multi-strand sections. The modified Frankel-Eshelby model for diffusion sintering is integrated with the moment of inertia

calculations to evaluate the time and speed dependent coalescence and resulting mechanical characteristics of specimens. Practical implementation of adaptive flat layer slicing allowed building test specimens with varying process conditions. Three point bending tests conducted on specimens produced with varying layer thicknesses allowed validation of the theoretical models developed.

In general, the inter-road and inter-layer coalescence depends on the size of the filament and the time given for a unit length to be deposited, considering the temperature to be uniform. While predictions based on the analytical models developed are in similar lines, the effect of varying layer thickness also interacts with the print speed. With the layer thickness fixed, as the speed of printing increases, the time for a unit length of deposition decreases resulting in a decrease in coalescence due to a shorter sintering time. On the other hand, with a constant speed of printing, as the filament size decreases, there is more time spent with each unit volume or area filled, and the coalescence is better and the mechanical characteristics are improved. Based on these observations, it is clear that true benefits of adaptive slicing can only be realised by properly adjusting the filament size, print speed and total time of printing at any zone within a given part.

Raster angle orientations dictate the pattern of filling the fused material and commercial systems often use 45˚ criss-cross patterns across successive layers. Theoretical understanding of the raster angle effects was attempted earlier using the classical lamination theory. Considering the complexities arising, analytical models are developed applying the elastic plane stress theory to a single strand considered at different orientations. The inter-road sintering phenomena predicted by the modified Frenkel-Eshelby model are again combined with the force equilibrium equations

to integrate the coalescence aspects with the raster angle mechanics. Specimens are printed with varying raster angles for tensile tests aimed at establishing the true role of the raster angle.

Results of tensile tests clearly demonstrated the significance of raster orientation and the ultimate tensile strength is found to decrease with increasing raster angles. The analytical predictions are also in similar lines and there is a good correlation between the two results. Both normal stress and elastic modulus values decreased with increasing raster angle, but to a varying degree, as dictated by the inter-road coalescence. However, the normal strain values varied differently at different levels of coalescence. The Poisson's ratio values generally increased with increasing raster angles and again with some interaction effects from coalescence. However, at higher coalescence and mid-range of raster angles, the Poisson's ratio values predicted are greater than 0.5, which appears to be an anomaly, but is also reported earlier, with specific structure-dependent materials.

Curved layer slicing evolved as a possible means of overcoming the typical shortcomings of flat layers, including stair-step effects and the fibre discontinuity in specific cases. Considering the lack of ready solutions, mathematical algorithms are developed based on a three-plane intersection scheme and successfully applied to selected solid models. The split-node problem arising is resolved either by evaluating average locations and eliminating the duplicate nodes or by creating new triangular elements with the nodes additionally created.

Test pieces of light-curved shapes are printed on the FDM test bed based on the curved layer and raster path data generated. While clearly demonstrating improved surface qualities, curved

layer specimens also performed much better under three point bending loads, compared to the flat layer counter parts. Fracture modes clearly differentiated the curved layer specimens with much better resistance due to the combined action of the continuous fibre structure against the flat layer samples, suffering from stress concentration effects and shear failure at the weak interfaces between flat layers.

Flat layers of varying thicknesses can be generated within a given solid model based on mathematical algorithms capable of identifying specific features that necessitate the use of adaptive layers. The algorithm based on the evaluation of the cusp height is used in the current work for further enhancement and implementation. The residual height calculations are included to handle the issues with missing details that are smaller than the cusp height considered. Uniform, adaptive and curved layer slicing solutions are also comparatively assessed by means of light-curved parts printed and tested under three point bending.

The curved layer algorithm is further enhanced with the adaptive slicing capability next, again based on cusp and residual height criteria. With more complex side surface details, the curved layer algorithm needed further amendments. The angle of the outward normal for each facet is first used to identify the top surface facets. Considering the maximum height difference between the collected triangular facets an offset volume is segregated and then all the facets within this volume are considered for curved layer offsetting. Flipped-element problems often arise with slanting side surfaces and are eliminated by comparing the directions of outward normal lines from the offset elements, while split-node issues are resolved in similar lines, as with uniform curved layers.

The practical significance of adaptive curved layer slicing is evaluated again by means of three point bending tests conducted on the light-curved parts as used for other similar tests. A mixed-mode solution to create both curved and flat layers within the domain of a given model is developed next. Chordal height calculations are used as the criterion to divide the solid model into flat and curved regions. The algorithm developed assumes a pre-determined print orientation for the given part and works starting from the top surface, filling the upper part of the domain with several curved layers and the flat layer scheme takes over, once the chordal-height criterion is satisfied. .

Finally, all the alternative slicing schemes investigated and the raster orientation choices are combined into a single algorithm with multiple options and coded using MATLAB. Considering solid models of varying complexities, three possible scenarios evolved: a direct and automatic routine for relatively simple shapes, dividing solid models of certain forms into two domains, and a more general scheme with multiple subdivisions for more complex solid models. Referred to as integrated alternative slicing, the new scheme is tested processing three typical cases requiring the three solution options developed.

While the adaptive flat layer slicing algorithm implemented is effective together with the residual height amendments, the experimental comparison showed some improvement with the basic curved layer slicing over both uniform and adaptive flat layers. The curved layer adaptive slicing algorithm performed well when implemented on light-curved parts with both slanting side surfaces and very fine projecting details. Reduced stair-step effects resulted with the use of finer curved layers within the zone of slanting side surfaces. The adaptive curved layer slicing

scheme is also effective in capturing very fine details in the solid model and alter the layer thickness accordingly, while maintaining the curved layer profiles to be achieved for fibre continuity. The three point-bending tests conducted on light-curved parts printed indicated adaptive curved layer to be better performing under mechanical loads. With the total time of printing for all cases kept the same, the sample with the thickest curved layers is printed with the slowest speed, allowing for more sintering time per unit printed length and consequently, better mechanical attributes of the part.

The integrated alternative slicing schemes are successfully developed and applied in three cases with varying complexities. While in all cases the part print orientation is predetermined, the slicing attributes are different and varied based on geometrical complications of specific solid models. The first case is the same light-curved part as used for most experimental and analytical modelling work done in the current research. The integrated slicing scheme automatically identified the top portion as best processed with curved layers and also effectively ascertained the boundary layer between curved and flat layered regions using the chordal height criterion.

The second case is slightly more complex, and needed the second approach, where a user defined split-plane is a prerequisite. For the solid model considered, both top and bottom surfaces needed curved layer filling based on the outer features and hence the algorithm filled the two regions with curved layers from both ends, until the two fronts met on the plane of separation. A bearing housing is used as the most general and relatively complex case, including multiple features and regions. The third approach is needed, dividing the total domain into several subdomains and applying the integrated alternative slicing schemes to process each of

them. One of the subdomains required further subdivision into three smaller volumes before being filled with layers of appropriate structures.

Overall, the integrated alternative slicing scheme performed well in capturing the specific requirements of critical geometries considered. Curved outer surface profiles received curved layer filling close to the boundary. Sharply varying features or finer part details received filling by thinner layers. Appropriate raster orientations could also be employed for different layers in different regions based on the requirements by the local conditions. The knowledge gained from the analytical and experimental evaluations undertaken on the raster mechanics, as well as adaptive flat and curved layers sufficiently supports the mixed layer structures developed by the integrated slicing schemes to be better solutions compared to the conventional uniform flat layer approach. Evidently, the analytical and experimental work done, the results generated and the inferences drawn, together with the enhanced layer structures evident from the case studies considered at the end give strength to the hypothesis that fused deposition modelling can be further enhanced using appropriate combinations of alternative slicing and deposition schemes. More specific conclusions drawn from different aspects investigated are listed in the next section.

7.3 Significant conclusions drawn based on the results of the current research

Adaptive flat layer slicing

- Analytical models are built based on the second moment of area calculations and modified Frankel-Eshelby equations to predict the effects of varying thicknesses and the associated print speed and time interactions
- Based on the predictions by the analytical models, the moment of inertia and consequently the bending strength are observed to decrease with increasing print speed and increase with increasing total print time.
- For a part of given dimensions, if the print speed is kept constant, the coalescence increases with increasing number of layers.
- Similarly, with a part of fixed dimensions, both second moment of area and bending load steeply rise with increasing number of layers and stabilize after about 10-15 layers.
- Again, with the part dimensions fixed, and with a given number of layers (fixed layer thickness), coalescence, second moment of area, and bending load decrease with increasing print speed, almost as hyperbolic functions.
- For a given part, coalescence, second moment of area, and bending load decreased with increasing number of layers, with the total print time fixed at 75 s.
- Also, with fixed part dimensions, coalescence, second moment of area, and bending load increased steadily with increased total time when the number of layers is equal to 10.
- Three point bending tests on specimens printed with dimensions 50mm X 20mm X 4mm, resulted in both thinner and thicker layers employed at relatively slow speeds giving slightly better compressive loads than those printed at higher speeds

- Again, for parts of the same dimensions, with the total print time kept constant, thicker layers gave better mechanical properties.
- From a different viewpoint, better mechanical properties achieved with thicker layers are associated with reduced print speeds and consequently result in increased total print times.
- Analytical models also predicted the maximum compressive stress values to be higher with thinner layers while printing a given sample of fixed dimensions at a given speed.
- Similarly, the maximum bending stress of samples of fixed dimensions decreased with increasing speed of printing with both thicker and thinner layers.
- For the same parts, the bending stress increased with increasing total time of printing.

Raster angle mechanics

- Tensile tests conducted on specimens produced with varying raster angles proved that the tensile strength gradually decreases with increasing raster angle.
- The maximum and minimum stresses are 30.79 MPa and 10.08 MPa obtained at 0˚ and 90˚ respectively.
- Analytical models are developed to evaluate the raster angle effects combining the elastic plane stress theory with the inter-strand coalescence on single strands considered at varying angular orientations.
- The ultimate strength model predicted the maximum and minimum stresses as 36.19 MPa and 14.05 MPa at raster orientations 0˚ and 90˚ respectively

- Analytical predictions correlated well with both experimental results of the current work and results reported in the literature in the case of the ultimate stress.
- The elastic modulus decreased with increasing raster angle and attained a minimum at around 50˚ to 60˚, depending on the coalescence level.
- Shear stress values in general decreased with increasing raster angles but to varying degrees, depending on the coalescence values.
- The shear modulus remains stable at lower raster angles, but gradually decreases beyond 45˚at varying rates depending on the magnitude of coalescence.
- Analytically, the Poisson's ratio is observed to vary widely with varying coalescence and raster angles and the possibility of achieving values above 0.5 is noted.
- The plastic spin is found to peak at around 45˚ raster angle, for different levels of coalescence.

Uniform curved layer slicing

- The three plane offset procedure proved to be a better enhancement for curved layer slicing.
- Split-node problems arising while offsetting specific triangular facets can be resolved either by finding average nodal locations or by constructing new elements.
- Deposition path generation with varying raster angles has been successfully implemented with curved layer slices.
- Curved layer fused deposition modelling is successfully implemented on a FDM test bed using a couple of different materials.

- Curved layer specimens exhibited better surface qualities as well as meso-structures resulting from long continuous fibres with better inter-road and inter-layer coalescence.
- The average fracture compressive load of curved layer parts under three point bending increased almost by 40%, compared to that of the flat layer counter parts.
- Flat layer parts fail relatively easily due to fracture cracks initiated at the bottom and growing across the specimen.
- Flat layer samples also undergo shear failures resulting from weak inter-layer bonding.
- Curved layer samples perform better due to a number of sufficiently fused parallel filaments acting together to resist deformation, crack formation, and growth.
- SEM photographs show evidence of fibre continuity resulting in better part performance in the case of curved layer fused deposition modelling.

Integrated alternative slicing

- An adaptive flat layer slicing scheme is identified, enhanced, and practically implemented.
- Uniform and adaptive flat layer and curved layer samples are evaluated experimentally comparing bending stresses.
- Three point bending test results show that curved layer samples perform relatively better.
- The curved layer slicing scheme is enhanced with the adaptive slicing option
- Solid models analysed with the adaptive curved layer approach proved the algorithm to be effective in capturing sharply varying surface slopes or very fine details in solid models.

- With the total print time kept constant, thicker curved layers used to print test specimens of fixed dimensions gave the best compressive load results.
- With specimens of similar dimensions, and the total time of printing fixed at around 480 seconds, thicker curved layers appear to be more effective.
- A region based sub-division method is developed for combining both flat and curved layer approaches together within the domain of a given solid model using a chordal-error criterion.
- The mixed flat and curved layer approach usually takes more time to print a part of given dimensions, compared to the uniform flat layer approach, but scores better than the uniform curved layer method.
- The surface and internal meso-structures are much better with the mixed flat and curved layer slicing approach.
- An integrated alternative slicing algorithm is developed combining uniform and adaptive flat and curved layers and the raster angle aspects together and coded in MATLAB.
- The integrated alternative slicing scheme operates in three possible ways: a direct and automatic routine for relatively simple shapes, dividing solid models of certain forms into two domains, a more general scheme with multiple subdivisions for more complex solid models
- Three case studies are considered and successfully processed, evaluating the effectiveness of the integrated slicing scheme.
- The integrated alternative slicing schemes are successful in handling different geometrical complexities, the layer patterns are observed to overcome typical

shortcomings such as stair-step effects, while allowing for other benefits such as fibre continuity in specific zones.

- The meso-structures are shown to be improved with the integrated schemes based on specific sections of CAD models and the benefits are envisioned to be equally good in all cases studied.

7.4 Future work

Several alternative slicing and deposition styles are attempted and evaluated in the current work. The analytical models developed and the experimental results obtained provided enough evidence to support the hypothesis that appropriate combinations of processing schemes are essential to improve the effectiveness of the process. However, hardware limitations are the main stumbling blocks in the practical implementation of the integrated schemes proposed. While a three axis system is insufficient, most commercial FDM systems are in fact very limited in terms of the control over the Z-motion. Also, the make-shift experimental facilities use a hot plate as the print form to control the envelope temperature. Ideally, a closed print chamber with a complete control over the envelope temperature is essential. Further, using a single deposition head to achieve filaments of varying diameters is not fully effective in real world applications.

The analytical models developed for adaptive slicing and raster orientation effects consider both geometrical and process parameters. However, the thermodynamic effects are neglected in the current cases, assuming that the filament and envelope temperatures are sufficiently controlled to maintain the substrate at the appropriate temperature. Flat and curved layer slicing schemes are

developed for both uniform and adaptive layers, based on solid modelling algorithms. However, considering the numerous situations analysed, the solutions are often limited in capabilities, and may not be fully effective with more complex solid models. Similar limitations are also associated with the integrated slicing schemes developed at the end. The following are possible improvements suggested for the future in order to understand the mechanics of FDM better and achieve further process enhancements:

- Enhancement of the hardware systems allowing for better control over the Z-motion as well as more degrees of freedom such as swivelling deposition head and/or print platforms.
- Multiple deposition heads to be used to achieve controlled variation of layer thicknesses
- Further enhancement of the analytical models giving due considerations to the thermal history of fused deposition modelling, representing the physics of the problem close to the reality
- Development of more general slicing schemes capable of handling solid models of any complexity for flat and curved layer slicing using both uniform and adaptive layers integrated with a proper choice of raster orientations in different regions.

References

[1] X. Yan and P. Gu, "A review of rapid prototyping technologies and systems," *Computer-Aided Design,* vol. 28, pp. 317-318, 1996.

[2] L. Kimble, "The selective laser sintering process: applications of a new manufacturing technology," in *PED—Intell. Des. Manfg Prot.*, 1992.

[3] W. K. Swainson, "METHOD, MEDIUM AND APPARATUS FOR PRODUCING THREE-DIMENSIONAL FIGURE PRODUCT." vol. 4041476, U. S. Patent, Ed. USA, 1971.

[4] W. K. Swainson and S. D. Kramer, "THREE-DIMENSIONAL SYSTEMS." vol. 4288861, U. S. Patent, Ed. USA: Formigraphic Engine Corporation, San Francisco, Calif, 1979.

[5] C. W. Hull, "Apparatus For Production of Three Dimensional Objects by Stereolithography." vol. 4575330, U. S. Patent, Ed. USA: UVP, Inc., San Gabriel, Calif, 1984.

[6] K. G. Cooper, "What Is Rapid Prototyping," in *Rapid prototyping technology selection and application* New York: Marcel Dekker, 2001, p. 1.

[7] N. P. Karapatis, J. P. S. v. Griethuysen, and R. Glardon, "Direct rapid tooling: a review of current research," *Rapid Prototyping Journal*, vol. 4, pp. 77-89, 1998.

[8] M. Rudgley, "Rapid manufacturing-the revolution is beginning," in *Proceedings of the uRapid*, Amsterdam, Netherlands, 2001, pp. 441-444.

[9] G. N. Levy, R. Schindel, and J. P. Kruth, "Rapid manufacturing and rapid tooling with layer manufacturing (LM) technologies, state of the art and future perspectives," *CIRP Annals - Manufacturing Technology*, vol. 52, pp. 589-609, 2003.

[10] ASTM, "Committee F42 on Additive Manufacturing Technologies," American Society for Testing and Materials (ASTM), 2009.

[11] J. Scott, N. Gupta, C. Weber, S. Newsome, T. Wohlers, and T. Caffrey, "Additive Manufacturing: Status and Opportunities," Science and Technology Policy Institute 2012.

[12] J. W. Halloran, V. Tomeckova, S. Gentry, S. Das, P. Cilino, D. Yuan, R. Guo, A. Rudraraju, P. Shao, T. Wu, T. R. Alabi, W. Baker, D. Legdzina, D. Wolski, W. R.

Zimbeck, and D. Long, "Photopolymerization of powder suspensions for shaping ceramics," *Journal of the European Ceramic Society*, vol. 31, pp. 2613-2619, 2011.

[13] Wikipedia, "Stereolithography," http://en.wikipedia.org/wiki/Stereolithography.

[14] S. S. Crump, "Apparatus and method for creating three-dimensional objects," U. S. Patent, Ed. USA: Stratasys, Inc., Minneapolis, Minn, 1989.

[15] Wikipedia, "Fused deposition modeling," Available from: http://en.wikipedia.org/wiki/Fused_deposition_modeling.

[16] C. R. Deckard, "Method and apparatus for producing parts by selective sintering." vol. 4863538, U. S. Patent, Ed. USA: Board of Regents, The University of Texas System, 1989.

[17] Wikipedia, "Selective laser sintering," Available from: http://en.wikipedia.org/wiki/Selective_laser_sintering.

[18] M. Lindemann and D. Graf, "PROCESS AND DEVICE FOR PRODUCING A SHAPED BODY BY SELECTIVE LASER MELTING." vol. 7047098, U. S. Patent, Ed. USA: Trumpf Werkzeugmaschinen GmbH & Co., K. G. Ditzingen, 2002.

[19] R. Larson, "Method and device for producing three-dimensional bodies." vol. 5786562, U. S. Patent, Ed. USA: Arcam Limited, 1998.

[20] EE|Times, "Rapid prototypes move to metal components," Available from: http://www.eetimes.com/document.asp?doc_id=1274037.

[21] F. P. Jeantette, D. M. Keicher, J. A. Romero, and L. P. Schanwald, "Method and system for producing complex-shape objects." vol. 6046426, U. S. Patent, Ed. USA: Sandia Corporation, 2000.

[22] D. M. Keicher, C. L. Atwood, D. L. Greene, M. L. Griffith, L. D. Harwell, F. P. Jeantette, J. A. Romero, L. P. Schanwald, and D. T. Schmale, "Energy-beam-driven rapid fabrication system." vol. 6476343, U. S. Patent, Ed. USA: Sandia Corporation, 2002.

[23] Wikipedia, "Cladding (metalworking)," Available from: http://en.wikipedia.org/wiki/Cladding_(metalworking).

[24] H. Gothait, "Apparatus and method for three dimensional model printing." vol. 6259962, U. S. Patent, Ed. USA: Objet Geometries Ltd., 2001.

[25] K. Silverbrook, "3-D OBJECT CREATION SYSTEM USING MULTIPLE MATERIALS IN MULTIPLE LAYER," U. S. Patent, Ed. USA: Silverbrook Research Pty Ltd, 2004.

[26] K. Silverbrook, "THREE DIMENSIONAL OBJECT PRINTING," U. S. Patent, Ed. USA: Silverbrook Research Pty Ltd, 2006.

[27] Custompartnet, "Inkjet Printing," Available from: http://www.custompartnet.com/wu/ink-jet-printing.

[28] K. G. Cooper, "Fused Deposition Modeling," in *Rapid prototyping technology selection and application* New York: Marcel Dekker, 2001, pp. 68-87.

[29] Custompartnet, "Fused Deposition Modeling," Available from: http://www.custompartnet.com/wu/fused-deposition-modeling.

[30] STRATASYS, "http://www.stratasys.com/."

[31] R. v. Weeren, M. Agarwala, V. R. Jamalabad, A. Bandyophadyay, R. Vaidyanathan, N. Langrana, A. Safari, P. Whalen, S. C. Danforth, and C. Ballard, "Quality of parts processed by fused deposition," in *Solid Freeform Fabrication Symp* Austin TX, 1995.

[32] M. K. Agarwala, V. R. Jamalabad, N. A. Langrana, A. Safari, P. J. Whalen, and S. C. Danforth, "Structural quality of parts processed by fused deposition," *Rapid Prototyping Journal*, vol. 2, pp. 4-19, 1996.

[33] C. T. Bellehumeur, L. Li, Q. Sun, and P. Gu, "Modelling of bond formation between polymer filaments in the fused deposition modelling process," *Journal of Manufacturing Processes*, vol. 6, pp. 170-178, 2004.

[34] J. F. Rodr ́guez, J. P. Thomas, and J. E. Renaud, "Tailoring the mechanical properties of fused deposition manufactured components," in *Rapid Prototyping and Manufacturing*, Dearborn, MI, 1999, pp. 629-643.

[35] J. F. Rodr ́guez, J. P. Thomas, and J. E. Renaud, "Characterization of the mesostructure of fused deposition acrylonitrile butadiene-styrene materials," *rapid Prototyping Journal*, vol. 6, pp. 176-185, 2000.

[36] J. F. Rodr ́guez, J. P. Thomas, and J. E. Renaud, "Mechanical behaviour of acrylonitrile butadiene styrene (ABS) fused deposition materials, experimental investigation," *rapid Prototyping Journal*, vol. 7, pp. 148-158, 2001.

[37] C. S. Lee, S. G. Kim, H. J. Kim, and S. H. Ahn, "Measurement of anisotropic compressive strength of rapid prototyping parts," *Journal of Material Processing Technology*, vol. 187-188, pp. 627-630, 2007.

[38] A. Bellini, "Fused Deposition of Ceramics: A Comprehensive Experimental, Analytical and Computational Studay of Material Behavior, Fabrication Process and Equipment Design," Drexel University, 2002.

[39] S. H. Choi and S. Samavedam, "Modelling and optimisation of Rapid Prototyping," *Computer in Industry*, vol. 47, pp. 39-53, 2002.

[40] S. O. Onuh and K. K. B. Hon, "Optimising build parameters for improved surface finish in stereolithography," *International Journal of Machine Tools and Manufacture*, vol. 38, pp. 329-342, 1998.

[41] E. Sabourin, S. A. Houser, and J. H. Bohn, "Adaptive slicing using stepwise uniform refinement," *rapid Prototyping Journal*, vol. 2, pp. 20-26, 1996.

[42] C. K. Chua, K. F. Leong, and C. S. Lim, "Rapid Prototyping Data Formats," in *Rapid prototyping: Principle and Application*: World Scientific, 2003, pp. 237-294.

[43] Y. Yang, J. Y. H. Fuh, H. T. Loh, and Y. G. Wang, "Equidistanct path generation for improving scanning effciency in layered manufacturing," *rapid Prototyping Journal*, vol. 8, pp. 30-37, 2002.

[44] S. H. Masood, W. Rattanawong, and P. Iovenitti, "Part Build Orientation Based on Volumetric Error in Fused Deposition Modelling," *Advanced Manufacturing Technology*, vol. 16, pp. 162-168, 2000.

[45] R. Anitha, S. Arunachalam, and P. Radhakrishnan, "Critical parameters influencing the quality of prototypes in fused deposition modelling," *Journal of Material Processing Technology*, vol. 118, pp. 385-388, 2001.

[46] M. Montero, S. Roundy, D. Odell, S.-H. Ahn, and P. K. Wright, "Material Characterization of Fused Deposition Modeling (FDM) ABS by Designed Experiments," in *Rapid Prototypoing and Manufacturing Conference, Society of Manufacturing Engineers* Cincinnati, OH, 2001.

[47] S. H. Ahn, M. Montero, D. Odell, S. Roundy, and P. K. Wright, "Anisotropic material properties of fused deposition modeling ABS," *rapid Prototyping Journal*, vol. 8, pp. 248-257, 2002.

[48] C. W. Ziemian and P. M. CrawnIII, "Computer aided decision support for fused deposition modeling," *rapid Prototyping Journal*, vol. 7, pp. 138-147, 2001.

[49] M. H. Too, K. F. Leong, C. K. Chua, Z. H. Du, S. F. Yang, C. M. Cheah, and S. L. Ho, "Investigation of 3D Non-Random Porous Structures by Fused Deposition Modelling," *Advanced Manufactuing Technology*, vol. 19, pp. 217-223, 2002.

[50] A. K. Sood, R. K. Ohdar, and S. S. Mahapatra, "Improving dimensional accuracy of Fused Deposition Modelling processed part using grey Taguchi method," *Materials and Design*, vol. 30, pp. 4243-4252, 2009.

[51] D. Ahn, J.-H. Kweon, S. Kwon, J. Song, and S. Lee, "Representation of surface roughness in fused deposition modeling," *Journal of Material Processing Technology*, vol. 209, pp. 5593-5600, 2009.

[52] A. K. Sood, R. K. Ohdar, and S. S. Mahapatra, "Parametric appraisal of mechanical property of fused deposition modelling processed parts," *Materials and Design*, vol. 31, pp. 287-295, 2010.

[53] M. A. Yardimci, S. I. Guceri, M. Agarwala, and S. C. Danforth, "Part quality prediction tools for fused deposition processing," in *Solid Freeform Fabrication Symp* Austin, TX, 1996.

[54] Q. Sun, G. M. Rizvi, C. T. Bellehumeur, and P. Gu, "Effect of processing conditions on the bonding quality of FDM polymer filaments," *rapid Prototyping Journal*, vol. 14, pp. 72-80, 2008.

[55] L. M. Galantucci, F. Lavecchia, and G. Percoco, "Experimental study aiming to enhance the surface finish of fused deposition modeled parts," *CIRP Annals - Manufacturing Technology*, vol. 58, pp. 189-192, 2009.

[56] A. Boschetto, V. Giordano, and f. Veniali, "3D roughness profile model in fused deposition modelling," *rapid Prototyping Journal*, vol. 19, pp. 240-252, 2013.

[57] G. Q. Jin, W. D. Li, and L. Gao, "An adaptive process planning approach of rapid prototyping and manufacturing," *Robotics and Computer-Integrated Manufacturing*, vol. 29, pp. 23-38, 2013.

[58] D. Croccolo, M. D. Agostinis, and G. Olmi, "Experimental characterization and analytical modelling of mechanical behavior of fused deposition processed parts made of ABS-M30," *Computational Materials Science*, vol. 79, pp. 506-518, 2013.

[59] M. A. Yardimci and S. I. Guceri, "Thermal Analysis of Fused Deposition," in *ASME Material Division*, 1995, pp. 1225-1235.

[60] L. Li, Q. Sun, C. Bellehumeur, and P. Gu, "Composite Modelling and Analysis of FDM Prototypes for Design and Fabrication of Functionally Graded Parts," in *Solid Freeform Fabrication Symposium*, Austin, Texas, 2001, pp. 187-194.

[61] O. Pokluda, C. T. Bellehumeur, and J. Vlachopoulos, "Modification of Frenkel's Model for Sintering," *AlChE journal*, vol. 43, pp. 3253-3256, 1997.

[62] F. Yang and R. Pitchumani, "Healing of Thermoplastic Polymers at an Interface under Nonisothermal Conditions," *Macromolecules*, vol. 35, pp. 3213-3224, 2002.

[63] Q. Sun, G. M. Rizvi, C. Bellehumeur, and P. Gu, "Experimental Study of the Cooling Characteristics of Polymer Filaments in FDM and Impact on the Mesostructures and Properties of Prototypes," in *Solid Freeform Fabrication Symposium* Austin, TX, 2003.

[64] J. F. Rodríguez, "Modelling the mechanical behaviour of fused deposition acrylonitrile-butadiene-styrene polymer components," in *Departamento de Mecánica*. vol. PhD Caracas, Venezuela: Universidad Simón Bolívar, 1999.

[65] K. D. Kim, L. H. Sperling, and A. Klein, "Reptation time, temperature, and cosurfactant effects on the molecular interdiffusion rate during polystyrene latex film formation," *Macromolecules*, vol. 27, pp. 6841-6850, 1994.

[66] S. C. Danforth and A. Safari, "Solid free form fabrication: novel manufacturing opportunities for electroceramics," in *10th IEEE International Symposium on Application of Ferroelectrics,*, 1996, pp. 183-8.

[67] M. A. Jafari, W. Han, F. Mohammadi, A. Safari, S. C. Danforth, and N. Langrana, "A novel system for fused deposition of advanced multiple ceramics," *rapid Prototyping Journal*, vol. 6, pp. 161-175, 2000.

[68] S. H. Masood and W. Q. Song, "Development of new metal/polymer materials for rapid tooling using Fused deposition modelling," *Materials and Design*, vol. 25, pp. 587-594, 2004.

[69] A. Bandyopadhyay, R. K. Panda, V. F. Janas, M. K. Agarwala, S. C. Danforth, and A. Safari, "Processing of Piezocomposites by Fused Deposition Technique," *Journal of the American Ceramic Society*, vol. 80, pp. 1366-1372, 1997.

[70] D. Espalin, K. Arcaute, D. Rodriguez, F. Medina, M. Posner, and R. Wicker, "Fused deposition modeling of patient-specific polymethylmethacrylate implants," *rapid Prototyping Journal,* vol. 16, pp. 164-173, 2010.

[71] P. Ng, P. S. V. Lee, and J. C. H. Goh, "Prosthetic sockets fabrication using rapid prototyping technology," *rapid Prototyping Journal,* vol. 8, pp. 53-59, 2002.

[72] D. W. Hutmacher, T. Schantz, I. Zein, K. W. Ng, S. H. Teoh, and K. C. Tan, "Mechanical properties and cell cultural response of polycaprolactone scaffolds designed and fabricated via fused deposition modeling," *Journal of Biomedical Materials Research,* vol. 55, pp. 203-216, 2001.

[73] A. Bellini and S. I. Guceri, "Mechanical characterization of parts fabricated using fused deposition modeling," *Rapid Prototyping Journal,* vol. 9, pp. 252-264, 2003.

[74] N. Venkataraman, S. Rangarajan, M.J. Matthewson, B. Harper, A. Safari, S. C. Danforth, G. Wu, N. Langrana, S. Guceri, and A. Yardimci, "Feedstock material property - process relationships in fused deposition of ceramics (FDC)," *rapid Prototyping Journal,* vol. 6, pp. 244-252, 2000.

[75] A. Bellini, L. Shor, and S. I. Guceri, "New developments in fused deposition modeling of ceramics," *rapid Prototyping Journal,* vol. 11, pp. 214-220, 2005.

[76] I. Zein, D. W. Hutmacher, K. C. Tan, and S. H. Teoh, "Fused deposition modeling of novel scaffold architectures for tissue engineering applications," *Biomaterials,* vol. 23, pp. 1169-1185, 2002.

[77] J. Mireles, H. Kim, I. H. Lee, D. Espalin, F. Medina, E. MacDonald, and R. Wicker, "Development of a Fused Deposition Modeling system for low temperature metal alloys," *Journal of Electronic Packaging,* 2012.

[78] L. Li, Q. Sun, C. Bellehumeur, and P. Gu, "Composite Modeling and Analysis for Fabrication of FDM Prototypes with Locally Controlled Properties," *journal of Manufacturing Processes,* vol. 4, pp. 170-178, 2002.

[79] O. S. Es-Said, J. Foyos, R. Noorani, M. Mendelson, R. Marloth, and B. A. Pregger, "Effect of Layer Orientation on Mechanical Properties of Rapid Prototyped Samples," *Materials and Manufacturing Processes,* vol. 15, pp. 107-122, 2000.

[80] B. H. Lee, J. Abdullah, and Z. A. Khan, "Optimization of rapid prototyping parameters for production of flexible ABS object," *Journal of Material Processing Technology*, vol. 169, pp. 54-61, 2005.

[81] A. W. Fatimatuzahraa, B. Farahaina, and W. A. Y. Yusoff, "The effect of employing different raster orientations on the mechanical properties and microstructure of Fused Deposition Modeling parts," in *Business, Engineering and Industrial Applications (ISBEIA), 2011 IEEE Symposium on. IEEE, 2011*. Langkawi, Malaysia, 2011.

[82] W. Cheng, F. Y. H. Fuh, A. Y. C. Nee, Y. S. Wong, H. T. Loh, and T. Miyazawa, "Multi-objective optimization of part-building orientation in stereolithography," *Rapid Prototyping Journal*, vol. 1, pp. 12-23, 1995.

[83] G. M. Fadel and C. Kirschman, "Accuracy issues in CAD to RP translations," *rapid Prototyping Journal*, vol. 2, pp. 4-17, 1996.

[84] Y. Suh and M. J. Wozny, "Adaptive slicing of freeform fabrication processes," in *Solid Freeform Fabrication Symposium*, University of Texas, Austin, TX, 1994, pp. 404-411.

[85] P. Kulkarni and D. Dutta, "An accurate slicing procedure for layered manufacturing," *Computer Aided Design*, vol. 28, pp. 683-697, 1996.

[86] E. Sabourin, S. A. Houser, and J. H. Bohn, "Accurate exterior, fast interior layered manufacturing," *rapid Prototyping Journal*, vol. 3, pp. 44-52, 1997.

[87] R. L. Hope, R. N. Roth, and P. A. Jacobs, "Adaptive slicing with sloping layer surfaces," *Rapid Prototyping Journal*, vol. 3, pp. 89-98, 1997.

[88] J. Tyberg and J. H. Bohn, "Local adaptive slicing," *rapid Prototyping Journal*, vol. 4, pp. 118-127, 1998.

[89] D. Cormier, K. Unnanon, and E. Sanii, "Specifying non-uniform cusp heights as a potential aid for adaptive slicing," *rapid Prototyping Journal*, vol. 6, pp. 204-211, 2000.

[90] M. Kumar and A. R. Choudhury, "Adaptive slicing with cubic patch approximation," *Rapid Prototyping*, vol. 8, pp. 224-232, 2002.

[91] R.-S. Lin, "Adaptive slicing for rapid prototyping," in *Software Solutions for Rapid Prototyping*, I. Gibson, Ed. London: Professional Engineering Publishing, 2002.

[92] K. Thrimurthulu, P. M. Pandey, and N. V. Reddy, "Optimum part deposition orientation in fused deposition modeling," *International Journal of Machine Tools & Manufactue*, vol. 44, pp. 585-594, 2004.

[93] M. Y. Zhou, J. T. Xi, and J. Q. Yan, "Adaptive direct slicing with non-uniform cusp heights for rapid prototyping," *International Journal of Advanced Manufacturing Technology*, pp. 20-27, 2004.

[94] J. Owen, *STEP: an introduction. Information geometers*, 2nd ed. Winchester, UK, 1997.

[95] W. Ma, W.-C. But, and P. He, "NURBS-based adaptive slicing for efficient rapid prototyping," *Computer Aided Design*, vol. 36, pp. 1309-1325, 2004.

[96] L. Zeng, L. M.-L. Lai, D. Qi, Y.-H. Lai, and M. M.-F. Yuen, "Efficient slicing procedure based on adaptive layer depth normal image," *Computer Aided Design*, vol. 43, pp. 1577-1586, 2011.

[97] S. Wang, Y. Wang, C. S. Chen, and X. Zhu, "An adaptive slicing algorithm and data format for functionally graded material objects," *The Internatinal Journal of Advanced Manufacturing Technology*, vol. 65, pp. 251-258, 2013.

[98] R. Jamieson and H. Hacker, "Direct Slicing of CAD Models for Rapid Prototyping," *Rapid Prototyping Journal*, vol. 1, 1995.

[99] X. Chen, C. Wang, X. Ye, Y. Xiao, and S. Huang, "Direct Slicing from PowerSHAPE Models for Rapid Prototyping," *International Journal of Advanced Manufacturing Technology*, vol. 17, pp. 543-547, 2001.

[100] B. Starly, A. Lau, W. Sun, W. Lau, and T. Bradbury, "Direct slicing of STEP based NURBS models for layered manufacturing," *Computer-Aided Design 37 (2005)*, pp. 387-397, 2005.

[101] Y. Qiu, X. Zhou, and X. Qian, "Direct slicing of cloud data with guaranteed topology for rapid prototyping," *International Journal of Advanced Manufacturing Technology*, vol. 53, pp. 255-265, 2011.

[102] Z. Zhao and L. Laperriere, "Adaptive direct slicing of the solid model for rapid prototyping," *International Journal of Production Research*, pp. 69-83, 2000.

[103] D. L. Bourell, M. C. Leu, and D. W. Rosen, "Roadmap for Additive Manufacturing: Identifying the Future of Freeform Processing," The University of Texas, Austin 2009.

[104] D. A. Klosterman, R. P. Chartoff, N. R. Osborne, G. A. Graves, A. Lightman, G. Han, A. Bezeredi, and S. Rodrigues, "Development of a curved layer LOM process for monolithic ceramics and ceramic matrix composites," *Rapid Prototyping Journal*, vol. 5, pp. 61-71, 1999.

[105] D. Chakraborty, B. A. Reddy, and R. Choudhury, "Extruder path generation for Curved Layer Fused Deposition Modeling," *Computer Aided Design*, vol. 40, pp. 235-243, 2008.

[106] B. Huang, "Development of a Software procedure for Curved Layered Fused Deposition Modeling (CLFDM)," in *School of Engineering*. vol. Master of Engineering Auckland: Auckland University of Technology, 2009, p. 137.

[107] Y. Chen, C. Zhou, and J. Lao, "A layerless additive manufacturing process based on CNC accumulation," *rapid Prototyping Journal*, vol. 17, pp. 218-227, 2011.

[108] J.-W. Choi, F. Medina, C. Kim, D. Esplin, D. Rodriguez, B. Stucker, and R. Wicker, "Development of a mobile fused deposition modeling system with enhanced manufacturing flexibility," *journal of Material Processing Technology*, vol. 211, pp. 424-432, 2011.

[109] J. D. Eshelby, "in the discussion that accompanies the following paper: A. J. Shaler Seminar on the kinetics of sintering,," *Transactions of the American Institute of Mining and Metallurgical Engineers*, vol. 185, pp. 796-813, 1949 1949.

[110] M. K. Agarwala, R. V. Weeren, A. Bandyopadhyay, P. J. Whalen, A. Safari, and S. C. Danforth, "Fused deposition of ceramics and metals: An overview," in *Solid Freeform Fabrication Symposium*, The University of Texas, Austin, 1996, pp. 385-92.

[111] S. H. Ahn, C. Baek, S. Lee, and I. S. Ahn, "Anisotropic tensile failure model of rapid prototyping parts - fused deposition modeling (FDM)," *International Journal of Modern Physics B*, vol. 17, pp. 1510-1516, 2003.

[112] F. Xu, H. T. Loh, and Y. S. Wong, "Considerations and selection of optimal orientation for different rapid prototyping system," *Rapid Prototyping Journal*, vol. 5, pp. 54-60, 1999.

[113] Y. Yang, J. Y. H. Fuh, and H. T. Loh, "An Efficient Scanning Pattern for Layered Manufacturing Processes," in *International Conference on Robotics & Automation* Seoul, Korea, 2001.

[114] P. M. Pandey, N. V. Reddy, and S. G. Dhande, "Slicing procedures in layered manufacturing: a review," *rapid Prototyping Journal*, vol. 9, pp. 274-288, 2003.

[115] A. Dolenc and I. Makela, "Slicing procedures for layered manufacturing techniques," *Computer Aided Design*, vol. 26, pp. 119-126, 1994.

[116] P. M. Pandey, N. V. Reddy, and S. G. Dhande, "Real time adaptive slicing for fused deposition modelling," *international Journal of Machine Tools & Manufactue,* vol. 43, pp. 61-71, 2003.

[117] K. Tata, G. Fadel, A. Bagchi, and N. Aziz, "Efficient slicing for layered manufacturing," *rapid Prototyping Journal,* vol. 4, pp. 151-167, 1998.

[118] K. Mani, P. Kulkarni, and D. Dutta, "Region-based adaptive slicing," *Computer Aided Design,* vol. 31, pp. 317-333, 1999.

[119] ASTMF2915-12, "Standard Specification for Additive Manufacturing File Format (AMF) Version 1.1," A. International, Ed. West Conshohocken, PA, 2012, 2012.

[120] J. Frenkel, "Viscous Flow of Crystalline Bodies under the Action of Surface Tension," *Journal of Physics (USSR),* vol. 9, pp. 385-91, 1945.

[121] R. W. Hopper, "Coalescence of Two Equal Cylinders: Exact Results for Creeping Viscous Plane Flow Driven by Capillarity," *Journal of the American Ceramic Society,* vol. 67, pp. C-262–C-264, 1984.

[122] R. W. Hopper, "Plane Stokes flow driven by capillarity on a free surface," *Journal of Fluid Mechanics,* vol. 213, pp. 349-375 1990.

[123] R. W. Hopper, "Plane Stokes flow driven by capillarity on a free surface. Part 2. Further developments," *Journal of Fluid Mechanics,* vol. 230, pp. 355-364 1991.

[124] C. T. Bellehumeur, M. K. Bisaria, and J. Vlachopoulos, "An Experimental Study and Model Assessment of Polymer Sintering," *Polymer Engineering and Science,* vol. 36, 1996.

[125] L. Li, C. Bellehumeur, Q. Sun, and P. Gu, "Investigation of bond formation in FDM process," in *Solid Freeform Fabrication Symp.*, Austin, TX, 2002, pp. 1-8.

[126] J. P. Thomas and J. F. Rodr ́guez, "Modeling the fracture strength between fused-deposition extruded roads," in *Solid Freeform Fabrication Symp.*, Austin, TX, 2000, pp. 16-23.

[127] " Makerbot Industries http://www.makerbot.com/," 2011.

[128] R. W. Gray, D. G. Baird, and D. G. Bohn, "Effects of processing conditions on short TLCP fiber reinforced FDM parts," *rapid Prototyping Journal,* vol. 4, pp. 14-25, 1998.

[129] ASTM, "D3039-07 Standard Test Method for Tensile Properties of Polymer Matrix Composite Materials," West Conshohocken, PA, USA, 2007: ASTM International, 2007.

[130] E. Lokensgard, "Chapter 6 Properties and Tests of Selected Plastics " in *Industrial Plastics: Theory and Application*: Delmar Cengage Learning; 5 edition 2008.

[131] J. B. Haddow and T. M. Hrudey, "A Finite Strain Theory for Elastic-Plastic Deformation," *International Journal of Non-Linear Mechanics*, vol. 6, pp. 435-450, 1971.

[132] J. F. Rodr ́guez, J. P. Thomas, and J. E. Renaud, "Mechanical behaviour of acrylonitrile butadiene styrene fused deposition materials modeling," *rapid Prototyping Journal*, vol. 9, pp. 219-230, 2003.

[133] L. L. Bucciarelli, "CHAPTER 4 Stress, Strain, Stress-Strain," in *ENGINEERING MECHANICS FOR STRUCTURES*: http://web.mit.edu/emech/dontindex-build/full-text/emechbk_4.pdf, 2002.

[134] Z. Hu, K. Lee, and J. Hur, "Determination of optimal build orientation for hybrid rapid-prototyping," *Journal of Material Processing Technology*, vol. 130-131, pp. 378-383, 2002.

[135] D. F. Rogers and J. A. Adams, "Surface Description and Generation," in *Mathematical Elements for Computer Graphics* New York: McGraw-Hill Publishing Company, 1990.

[136] "ASTM F2915 - 12 Standard Specification for Additive Manufacturing File Format (AMF) Version 1.1," West Conshohocken, PA 2011.

[137] D. Harlev, "stlread." vol. 07 Jan 2005, 04 Jan 2005 pp. This function reads a binary SPL file into X, Y, Z, C matrixes compatible with the MATLAB patch function.

[138] X. Qu and B. Stucker, "A 3D surface offset method for STL-format models," *Rapid Prototyping Journal*, vol. 9, pp. 133-141, 2003.

[139] Fab@Home, "http://www.fabathome.org/wiki/index.php?title=Main_Page."

[140] FabEpoxy, "http://www.kraftmark.biz/pdfs/Fabepoxy/FabEpoxy.infosheet.pdf."

[141] STRATASYS, "FORTUS 360mc."

[142] M. T. Hayasi and B. Asiabanpour, "A new adaptive slicing approach for the fully dense freeform fabrication (FDFF) process," *Journal of Intelligent Manufacturing*, vol. 24, pp. 683-694, 2013.

[143] Y. A. Jin, Y. He, and J. Z. Fu, "An Adaptive Tool Path Generation for Fused Deposition Modeling," *Advanced Materials Research,* vol. 819, pp. 7-12, 2013.

Appendices

Appendix 1 Evaluation of meso structures with varying print speed and raster angle orientations

It may be noted that some attempts were made during the course of this project to evaluate the meso structures and variation of coalescence with varying process conditions. Though it is practically not feasible to consider varying layer thicknesses over a wide range with current experimental facilities, two thicknesses 0.5 mm and 1.0 mm are implemented, with varying print speeds and the following SEM photomicrographs are generated. The problem is that the knife-cutting of the samples for studying under SEM was tough and resulted in flaking. Literature presents a method of using liquid nitrogen treatment and subsequent guillotine chopping, but considering lack of facilities and the health and safety concerns, such a system could not be acquired, and so, these trials are not taken up more intensively. The information generated is included here:

Coalescence vs. print speed

Coalescence values are measured based on the mesostructures as shown in the photomicrographs of Fig. A1.1 to A1.6.

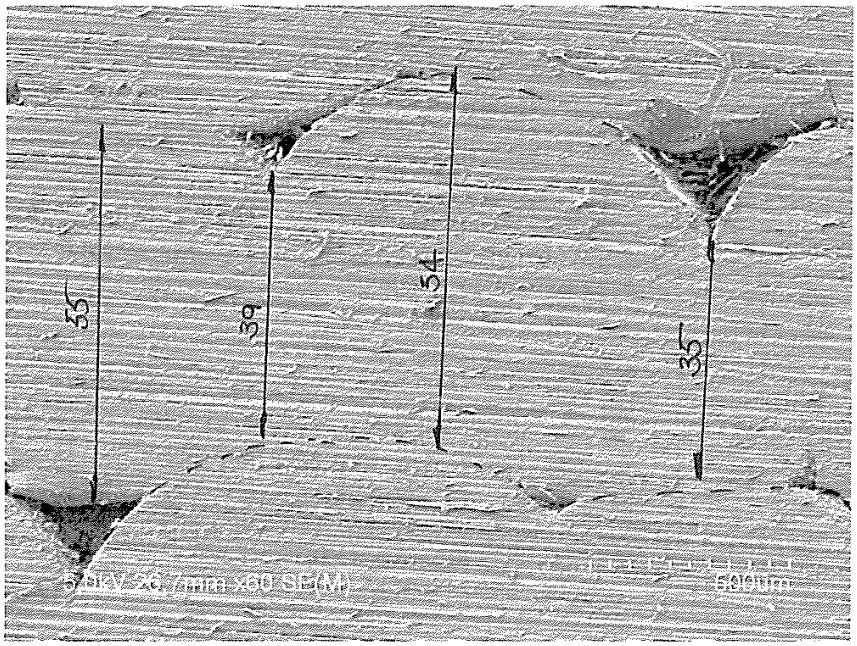

10 mm/s

Figure A1.1 Meso structure of FDM test part of 10mm/s print speed (Average coalescence: 0.68)

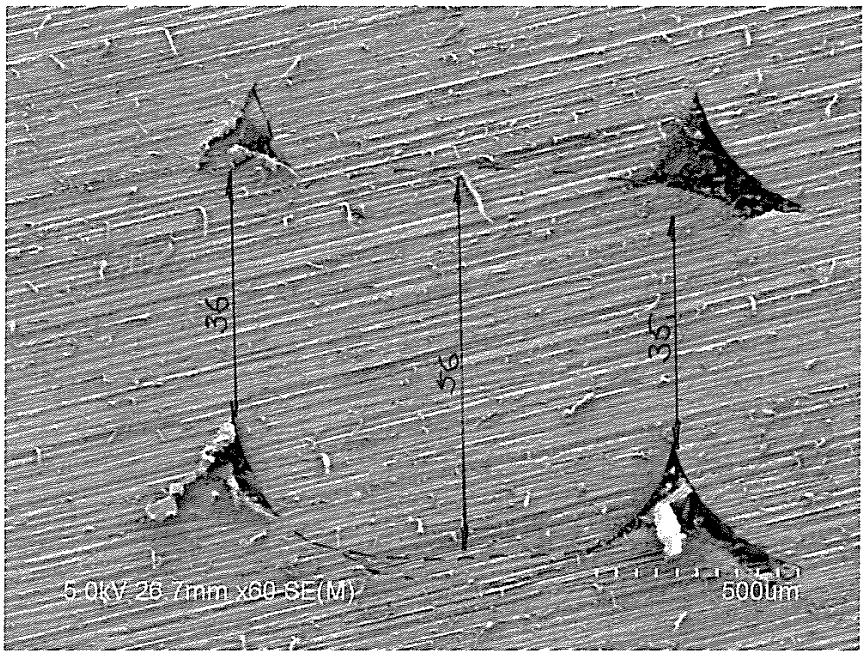

13 mm/s

Figure A1.2 Meso structure of FDM test part of 13mm/s print speed (Average coalescence: 0.64)

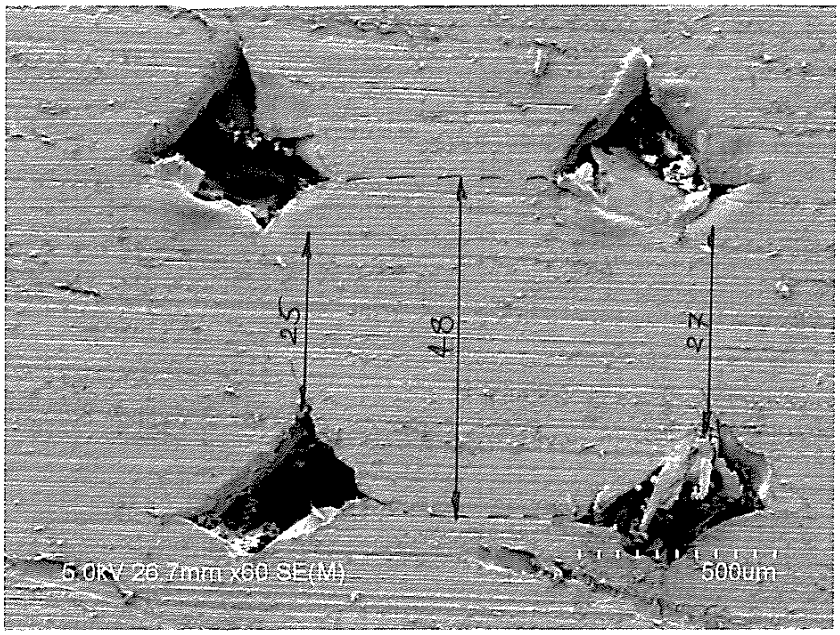

15 mms/

Figure A1.3 Meso structure of FDM test part of 15mm/s print speed (Average coalescence: 0.54)

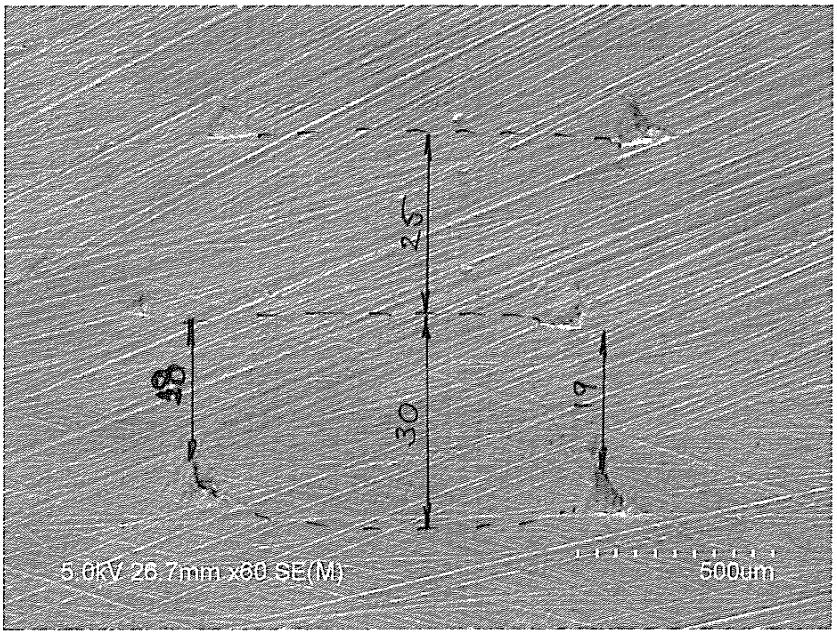

35 mm/s

Figure A1.4 Meso structure of FDM test part of 35mm/s print speed (Average coalescence: 0.68)

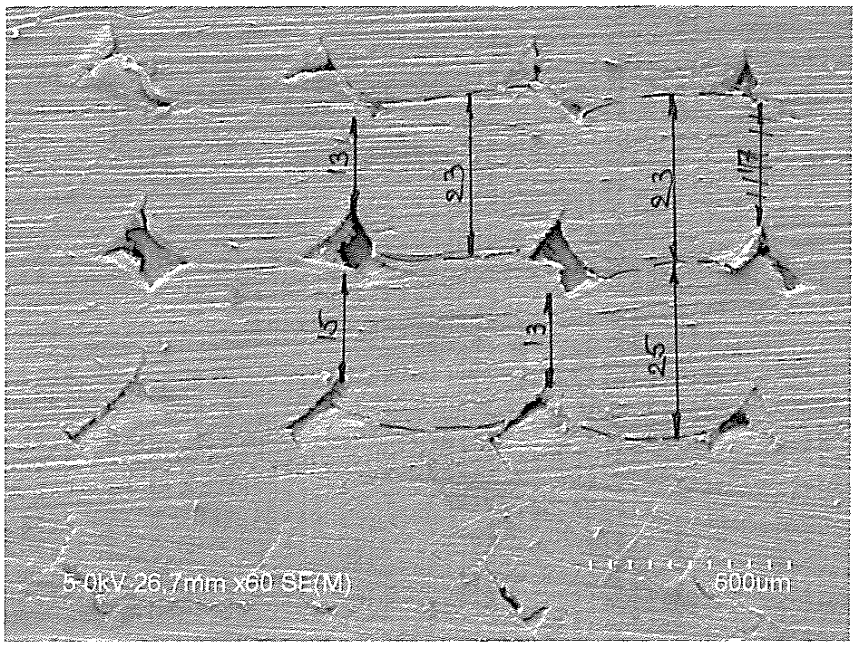

55 mm/s

Figure A1.5 Meso structure of FDM test part of 55mm/s print speed (Average coalescence: 0.585)

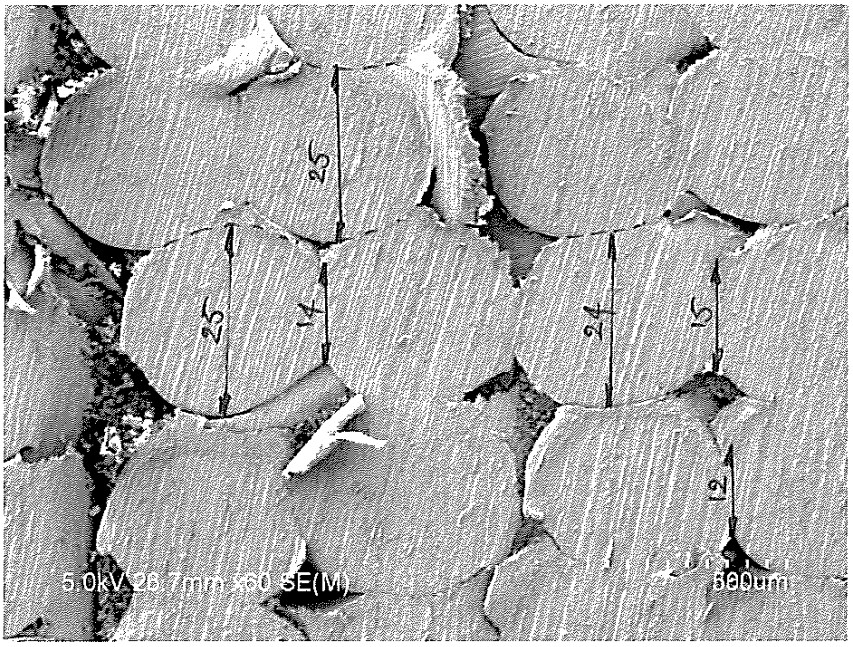

60 mm/s

Figure A1.6 Meso structure of FDM test part of 60mm/s print speed (Average coalescence: 0.553)

The coalescence results are consolidated in Table A1.1:

Table A1.1 Variation of coalescence with speed

Layer Thickness	**0.5**		
Print Speed	35 mm/s	55 mm/s	60 mm/s
Predicted Coalescence	0.6536	0.56	0.5362
Measured Coalescence	0.68	0.585	0.55

Layer Thickness	**1.0**		
Print Speed	10 mm/s	13 mm/s	15 mm/s
Predicted Coalescence	0.6782	0.5948	0.5538
Measured Coalescence	0.68	0.64	0.54

Coalescence vs. raster angle

SEM photographs of cross sections of samples produced while printing with varying raster angles are included in Fig's A.1.7 to A.1.13. All sections are perpendicular to the longitudinal axes. The variations seen in the mesostructures are due to varying raster orientations. However, coalescence needs to be assessed based on sections perpendicular to the orientation of strands. It may be noted that the coalescence will not vary along those sections as the print speed and layer thickness conditions used are the same. And the raster orientations are aligned in the same direction across multiple layers. These results are consolidated in Table A.1.2.

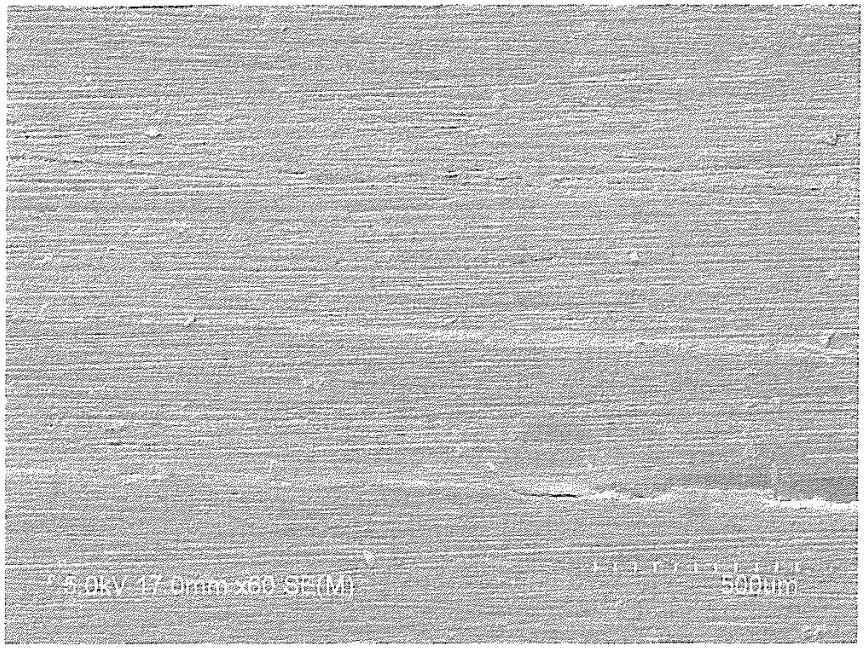

90˚

Fig. A1.7 Meso structure of FDM test part of 90˚

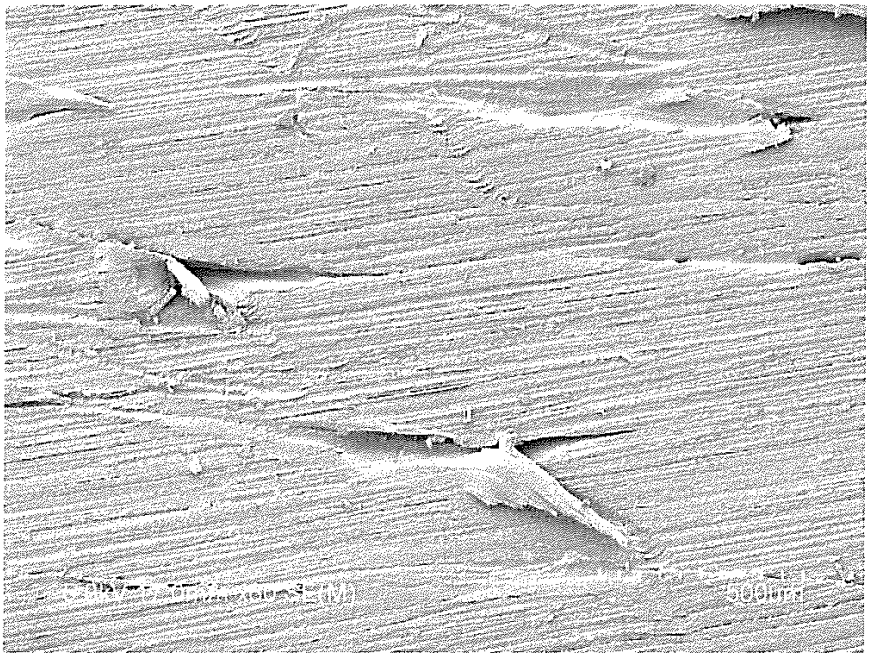

75˚

Fig. A1.8 Meso structure of FDM test part of 75˚

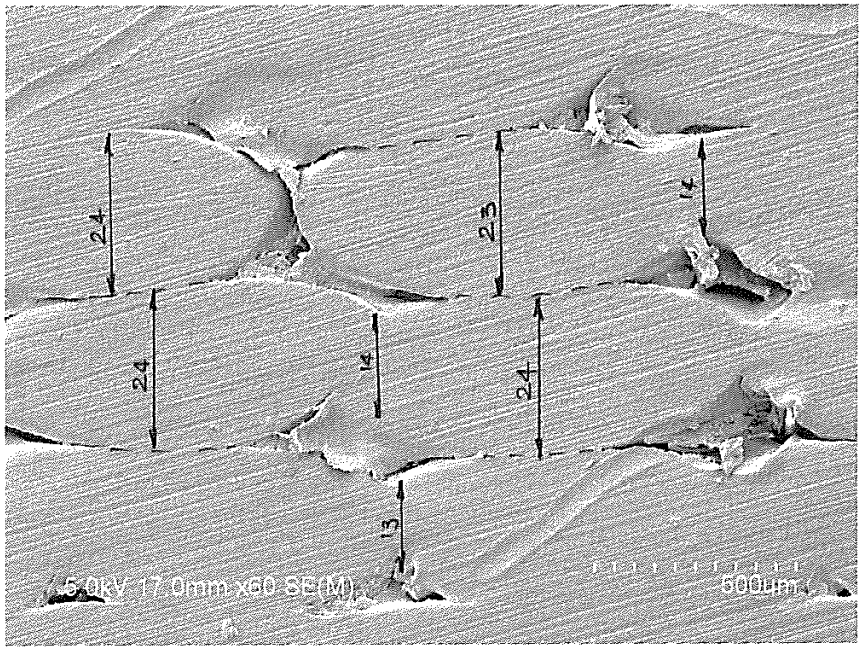

60˚

Fig. A1.9 Meso structure of FDM test part of 60˚ (Average coalescence: 0.575)

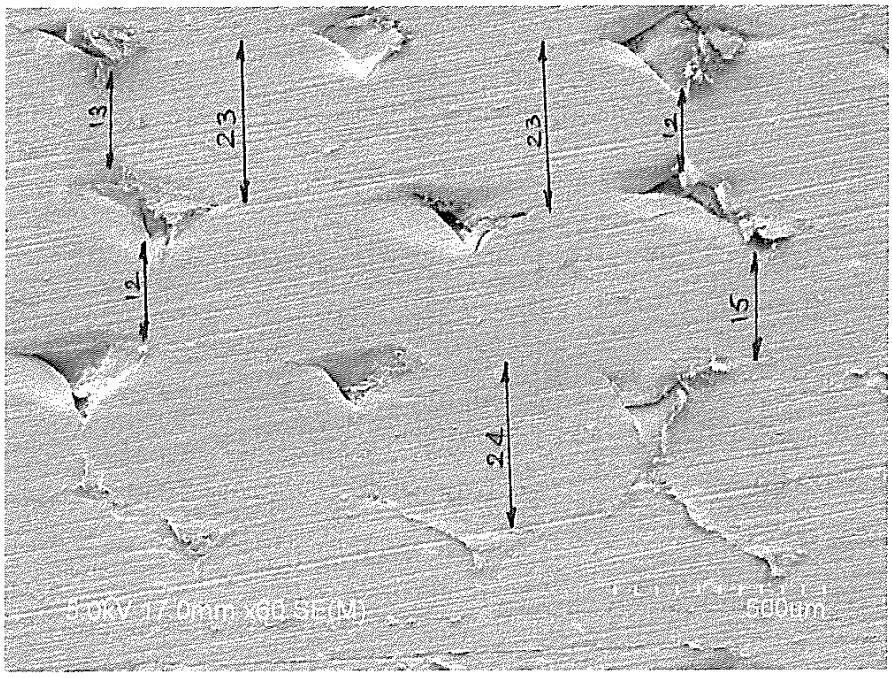

45˚

Fig. A1.10 Meso structure of FDM test part of 45˚ (Average coalescence: 0.575)

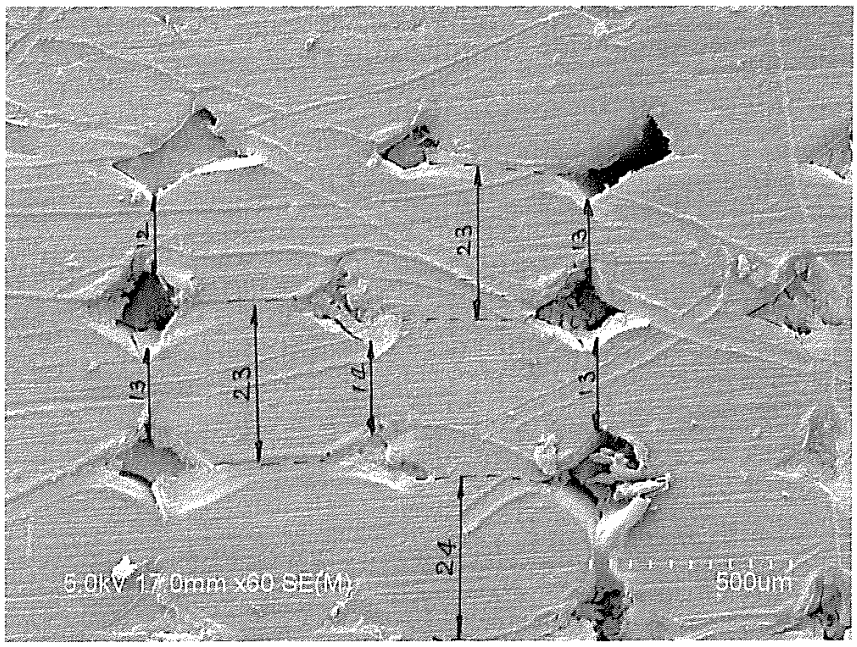

30˚

Fig. A1.11 Meso structure of FDM test part of 30˚ (Average coalescence: 0.555)

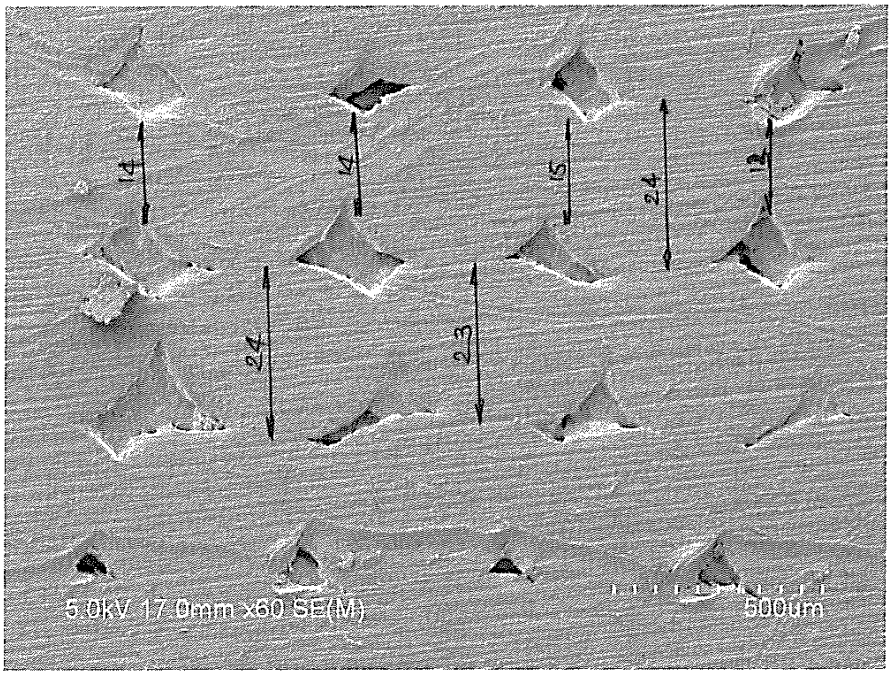

15˚

Fig. A1.12 Meso structure of FDM test part of 15˚(Average coalescence: 0.595)

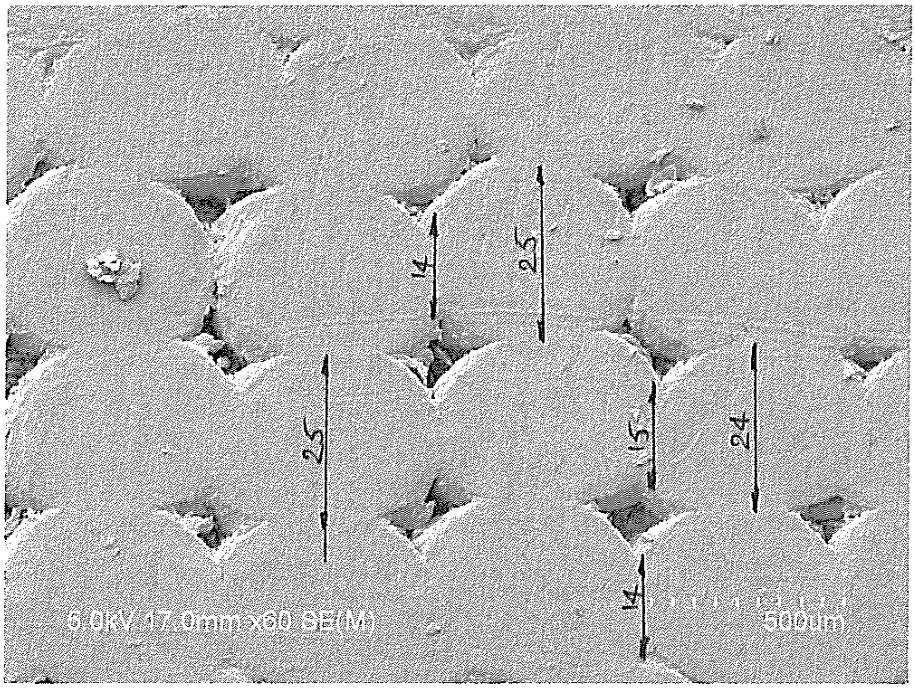

0˚

Fig. A1.13 Meso structure of FDM test part of 0˚ (Average coalescence: 0.595)

Table A1.1 Coalescence vs. angle

Layer Thickness	**0.5**	
Angle	***Predicted Coalescence***	***Measured Coalescence***
0˚	0.56	0.60
15˚	0.56	0.60
30˚	0.56	0.56
45˚	0.56	0.58
60˚	0.56	0.58
75˚	0.56	n/a
90˚	0.56	n/a

Appendix 2 Evaluation of test result with varying print speed and build style

Considering the variations in experimental results, it is understood that a statistical evaluation of some of the significant results reported is essential. The following table provide this with data from specific tables from different chapters:

Chapter 3: Table 3.2

Considering the results of Table 3.2, it may be noted that equivalent loads are calculated to avoid the effects of varying dimensions from one sample to the other. Considering the experimental trends, errors within $\pm 5\%$ are considered to be acceptable.

First, equivalent values are calculated using the dimensions of samples shown in Table A2.1.

Table A2.1 Equivalent loads and standard deviation of Table 3.2

Print Speed (mm/s)	Width (mm)	Height (mm)	Equivalent Load (N)					Standard Deviation (N)
			Part 1	Part 2	Part 3	Part 4	Average	
35	5.40	21.76	285.83	247.33	245.98	276.58	263.93	20.31
40	5.02	20.40	262.26	269.32	283.84	275.75	272.79	9.20
45	4.68	20.18	262.81	267.63	258.95	266.43	263.96	3.92
50	4.10	20.00	297.92	265.87	288.72	280.79	283.32	13.58
55	4.02	19.84	294.09	289.76	281.45	273.13	284.61	9.28
60	4.06	19.70	248.33	246.36	241.76	229.60	241.52	8.40

The average values and the confidence levels are shown in Table A2.2. Two types of preset standard errors were used to evaluate the confidence level: ($\pm 5\%$) and ($\pm 10\%$). Within the $\pm 5\%$

band width of the standard error, the confidence level varied with print speed and the lowest is 90.3%. Within the ±10N band width of the standard error, the lowest confidence level is 83.7%.

Table A2.2 Print speed vs. Confidence level

Print Speed (mm/s)	Model Average (N)	Confidence level (±5%)	Confidence level (±10N)
35	263.93	90.3%	83.7%
40	272.79	99.8%	98.5%
45	263.96	100%	100%
50	283.32	98.2%	92.7%
55	284.61	99.9%	98.4%
60	241.52	99.7%	99.1%

Based on the results shown in Table A2.2, the confidence levels of trials with varying speed are at above 90% confidence. It is concluded that the confidence level for all the results in Table 3.2 is 80%.

Chapter 3: Table 3.3

From Table 3.3, the result loads were obtained from the three point bending test. Equivalent loads were calculated for the confidence. The dimensions of the sample are shown in Table A2.3 below.

Table A2.3 Equivalent loads and standard deviation of Table 3.3

Print Speed (mm/s)	Width (mm)	Height (mm)	Equivalent Load (N)					Standard Deviation (N)
			Part 1	Part 2	Part 3	Part 4	Average	
9	4.50	20.44	288.89	292.75	268.27	265.95	278.97	13.81
10	4.22	19.492	287.16	258.28	266.40	285.35	274.30	14.21
13	4.10	19.96	281.03	306.78	302.97	302.46	299.23	12.24
15	4.00	19.80	276.43	258.24	272.05	267.68	268.60	7.77

The average values and the confidence levels are shown in Table A2.4. Two types of preset standard error were used to evaluate the confidence level: ($\pm$5%) and ($\pm$10N). Within the $\pm$5% band width of the standard error, the confidence levels varied again with print speed and the lowest being 97.3%. Within the $\pm$10N band width of the standard error, the lowest confidence level is 92.1%.

Table A2.4 Print speed vs. Confidence level

Print Speed (mm/s)	Model Average (N)	Confidence level ($\pm$5%)	Confidence level ($\pm$10N)
9	278.97	97.8%	92.6%
10	274.30	97.3%	92.1%
13	263.96	99.2%	94.9%
15	283.32	99.9%	99.4%

Based on the data given in Table A2.4, the results from experimental trials with varying speed are above the 90% confidence level. It is concluded that the confidence level for all the results in Table 3.3 is 90%.

Chapter 5: Table 5.1

From table 5.1, the result loads were obtained from the three point bending test. Maximum compressive loads were calculated for the confidence. The dimensions of the sample are shown in Table A2.5 below.

Table A2.5 Equivalent loads and standard deviation of Table 5.1

Build Style	Maximum Compressive Load (N)					Standard Deviation
	Part 1	Part 2	Part 3	Part 4	Average	
Flat Layer	220.000	233.666	227.000	228.333	227.250	5.63
Curved Layer	326.666	316.666	314.000	322.666	319.999	5.73

The average values and the confidence levels are shown in Table A2.6. Within the ±5% band width of the standard error, the confidence level varied with print speed and the lowest being 99.9%. Within the ±10N band width of the standard error, the lowest confidence level is 99.9%.

Table A2.6 Print speed vs. Confidence level

Build Style	Model Average (N)	Confidence level (±5%)	Confidence level (±10N)
Flat Layer	227.250	99.9%	99.9%
Curved Layer	319.999	100%	99.9%

Appendix 3 Load deflection of bending tests with varying printing speed

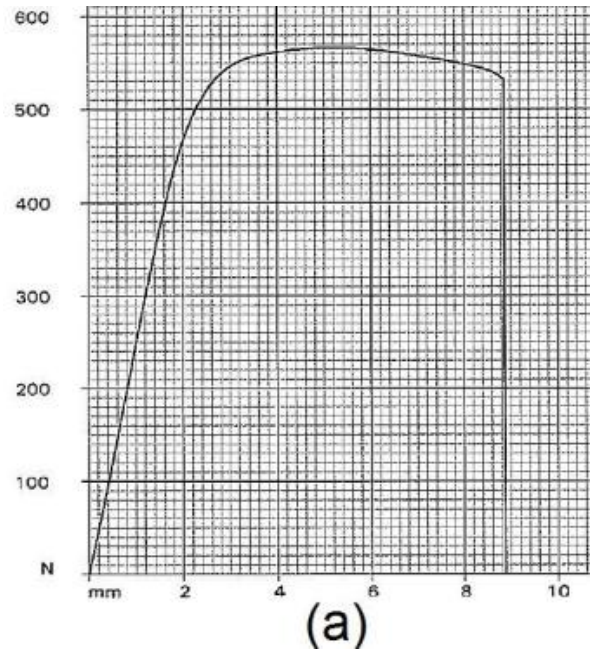

Fig. A3. 1 Load deflection diagrams from three point bending tests of thinner layer parts with print speed at 35 mm/s (Sample 1)

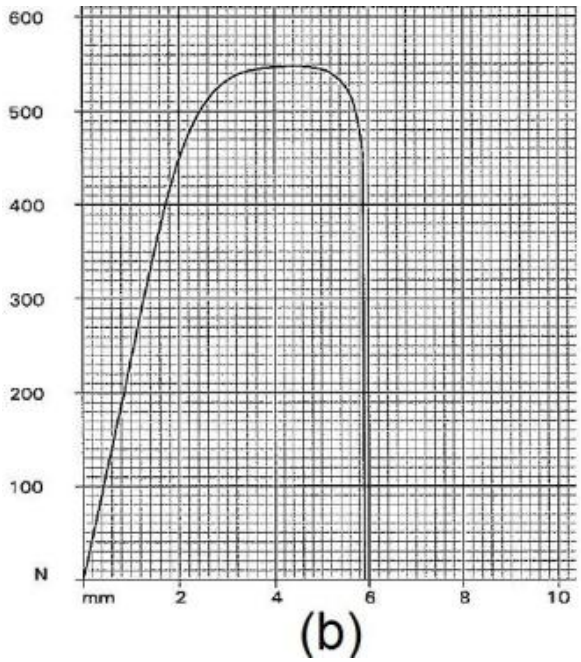

Fig. A3. 2 Load deflection diagrams from three point bending tests of thinner layer parts with print speed at 35 mm/s (Sample 2)

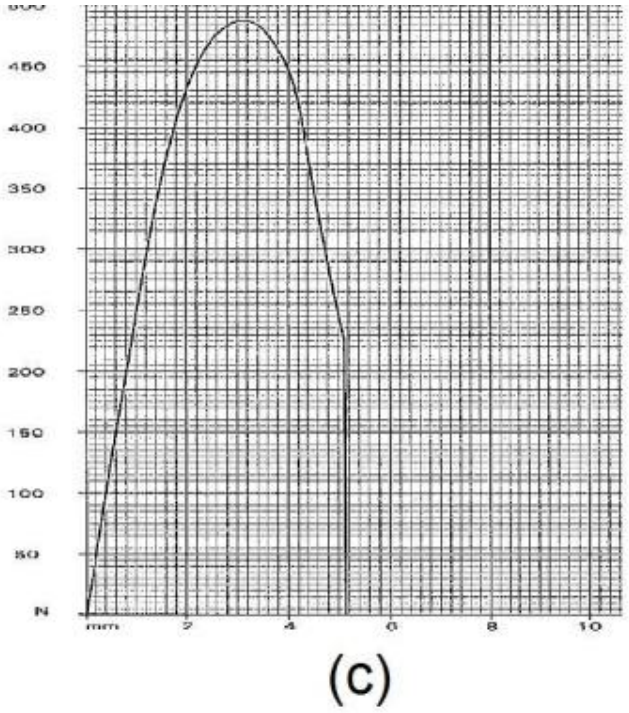

Fig. A3. 3 Load deflection diagrams from three point bending tests of thinner layer parts with print speed at 35 mm/s (Sample 3)

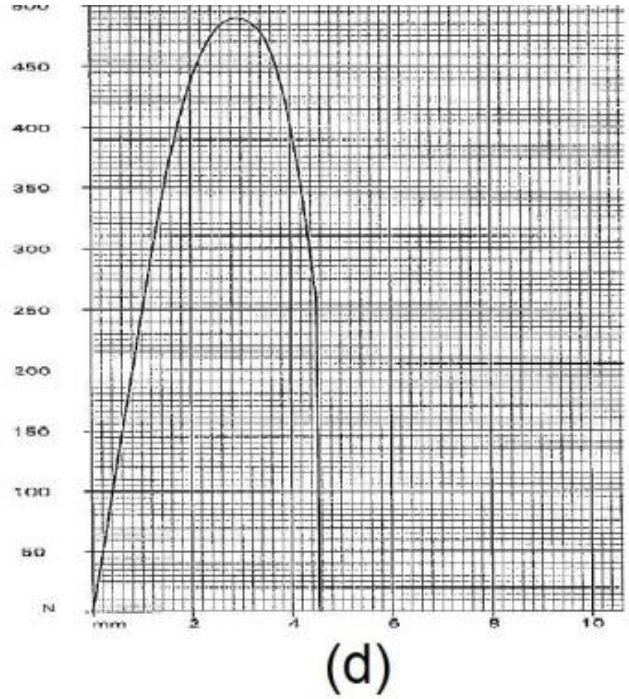

Fig. A3. 4 Load deflection diagrams from three point bending tests of thinner layer parts with print speed at 35 mm/s (Sample 4)

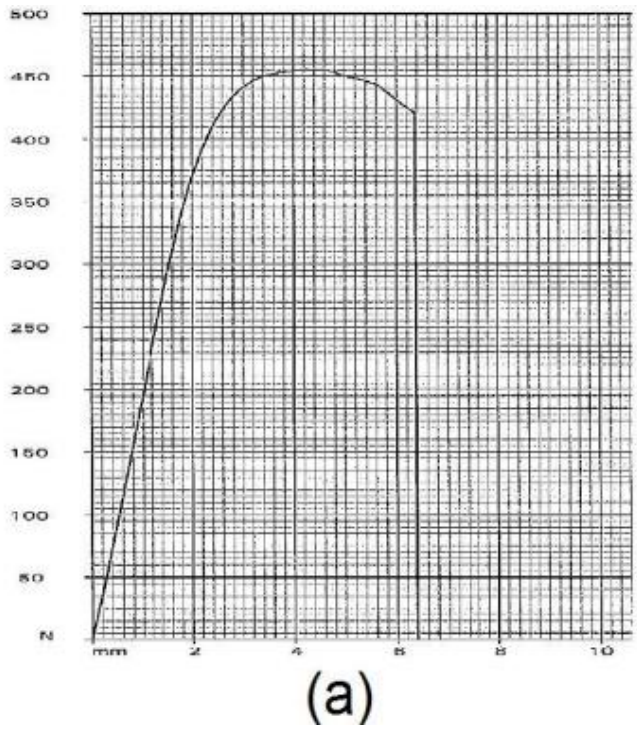

Fig. A3. 5 Load deflection diagrams from three point bending tests of thinner layer parts with print speed at 40 mm/s (Sample 1)

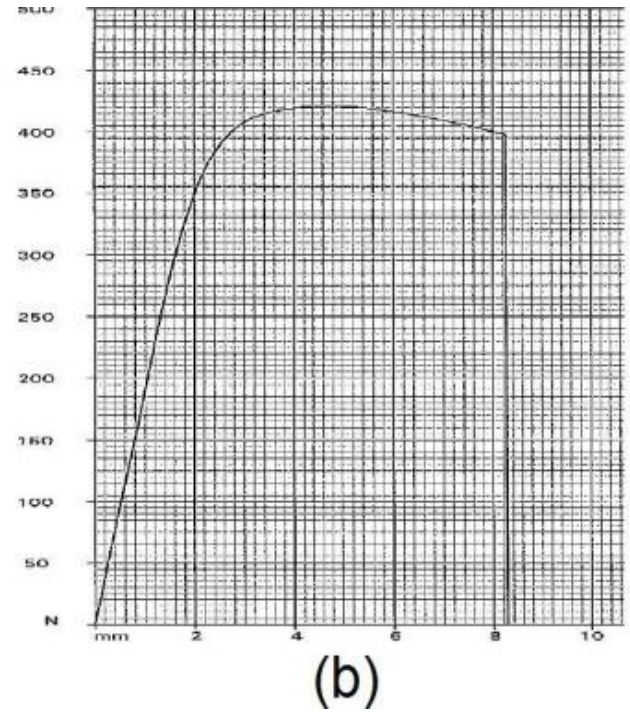

Fig. A3. 6 Load deflection diagrams from three point bending tests of thinner layer parts with print speed at 40 mm/s (Sample 2)

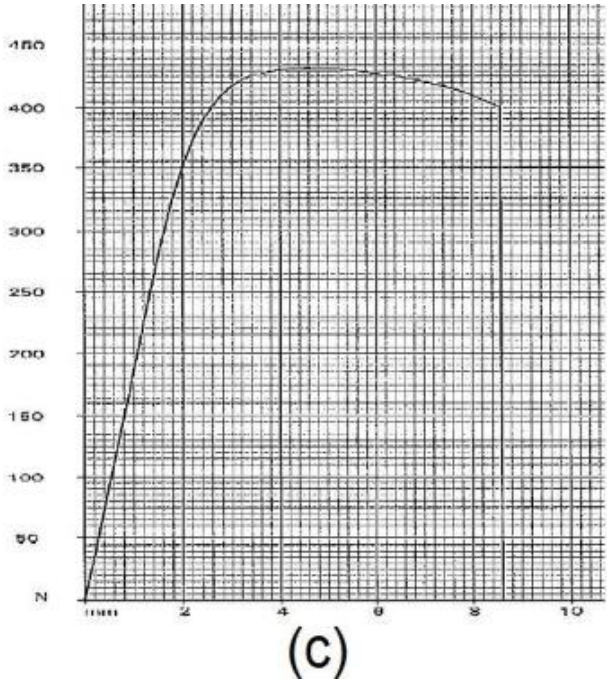

Fig. A3. 7 Load deflection diagrams from three point bending tests of thinner layer parts with print speed at 40 mm/s (Sample 3)

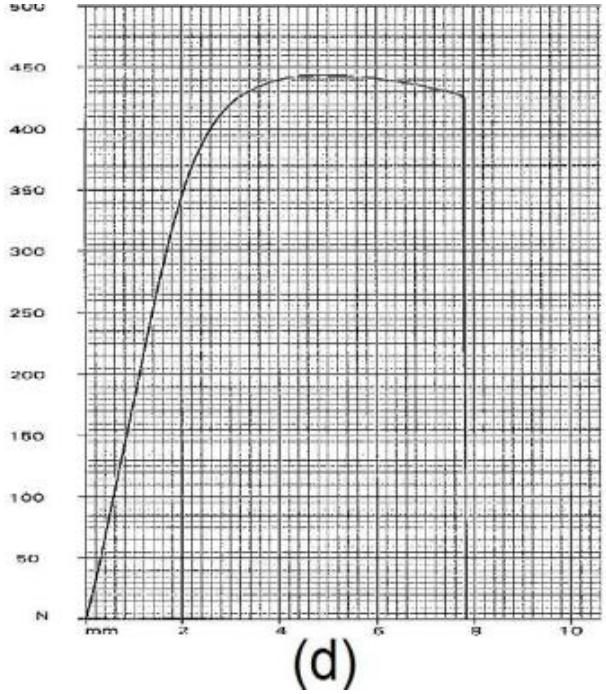

Fig. A3. 8 Load deflection diagrams from three point bending tests of thinner layer parts with print speed at 40 mm/s (Sample 4)

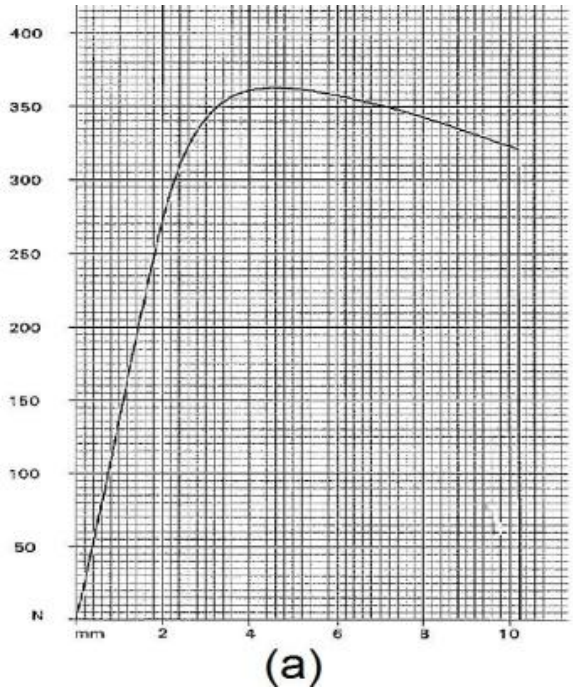

Fig. A3. 9 Load deflection diagrams from three point bending tests of thinner layer parts with print speed at 45 mm/s (Sample 1)

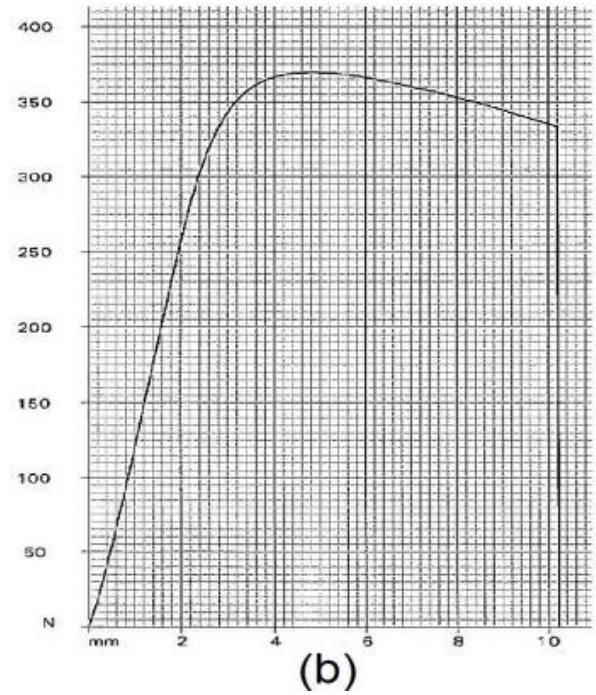

Fig. A3. 10 Load deflection diagrams from three point bending tests of thinner layer parts with print speed at 45 mm/s (Sample 2)

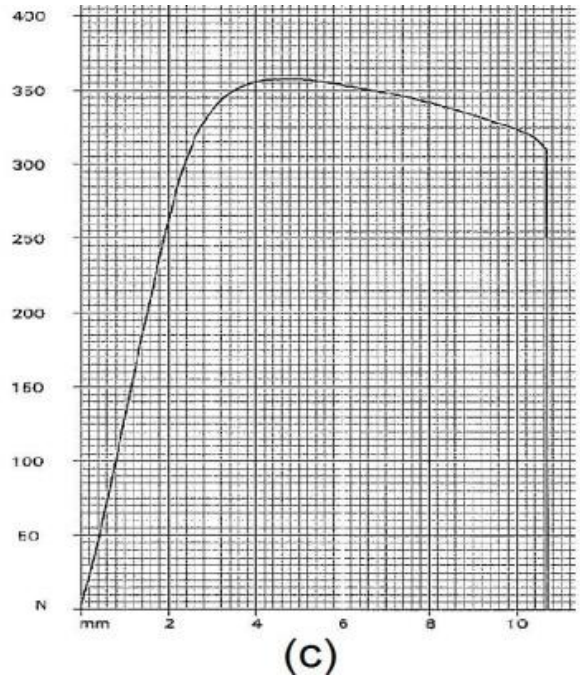

Fig. A3. 11 Load deflection diagrams from three point bending tests of thinner layer parts with print speed at 45 mm/s (Sample 3)

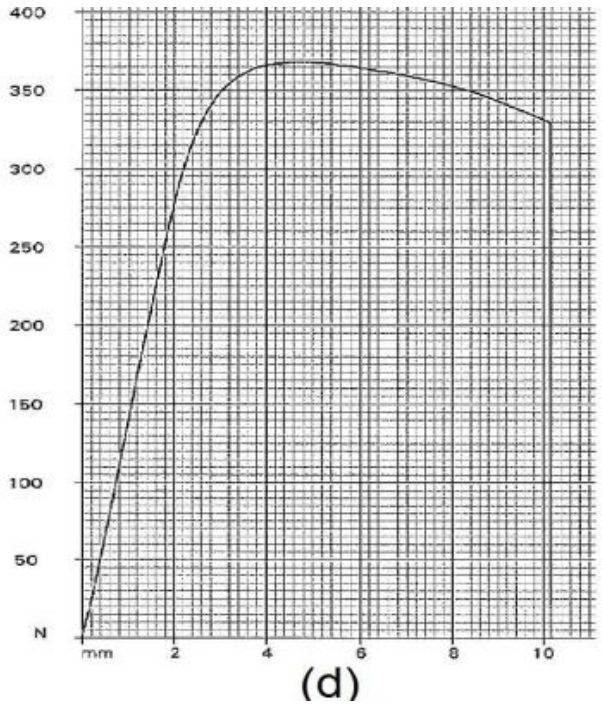

Fig. A3. 12 Load deflection diagrams from three point bending tests of thinner layer parts with print speed at 45 mm/s (Sample 4)

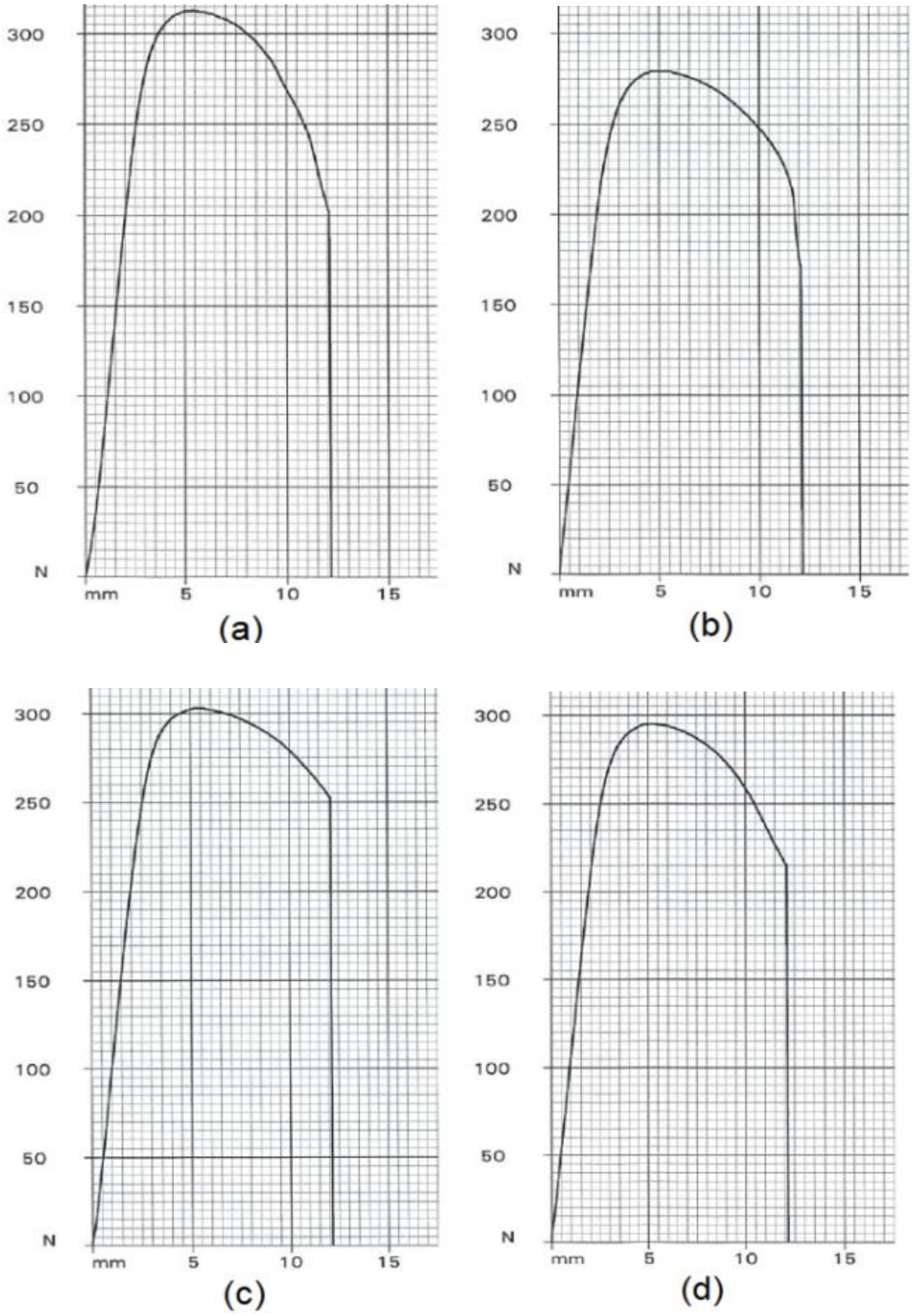

Fig. A3. 13 Load deflection diagrams from three point bending tests of thinner layer parts with print speed at 50 mm/s

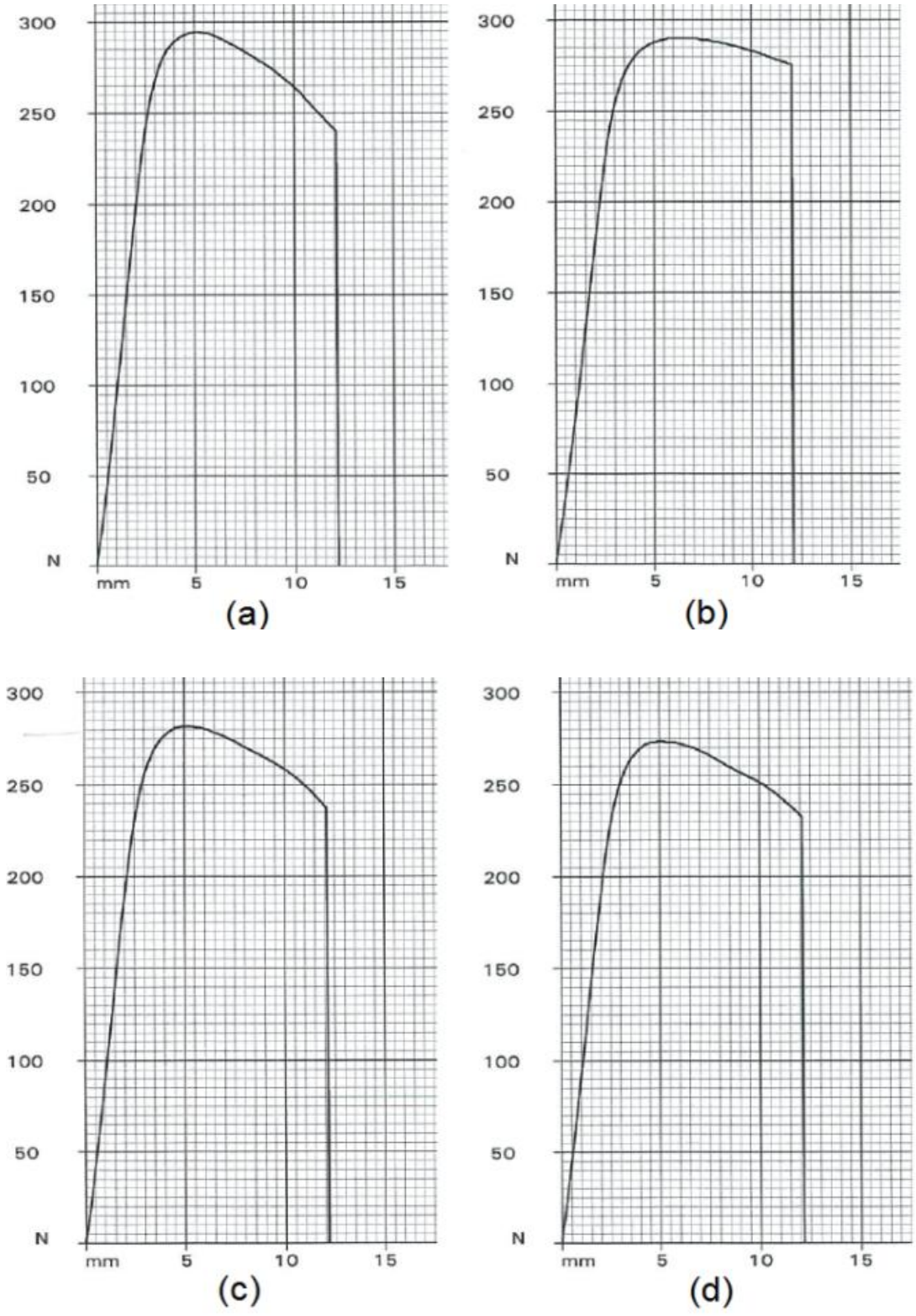

Fig. A3. 14 Load deflection diagrams from three point bending tests of thinner layer parts with print speed at 55 mm/s

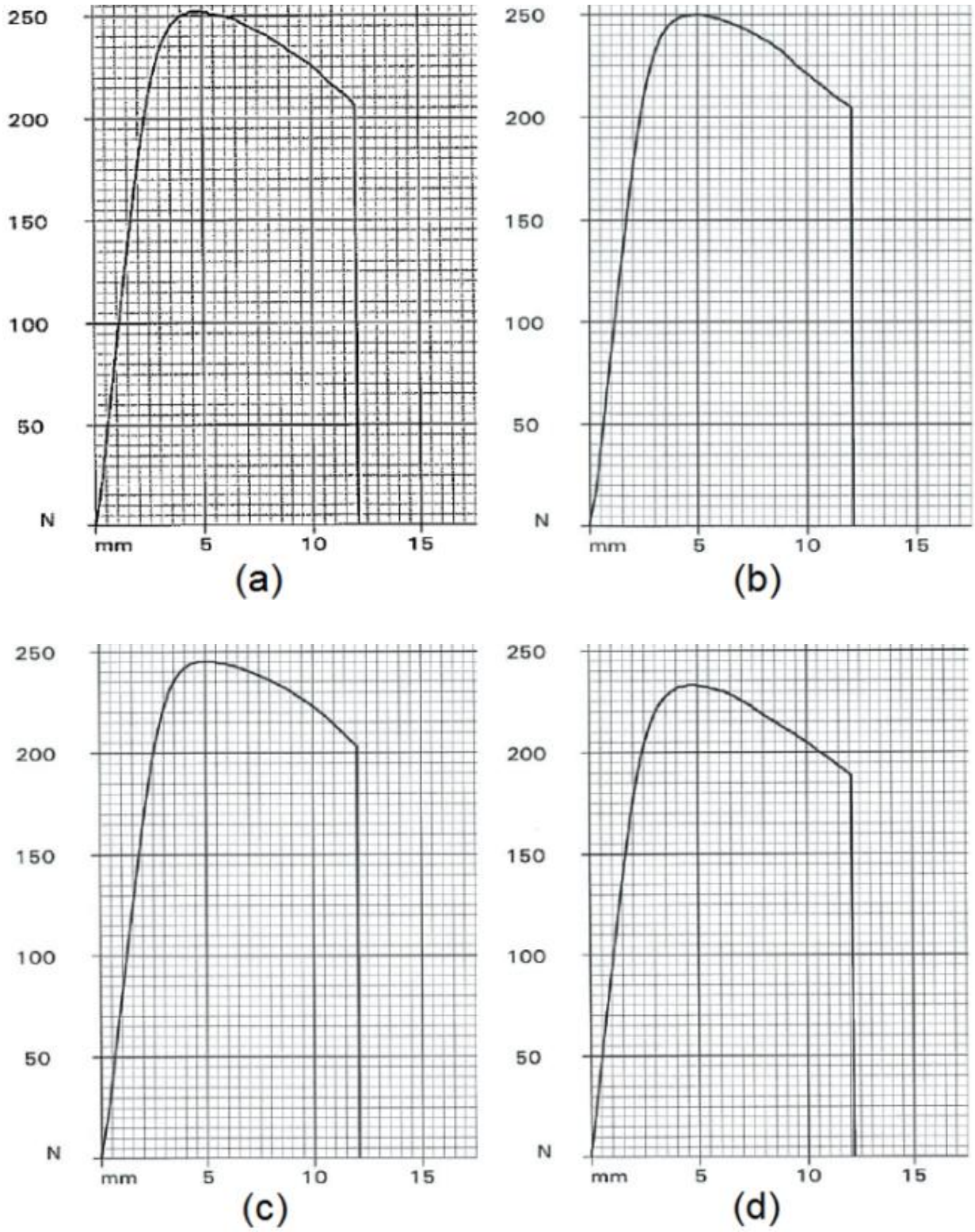

Fig. A3. 15 Load deflection diagrams from three point bending tests of thinner layer parts with print speed at 60 mm/s